UNIVERSITÉ DE STRASBOURG

ÉCOLE DOCTORALE SCIENCES CHIMIQUES

Institut de Chimie et Procédés pour l'Energie, l'Environnement et la Santé (ICPEES)

THÈSE présentée par :

Xiong Zhang

soutenue le : **13 Mai 2022**

pour obtenir le grade de : **Docteur de l'Université de Strasbourg**

Discipline/ Spécialité: Chimie / Chimie

Fe-N-C catalysts toward electrocatalytic oxygen reduction reaction

Catalyseurs Fe-N-C pour la réaction électrocatalytique de réduction de l'oxygène

THÈSE dirigée par :

Dr. Cuong Pham-Huu	Directeur de recherche, CNRS, Strasbourg
Dr. Sergey Pronkin	Maitre de conférences, Université de Strasbourg

RAPPORTEURS :

Prof. Timo Jacob	Professeur, Ulm University
Dr. Enrique Garcia-Bordejé	Directeur de recherche, CSIC, Zaragoza

---

AUTRES MEMBRES DU JURY :

Dr. Katia Araujo Da Silva	Maitre de conferences, Université Clermont Auvergne
Prof. Sylvie Bégin	Professeur, Université de Strasbourg

Xiong Zhang

Catalyseurs Fe-N-C pour la réaction électrocatalytique de réduction de l'oxygène

Résumé

L'électrocatalyseur Fe-N-C est en train de devenir un sujet de recherche stimulant avec de grands espoirs pour les dispositifs énergétiques de la prochaine génération en raison de sa haute activité intrinsèque ORR comparable à celle de l'électrocatalyseur des métaux du groupe du platine (PGM). Cependant, une stratégie de préparation très efficace avec une performance catalytique améliorée et une grande robustesse, employant des composants non critiques, est d'une grande importance pour le développement de l'électrocatalyseur Fe-N-C. L'identification de la nature du site actif pour le matériau Fe-N-C pyrolytique est toujours un sujet de débat animé en raison de la présence potentielle de sites actifs multiples.

Dans ce travail, nous avons développé des catalyseurs avec des atomes uniques de Fe décorés de N dans du carbone poreux par pyrolyse à haute température en utilisant des composants bruts rentables et non toxiques. La variation systématique de la composition des précurseurs N, et C et de divers agents structurants, ainsi que les conditions des différentes étapes nous ont permis de déterminer les paramètres optimaux pour une synthèse en plusieurs étapes. Diverses technologies caractéristiques, notamment TGA/TPD-MS, Raman, BET, XRD, XPS, HAADF-STEM et XAS ont été appliquées pour étudier la composition et la structure des catalyseurs Fe-N-C synthétisés. Les performances électrocatalytiques des catalyseurs ont été étudiées par des mesures de (R)RDE et des tests de durabilité accélérés. Cette étude nous a permis de démontrer que les électrocatalyseurs Fe-N-C avec une structure et une composition optimisées offrent des performances stables d'électroréduction de l'oxygène 4e- dans un électrolyte KOH 0.1 M avec une activité supérieure à celle des catalyseurs de référence 20% Pt/C. Plus important encore, la nature des sites actifs et la corrélation structure-performance des électrocatalyseurs tels qu'ils sont obtenus sont systématiquement étudiées. Ce travail vise à fournir une compréhension fondamentale du catalyseur Fe-N-C, à la fois du point de vue de la conception du matériau et de la nature des sites actifs, ce qui devrait favoriser le développement de la prochaine génération d'électrocatalyseurs pour la technologie des piles à combustible.

Abstract

Fe-N-C electrocatalyst is becoming a challenging research topic with great expectations for the next-generation energy devices due to its high intrinsic ORR activity comparable to platinum group metals (PGM) electrocatalyst. However, a high effective preparation strategy with improved catalytic performance and high robustness, employing noncritical components is of great importance for the development of Fe-N-C electrocatalyst, and the identification nature of active site for pyrolytic Fe-N-C material is still a topic of heated debate due to potential presence of multiple active sites.

In this work we developed catalysts with N-decorated single atom Fe catalysts in porous carbon by high temperature pyrolysis using cost-effective, non-toxic raw components. Systematic variation of composition of N, and C precursors and various structuring agents, as well as conditions of different steps allowed us to determine the optimal parameters for a multi-step synthesis. Various characteristic technologies, including TGA/TPD-MS, Raman, BET, XRD, XPS, HAADF-STEM and XAS have been applied to study the composition and structure of synthesized Fe-N-C catalysts. The electrocatalytic performance of the catalysts were studied by (R)RDE measurements and accelerated durability tests. This study allowed us to demonstrate that Fe-N-C electrocatalysts with optimized structure and composition provide stable 4e$^-$ oxygen electroreduction performance in 0.1 M KOH electrolyte with activity outperforming benchmark 20% Pt/C catalysts. Most importantly, the nature of active sites and structure-performance correlation of as-obtained electrocatalysts are systematically investigated. The work aims to provide fundamental understanding of Fe-N-C catalyst from both material design and natura of active sites which is believed to favor the development of next generation electrocatalyst for fuel cell technology.

Acknowledgements

It is a long but exciting journey for my Ph.D. study in Fracnce, but at the same time which is full of opportunities and challenges. This thesis is performed under the supervision of Dr. Cuong Pham-Huu and Dr. Sergey Pronkin at Institute of Chemistry and Processes for Energy, Environment and Health (ICPEES), UMR 7515, CNRS and Université de Strasbourg. First of all, I would like to express my sincere gratitude to all people who have contributed to this work and to those people who have given me help during my stay at Strasbourg. The China Scholarship Council (CSC) is greatly acknowledged for the financial supporting of my Ph.D. study, which not only provides me a great chance to complete Ph.D. study in France, but also gives me possibility to experience different cultures and lives.

Great appreciate to my supervisor Dr. Cuong Pham-Huu, for his scientific guidance, well-time encouragement and constant support during my research. I am deeply affected by his profound knowledges and optimistic attitude toward scientific research. He is so kind and patient which provides a great atmosphere in the lab for conducting research. I really enjoy the time of staying in the lab. I will be also grateful to my co-supervisor Dr. Sergey Pronkin for his patient guidance, help and fruitful discussion during my research, I would like to send my best wishes for his future academic career. Special thanks to Dr. Lai Truong-Phuoc, he is so generous to share his experience and knowledge with me and offer enormous help to me on both technical and scientific issues. There is no doubt that he is one of the most important person for my research career who leads the way for me to invlove in electrocatalysis. Drs. Giuliano Giambastiani and Tristan Asset are also equally appreciated for great efforts of management of pubilications. I have learned a lot from them, and especially Giuliano who he is not only an excellent scienctist, but also a genius artist.

I am indebted to Prof. Sylvie Bégin (IPCMS, Université de Strasbourg), Dr. Katia Araujo Da Silva (Université Clermont Auvergne), Dr. Prof. Timo Jacob (Ulm University), and Dr. Enrique Garcia-Bordejé (CSIC) who gave me the honor and pleasure to be part of the jury of my PhD thesis, judging constructively my work.

I would like to thank my former supervisor Prof. Wei Chu during my master period and my senior Dr. Wei Wang, who recommended me to come to the lab of Dr. Cuong Pham-Huu. Special thanks to Dr. Wei Wang for the warm cares and helps in the daily life in the early days of my coming to France.

Many thanks would be given to Dr. Jean-Mario Nhut, Dr. Cuong Duong-Viet, Dr. Housseinou Ba, Dr. Fabrice Vigneron, Dr. Anurag Mohanty, Dr. Zhenxin Xu, Dr. Mallikarjuna as well as pretty and brave Dr. Camila Rivera-Carcamo, for their kindly help and accompany, it is great pleasure to know you all.

I would like to thank Dr. Vasiliki Papaefthimiou, Secou Sall, Alain Rach, Thierry Romero, Christophe Melart, Christophe Sutter, Dr. Thierry Dintzer and other technical staff as well as administrative team in ICPEES for their kindly technical support and help.

My thanks are also equally given to all my colleagues Camille Voros, Franck Razafindrainibe, Quentin Maerklen, Lu Fang, Tuan Hoang Trinh for their warm accompany and help in my daily life.

Many thanks to all my Chinese friends in Strasbourg- Dingkai Chen, Han Peng, Qianwen Zheng, Liping Zhong, Yu Zhang, Jinming Zhang, Qingyang Xi for their nice accompany and help in my daily life.

In the end, I would like to express sincerely gratitude to my family for their forever love and support.

Xiong ZHANG 22th February, 2022, Strasbourg, France

Table of Content

Résumé

1. Introduction

La réduction de l'utilisation des combustibles fossiles et l'amélioration du rendement de conversion des sources d'énergie propres et renouvelables deviennent une priorité urgente de la chimie et du génie chimique modernes. Aborder ces objectifs sont des questions cruciales, non seulement liées à l'épuisement constant des combustibles fossiles, mais aussi pour faire face à toutes les principales préoccupations environnementales et climatiques causées par leur utilisation massive. La technologie basée sur l'utilisation des piles à combustible suscite un grand intérêt dans l'exploration de systèmes énergétiques durables, car elle permet de combiner des émissions zéro carbone avec une efficacité de conversion énergétique élevée pour le même dispositif [1]. Malgré cela, l'exploitation des dispositifs de piles à combustible est limitée par le coût élevé de ses composants, en particulier des matériaux servant d'électrodes qui sont à base de métaux nobles, chers et peu abondants. Une concentration de l'ordre de 0,4 mg· cm^{-2} de platine est généralement nécessaire à la cathode de la pile à combustible pour réaliser la réaction de réduction de l'oxygène en raison d'une cinétique très lente de cette réaction [2]. Par conséquent, la synthèse de matériaux servant de base aux électrodes, à faible coût avec des performances catalytiques améliorées et d'une grande robustesse, utilisant des composants non critiques, devient un sujet de recherche stimulant avec de grandes attentes pour les dispositifs énergétiques de prochaines générations.

La recherche de systèmes électrocatalytiques plus robustes a été fortement active pendant les dernières décennies. Les premiers travaux se sont principalement concentrés sur l'étude des catalyseurs moléculaires, plus précisément des complexes macrocycliques Fe-N_4 [3-5], tandis qu'une activité et une stabilité plus élevées peuvent être obtenues par une approche de pyrolyse à haute température (appelée catalyseur Fe-NC) [6, 7]. La nature du site actif du matériau pyrolytique Fe-NC fait toujours l'objet d'un débat dans le domaine en raison de la présence potentielle de plusieurs sites actifs tels que des sites dopés N sans métal, des nanoparticules à base de Fe et des fragments FeN_xC_y[8]. Dans le même temps, l'identification des sites actifs est d'une grande importance dans la conception rationnelle des catalyseurs d'électrocatalyse présentant de meilleures performances et stabilité. Malgré la pluralité des sites actifs existant dans le catalyseur Fe-NC, le site actif le plus probable proposé dans la littérature est largement revendiqué comme étant des analogues structuraux du centre Fe-N_4. La plupart des travaux se sont concentrés sur l'amélioration des performances des catalyseurs dans les processus électrocatalytiques clés [9-11]. Il est communément admis que le contrôle des caractéristiques structurelles électroniques et géométriques des sites métalliques actifs est l'outil clé pour obtenir des catalyseurs présentant des performances uniques et améliorées dans ce domaine de recherche très concurrentiel [12, 13].

Certains d'entre nous ont récemment proposé une technologie synthétique écologique (verte) et polyvalente pour la préparation de matériaux à base de carbone mésoporeux enrichis en azote à partir de matériaux de base non toxiques, issus des produits de l'alimentaire, et bon marché [14, 15]. Une telle approche a été utilisée avec succès pour obtenir des poudres aux structures de mousse 3D hiérarchiquement organisées et aux composites organiques-inorganiques [16-18], qui seront ensuite utilisés en tant que systèmes sans métal efficaces et stables pour catalyser un nombre relativement important de procédés chimiques industriels. Les sources de carbone et azote utilisées pour la synthèse de ces nouveaux matériaux ont été sélectionnées parmi des matières premières solides couramment disponibles où l'eau est utilisée comme solvant dans la plupart des cas. Le D-glucose ($C_6H_{12}O_6$) a été sélectionné comme source de carbone, un agent levant (c'est-à-dire carbonate d'ammonium $(NH_4)_2CO_3$) comme source d'azote et de l'acide citrique ($C_6H_8O_7$) comme support sacrificiel, pour la fixation de l'ammoniac libéré lors de la décomposition du carbonate sous forme de citrate d'ammonium ($HO\text{-}C_3H_4(COO)_3H_x(NH_4)_{3-x}$) avec x = 0-3). Des traitements thermiques successifs et contrôlés des matériaux ont conduit par la suite à des réseaux carbonés mésoporeux présentant des surfaces spécifiques relativement élevées (de l'ordre de 150 $m^2 \cdot g^{-1}$) et des teneurs en azote allant jusqu'à 5 % en poids. Dans cette thèse, le D-glucose de qualité alimentaire et/ou l'acide citrique comme précurseur de carbone, les sels d'ammoniac inorganiques ou l'urée comme source d'azote, sont utilisés comme squelette principal pour la préparation du catalyseur Fe-NC. Les propriétés physico-chimiques et les performances électrocatalytiques pour la réaction ORR ainsi que la relation structure-performance des électrocatalyseurs obtenus sont systématiquement étudiées. En particulier, l'effet de l'ajout de médiateur structurel (KSCN, SiO_2 et noir de carbone) sur la nature des sites actifs et sur l'activité des produits finaux a également été examiné. Le présent travail vise à fournir une compréhension fondamentale du catalyseur Fe-NC à partir de la conception des matériaux et de la nature des sites actifs, ce qui favoriserait le développement d'électrocatalyseurs de prochaine génération pour la technologie des piles à combustible.

2. Résultats et discussions

2.1 Catalyseur Fe-NC inséré dans le réseau de carbone dopé avec de l'azote pour la réaction de réduction de l'oxygène.

Dans ce travail, un protocole original a été développé pour la synthèse de catalyseurs contenant des atomes de fer isolés stabilisés par des atomes de carbone et d'azote, Fe-NC, à haute densité. Le catalyseur est préparé à partir de matériaux de base bon marché et de qualité alimentaire: le D-glucose sert comme principal précurseur de carbone, le $(NH_4)_2CO_3$ comme source d'azote et l'acide citrique comme composant sacrificiel pour stabiliser les ions Fe^{3+} et NH_4^+. La combinaison d'ions citrate chélatants avec le ligand auxiliaire monodentéSCN$^-$ s'est établie comme une "porte ouverte" pour accueillir les ions fer solubles dans l'eau sous la forme de fragments Fe-NC dans les réseaux CN (phase pré-catalyseur, Fe/NSMC-W). Le pré-catalyseur ainsi synthétisé est alors traité thermiquement en présence de NH_3 (dopage thermochimique) pour obtenir le catalyseur final (Fe/NSMC-SHT). Les rôles spécifiques de l'effet du traitement KSCN et NH_3 ont été étudiés.

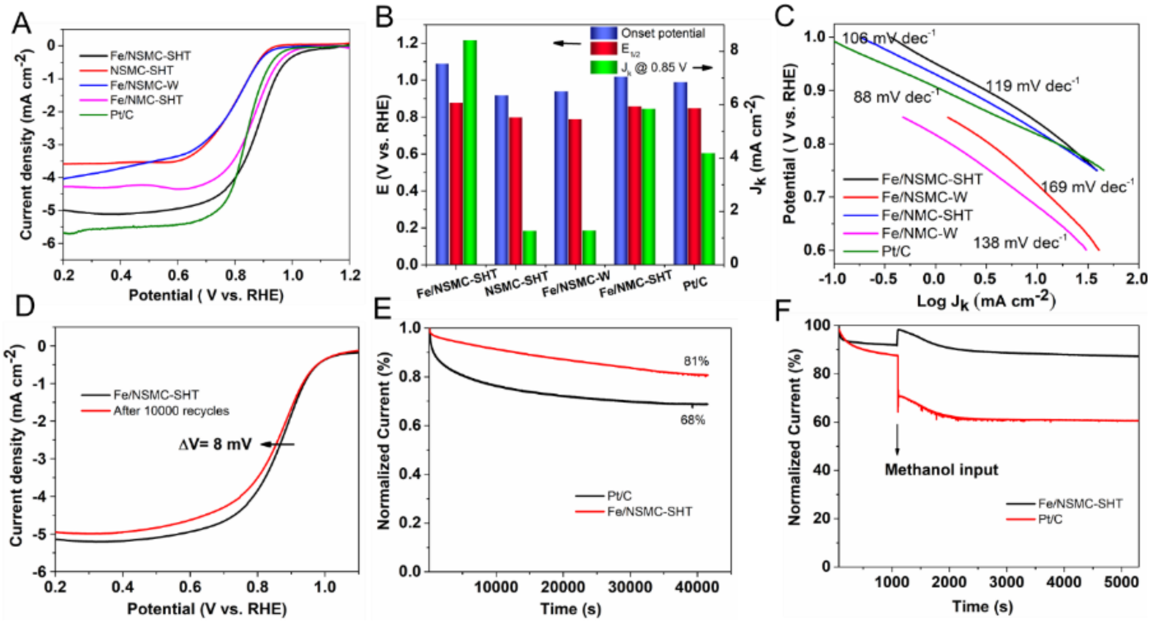

Figure 1. (A) Courbes de polarisation ORR, (B) Potentiel d'apparition, potentiel demi-onde ($E_{1/2}$) et densité de courant cinétique (J_k) pour différents catalyseurs, (C) Courbes de Tafel pour les catalyseurs préparés, (D) Test de durabilité accéléré (ADT) pour Fe/NSMC-SHT, (E) Réponse CA pour Fe/NSMC-SHT, (F) Test de tolérance au méthanol pour Fe/NSMC-SHT.

Le résultat montre que le KSCN sert de médiateur de surface permettant d’empêcher la génération de nanoparticules à base de Fe, maximisant ainsi la présence de sites actifs de Fe sous forme d’atomes isolés. Le post-traitement avec NH_3 introduit en outre les groupements fonctionnels contenant des terminaisons N hautement basiques, et une meilleure exposition des sites actifs de Fe atomique, produisant ainsi une porosité plus abondante et une accessibilité des réactifs plus aisée. L'existence de sites Fe sous forme d’atomes isolés et la nature des sites actifs sur le catalyseur modèle (Fe/NSMC-SHT) sont extensivement caractérisées par la microscopie électronique à transmission en champ sombre annulaire à angle élevé (HAADF-STEM), et par la spectroscopie d'adsorption aux rayons X (XAS). Les résultats révèlent que le catalyseur Fe/NSMC-SHT présente une morphologie inattendue avec une phase mixte contenant des atomes de Fe isolés et des petites particules de Fe. Les analyses détaillées par l'ajustement d'une structure fine d'adsorption de rayons X étendue (EXAFS) ont indiqué que le mélange contenant des sites de fer N-coordonnés (Fe-NC) sous forme d'atomes uniques et des nanoparticules sont des espèces polyatomiques à l’interface entre l'oxyhydroxyde de fer et une matrice à base de carbone dopé à l'azote tel qu'identifié. Le catalyseur Fe/NSMC-SHT ainsi préparé présente des activités en électrocatalyse, pour la réaction de réduction d’oxygène réalisée en milieu alcalin, qui se rangent parmi les meilleures reportées à l’heure actuelle pour les catalyseurs à base de fer sous forme d’atomes isolés (Figure. 1). En conclusion de cette étude nous avons réussi à préparer des catalyseurs à base de fer, une partie sous forme d’atomes isolés et une autre sous forme de nanoparticules, par une méthode de synthèse simple, faisant appel à des matières premières à base alimentaire, et qui présente des performances en électrocatalyse parmi les meilleures pour cette catégorie d’électrocatalyseurs.

2.2 Catalyseur à base d'atomes isolés FeN_4-Cl dispersés dans un réseau mésoporeux de carbone dopé à l'azote utilisant la silice comme porogène.

Dans les travaux précédents, nous avons reporté une nouvelle voie de synthèse des catalyseurs à base d'atomes isolés de fer, stabilisés par des liaisons N et C, avec l'aide de ligand auxiliaire thiocyanate monodentate et un traitement thermochimique avec de NH_3. Dans ce présent chapitre, une nouvelle stratégie est rapportée, et permet d'éviter le traitement thermochimique sous NH_3 en utilisant uniquement un sel inorganique $(NH_4)_2CO_3$ et l'acide citrique comme précurseur d'azote et de carbone respectivement. L'adjonction d'un porogène à base de silice permet l'obtention d'un catalyseur avec une structure poreuse et hiérarchisée, contenant des micropores interconnectés, des mésopores bimodaux et des macropores avec une distribution de pores ajustable. L'interconnectivité entre les différents réseaux poreux permet d'augmenter l'accessibilité des sites actifs aux réactifs et d'améliorer les performances en électrocatalyse. Il est important de noter que la concentration des atomes d'azote peut être finement ajustée en utilisant des sources séparées pour le carbone et l'azote, ce qui permet une meilleure optimisation des performances électrochimiques du catalyseur. Le mécanisme de formation respectif du carbone poreux hiérarchique décoré avec des atomes isolés de fer est proposé sur la Figure 2.

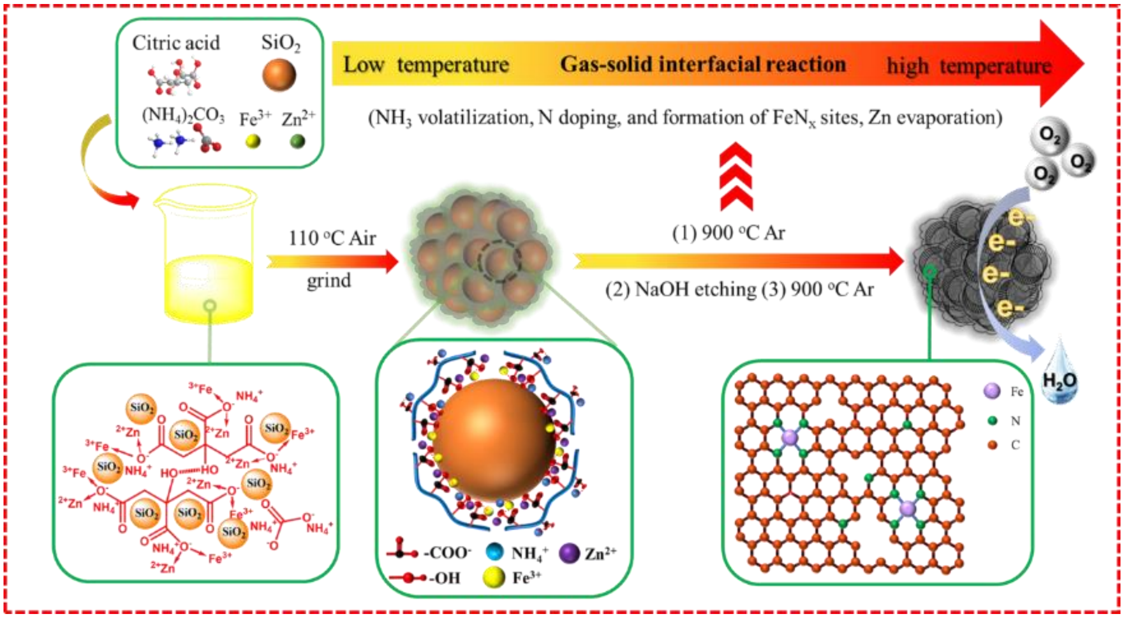

Figure 2. Schéma du mécanisme proposé pour la formation de carbone poreux hiérarchique dopé N décoré de Fe atomique.

Les analyses HAADF-STEM et XAS montrent que le catalyseur modèle contient des sites de fer atomiquement dispersés, principalement sous la forme de noyaux Cl-FeN_4 avec l'ion métallique logé dans une sphère de coordination pyramidale. D'autre part, l'influence de la teneur en N dans le mélange de précurseurs et les concentrations en Fe dans les catalyseurs sur l'activité ORR ont été systématiquement étudiées, afin de déterminer la relation entre les performances électrochimiques et les caractéristiques du catalyseur. Les résultats démontrent que le catalyseur ^{2}Fe/NHPC^{5AC} présente des performances électrochimiques en ORR optimales (Figure 3). Il semblerait que l'utilisation simultanée du $ZnCl_2$ et de SiO_2 joue un rôle crucial dans la production de sites uniques Cl-FeN_4 avec une densité de sites plus élevée, garantissant une activité électrochimique la plus élevée en ORR. Les résultats des caractérisations ont permis d'identifier la nature des sites actifs comme étant la fraction Cl-FeN_4 combinée avec des sites N pyridiniques.

Il est à noter également que les fragments Cl-FeN_4 sont aussi considérés comme les sites les plus actifs pour la réaction ORR, tandis que les nanoparticules à base de Fe ne montrent aucune activité dans des conditions réactionnelles en milieu alcalin.

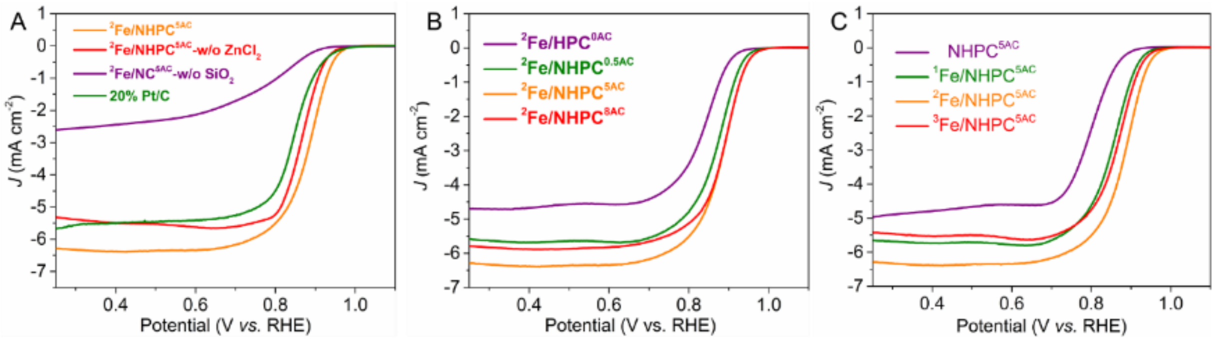

Figure 3. Courbes LSV (A) des catalyseurs de contrôle, (B) les catalyseurs produits par différentes additions de $(NH_4)_2CO_3$, et (C) les catalyseurs obtenus par diverses charges de Fe. Toutes les données sont enregistrées sous O_2 saturée en solution KOH à 0.1 M pour des vitesses de balayage de 10 mV· s^{-1} et de rotation de 1600 tours par minute.

2.3 Mise en œuvre d’une procédure de fabrication des électrocatalyseurs à base de Fe-NC pour la réaction d’ORR.

Dans le précédent travail, nous avons proposé une nouvelle voie de synthèse de carbone poreux hiérarchisé décoré avec des atomes uniques de fer en utilisant du $(NH_4)_2CO_3$ et de l'acide citrique comme sources d’azote et de carbone respectivement pour être utilisé comme électrocatalyseur pour la réaction d’ORR. Dans ce présent chapitre, le D-glucose est utilisé comme seule source de carbone. Le glucose est également connu comme excellent agent chélatant pour l'ancrage du cation métallique (ici les ions Fe^{3+}) dans la solution de précurseur [19, 20]. Plus important encore, le rendement de carbonisation du glucose, qui est plus élevé que celui de l'acide citrique, permet de produire des catalyseurs à plus grande échelle en vue des transferts technologiques futurs.

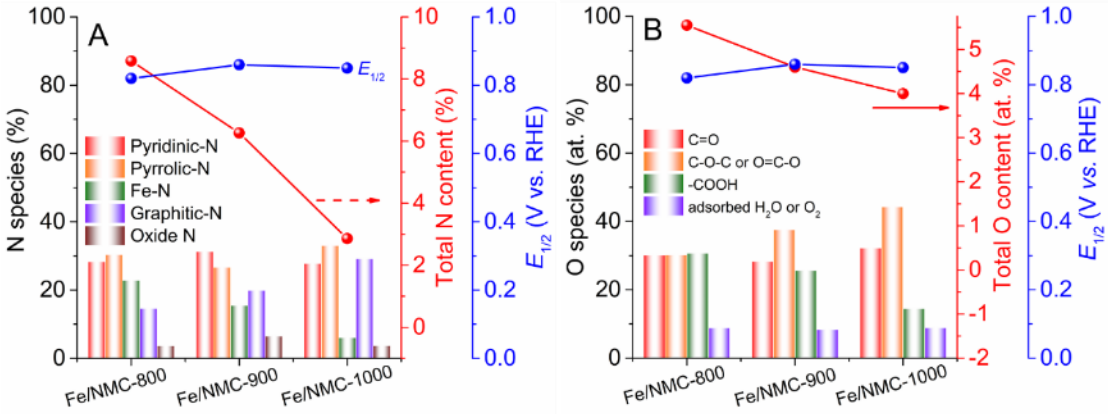

Figure 4. (A) Corrélation entre la composition en azote et l'activité ORR; (B) corrélation entre la composition en oxygène et l'activité ORR.

La synthèse consiste aussi à utiliser du chlorure d'ammonium (NH_4Cl) comme source d'azote tout au long du procédé de préparation, ainsi que la silice comme agent de porogène pour la fabrication des structures hôtes à base de carbone poreux hiérarchisé qui sera décoré par la suite avec des atomes isolés de Fe dispersés de manière homogène sur la surface de l'électrocatalyseur. On constate également que la température de pyrolyse a une influence significative sur l'activité ORR du catalyseur final. En établissant une relation structure-performance, l'activité ORR semble être fortement dépendante de la température de pyrolyse, et l'activité en ORR est influencée par la densité des sites actifs ainsi que la conductivité électronique (Figure 4). Le catalyseur optimal, obtenu à une température de pyrolyse de 900 °C, présente une excellente activité ORR ($E_{1/2}$ = 0,86 V), une excellente durabilité ainsi qu'une résistance à la désactivation en présence du méthanol qui surpassent celles obtenues sur le catalyseur Pt/C commercial en milieu alcalin. En milieu acide, le Fe/NMC-900 présente également une activité ORR relativement intéressante, avec $E_{1/2}$ de 0,63 V et une bonne stabilité. Les résultats obtenus confirment l'importance de la température de pyrolyse sur les propriétés géométriques et électroniques du catalyseur, qui à leur tour, influencent fortement l'activité en ORR.

2.4 Effet coopératif entre les atomes uniques de Fe et des nanoparticules Fe_3O_4/Fe_3C supportés sur une structure hôte hybride de nanofeuillets de graphène/noir de carbone pour la réaction d'ORR.

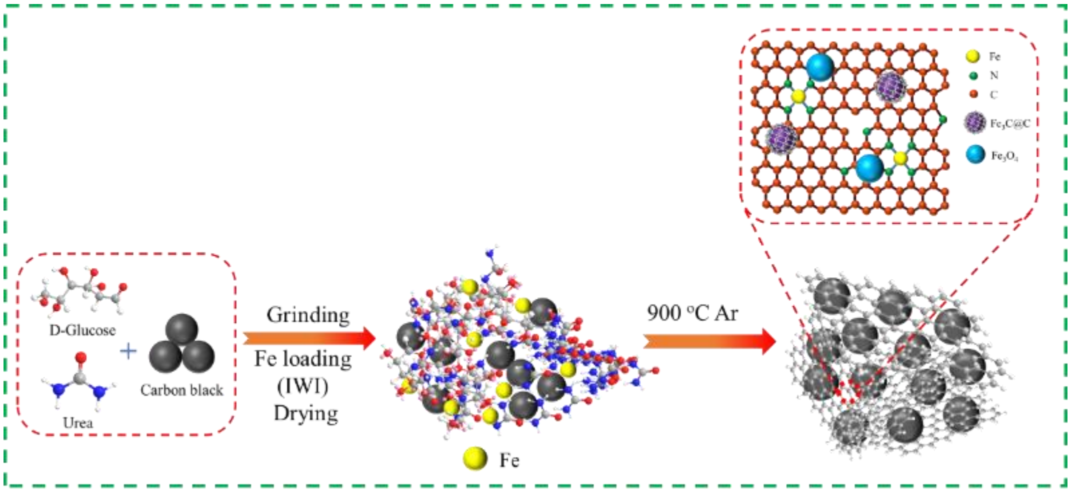

Figure 5. Schéma de la procédure de fabrication de l'électrocatalyseur hybride $^{4.5}$Fe@NGC/CB.

Dans le précédent travail, nous avons utilisé deux étapes thermochimiques à haute température en utilisant le SiO_2 comme porogène pour la préparation d'électrocatalyseurs à sites uniques en Fe hautement actifs pour la réaction d'ORR. Dans le présent travail, nous investiguons l'influence de l'utilisation des nanoparticules de noir de carbone à la place des nanoparticules de SiO_2 qui nécessitent un post-traitement fastidieux pour l'obtention de la porosité finale. En effet, contrairement aux nanoparticules de SiO_2, celles de noir de carbone permettent une amélioration en rendement du matériau final, mais elles participent également dans la génération de l'hétérostructure souhaitée sans avoir besoin d'avoir recours au post-traitement pour enlever les nanoparticules de SiO_2 comme précédemment. Plus précisément, nous développons dans ce chapitre une stratégie facile et évolutive pour améliorer la préparation des catalyseurs hybrides enrichis avec d'abondantes fractions FeN_x en interaction avec une couche de carbone hautement graphitique encapsulant des nanoparticules Fe_3C/Fe_3O_4. La synthèse est réalisée en utilisant une imprégnation d'humidité naissante d'une solution aqueuse de Fe directement sur un mélange contenant glucose, urée et noir de carbone, traitée ensuite directement par l'unique étape de pyrolyse (Figure 5). L'électrocatalyseur, tel que préparé, présente une hétérostructure composée de noir de carbone dopé avec des atomes d'azote, jouant le rôle d'échafaudage de carbone primaire, et de graphène dopé N entrelacé comme phase de carbone secondaire, présentant une structure poreuse hiérarchique avec un mélange de différents types de pores, e.g. micro-, méso- et macropores. également produits en utilisant différentes quantités de précurseur de Fe. Le catalyseur optimal avec une quantité appropriée d'ajout de Fe ($^{4.5}$Fe@NGC/CB) affiche une performance ORR supérieure (Figure 6A). Une série d'expériences de contrôle telles que la lixiviation acide de $^{4.5}$Fe@NGC/CB et le test d'empoisonnement KSCN ont révélé sans ambiguïté que les fractions FeN_x sont de véritables sites actifs (Figure 6B et Figure 6D) vers l'ORR et les nanoparticules de Fe_3O_4 ne montrent aucune activité mais exerce un effet de promotion positif sur l'activité des sites FeN_x via une interaction électronique (Figure 6C).

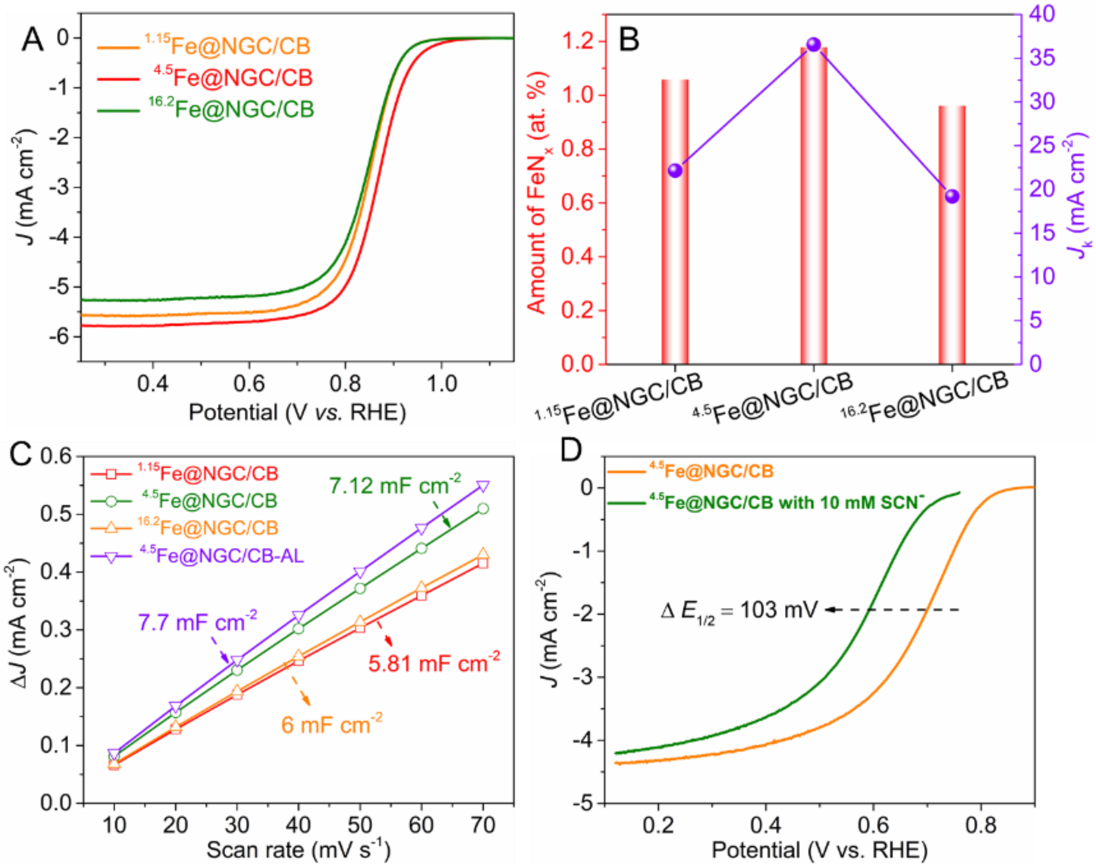

Figure 6. (A) Les courbes de polarisation en régime permanent des échantillons produits par l'utilisation de différents précurseurs de Fe à des vitesses de balayage de 10 mV·s^{-1} et de rotation de 1600 tr/min en milieu réactionnel constitué par de l'O_2 - électrolyte KOH à 0,1 M saturé; (B) La corrélation entre la quantité de fractions FeN_x et l'activité ORR pour les échantillons avec des charges de Fe variables; (C) Courbes d'ajustement linéaire des courants capacitifs par rapport aux taux de balayage, en mV·s^{-1}, pour les échantillons avec des charges de Fe variables ainsi que l'échantillon $^{4.5}$Fe@NGC/CB-AL après une lixiviation à l'acide; (D) Courbes LSV de l'échantillon $^{4.5}$Fe@NGC/CB, avant et après l'ajout de 10 mM de KSCN, dans une solution saturée en O_2 de H_2SO_4 à 0,5 M pour des vitesses de balayage de 10 mV· s^{-1} et de rotation de 1600 tr/min.

3. Conclusions et perspectives

En conclusion, nous avons pu développer des nouvelles méthodes de synthèse des catalyseurs électrochimiques à base de Fe dispersé atomiquement dans une matrice carbonée, dopée avec des atomes d’azote, en utilisant des matières premières à base de produits alimentaires non toxiques. La synthèse met également en œuvre des composés chimiques simples tels que KSCN, SiO_2, $ZnCl_2$, qui jouent le rôle de stabilisateurs pour la formation de sites Fe atomiquement dispersés dans l’ensemble du catalyseur. Nous avons pu mettre en évidence les bénéfices en utilisant une étape de post-traitement sous ammoniac en vue d’améliorer par l’intermédiaire des groupements fonctionnels riches en azote l’exposition et la stabilisation des sites actifs à base de fer pour la réaction d’ORR. Les études d’optimisation ont permis d’ajuster la composition chimique des différents composites, à savoir la concentration en fer et en azote pour la stabilisation des sites actifs, la température de pyrolyse pour l’obtention des catalyseurs finaux, et d’obtenir des activités en ORR améliorées. Les résultats obtenus sur différents matériaux synthétisés dans cette étude ont permis de montrer que la phase active est constituée par le fragment FeN_x, les nanoparticules à base de Fe_3O_4 ne jouant pas de rôle actif mais participant probablement dans l’amélioration des interactions électroniques avec les sites actifs. Néanmoins, il est à préciser que l’effet synergique varie en fonction des systèmes. Il convient de noter que notre approche synthétique dans cette étude représente également une stratégie universelle pour la synthèse d'autres catalyseurs à atome de métal unique (Co-N-C, Mn-N-C, etc.), associés à des nanoparticules métalliques ou oxydes, pour diverses applications telles que la réduction électrochimique du CO_2 en gaz de synthèse.

Chapter 1

Literature Reviews

1. Introduction

The developments of green and sustainable energy conversion and storage systems go alongside with the development of renewable energy (RE) to reduce the problem of climate change [21, 22]. Fuel cells are proven to be clean electrochemical energy-converting device with high efficiency and zero emissions which have attracted great research interest to meet improving energy requirements in the future [23, 24]. The working mechanism for typical proton exchange membrane fuel cells (PEMFCs) mainly involves in two half-cell reactions, namely anodic oxidation reaction of H_2 fuels, and cathodic oxygen reduction reaction (ORR), with electric energy output and only pure water as by-product. The ORR process is the main limitation to the fuel cells efficiency due to the high overpotential and sluggish kinetic at cathode [25]. Nowadays, Platinum-based catalysts are generally regarded as the state-of-art electrocatalysts for ORR. However, the high cost and scarcity of Pt significantly impede the development of PEMFCs [26, 27]. To address this issue, several strategies have been put forward to decrease Pt loading so as to reduce overall cost of cathode: (1) downsize Pt nanostructure to improve atom utilization efficiency; (2) alloying with non-precious metal to decrease amount of Pt usage. Nowadays, considerable advances have been achieved by alloying strategy which not only reduces cost but also enhances ORR performance over pure Pt-based catalyst due to the alteration of intrinsic electronic structure of Pt metal and optimal oxygen absorption [28-30]; (3) Structural optimization such as shape-controlled, with aim to expose preferential facets of Pt for maximizing catalytic activity [31-33]. Despite tremendous efforts in Pt-based catalyst achieved, the synthetic procedure is often tedious and the optimized Pt-based catalyst is prone to agglomerate or deactivated during electrochemical process, leading to poor long-term durability operation. Most importantly, the limited Pt reserves in the long-term makes Pt-based catalyst large-scale application less promising for future deployment.

Earth-abundant non-precious metal catalysts with much lower cost compared to Pt-based compounds have received an ever growing interest for both environmental and economically point of view [34]. Recently, the strong driving force for commercialization of low-costs fuel cells has stimulated a great deal of research interests in exploration of non-precious metal catalysts. Among a variety of them, transition metal and nitrogen co-doped carbon materials, denoted as M-N-C (M = Fe, Co, Cu, Mn) with high intrinsic activity toward ORR are become promising potential candidates for the replacement of Pt catalysts [35-37].

For the first time, cobalt phthalocyanine has been proposed in 1964 by Jasinski as an active catalyst for ORR process which opened an avenue for exploring non-precious metal ORR catalysts [38]. Following this pioneering work, electrocatalysts prepared by high temperature pyrolysis of metal-macrocycle complex adsorbed on carbon substrate, contributed to a significant enhancement of ORR activity [5, 39, 40]. In 1989, the breakthrough progress was reported by Yeager et al. that the M-N-C could be acquired through pyrolysis of separated metal precursor, carbon and nitrogen source which enabled better flexibility and control of the electrocatalysts preparation [41]. Immediately, extensive efforts have been devoted to the development of such catalysts [42-44]. Among these emerging M-N-C catalysts, Fe-N-C, which can be regarded as one of the most promising replacements for precious Pt catalyst, has been intensively investigated over the past decades. The large interest on such catalyst is not only due to its environment-friendliness and cost effectiveness as well as comparable or superior activity toward ORR but also due to its intrinsic methanol/CO poisoning-tolerance. The latter is severe problem for Pt-based catalyst, and even trance amount of CO (as low as 10 ppm) will result in dramatical degradation of catalytic activity [45-47]. To date, tremendous advancements have been obtained regarding the preparation of Fe-N-C and its application in fuel cell as well. Despite recent progress, the groundbreaking progress in both activity and stability is not reported yet. In view of complicated coordination environment especially for those fabricated via high temperature pyrolysis, development and optimization of Fe-N-C are hindered by lack of understanding of the reaction mechanism and identification of precise nature of the active site. Thereby, there is still room for the improvement of performance on Fe-N-C by rational modulation of active sites and structure engineering for the sake of effective electrocatalyst design for ORR.

2. The mechanism and electrochemical evaluation of ORR

2.1 The mechanism of ORR

Table 1. Overall reaction equations of ORR in acidic and alkaline solution.

Electrolyte	Reactions
Acidic solution	4 e^- reaction: $O_2 + 4\ H^+ + 4\ e^- \rightarrow H_2O$
	2 e^- reaction: $O_2 + 2\ H^+ + 2\ e^- \rightarrow H_2O_2$
	Serial reaction: $O_2 + 2\ H^+ + 2\ e^- \rightarrow H_2O_2$ $H_2O_2 + 2\ H^+ + 2\ e^- \rightarrow 2\ H_2O$
Alkaline solution	4 e^- reaction: $O_2 + H_2O + 4\ e^- \rightarrow 4\ OH^-$
	2 e^- reaction: $O_2 + H_2O + 2\ e^- \rightarrow OOH^- + OH^-$
	Serial reaction: $O_2 + H_2O + 2\ e^- \rightarrow OOH^- + OH^-$ $OOH^- + H_2O + 2\ e^- \rightarrow 3\ OH^-$

The ORR process primary depends on the physicochemical surface properties of electrocatalysts. The overall reaction equations can be depicted in Table 1, where ORR proceeds by either four-electron (4 e^-) pathway with H_2O (acidic media) and OH^- (alkaline media) as reduction products or two-electron (2 e^-) pathway with H_2O_2 (in acid) and HO_2^- (in alkaline) as products. Obviously, direct four-electron pathway is more preferred due to higher efficiency of energy utilization while the H_2O_2 product from two-electron pathway is highly desired for the replacement of industrial energy-intensive anthraquinone-based method [48].

The detailed microscopic mechanism of ORR process can be classified into three pathways as summarized in Figure 1. Typically, the oxygen molecule is first adsorbed and activated on the surface of catalyst to form O_2*, herein the * is denoted as active site of catalyst, followed by O-O bond cleavage in three different manners:

(1) Dissociation pathway: The O-O bond in O_2* is cleaved directly into two O* intermediates (reaction II), which then are successively reduced to OH* and H_2O* (IV) and eventually end up with desorption of H_2O* (V) along with the active site released again.

(2) Association pathway: the OOH* are first generated from O_2* (VI), then O-O bond in OOH* is cleaved into O* and OH* (VII), followed by the successive reduction to form H_2O.

(3) The second association pathway: the O_2* is sequentially reduced to OOH* and HOOH* (VIII), then 2 OH* (IX) can be generated and finally reduced to H_2O

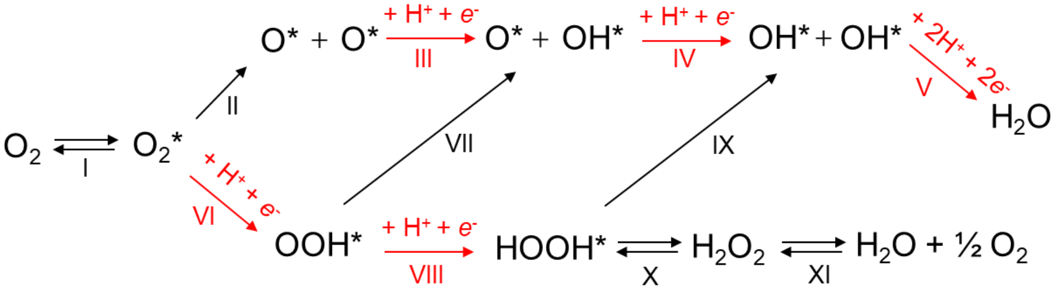

Figure 1. The microscopic reaction pathway toward ORR.

The ORR reaction pathway mainly depends on the initial dissociating energy barrier of absorbed O_2 molecule on the surface of active site. The O_2 dissociating energy barrier on carbon materials surface is relatively high, as reported by some DFT studies [49], thus not favorable for four-electron transfer pathway. As a result, the experimental measured electron transfer numbers for most carbon materials reported to date are much less than 4. On the contrary, the dissociating energy barrier on metal surface is much lower than that occurred on carbon materials especially for noble metal Pt. For example, the O_2 dissociating energy barrier on the surface of Pt (111) is calculated to be less than 0.3 eV (or ca. 29 kJ/mol), consequently taking four-electron transfer pathway [50]. The theoretical computation result is also consistent with experimental finding that Pt-based catalysts and other transition metal always present perfect four-electron selectivity. In addition, some studies also reported that the O_2 degree of coverage on the surface of catalyst plays a crucial role for O-O bond cleavage [51], the O-O bond is prone to cleave with the lowest dissociating energy barrier at low oxygen coverage before OH* formation (dissociation mechanism), whereas a high oxygen coverage induces O-O bond cleavage with a higher energy barrier thus favoring the formation of OOH* intermediate (association pathway).

Damjanovic et al. [52] proposed a model which is mostly used for evaluation of ORR rate constant and identification of reactive intermediates by means of rotating ring-disk electrode voltammograms (Figure 2(a)). However, the actual reaction process might be even more complicated due to the disproportionation reaction of intermediate H_2O_2 (reaction XI in the Figure 1) and equilibrium between adsorbed and dissolved H_2O_2 on the surface of electrode. It is taken into account in more general reaction kinetic model proposed by Wroblowa et al. [53], as shown in Figure 2(b). Ohsaka et al. [54] applied these two type of models to evaluate O_2 reduction process, they found that the Fe in Fe-N-C catalyst plays a crucial role for four-electron process, whereas in the case of N-C catalyst , two-electron pathway dominate ($k_1 < k_2$). Besides, it is also believed that the reaction pathway is closely linked with the loading density of catalyst, where high loading density contributes to four-electron pathway ($k_1 >> k_2$) whilst the two-electron reduction of O_2 becomes more pronounced at low loading density [55-57].

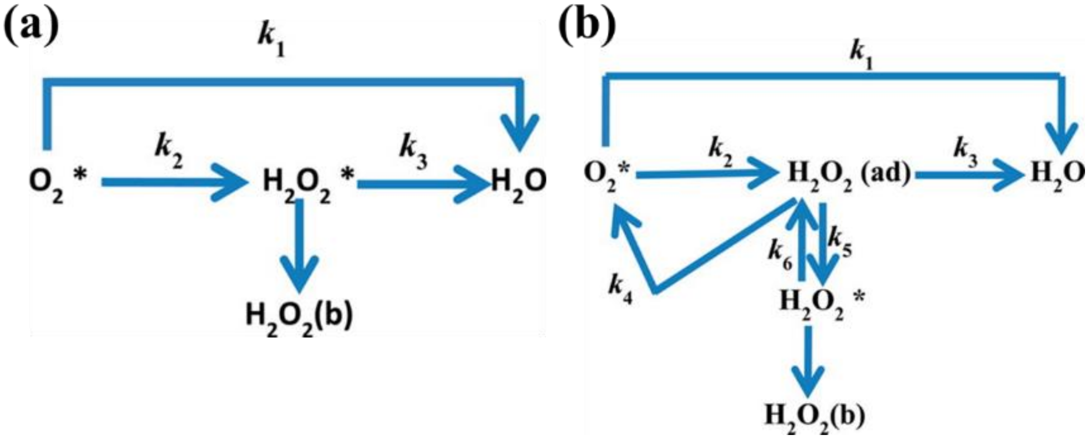

Figure 2. (a) Damjanovic and (b) Wroblowa model for ORR process. Reproduced from Ref. [54]

Owing to the simultaneous presence of multiple active sites with totally different structural features and kinetic parameter, the ORR pathway on different active sites can be described as shown in Figure 3:

(a) dual sites 2 × 2 e^- model where O_2 is reduced to H_2O_2 and H_2O successively on two different active sites.

(b) the single site 2 + 2 e^- with reduction of O_2 into H_2O on the same active site.

(c) the direct 4 e^- mechanism on the single active site.

The detailed reaction mechanism is specifically dependent on the electrode materials and pH used during ORR. Some researchers believed that ORR preferred to proceed through the 2 e^- reduction pathway on metal-free carbon-based catalysts with H_2O_2 as production [58-61]. Jaouen and Dodelet revealed a direct 4e^- mechanism on Fe-N-C as they observed that the H_2O_2 yield is nearly independent of the loading density and rotation speeds. The electroreduction of H_2O_2 shows a negligible contribution to the overall reaction kinetic [62]. Tylus et al [63] proposed indirect four-electron process with different reduction pathways depended on pH of electrolyte. ORR catalyzed by Fe^{2+}-N_4 center proceeded through single site 2 + 2 e^- mechanism without any desorption of reactive intermediates in alkaline electrolyte while dual-site 2 × 2 e^- mechanism is governed in acid media with concomitant Fe/Fe_xO_y nanoparticles as secondary active site for reduction of desorbed H_2O_2.

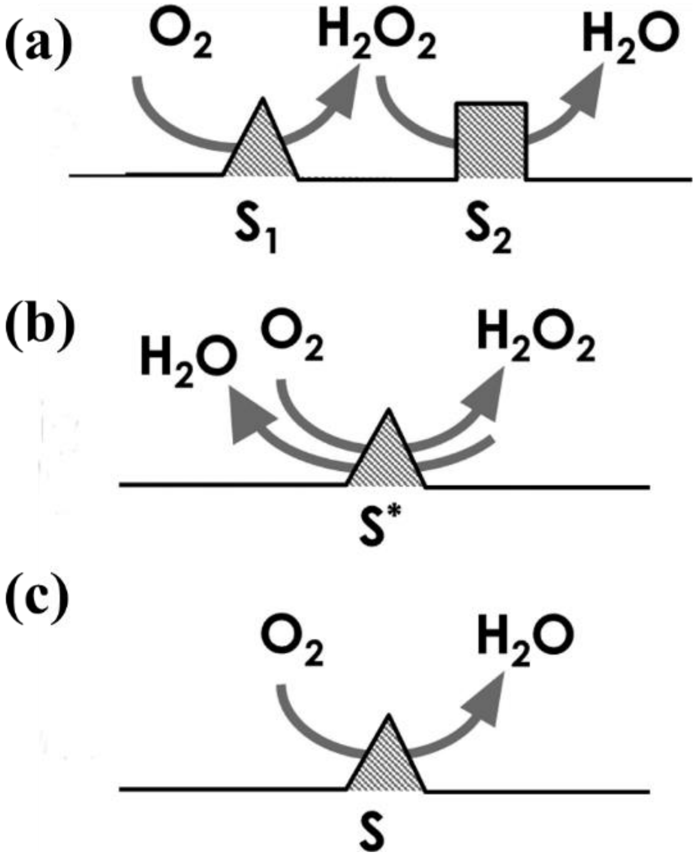

Figure 3. Possible reaction pathways and active sites of performing the ORR process. (a) dual site 2 × 2 e^-, (b) single site 2 + 2 e^-, and (c) single site direct 4 e^- mechanism. Reproduced from Ref. [64]

On the other hand, researchers focused on determining the rate determining step (RDS) which is of importance to understand the sequence of electron and proton transfer. In most cases, the overall ORR process rate is determined by one of the following three steps. (1) the first electron transfer process, (2) hydration of absorbed oxygen, and (3) the desorption of intermediates production.

A large number of theoretical simulations have mentioned that the first reduction step of adsorbed molecular oxygen is RDS of ORR [65-68]. For instance, Anderson's group found that the first electron transfer step had the highest reaction barrier, and proton transfer was involved in the RDS in acid medium where the peroxyl radical, OOH(ads) was the first reduction intermediate. In the basic mechanism, the superoxide, O_2^-(ads) is thought to be the first reduction intermediate without proton transfer [69, 70]. Janik and Taylor et al. suggested that electron transfer precedes the protonation of the adsorbed O_2 molecule [71]. Differently, Goddard reported the reaction pathway and barriers for the oxygen reduction reaction (ORR) on platinum, and they claimed that OH* could be formed with aid of O* hydration and this process possessed highest barrier energy. It suggested that decreasing the barrier for O* hydration while providing hydrophobic condition for the OH and H_2O formation steps is a highly efficiency strategy to improve ORR performance [72].

Recently, it has also been widely approved that the absorption energy of oxygenated species such as O* and OH* plays a pivotal role for ORR on the surface of metal catalyst, but they are turned out to be difficult for experimental identification [73, 74]. The extraordinary efforts carried out by density functional theory (DFT) for surface process have significantly promoted the development of electrocatalysts field. Norskov et al. [75] introduced a detailed procedure for calculating free energy of intermediates as function of applied electrode potential using DFT calculation in the process of electrochemical reaction. They found that the adsorbed oxygen and hydroxyl intermediates tended to be stable at potential close to equilibrium, while the electron and proton transfer are not taking place. The adsorption energy of these intermediates gradually decreased as the increasing of potential subsequently reaction may proceed, which clarified the origin of the overpotential for electrochemical process. According to Sabatier principle, high performance electrocatalysts for ORR should possess moderate binding energy with oxygenated species. If the adsorption on the electrode surface is too weak, the ORR process will be limited by the transformation of proton-electron transfer into adsorbed O_2 or restrained by O-O bond cleavage. On the other hand, too strong binding force will lead to difficulties in the desorption step of OH^- and H_2O from the surface of the catalyst. The variation of absorption energy is dependent of the electronic structure of the electrode surface, which can be described by the coupling between the adsorbate valence states and the metal d-states for the transition metals [76-78]. The higher the energy of the d-states is, the stronger the interaction with adsorbate states is. In view of the fact described above, Norskov established the correlation between metal-O bond interaction and the position of metal d states relative to Fermi energy level [79, 80]. As a result, the regulation of electronic structure of electrocatalyst is believed to be a feasible way to optimize the adsorption of intermediates accordingly the enhancement of activity.

2.2 Electrochemical evaluation of ORR

For hydrogen-fed fuel cell, the overall chemical reaction equation can be described as follow:

$$H_2 + 1/2\ O_2 = H_2O\ (l)$$

Under standard conditions (298 K and 1 atm), the thermal energy (ΔH) for this reaction is 285.8 kJ mol^{-1}, and the free energy for useful work (ΔG) is 237.1 kJ mol^{-1}. The thermal efficiency for ideal fuel cell can be determined to be:

$$\eta_{ideal} = \Delta G / \Delta H = 237.1\ kJ\ mol^{-1} / 285.8\ kJ\ mol^{-1} = 0.83$$

Under actual condition, the cell thermal efficiency: $A = E_{useful} / \Delta H = 0.83 * E_{useful} / \Delta G = 0.83\ E_{actual} * I / E_{ideal} * I = 0.83\ E_{actual} / E_{ideal}$, wherein $E_{ideal} = 1.23$ V, thus $A = 0.675\ E_{actual} = 0.675\ (E_{cathode} - E_{anode})$, generally, O_2 can be reduced into H_2O on the side of cathode with certain overpotential

(E_{op}). The equation can ultimately be converted to A = 0.67 [($E_{cathode}$-E_{op})-E_{anode}] with taking the E_{op} into consideration. Accordingly, the higher thermal efficiency which corresponds to maximum energy utilization efficiency featured by higher E_{ORR} would be achieved with lowest overpotential. As the E_{op} is closely associated with cathode electrode materials, the rational design of electrocatalyst with optimized overpotential is highly desired.

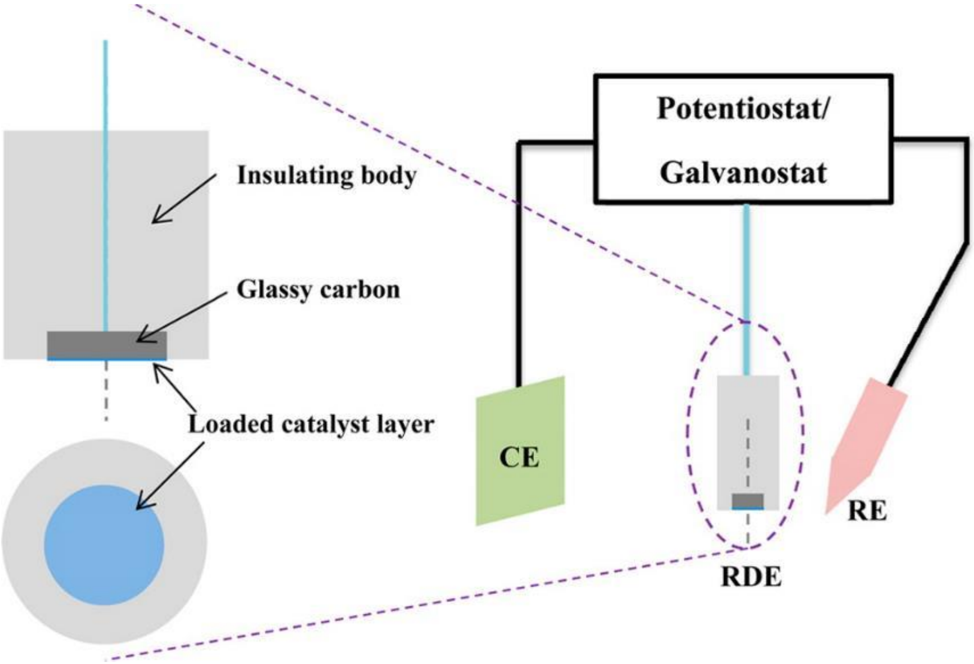

Figure 4. Schematic diagram of typical rotating-disk electrode (RDE) testing setup in three-electrode configuration. Reproduced from Ref. [81]

In a model three-electrode cells only O_2 dissolved in electrolyte reaching the electrode surface are participating in reduction of O_2, and solubility of O_2 in aqueous electrolytes is low ($1.26*10^{-1}$ mol/L at 25 °C in 0.1M KOH). In order to control and force the mass transport of O_2 in solution, rotating disk electrode (RDE) measurement with three electrode system is developed for the evaluation of electrochemical performance, as depicted in Figure 4.

Figure 5 displays the typical ORR polarization curve for model catalyst with three-electrode system. The curve can be divided into three parts. In the region of kinetic control, the rate of reaction is the slowest and it will gradually increase as the overpotential increases. A dramatic increase of current density with overpotential results in depletion of near-electrode area of O_2 and mixed kinetic-diffusion control of the reaction at higher overpotentials. As the overpotential increases further, the near-electrode layer is getting completely depleted of O_2, and the reaction rate is determined exclusively by the rate of mass transport of O_2 toward electrode surface, which does not depend on electrode potential.

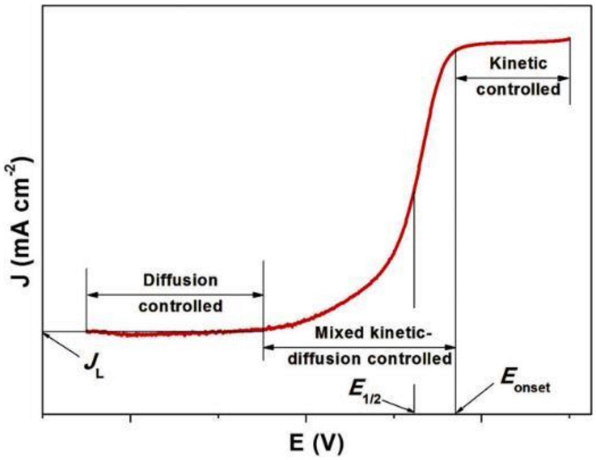

Figure 5. Typical ORR polarization curve. Reproduced from Ref. [82]

Hence, a well-defined current density plateau occurs in so-called diffusion-controlled zone. The limiting current density J_L of the plateau is closely related to diffusion rate of reactant and electrode rotation rate. It is well known that the limiting current density increases as the rotation rate increases due to the enhanced mass transport of reactant by forced convection. When porous electrodes are used, the abundant porosity of electrode particularly for hierarchical porous configuration with high reactant accessibility to exposed active site is highly anticipated for achievement of high diffusion current density as well as ultimate availability of higher energy efficiency [83].

The phenomenon is in accordance with the result that ORR tends to proceed via more efficient four-electron pathway with higher catalyst loading as aforementioned [57]. Two important parameters, half-wave potential ($E_{1/2}$) which can be read in the area of mixed kinetic-diffusion control and onset potential which usually is calculated by threshold current density of 0.1 mA / cm^2 [84], can be used as indicators for evaluation of electrochemical activity. The more positive these values are, the more active are the catalysts. The kinetic current density (j_k) is another vital criterion for evaluation of electrocatalyst, which can be obtained by polarization curves with mass-transport correction through Levich-Koutechky (K-L) equation as follow:

$$\frac{1}{j} = \frac{1}{j_L} + \frac{1}{j_K} = \frac{1}{0.62nFC_0(D_0)^{2/3}\,v^{-1/6}w^{1/2}} + \frac{1}{nFkC_0} \qquad (1)$$

Where j is measured current density and j_L refers to diffusion limited current density. It is noting that the measured current density should be corrected by elimination of background contribution to exclude interference of capacitive current density especially for porous carbon materials with high specific surface area; ω represents the angular velocity, n is the number of transfer electron, C_0 is oxygen bulk concentration, D_0 is diffusion coefficient of O_2 in electrolyte, υ is the kinematic viscosity of the electrolyte, and k signifies the electron-transfer rate constant. The j_K value is usually compared at a the same relatively high applied potential (i.e. 0.9 V vs. RHE for Pt -based catalyst) depending on different electrode materials due to the smaller inaccuracy of mass-transport [85]. Besides, the electron transfer number n for ORR process can also be calculated directly from K-L equation. At a certain overpotential $\eta = E - E_{eq}$, the overall current density for a certain reaction step can be expressed as follows [21]:

$$j = j_f + j_b = j_0[C_O/C_O^{*}\exp(-\alpha f\eta) - C_R/C_R^{*}\exp\big((1-\alpha)f\eta\big) \qquad (2)$$

Where j_f is forward current density for a certain chemical reaction, j_b is backward current density,

j_0 is exchange current density derived from equilibrium potential, f is defined as F/RT, α is the transfer coefficient, C_o* and C_R* are bulk oxygen concentration for oxidized and reduced species respectively, C_o and C_R are the counterparts for surface oxygen concentration. In kinetic controlled region, the O_2 concentration differences from bulk and surface of solution are negligible ($C_o^* = C_o$, $C_R^* = C_R$). Thus, the equation can be simplified as well-known Butler-Volmer equation:

$$j = j_0\left[\exp(-\alpha f\eta) - \exp\left((1-\alpha)f\eta\right)\right] \quad (3)$$

The equation implies that the higher the exchange current density (j_0), the more accelerated reaction kinetic. Furthermore, the above equation can be converted into two parts due to the irreversibility of ORR at higher overpotential ($\eta > 50$ mA) under the operation condition:

$$j_a = j_0 \exp\left(\frac{\alpha_a nF\eta_a}{RT}\right) \quad (4)$$

$$j_c = -j_0 \exp\left(-\frac{\alpha_c nF\eta_c}{RT}\right) \quad (5)$$

Where j_a and j_c signify current density of anode and cathode respectively, and correspond semilogarithmic forms:

$$\eta_a = \frac{RT}{nF\alpha_a}\ln j - \frac{RT}{nF\alpha_a}\ln j_0 = b\ln j - a \quad (6)$$

$$\eta_c = \frac{RT}{nF\alpha_c}\ln j_0 - \frac{RT}{nF\alpha_a}\ln j = a - b\ln j \quad (7)$$

b refers to Tafel slope, one of the most important reaction mechanism descriptors. Tafel slopes are typically found at 60 mV dec^{-1} or 120 mV dec^{-1} in acidic media, while 40 mV dec^{-1} and 120 mV dec^{-1} is reported in basic media.

The change of Tafel slopes is thought to be potential-dependent. The different Tafel slope in high potential (40 vs. 60 mV dec^{-1}) for distinct electrolyte is associated to different elementary reaction step which depends on applied potential. The same Tafel slope in low potential (120 mV dec^{-1}) which is independent on pH suggests that first-electron reduction of oxygen is rate determining step which means the subsequent O-O bond breaking and reduction become facile [86-89].

To obtain the deeper understanding of kinetic mechanism, rotating ring-disk electrode (RRDE) system is established as depicted in Figure 6. In this configuration, O_2 reduction reaction proceeds on the disk electrode and its intermediate products (H_2O_2 or HO_2^-) are oxidized on ring electrode. The transportation efficiency of intermediate products from disk to ring electrode can be quantitatively described by collection efficiency N, which is the ratio of an amount of an intermediate detected on ring electrode to the amount formed on disk electrode. Generally, N is determined in a control experiment with standard reversible redox couple, for example [$Fe(CN)_6^{3-}$ /$Fe(CN)_6^{4-}$] solution. The potential window for ring electrode can be set between diffusion-limiting value for the oxidation of intermediates and onset potential for oxidization of H_2O or OH^- to O_2. Therefore, the yield of intermediate products and electron transfer number during ORR are calculated by recording ring and disk current density according to followed equations [90, 91]

$$X_{HO_2^-} = \frac{2\, j_R/\, N}{j_D + j_R/N} \quad (8)$$

$$n_{e^-} = \frac{4\, j_D}{j_D + j_R/N} \quad (9)$$

Where j_R is ring electrode current density, j_D is disk electrode current density, and N is collection efficiency.

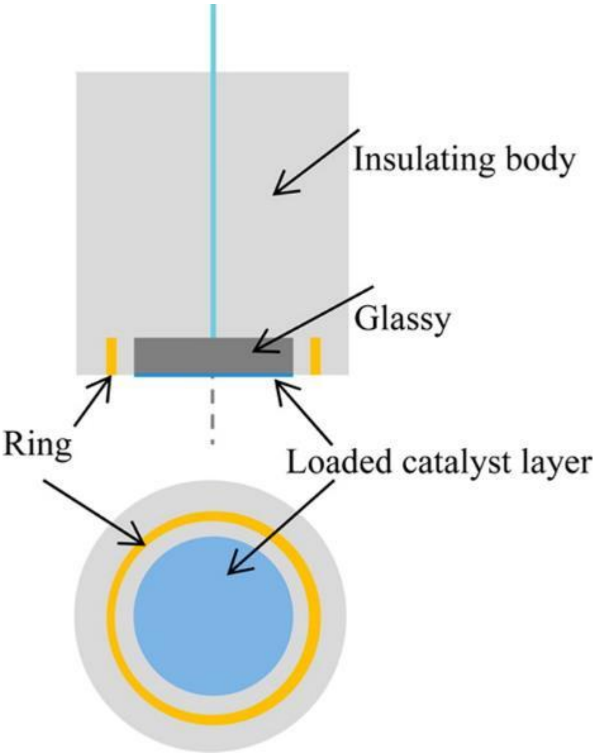

Figure 6. Schematic diagram of rotating ring-disk electrode system. Reproduced from Ref. [81]

The pH-dependence of ORR activity is also elucidated taking precious metal Pt as the reference system. More insight regarding pH-dependence behaviors for Fe-N-C can also be derived on the basis of Pt metal which will be stated in detail after. The ORR process is complicated not only because of multiple electron and proton transport steps and its competitive reaction involving in two-electron and four-electron pathway, but also due to its different reaction mechanism under various pH conditions [92]. The fundamental understanding of ORR performance gap between acid and alkaline media is of paramount importance for design of high performance electrocatalysts.

Mukerjee et al. [93] found that higher intermediate product yield is obtained at 0.1 M NaOH than that at 0.1 M $HClO_4$ solution and the byproduct continues to increase as the improved concentration of NaOH electrolyte (Figure 7b and c), The consistence between Pt-OH formation arising from specifically absorbed hydroxide anion as seen from CV curves (Figure 7a) and the sharp increase in ring current (i.e. yield of an intermediate of ORR) in alkaline media demonstrated the interaction between O_2 molecule and hydroxyl species on the electrode surface. Subsequently, the mechanistic origin for the so-called kinetic facility of ORR in alkaline media for Pt electrocatalysts are investigated from the perspectives of the changes in the double-layer structure and the reaction mechanisms [94, 95]. As shown in Figure 7d, in acidic media, the chemisorbed O_2 molecules (with either nondissociatively or dissociatively absorbed), solvent water dipoles and specifically adsorbed hydroxyl species constitute Inner-Helmholtz Plane (IHP), while the H_3O^+ ion and solvated O_2 populate Outer-Helmholtz Plane (OHP). The direct or series $4e^-$ reaction predominantly proceeds by reduction of adsorbed O_2 at IHP by a proton transfer from OHP to IHP, so-called inner sphere electron transfer (ISET), resulting in water as dominating products without desorption of intermediates. In the case of alkaline media, water molecules play double role of solvent and source of proton required for ORR. The constituents in IHP differ appreciably from those in acid media, where the specifically adsorbed hydroxyl species (mainly stem from adsorption of OH^- anion), solvent water dipoles and adsorbed O_2 serve as IHP while solvated O_2 molecule, alkali metal ion populate OHP. The ORR takes place via both ISET and outer-sphere electron transfer (OSET) with water as proton source instead of H_3O^+. For OSET mechanism, solvated molecular O_2 weakly interacts with adsorbed hydroxyl species to promote a $2\ e^-$ reaction pathway to HO_2^- anion as a reaction product which desorbs from the surface of catalyst. Therefore, the slower kinetic and higher H_2O_2 yield are ascribed to the contribution of OSET.

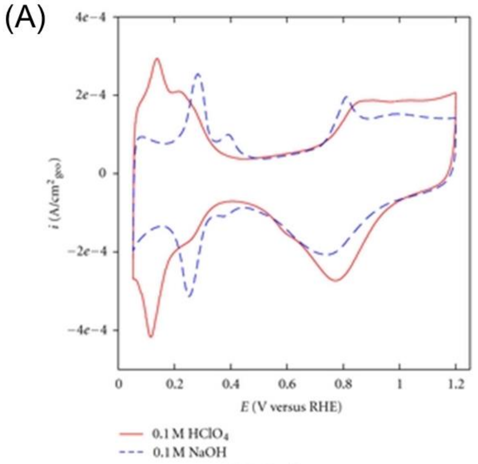

(a) Cyclic voltammetry

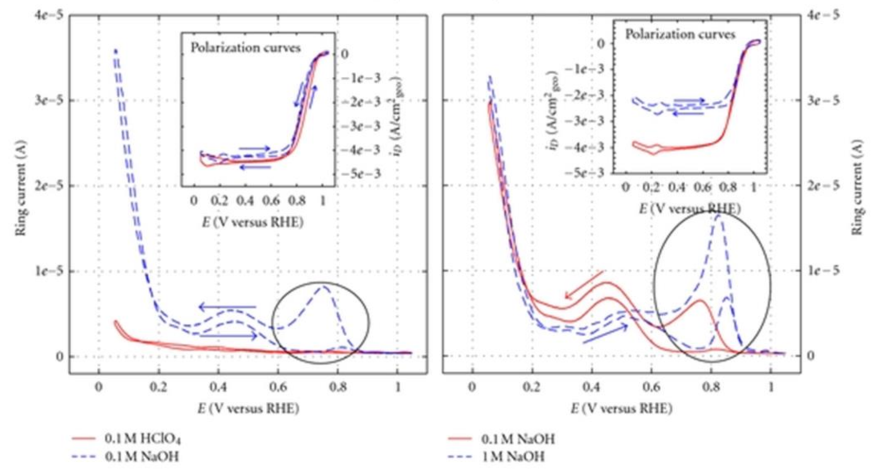

(b)

(c)

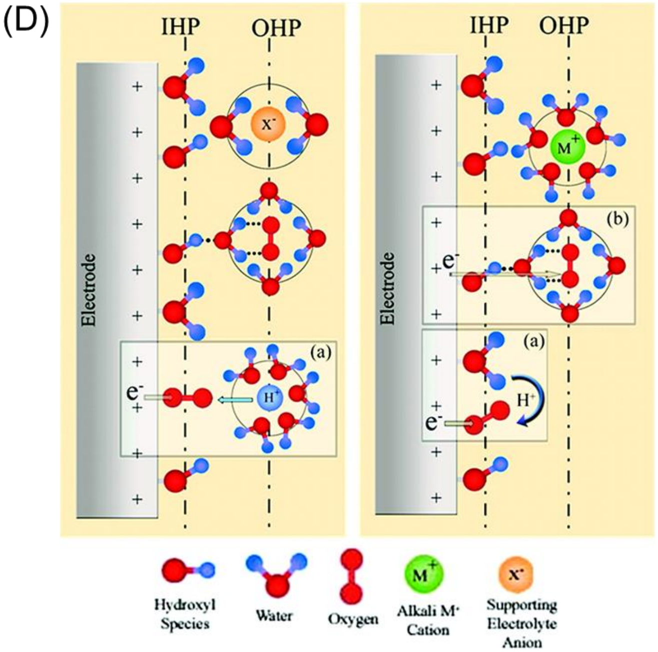

Figure 7. Comparison of electrochemical characteristics of BASF-ETEK 30% Pt/C in 0.1 M $HClO_4$, 0.1 M NaOH, and 1.0 M NaOH electrolytes. (a) CV in argon-saturated electrolytes, (b, c) Ring currents measured during ORR study at 900 rpm in O_2-saturated electrolytes. Insets in (b, c) show the corresponding ORR polarization curves at 900 rpm. Scan rate: 20 mV/s. E_{Ring} = 1.1 V versus RHE in 0.1 M NaOH and 1.3 V versus RHE in 0.1 M $HClO_4$. Catalyst loading: 15 μg Pt/cm^2 on 5.61mm Glassy Carbon disk electrode. Adapted from Ref. [93], (d) Schematic illustration of the double-layer structure during ORR in acidic (left) and alkaline (right) conditions. Reproduced from Ref. [94]

3. Outline of Fe-N-C

It is generally believed that FeN_x sites are active for four-electron ORR process [96]. For instance, Ohsaka et al. [97] reported the introduction of Fe led to a larger increase in the rate constant of four-electron reduction than that of two-electron process. Furthermore, they estimated the rate constant k_1, k_2, k_3 of ORR corresponding to the four-electron direct reduction of O_2 to H_2O, the two-electron reduction of O_2 to H_2O_2 and two-electron reduction of H_2O_2 to H_2O respectively (see Figure 2). They claimed that only two-electron active site existed in the case of N-C while the FeN_x played a crucial role in making the four-electron active site ($k_1 >> k_2$) as well as it may catalyze the H_2O_2 reduction to H_2O, resulting in the enhanced ORR performance [54]. Artyushkova et al. [64] analyzed more than 45 Fe-N-C electrocatalysts and proposed that pyrrolic nitrogen acted as a site for partial O_2 reduction to H_2O_2 and pyridinic nitrogen displayed catalytic activity in reducing H_2O_2 to H_2O, whereas Fe coordinated to N (FeN_x) serves as an active site for four-electron direct reduction of O_2 to H_2O. The indispensable role of efficient four-electron transfer process for FeN_x was confirmed by Gewirth et al. [98] who demonstrated that in the absence of Fe the carbon and nitrogen site in the catalyst exhibited a larger overpotential and lower selectivity for the four-electron reduction of oxygen in both acidic and alkaline conditions.

Choi et al. [99] elucidated the reaction mechanism of Fe-N-C with several underlying active sites in acid media as depicted in Figure 8 and demonstrated that FeN_xC_y moieties and Fe@N-C (Fe nanoparticles encapsulated into carbon layer) species were moderately active toward reduction of H_2O_2, proving their possible roles in both direct (major path) and indirect four-electron ORR pathways. In the latter, the released H_2O_2 was further reduced in another site (FeN_xN_y and Fe@N-C), while electrolyte-exposed Fe nanoparticles and N-doped carbon are inactive toward peroxides reduction reaction (PRR).

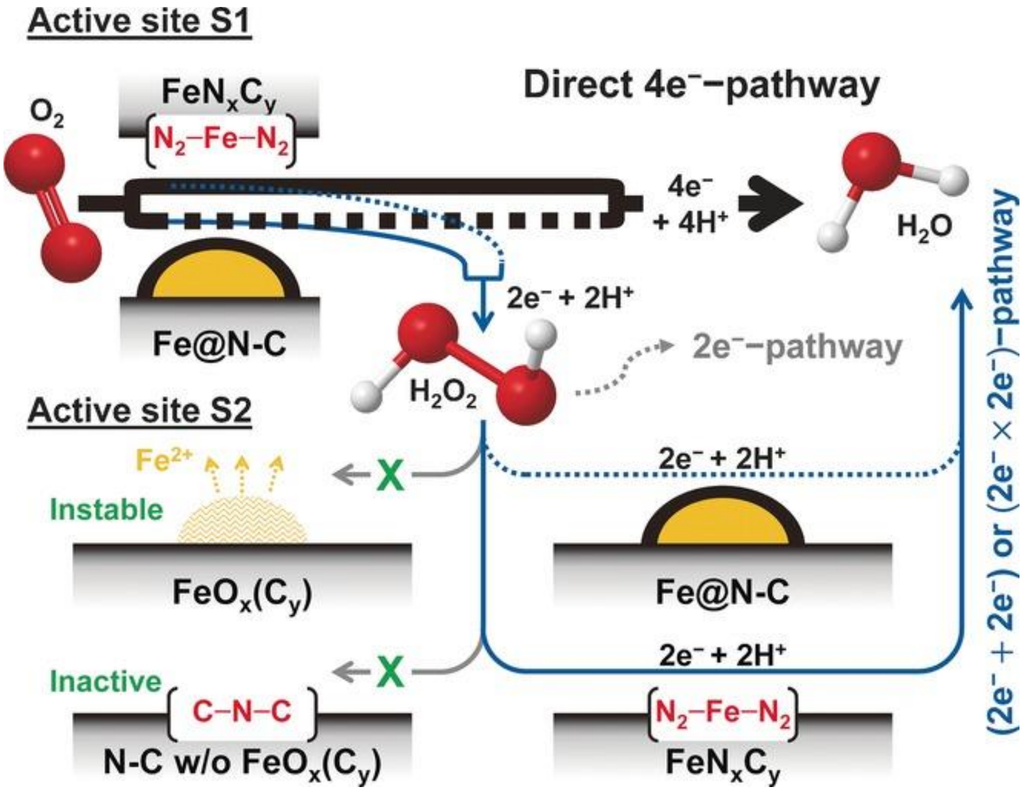

Figure 8. ORR mechanisms on Fe-N-C catalyst in acid medium. The site S1 is FeN_xC_y moieties or Fe@N-C. FeN_xC_y mostly catalyzes direct 4 e^- ORR, along with a minor fraction of H_2O_2. Fe@N-C produces higher fraction of H_2O_2 in comparison to FeN_xC_y. The released H_2O_2 is then reduced to H_2O on site S2, either FeN_xC_y or Fe@N-C. Surface-exposed Fe particles and N groups without subsurface Fe are PRR inactive. Reproduced from Ref. [99]

Similar to Pt/C catalyst, the Fe-N-C also presents distinct pH-dependence. However, contrary to the behavior of Pt/C, the apparent ORR activity of Fe-N-C is much higher with lower H_2O_2 yield in alkaline media than those in acidic condition [93, 100, 101]. The improved performance in basic media can be rationalized by variation of adsorption strength of reactant and intermediate. For Pt/C catalyst in alkaline media, the specifically adsorbed OH^- on the IHP act as a bridge for OSET as well as site blockage for ISET which leads to slower reaction kinetic and larger yield of 2 e^- products. On the contrary, the adsorbed OH^- on the IHP of Fe-N-C is not stable and easily replaced by molecular O_2. As such OSET is inhibited on the Fe-N-C, ensuring predominant 4 e^- reduction of O_2 in the alkaline medium [102]. Meanwhile, hydrogen peroxide intermediates HO_2^-, which is a Lewis basic, can be stably adsorbed and immediately reduced to the 4 e^- product on Fe^{2+} active site (Lewis acid sites) via the formation of stabilized acid–base adducts. On the other hand, the neutral intermediate H_2O_2 negates its Lewis basic property and undermines its stabilization on Fe^{2+}, ultimately facilitating the 2 e^- process and enhanced H_2O_2 yield [95, 103]. There is another hypothesis that the protonation of doped nitrogen atom in Fe-N-C hinders the charge delocalization and thus degrades its electrocatalytic activity in acid media [104]. Rauf et al. [105] proposed that the protonation of pyridinic N would greatly decrease the charge density (Lewis basicity) of adjacent carbon atoms thus reducing the affinity to O_2 and ORR activity in acidic media. If FeN_x active sites were concerned, the electron density of Fe-center also would be reduced significantly due to the low basicity of adjacent carbon, which result in negative shift of Fe^{2+}/Fe^{3+} redox potential and decreased ORR activity.

Herranz et al. [106] demonstrated that protonation of basic N-group and subsequent anion binding resulted in a decreased turnover frequency of FeN_4 sites for the ORR as shown in Figure 9a. Pyridinic nitrogen is possible candidate for basic-N group since pyridine has a low of pK_a of

5.2. However, the FeN_4 site was assumed to possess higher turnover frequency for the ORR as long as nearby basic N-groups were protonated but not anion bound. The result was verified that the ORR activity could be restored through heat treatment or acid washing of protonated catalyst with removal of bound anion (Figure 9b). Generally, the FeN_xC_y structure, Fe/FeC_x@N-C, and N-doped carbon are all relatively active in alkaline media [107, 108]. But in acid electrolyte, the N-doped carbon free of Fe-based particles shows negligible activity with considerable H_2O_2 yield [99]. By introducing inorganic Fe-based compounds encased by carbon overlayer, the ORR activity increases sharply. These Fe-based nanoparticles play a crucial role in the electrocatalysis by imparting a synergistic effect on the N-doped carbon that allows stabilization of the peroxide intermediate and enable the full 4 e^- reduction of oxygen to water [109].

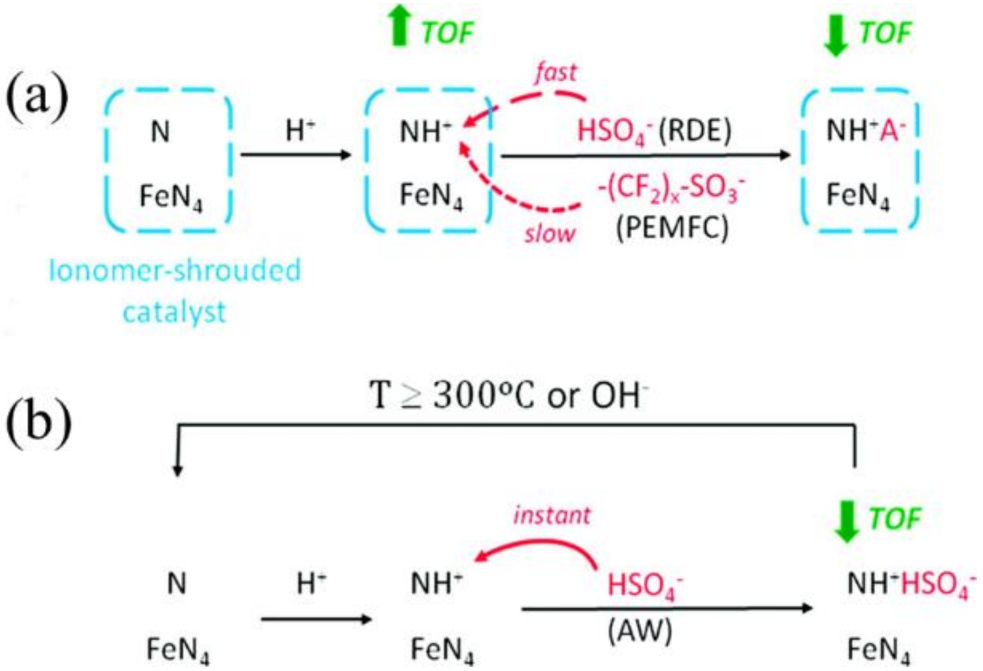

Figure 9. Change of the chemical state of protonable N-groups and simultaneous change of the turnover frequency (TOF) for the ORR of FeN_4 catalytic sites when the Fe/N/C catalyst is shrouded by proton-conducting ionomer (a) or directly in contact with an aqueous acidic solution (b). In case (b), the acid-washed catalyst can be reactivated either thermally or chemically. Reproduced from Ref. [106]

4. Nature of active site for Fe-N-C

As alternative electrode materials for Pt/C, one particular family for non-precious metal catalyst (NPMC) is MN_4 type complex which has been extensively explored. The metal atom M acts as central of molecular moiety coordinated by four pyrrolic nitrogen atoms constituting square-planar configuration. The most studied macrocycle complexes have focused on transition-metal phthalocyanines (M-Pcs) and metal porphyrins (M-Ps) as well as their analogues, with supported or without supported by various carbon substrates [110]. Although the activity has been significantly improved by recent studies, the lack of long-term stability required for continuous operation in a fuel cell still remains enormous challenge. To overcome this key issue, the catalysts pyrolyzed at high temperature containing these metal-macrocycle complexes or mixture of individual Fe inorganic precursor and N/C-containing organic molecules have been well developed and demonstrated enhanced durability toward fuel cell application. It appears that FeN_4 or FeN_x centers can be well preserved and act as potential active sites which are responsible for high activity of ORR after pyrolysis. Nevertheless, in most cases particularly for Fe-N-C catalysts synthesized by pyrolysis of iron precursor, N-containing precursor and C resources, the resulting materials typically present highly heterogeneous structure with multiple active components. To date, three type of active sites are proposed to exhibit considerable catalytic activity toward ORR, namely, N-doped carbon moiety (denoted as N-C), iron-based species encased in N-doped carbon (denoted as Fe@N-C), and atomically dispersed iron embedded in carbon matrix (denoted as Fe-N-C).

At present, it is widely believed that Fe atom acts as adsorption/desorption site of reactant O_2 or oxygenated intermediate. Thus high turnover frequency (TOF) can be obtained by adjusting the Fe-O binding energy [111, 112]. For instance, Kramm et al. [113] presented a simple and feasible way to reduce the contribution of inorganic metal species even down to zero. Such catalyst revealed the desired homogeneous composition of FeN_4 site in the carbon matrix accompanied by a significant enhancement in ORR activity, the desired FeN_4 catalysts displayed onset potential of 0.88 V and kinetic current density of 3.15 A g^{-1} at applied potential of 0.8 V. Zhang et al. [114] achieved complete atomic dispersion of FeN_4 sites based on Mössbauer spectroscopy date by regulation of doped Fe content in the zeolitic imidazolate framework (ZIF)-8 precursor and the optimal Fe-N-C catalyst with highest FeN_4 active sites presented exceptional activity with onset potential as high as 0.88 V in H_2SO_4 solution. Choi et al. [99] proposed that Fe-N-C moieties were more selective than Fe particles encapsulated in N-doped carbon toward 4 e^- ORR process, and N-doped carbon free of Fe-based specie exposed to electrolyte was inactive toward reduction of H_2O_2 thus 2 e^- process dominated. On the contrary, other group reported that the role played by transition metal Fe in the catalyst precursor was only to catalyze the formation of active site for oxygen reduction reaction, and itself was not the component of active site and the ORR activity is exclusively attributed to N-C sites [115-117]. However, a real sense of “metal-free” N-doped carbon derived from metal-assisted high temperature synthesis remains debated because even trace amount of Fe can intensely boost the ORR activity [118, 119]. A large number of works have been implemented and respectable ORR activity have been achieved for N-doped carbon especially in alkaline media [120]. In addition to aid in the formation of Fe-N-C catalytic centers [121, 122], N atom can also be in-situ incorporated into carbon lattice during pyrolysis in several well-known form, such as graphite N, pyridinic N (hexagonal ring at the edge), and pyrrolic N (five-membered ring at edge) with sp2 hybridized and quaternary-oxidized N. Results of DFT calculations indicate that the intrinsic catalytic activity and the ORR reaction mechanism depend on the triple effect: the charge, the spin density and the coordinate state (ligand effect) of the carbon sites [123-126].

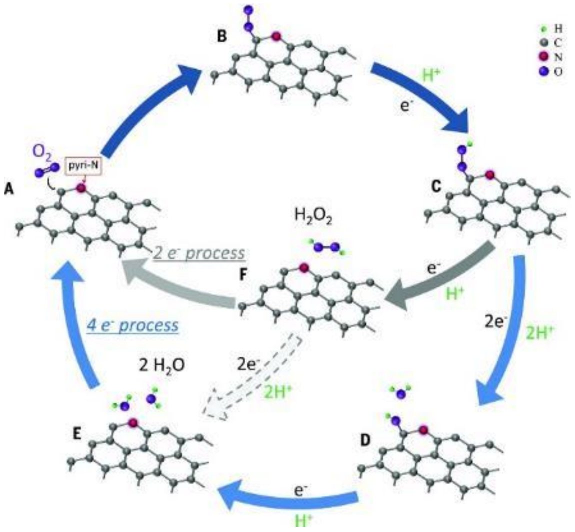

Figure 10. Schematic pathway for oxygen reduction reaction on nitrogen-doped carbon materials. Reproduced from Ref. [127]

The identification of active sites for N-C catalyst mainly focus on the type of N-containing functionalities. The suggested that underlying active sites for ORR are pyridinic N and graphitic N [116, 128-135]. Guo et al. [127] proposed reaction mechanism in the acid media on the basis of N-doped carbon as depicted in Figure 10. The active sites were created by pyridinic N and the adsorption site for O_2 was the carbon atom adjacent to the pyridinic N. The subsequent ORR could occur through the direct 4 e^- process or indirect 4 e^- process. The proposal was evidenced by Xing et al. [136] that oxygen reduction intermediate OH (ads) remained on the carbon atoms neighboring pyridinic nitrogen after ORR using Synchrotron-based X-ray photoelectron spectroscopy analyses. Although N-doped carbon materials have been proposed as effective electrocatalysts for ORR in acid media with either 2 + 2 e^- process or direct 4 e^- pathway [127], still they displays moderate catalytic activity as well as high H_2O_2 yield up to 30 % [129, 137]. To address this issue, metallic Fe or FeC_x species wrapped by graphitic carbon or N-doped carbon overlayer are proposed, which result in dramatically increase in activity, four-electron selectivity as well as durability in both acidic and basic electrolyte [138-141]. For example, Wen et al. [142]

reported nitrogen-enriched core-shell structured catalyst with iron-based composite (Fe/Fe_3C) nanorod as the core and graphite carbon as the shell ($N-Fe/Fe_3C@C$). Such catalyst exhibited a kinetic current density of 26.89 mA cm^{-2} at 0 V which is almost twice higher than that of the Pt/C catalysts (14.20 mA cm^{-2}) in neutral phosphate buffer solution. Strickland et al. [109] prepared Fe@N-C catalyst devoid of any direct metal-nitrogen coordination with Fe/Fe_xC surrounded by graphitic layers as shown in Figure 11. The resulting FePhen@MOF-$ArNH_3$ provided 40 mV and 90 mV improvements in terms of onset potential and half wave potentials respectively as well as one order of magnitude lower H_2O_2 yield compared to pristine Basolite-$ArNH_3$ without metal loading in acid media. They claimed that the presence of the subsurface Fe/Fe_xC was able to stabilize the peroxide intermediate on the active site thus promoted the selectivity toward the 4 e^- ORR pathway. Meanwhile, the reaction occurred primarily on the carbon-nitrogen structure in the outer skin of the nitrided carbon fibres and Fe/Fe_xC itself is not directly involved in the oxygen reduction pathway. Similar conclusion has also been proposed by Mukerjee's group [111]. Due to specific core-shell configuration, almost no significant performance loss was observed after 10000 potential cycles which might potential cycles which might be attribute to potential elimination of any Fenton-type process involving exposed iron ions culminating in peroxide initiated free-radical formation.

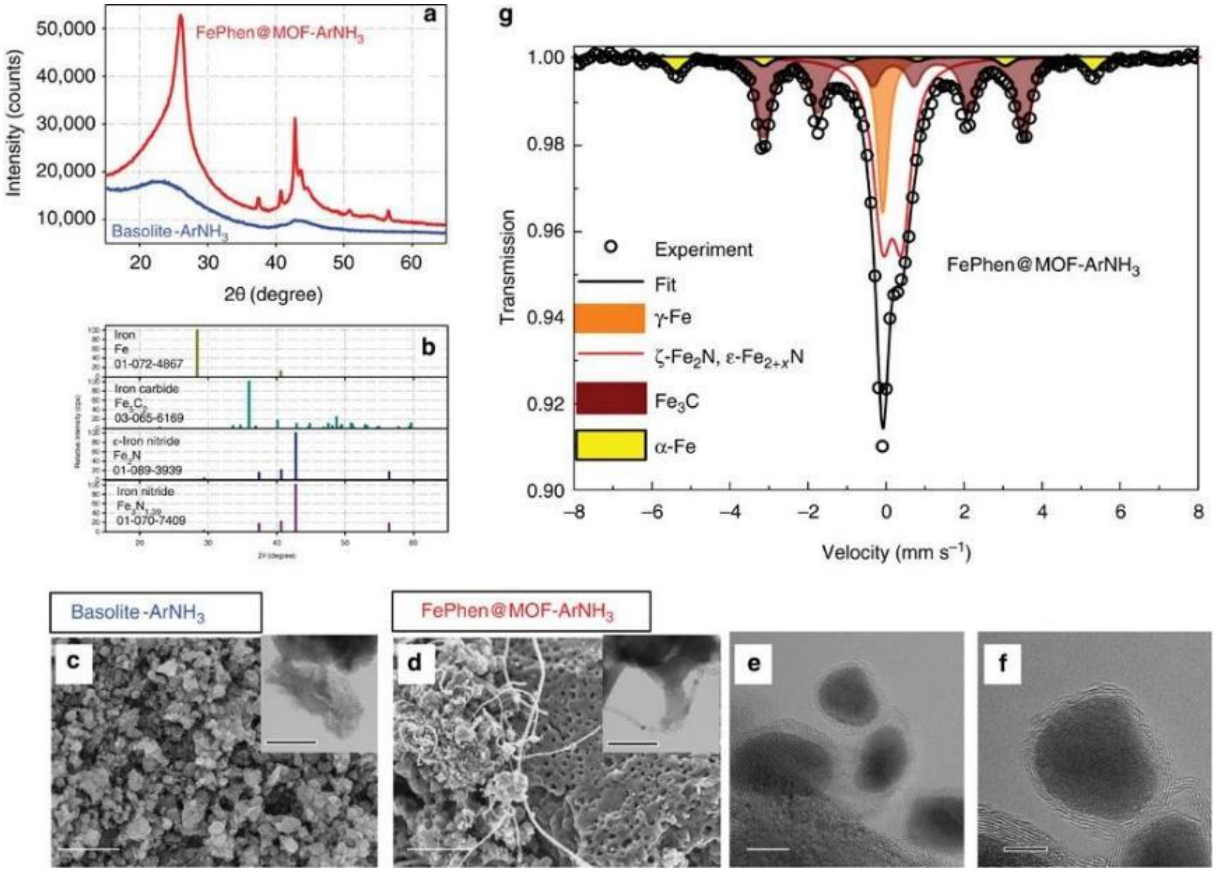

Figure 11. (a) X-ray diffraction pattern of FePhen@MOF-ArNH3 and Basolite-ArNH3. (b) Diffraction patterns of iron, iron carbide and iron nitrides. (c) SEM image of Basolite-ArNH3. Scale bar, 2 µm. Inset TEM image of amorphous carbon. Scale bar, 100 nm. (d) SEM image of FePhen@MOF-ArNH3. Scale bar, 2 µm. Inset TEM image of bamboo-jointed CNT. Scale bar, 100 nm. (e) HR-TEM image of iron encapsulated in bamboo joints of CNT in FePhen@MOF-ArNH3. Scale bar, 10 nm. (f) HR-TEM image of Fe/Fe$_x$C nanoparticle surrounded by graphite layers. Scale bar, 5 nm. (g) 57 Fe Mössbauer spectrum of FePhen@MOF-ArNH3 measured at room temperature. Reproduced from Ref. [109]

Apart from the pivotal role of coated iron-based species on N-doped carbon toward enhancement of ORR activity, it is also widely reported that these inorganic iron-based species sharply increase the ORR activity of Fe-N-C active sites [107, 143-146]. For example, Jiang et al. [147] developed a highly active Fe-N-C ORR catalyst containing FeN$_x$ coordination sites and

Fe/Fe_3C nanocrystals (Fe@C-FeNC) and revealed that the interaction between metallic iron and Fe-N_4 coordination structure favored the adsorption of oxygen molecule thus the superior catalytic activity of Fe@C-FeNC could be attributed to the Fe-N_x sites promoted by neighboring Fe/Fe_3C nanoparticles. Nevertheless, Kramm et al. [148] argued that an excessive iron-carbide formation led to disintegration of FeN_4-centers, hence limiting the number of ORR active sites on the final catalyst which in turn decreased the ORR activity. Similar results were also reported by other research groups suggesting that FeN_xC_y active sites possessed more superior catalytic activity and durability toward ORR than Fe@N-C sites in completely identical synthetic condition or the same system [114]. Specifically, Song et al. [112] revealed that activity order of different active sites of Fe-N-C in both acid and basic media combined with experimental and theoretical calcination follows: Fe-N_4/$_2$-C > Fe_4-N-C > N-C >> Fe_4-C > C.

Kumar et al. [149] made a comparison on activity after 1000 startup/shutdown cycles in fuel cell test between FeN_xC_y and Fe@N-C, and they found most of the metal-NC catalysts initially comprising MN_xC_y sites showed measurable ORR activity at 0.8 V, while those initially comprising M@N-C particles did not. The distinct contribution of activity for iron-based particles could be explained since the reactivity of M@N-C species varied with the thickness of the N-doped carbon shells surrounding the metal core, and this thickness may depend on different preparation routes and/or using different precursors [150, 151].

Although extensive efforts have pointed out the indispensable role of FeN_xC_y site toward ORR process [152], the exact structure of FeN_xC_y moiety required for high catalytic activity of ORR has been debated. Meanwhile, the underlying reaction mechanism of FeN_xC_y catalyst toward ORR also remains elusive. For most pyrolyzed catalysts derived from macrocycle phthalocyanine (FePc) or Fe porphyrin analogs, the coordination structure has been confirmed to be Fe-N_4 with pyrrolic-N atom surrounded, which typically inherit their parent macrocycle features. The ligands centered on Fe are partially destructed and only part of these Fe-N_4 sites could be responsible for the ORR activity [153]. On the other hand, the synthesized catalysts by high temperature pyrolysis for individual Fe precursor, nitrogen and/or carbon organic molecules exhibit highly diverse coordination configuration with possible one- to six-coordinated nitrogen as well as variety of N-doped (pyridinic N and pyrrolic N) on the basis of experimental or theoretical findings [154-161]. Li et al. [162] prepared a series of Fe-N-C catalysts with controllable FeN_x (x = 1,3,5) active sites by tuning pyrolysis temperature and revealed that the ORR activity and PEMFC performance follow the order $FeN_4 > FeN_3 > FeN_1$. Combined with theoretic calculations, they found that the FeN_4 is proved to have lowest formation energy among the types of FeN_x (x = 1-5). Lefevre and Dodelet [163, 164] reported simultaneous presence of FeN_2 and FeN_4 sites in Fe-based catalysts prepared from two iron precursors (Fe acetate or Fe porphyrin) adsorbed on a synthetic carbon. The synthesis consists of the pyrolysis of perylene tetracarboxylic dianhydride (PTCDA) in a reduction atmosphere, and the relative abundance of FeN_2 sites is dependent of used Fe precursor and pyrolysis temperature, the obtained FeN_2/C is more electrocatalytically active than FeN_4/C.

To date, the atomically dispersed Fe center surrounded by four nitrogen atoms have been unambiguous identified using advanced spectrum technology such as Mossbauer spectroscopy, X-ray absorption spectroscopy (XAS) and high-resolution aberration correction electron microscope to achieve image with atom size below 0.1 nm [111, 153, 165]. Duang’ group [166] reported the direct visualization of NiN_4, FeN_4, CoN_4 coordination moieties as depicted in Figure 12 (a-e)**,** Deng et al. [167] revealed atomic structure of FeN_4 center in graphene by combining high-angle annular dark-field scanning transmission electron microscopy (HAADF-STEM) coupled with electron energy loss (EEL) spectra around with Fe atom and low temperature scanning tunneling microscopy (Figure 12 (f-h)).

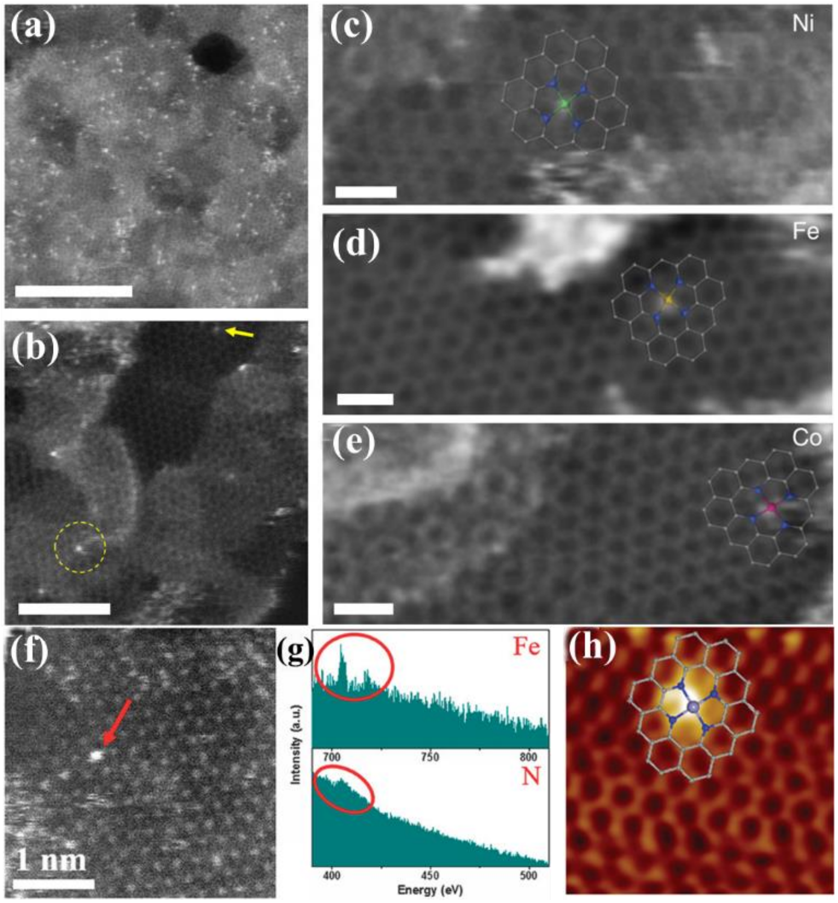

Figure 12. (a-e) Atomic structure characterizations of M-NHGFs by annular dark-field STEM. (f) High-angle annular dark-field scanning transmission electron microscopy (HAADF-STEM) image. (g) the electron energy loss spectroscopy (EELS) atomic spectra of elemental Fe and N from the bright dots. (h) Low temperature scanning tunneling microscopy (LS-STM) image of FeN_4/GN. Reproduced from Ref. [166, 167]

These advanced characteristic techniques especially for recently emerging in-situ X-ray absorption and Mossbauer spectroscopy under reaction condition provide a powerful support for deeper insights on electronic and geometry of FeN_4 moiety and evolution of active sites at applied potential toward ORR which facilitate the understanding of activity origin on Fe-N-C catalyst. [168, 169]. These results, combined with DFT calculation, allow to suggest two commonly accepted structures of active FeN_xC_y moieties: a metal ion coordinated by four pyridinic N, either occupying two-carbon-atom in-plane defect (MN_4C_{10}) [166, 170-172] or localized at armchair edges bridging two graphene sheets [$MN_{2+2}C_{4+4}$] [173, 174] as shown in Figure 13 (a-b). For example, Liu et al. [175] employed the first-principle density functional theory calculations to predict activation energy for O-O bond breaking and free-energy evolution as a function of electrode potential of ORR on three FeN_4-type active sites with different local carbon structures. It is found that the FeN_4 site surrounded by eight carbon atoms ($FeN_{2+2}C_8$) at the edge of micropores has the lowest activation energy for O-O bond breaking for promoting a direct four-electron ORR. Another MN_xC_y moiety typically is embedded in amorphous carbon with large number of five-membered carbon rings where M center is coordinated with pyrrolic N (Figure 13 (c-d)) [36, 176, 177], which could often be achieved by ZIF-based materials or as a derivation of FePc and Fe-porphyrins. It appears to be reasonable that porphyrin-type Fe moiety presents higher ORR activity with respect to pyridinic-typed Fe moiety due to the positive correlation between disorder of the carbon matrix and ORR reactivity.

Very recently, Zhang et al. [178] reported that the high-purity pyrrole-type FeN_4 catalyst exhibited more superior ORR activity with an ultrahigh active area current density of 6.89 mA m^{-2} in acid medium than that of pyridine-type FeN_4 site. By removing additional carbon atoms by ammonia treatment, pyrrole-type FeN_4 sites could be successfully achieved via chemical configuration transformation from pyridine nitrogen to pyrrole nitrogen as schematic illustrated in Figure 13e.

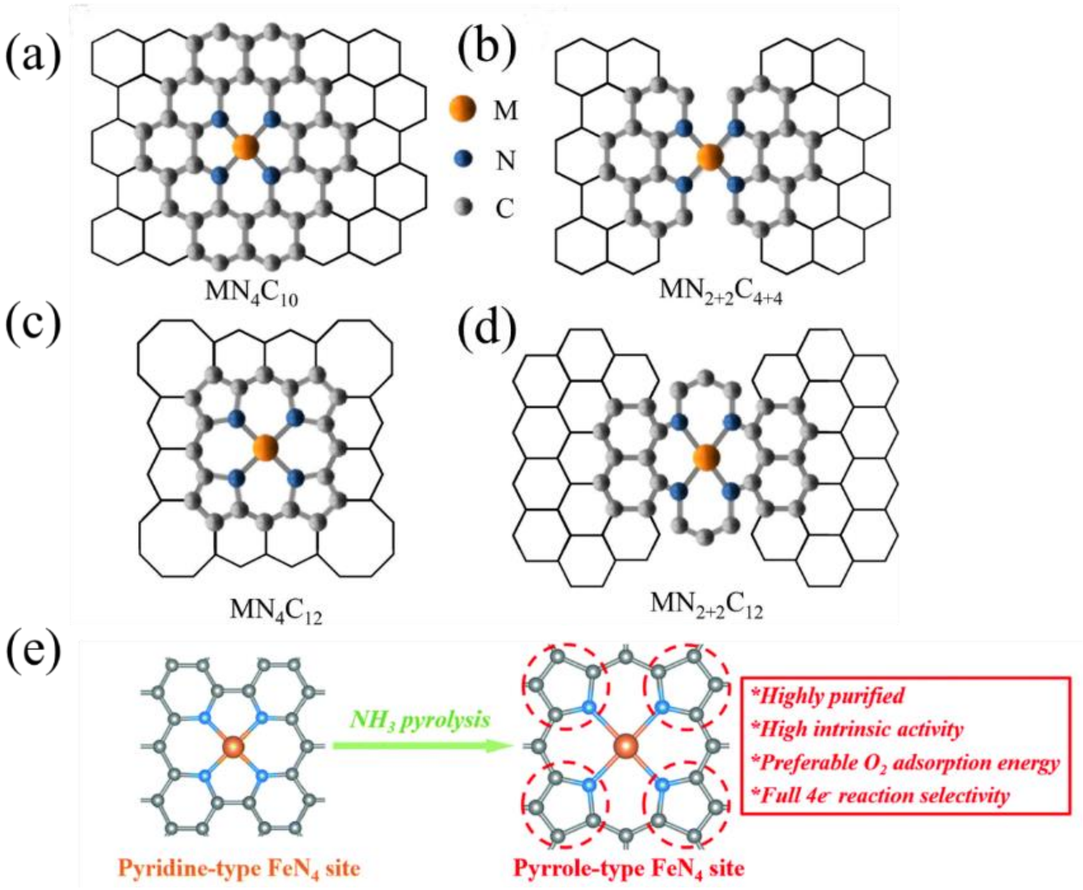

Figure 13. Proposed active site structures for Fe-centered moieties. (a) Pyridinic in-plane FeN_4C_{10} moiety, (b) pyridinic armchair edge $FeN_{2+2}C_{4+4}$ moiety, (c) porphyrinic in-plane FeN_4C_{12} moiety, (d) porphyrin zig-zag edge $FeN_{2+2}C_{12}$ moiety, (e) schematic illustration of preparation of high-purity pyrrolic-type FeN_4 site. Reproduced from Ref. [178, 179]

On the basis of Mössbauer spectrum results, some researchers propose there are typically three types of FeN_4 active sites coexisting in the Fe-N-C which may be responsible for high intrinsic ORR activity. They can be assigned to D1 (ferrous low-spin Fe^{2+}-N_4), D2 (ferrous intermediate spin Fe^{2+}-N_4 like FePc) and D3 (high spin $Fe^{2+}N_{2+2}$/C featuring a composite structure with a protonated basic nitrogen) respectively [168, 180]. It is widely accepted that D1 is predominant active site for high catalytic activity [167-169]. However, the exact FeN_4 structure has been debated due to the limitation of Mossbauer spectroscopy. For example, similar Mossbauer parameter for the D1 doublet could be observed for iron oxide nanoparticle or high-spin O_x-Fe^{3+}-N_4 site in room-temperature (RT) [119, 181, 182]. Zitol et al. [183] proposed two porphyrin-type architectures of FeN_4C_{12} moieties with two different O_2 adsorption configurations (the Fe atom is hexa- or penta-coordinated with 5th and/or 6th axial oxygen ligand), on the basis of ex situ X-ray absorption spectroscopy (XAS) analysis and DFT calculation, the obtained structure would preferentially generate via bridging two graphene sheets with zigzag edges. This viewpoint is further verified by other researchers [184], who suggested that doublet D1 could be assigned to $Fe(III)N_4C_{12}$ moieties in high-spin state and the doublet D2 is attributed to $Fe(II)N_4C_{10}$ moieties in low and medium spin. Recently, it has been reported that nature of D1 active site with high spin O_x-$Fe^{3+}N_4$ feature is severely altered by the variation of applied potential or during durability measurement [171]. Xiao et al. [185] claimed that high spin Fe^{3+}-N_4 configuration would convert to Fe^{2+}-N_4 at low potential, and the in-situ reduced Fe^{2+}-N_4 moiety can be responsible for high activity due to its high TOF value of ca.1.71 e s^{-1} $site^{-1}$. Li et al. [186] revealed that both sites initially contributed to the ORR activity but only D2 ($Fe(II)N_4C_{10}$) significantly contributes activity after 50 h of operation in fuel cell. The transformation of D1 ($Fe(III)N_4C_{12}$) into iron oxides ultimately results in loss of activity . Mukerjee’s group has made great efforts on the switching behavior of nature of active sites in Fe-N-C electrocatalysts under reaction condition by using advanced in-situ techniques [111, 119, 187]. Three important conclusions can be elucidated from their findings:

(1) the Fe^{2+}-sites are poisoned by the *OH from water activation above the redox potential as following equation: $Fe^{2+}\text{-}N_4 + H_2O \leftrightarrow OH_{ads}\text{-}Fe^{3+}\text{-}N_4 + H^+ + e^-$.

(2) at Fe^{3+}/Fe^{2+} redox transition potential, Fe^{3+}-N_4 can be reduced through redox mechanism described by Beck and Zagal [89, 188]: $Fe^{3+}\text{-}OH_{ads} + H^+ + e^- \leftrightarrow Fe^{2+} + H_2O$ (1); $Fe^{2+} + O_2 + H^+ +$

$e^- \rightarrow Fe^{3+}$-OOH_{ads}.

(3) D1 active site (high spin Fe^{3+}-N_4) at low potential (below $Fe^{2+}/^{3+}$ redox potential) is composed of a distorted Fe^{2+}-N_4 moiety embedded in amorphous carbon matrix characterized with out-of-plane Fe displacement. The central Fe ion moves back toward the plane upon the adsorption of oxygen specie in the axial position at high potential, the switching behavior is opposite as those in D2 active site (typical catalyst with FePc-like square order structure).

The easier escape of absorbed OH species on in-plane distorted Fe^{3+}-N_4 site induced by reduction at low potential, longer Fe-N distance as well as enriched charge of Fe center on out-plane Fe^{2+}-N_4 site results in higher Fe^{2+}/Fe^{3+} redox potential, stronger O_2 absorption and adjusted oxygenated intermediate binding energy. This factor leads to higher ORR activity of D1 active site than that of D2 site, which is also well explained that the carbonization is critical for Fe-based catalysts compared to that of original Fe-N_4 macrocycle [189]. On the basis of these findings, site-blocking effect resulted from water activation is proposed as crucial consideration of apparent activity, and intrinsic activity could be significantly improved by increasing the Fe^{3+}/Fe^{2+} redox transition potential [190, 191].

As previously mentioned, catalytic kinetic occurring on a wide range of electrode materials is governed by d-electron density of Fe center because the alteration of d-electron density greatly affects the σ-type bonding between Fe center and molecular O_2 orbital or oxygenated intermediate. The onset potential is accordance with Fe^{3+}/Fe^{2+} redox transition mechanism aforementioned [192-194]. In the early study, the ORR activity is considered to be positively correlated to electron density of Fe center. For instance, Kramm et al. [195] suggested a relationship between the electron density of the FeN_4 center and the catalytic activity. They found that electron transfer occurred from coordinated N atom to Fe metal in the FeN_4 site induced by the pyrolysis of the FeTMPPCl under higher temperatures, while an increase in electron density of the iron center enables an improvement in the turnover frequency during ORR. Likewise, Rauf et al. [105] proposed the protonation of pyridinic N in acidic media decreased the electron density of Fe center, which result in loss of ORR activity due to the weak affinity of O_2 toward Fe center of lower charge density. Nevertheless, there are growing consensus that the lower charge density of Fe center is crucial for the achievement of high ORR catalytic activity [196]. It is well known that the d-electron density of Fe center can be readily regulated by the surrounding π-conjugated ligand with various donating- or withdrawing-electron properties. For example, Seo et al. [197] reported FePc modified with electron donating diphenylphenthioether substituent presented lower catalytic activity than pristine FePc. Lower activity was attributed to stronger bonding of oxygen intermediate due to the enhance d-electron density imparted by enriched electron diphenylphenthioether ligand. Ramaswamy et al. [95] relocated the $Fe\text{-}N_4$ active site from a π-electron rich macrocyclic ligand environment to a relatively π-electron deficient graphitic carbon environment by pyrolysis of iron(III) meso-tetraphenylporphine chloride (FeTPPCl). The electron-withdrawing character of electron deficient graphitic carbon resulted in decreased electron density at the Fe center and downshift of the e_g-orbital away from Fermi-level, thus optimizing the adsorption strength of ORR intermediate and leading to higher turnover number. To further verify this proposal, they took advantage of stronger electron-withdrawing character of highly disordered graphitic carbon (ketjen EC600JD) acting as support. As expected, the TOF of as-prepared catalyst was significantly enhanced from $\sim 10\ s^{-1}\ site^{-1}$ to $\sim 30\ s^{-1}\ site^{-1}$ in alkaline media as a consequence of lower electron density of Fe center. On the other hand, the decreased charge density of Fe center positively shifts Fe^{3+}/Fe^{2+} redox transition potential, which finally lead to higher onset potential. Overall, these experimental and theoretical findings demonstrate that ORR catalytic activity of Fe-

N-C catalyst can be well modulated by changing the d-electron density of Fe center in the FeN_4 coordination configuration.

The preferential location of FeN_xC_y active site would explicitly offer useful guidance for rational design of ORR catalysts with more exposed active sites. It has been recognized that the enhanced microporosity could extremely facilitate improvement of ORR activity due to the larger number of accessible active sites exposed in open electrochemical system [7, 198]. Actually, the location of single atom Fe active sites strongly depends on the nature of FeN_xC_y. Mineva et al. [199] proposed that D1 site (porphyrin-type $O\text{-}Fe^{3+}\text{-}N_4C_{12}$) corresponds to surface-exposed sites while D2 (pyridinic type $Fe^{2+}\text{-}N_4C_{10}$) is bulk site that is inaccessible to O_2. This result suggests D1 site is probably located in micropore while D2 site is specifically located in in-plane of graphitic carbon. Similar conclusion is also made by Primbs et al. [200] that high spin Fe sites D1 are present in micropore and medium spin D2 are preferentially in mesopores. Concomitantly, there will be extra issue that the enriched defect Fe-N-C site is located at in-plane with divacancy substitution [166, 172] or on the edge of micropore/graphene sheet as well as slit between two graphene sheets [183, 201, 202] as depicted in Figure 14(a-b).

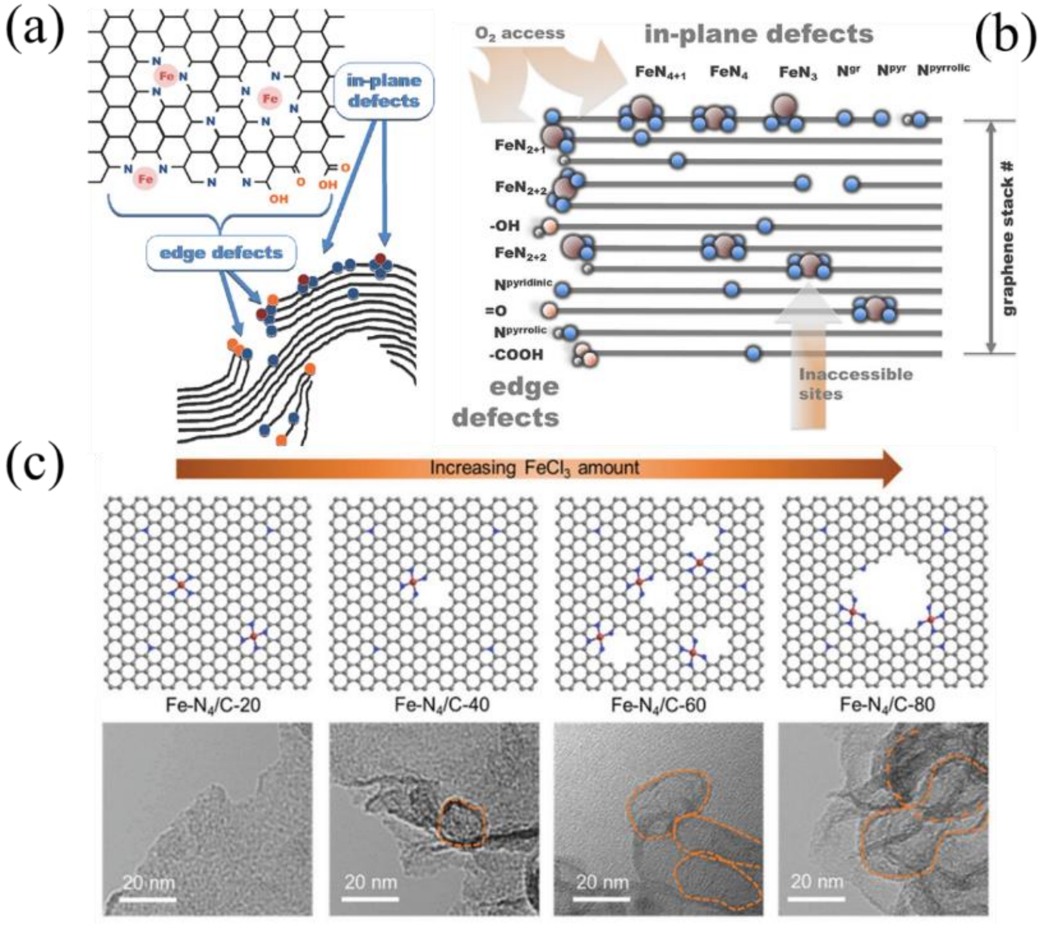

Figure 14. (a) Schematic representation of the transition metal-containing nitrogen defects in graphene sheet (Fe-N_x) and other possible defects that may have catalytic activity in ORR and its component reactions. (b) Illustration of potential active species and how position within the graphitic structure affects reactant access. Active species on the edges of graphitic planes are accessible without respect to the number of graphitic layers. Active species within the graphitic plane are accessible only on exterior planes. (c) The schematic illustration and transmission electron microscopy of (TEM) images of morphological evolution for Fe-N_4-C_x samples when varying the amount of reactant $FeCl_3$. Reproduced from Ref. [203-205].

It is clear that the electrochemical accessible active site number of FeN_4 moiety will significantly increase with the decrease of average graphene sheet numbers if majority of FeN_4 moiety are located at in-plane of graphene sheet. Workman et al. [204] found that sample with fewer graphitic layers exhibited increased kinetic performance in fuel cell test and this trend was consistent with the dominant active specie residing within the graphitic plane. For those FeN_4 moieties preferentially located at edge of micropore or graphene sheet, it is not closely linked with number of vertically stacked graphene sheets. On the contrary, increasing the edge site of graphene sheet or porosity with abundant edge in the lateral of graphene will play crucial role in the enhancement of catalytic activity. For instance, Jiang et al. [206] constructed hierarchical porous carbon structure by porosity engineering which transform local coordination of pyridinic-N like into edge -hosted $Fe\text{-}N_4$ moieties by selective C-N bond cleavage nearby Fe center. These sites demonstrated higher activity and long-term durability arising from the lower overall ORR barrier compared to intact atomic configuration. Likewise, Wang et al. [205] fabricated structurally controllable $Fe\text{-}N_4\text{-}C$ with adjustable quantity of hole equipped with different extent of edge site by simply varying the initial dosage of $FeCl_3$ precursor through two-step pyrolysis process followed by an acid leaching with in situ pore formed (Figure 14c). As a result, the ORR performance strongly depends on the concentration of edge site $Fe\text{-}N_4\text{-}C$ moiety and the higher amount of edge sites at a proper range is revealed to be more conducive of improvement of ORR catalytic activity. It is in accordance with density functional theory calculations that local electronic redistribution and bandgap shrinkage for edge-rich N-modified Fe endow it with a lower free-energy barrier toward direct four-electron ORR.

5. Material design on Fe-N-C

5.1 The formation mechanism of Fe-N-C

Generally, there are two requirements needed for improvement of Fe-N-C electrocatalyst performance: (1) the high density of active sites; (2) high intrinsic activity (or high TOF) of single active site [207]. Currently most of developed synthesis strategies primarily rely on trial and error approach to screen desired N, C and metal precursor or optimal pyrolysis temperature for maximization of catalytic activity [208]. Hence, the most institutive manner for achieving high activity catalyst is to increase the metal loading, while it is challenging to achieve high metal loading catalysts via traditional high temperature pyrolysis method due to unavoidable aggregation of ion species. The underlying mechanism for competitive formation of atomically FeN_x site and bulk Fe-based species is required to be unraveled prior to rational design of electrocatalyst.

Li et al. [209] studied that chemical transformation state from Fe precursor to exclusively ORR-active $Fe-N_4$ site by the use of in-situ X-ray absorption spectroscopy as schematically illustrated in Figure 15. The iron precursor is firstly transformed into Fe oxide below 300 ^{o}C, then to tetrahedral $Fe(II)-O_4$ between 300 ^{o}C and 600 ^{o}C by means of crystal-like melt transformation, finally Fe atom released by tetrahedral $Fe(II)-O_4$ above 600 ^{o}C was trapped into N-modified carbon defect in the “non-contact pyrolysis” manner, leading to the formation of $Fe-N_4$ sites by gas phase diffusion. The formation mechanism was further verified by the use of Fe precursor with no physical contact with N and C resources during pyrolysis and as expected, $Fe-N_4$ site was successfully achieved. Moreover, the proposed “non-contact pyrolysis” mechanism has recently been extended to other preparation strategy induced by chemical vapour deposition method [210]. It appears that there are some similarities of these fabrication strategies with bulk metal emitting and trapping of atoms during high temperature pyrolysis developed by Li and Wu’s research groups [211-215], albeit there are no report yet on the direct synthesis of FeN_4 site from bulk Fe-based specie. Overall, the synthesis methodology described above can be unified as “Top-down synthesis” which offers a deeper-level understanding for formation mechanism of atomically dispersed Fe site under high temperature pyrolysis and serves as guidance for preparation of effective ORR catalysts.

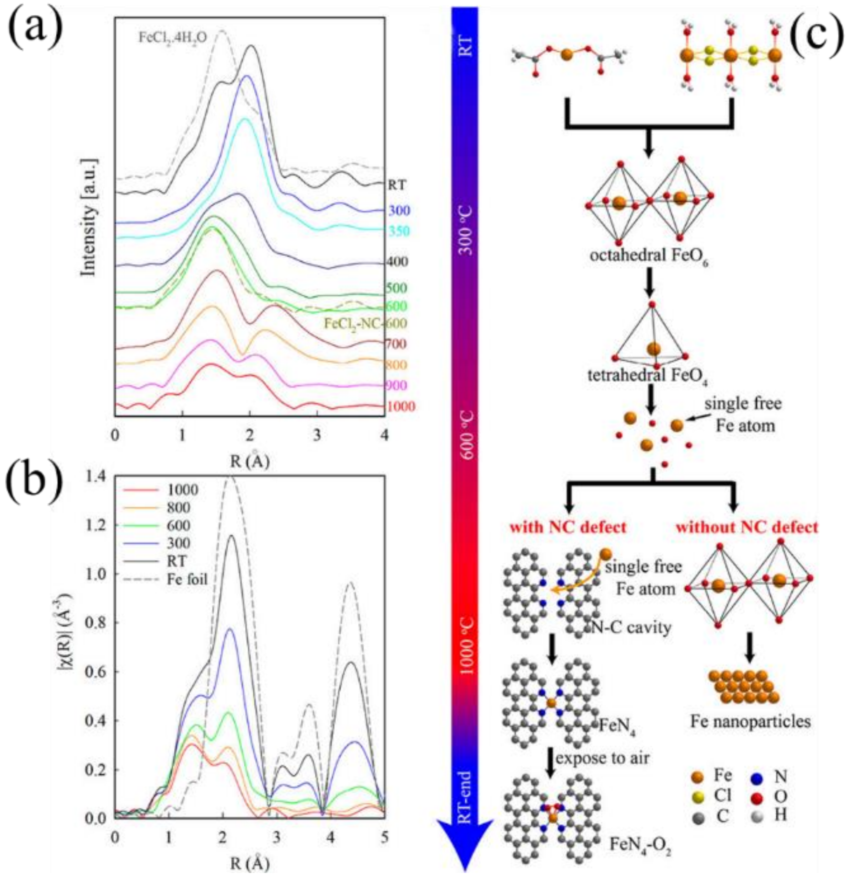

Figure 15. FT-EXAFS spectra of $FeCl_2\cdot 4H_2O$ mixed with SiO_2 collected with (A) temperature increasing from room temperature to 1000 ℃ together with and (B) cooling down to room temperature. (C) Schematic illustration of the common pathway up to 600 °C of the thermal evolution of iron compounds during pyrolysis, and then diverging pathways at T ≥ 600°C depending on the absence or presence of N-C defects. Note the FeN_4 configuration in the edge of two carbon planes displayed is only a representative case for illustration, without excluding other possible structures. Reproduced from Ref. [209]

Recently, considerable efforts have been devoted to development of Fe-N-C catalyst without agglomeration of Fe atoms during pyrolysis. Preliminary studies mainly pay attention to ball milling approach to disperse the iron atoms in carbon precursors [167, 216, 217]. On the basis of various design principles, wherein the synthetic protocols can be typically classified into protective atmosphere synthesis, sacrificial template method, coordination design method, confinement effect and the non-pyrolyzed method.

5.2 Protective atmosphere synthesis

The protective atmosphere assisted synthesis has emerged as an effective protocol for preparation of Fe-N-C, aside from the most commonly used Ar/N_2. A variety of protective gases have been employed including O_2 (air) [218], CO_2 [219, 220], NH_3 [221, 222], H_2/N_2 [113], $H_2/NH_3/Ar$ [163] etc. NH_3 has been most extensively studied as a protective gas involving the material preparation by high temperature pyrolysis, ascribing to its underlying triple roles: (1) afford partial N resources based on second NH_3 treatment of as-formed catalyst [223] [6, 224] or only N resource throughout pyrolysis procedure required to form FeN_x site by coordinating with Fe atom [225, 226]; (2) enlarge specific surface area by creating more micropores resulted from NH_3 etching effect. It is believed that the micropores improve ORR catalytic activity because the micropores can host most of active FeN_x sites [227, 228]; (3) introduce more N-bearing functionalities which have been revealed to be active for ORR especially in alkaline media.

5.3 Sacrificial template method

The sacrificial template method has recently been enormously applied for synthesis of high active atomic level Fe site. Generally, there are dual functions being responsible for formation of atomically dispersed Fe site with high performance:

(1) The pore-forming agent, it is well-known that hierarchical porous structure of carbon support will significantly facilitate the mass transport of reactants or electrolyte ions, thus improving the ORR activity. The implications of micropores have been well unveiled as a host of FeN_x active site aforementioned. In addition to that, the mesopores or macropores can serve as diffusion channel between active sites and the bulk solution, thus shorten the diffusion pathway

and accelerate the reaction. Due to importance of pore structure, the sacrificial template method offers a great potential for fabrication of Fe-N-C catalysts with hierarchical pore structure by elimination of template in post-treatment such as acid or basic solution leaching after pyrolysis.

(2) Interfacial constraint effect, the hard template can typically be employed as a “rigid” interface where immigrate and aggregate of iron atom in high pyrolysis temperature.is restricted. The interface thermal stress induced by high temperature would stabilize Fe atom and eventually preferentially generate atomically dispersed FeN_x catalytic sites incorporated in the carbon matrix. In traditional catalysis, such approach is usually used to prevent sintering of catalytic particles under high reaction temperature or harsh reaction condition [229, 230].

5.4 Coordination design method

Coordination site is of great importance for synthesis of Fe-N-C catalyst, which can serve as “paws” to absorb Fe atom or precursor preventing agglomeration during pyrolysis. Rational design of coordination site with N-containing function group as anchoring site to stabilize the Fe atom is expected to be an effective strategy for synthesis of Fe-N-C catalyst [13]. A large number of works have been reported based on coordination design strategy and all these as-prepared electrocatalysts show typically atomically dispersed FeN_x site without appreciable Fe agglomeration [231, 232]. Metal-organic hybrid frameworks assembled from metal ions and N-containing organic complexes have recently emerged as most common class of precursors for synthesis of Fe-N-C catalysts. There are mainly following several advantages for formation of atomically dispersed Fe:

(1) Organic linkers enriched heteroatom N bridges and isolates Fe ion in the form of complex-metal node, ensuring atomic-level dispersion of Fe during the pyrolysis process. Besides this, it also can be in-situ converted into N-doped carbon framework induced by heat treatment, offering strong anchoring site to bind isolated Fe atom.

(2) The metal-organic hybrid frameworks usually have abundant micropores volume with high specific surface area and tunable pore size distribution, which is highly conducive of accommodating more isolated Fe atoms and contributing to better electrocatalytic performance.

(3) The diversity and flexibility of organic linkers endow resulting Fe-N-C with different physicochemical properties after pyrolysis, thus enabling the maximum of catalytic activity.

5.5 Spatial Confinement method

Spatially confining single Fe atom into molecular-scale cage to prevent migration and agglomeration during pyrolysis has been developed as an effective strategy to prepare Fe-N-C catalyst. This spatial confinement method typically includes following two steps:

(1) The guest Fe precursors in the form of either inorganic Fe salts or Fe macrocycles are absorbed and confined into the pore cavities of host materials with high spatial distribution and mononuclear dispersion, these host materials are typically porous support materials with size-defined cavities such as MOF [233], ZIF [6, 234, 235] or porous N-doped carbon materials [236];

(2) Precursor ligands are removed and atomically dispersed Fe atoms are formed and stabilized by N atoms presented in carbon skeletons or derived from carbonization of organic scaffold induced by high temperature pyrolysis.

5.6 Pyrolysis-free method

High temperature pyrolysis involves tedious carbonization process and unpredictable Fe atom agglomeration. Thus, pyrolysis-free synthetic strategy is highly desirable in terms of its controllable coordination environment and cost-effective but challenging due to the intrinsic poor electrical conductivity. Directly grafting or incorporating Fe macrocycle complexes into conductive carbon matrix via π-π interaction and covalent functionalization are believed to be an effective approach to prepare atomically dispersed Fe catalyst [237-242]. In principle, this class of catalyst is inspired by enzymatic process and extensively studied in the preliminary stage [243].

6. Scope and outline of this thesis

In summary, extensive efforts have been devoted to the development of highly efficient Fe-N-C material towards ORR on both sides of mechanism and materials design. Although considerable progresses have been made in these fields, there are still some scientific and technological challenges remaining to be solved for the practical commercial application. The first issue is the identification of active site which is the fundamental prerequisites for the rational guidance in the synthesis of high active Fe-N-C. In fact, the knowledge of precise active site is still lacking especially for the multiple active sites existed in the Fe-N-C usually in the high Fe loading. The second point is the use of raw components. To date, almost all works take advantage of organic complex or polymer for the preparation of Fe-N-C catalyst. The exploitation of cost effective, non-toxic, earth-abundance feedstock with simple molecular structure is thought to be of great crucial for the consideration of practical application.

In this work, small molecular carbon and nitrogen precursor (particularly inorganic ammonia carbonate) are applied for the preparation of Fe-N-C catalysts. The explicit and well-defined molecular structure of precursors afford more rational understanding of the origin of final product's chemical-physical property. Electrocatalytic oxygen reduction reaction (ORR) is selected as target reaction and electrochemical activity and stability of as-prepared catalysts are evaluated by R(R)DE measurements. The roles of chemical composition at starting mixture and preparation conditions on nature of active site and ORR activity are systematically investigated. A comprehensive understanding of the structure-activity relationship on as-prepared catalyst will be given for the identification of ORR active sites.

Firstly, as described in the chapter 3, the two thermo-chemical steps in inert (A_r) and reactive (NH_3) atmosphere are employed for the preparation of high active atomically dispersed Fe catalyst, using glucose as main carbon source, citric acid as chelating reagent for hosting metal ions, ammonia carbonate as partial nitrogen source. Potassium thiocyanate (KSCN) is additionally introduced to tune chemical composition of final product. It is suggested that KSCN serves as a structural mediator for the preferentially generation of atomically dispersed Fe sites. Post NH_3 thermo-chemical treatment for as-prepared pre-catalyst phase, plays an important role for the enhanced ORR activity, the enhanced electrochemical activity is associated with change of surface properties.

Secondly, the chapter 4 presents the modified strategy, which is applied for the preparation of atomically dispersed Cl-FeN_4 sites where citric acid is used as only carbon source, ammonia carbonate as only nitrogen source. The simultaneously entering of SiO_2 and $ZnCl_2$ is critical for the generation of higher density single Cl-FeN_4 sites and is found to be indispensable for high ORR activity. On the other hand, the systematic variables such as different amount of ammonia carbonate and various amount of Fe loadings are also studied. As a result, the formation mechanism of Fe-N-C single atom catalyst based on gas-solid interface reaction is proposed and the real active sites are identified.

Thirdly, in the chapter 5, an active and durable single atom Fe catalyst toward ORR over both alkaline and acid media is developed based on pyrolysis approach with glucose as carbon source, NH_4Cl as nitrogen source, and $FeCl_3$ as metal precursor. It is found that pyrolysis temperature has a significant influence on ORR activity, and optimal pyrolysis temperature is 900 ºC. By establishing structure-performance relationship, the pyrolysis temperature dependent ORR activity is well clarified in terms of geometric and electronic properties, which is a result of trend-off between site density and intrinsic activity as well as electron conductivity.

Furthermore, the chapter 6 describes a facile and scalable one-step pyrolysis strategy, which is developed for the preparation of hybrid catalyst enriched abundant FeN_x moieties coupling with highly graphitic carbon layer encapsulated Fe_3C/Fe_3O_4 nanoparticles, where carbon black is used as support backbone and glucose as secondary carbon precursor, urea serves as nitrogen source. The obtained catalyst shows a hierarchical structure consisting of carbon black as primary carbon phase and graphene-like carbon sheet as secondary carbon phase. The influence of Fe loading on ORR activity is investigated and the optimal Fe loading is found to be 4.5 wt. %. A series of control experiments reveal that FeN_x moieties are real active sites toward ORR and Fe_3O_4 nanoparticle itself shows no activity but endows positive promotion effect on activity of FeN_x sites via electronic interaction.

The last chapter 7 will be devoted to the general conclusion, the further work and perspective are also discussed especially for the extended research in the other field with as-existed Fe-N-C system.

Chapter 2

Materials preparation, characterization and catalytic application

1. Catalyst preparation

1.1 Materials and catalysts (Chapter 3- the synthesis of Fe/NSMC-SHT and control samples)

1.1.1 Materials

D-glucose [$C_6H_{12}O_6$, 100 %, MW: 180.16 g mol^{-1}], citric acid [$C_6H_8O_7$ anhydrous, > 99.5 %, MW: 192.12 g mol^{-1}] and ammonium carbonate [$(NH_4)_2CO_3$, MW: 96.09 g mol^{-1}], were provided by ACROS OrganicTM, MYPROTEINTM and VWR Chemicals, respectively. Potassium thiocyanate (KSCN > 97 %; MW: 97.18 g mol^{-1}), Iron (III) chloride hexahydrate ($FeCl_3 \cdot 6H_2O$ > 98%, MW: 270.30 g mol^{-1}) and Nafion® (5 wt. % in isopropanol and water) were obtained from Merck and Fluka. Unless otherwise stated, all reagents and solvents were used as provided by commercial suppliers without any further purification/treatment.

1.1.2 Catalyst preparation

In a typical procedure, 1 g of D-glucose, 1.5 g of citric acid, 1.5 g of $(NH_4)_2CO_3$, and 0.1566 g of KSCN are dissolved into 25 mL of ultrapure water (Veolia Ultra Analytique, 18.2 Mohm.cm, TOC < 2 ppb) at room temperature. Afterwards, 0.1452 g of $FeCl_3 \cdot 6H_2O$ is dissolved into another 3 mL of water, followed by adding dropwise into above clear solution under stirring condition. The obtained yellow solution is stirred for 30 min and then transferred into oven at 110 ºC overnight. Then, the resulting gel mixture (denoted as Fe/NSMC-P) is subjected to first pyrolysis in Ar at 900 ºC for 1 h with a ramp of 5 ºC/min (denoted as Fe/NSMC). Next leaching in 0.5 M H_2SO_4 at 80 ºC is performed for 8 h. The leached sample is washed until neutral with water and ethanol for several times and dried at 75 ºC overnight (denoted as Fe/NSMC-W). Finally, the as-obtained sample undergoes the second NH_3 treatment at 900 ºC for 10 min, as denoted Fe/NSMC-SHT. For the sake of comparison, different control samples are also prepared under almost identical condition except without addition of Fe precursor (NSMC-SHT), without addition of

KSCN (before the first Ar thermal treatment: Fe/NMC-P, after the first Ar thermal treatment but without acid leaching: Fe/NMC, after acid leaching: Fe/NMC-W, after the second NH_3 treatment: Fe/NMC-SHT), without addition of Fe precursor and KSCN (corresponding to NMC-P, NMC, NMC-W, NMC-SHT).

1.2 Materials and catalysts (Chapter 4- the synthesis of ^{2}Fe/NHPC^{5AC} and control samples)

1.2.1 Materials

Citric acid [$C_6H_8O_7$ anhydrous, > 99.5 %, MW: 192.12 g mol^{-1}] and ammonium carbonate [$(NH_4)_2CO_3$, MW: 96.09 g mol^{-1}], are provided by Fisher Chemicals and ACROS Organics, respectively. Zinc chloride ($ZnCl_2$, anhydrous, > 98 %; MW: 136.286 g mol^{-1}) and silica (SiO_2, fumed, 7 nm, MW: 60 g mol^{-1}) are obtained by Sigma-Aldrich. Iron (III) chloride hexahydrate ($FeCl_3{\cdot}6H_2O$; > 98 %, MW: 270.296 g mol^{-1}) and Nafion® (5 wt. % in isopropanol and water) are obtained from Alfa Aesar and Fluka, respectively. Unless otherwise stated, all reagents and solvents are used as provided by commercial suppliers without any further purification/treatment.

1.2.2 Catalyst preparation

For a typical procedure, 2 g of citric acid (10.41 mmol), 5 g of $(NH_4)_2CO_3$ (52 mmol), 1.2 g of silica (20 mmol) are first dissolved in 25 mL ultrapure water (Veolia Ultra Analytique, 18.2 Mohm.cm, TOC < 2 ppb) under stirring until uniform liquid sol is obtained. Then, 0.024 g $FeCl_3{\cdot}6H_2O$ (0.087 mmol), 0.2435 g $ZnCl_2$ (1.75 mmol) are dissolved into another 3 mL distilled water, followed by adding dropwise into above sol. After continuous stirring for 30 minutes, the mixture solution is transferred to oven for drying at 110 ^{o}C overnight. The dried solid is well crushed into fine powder and calcinated at 900 ^{o}C for 2 h under Ar atmosphere. Next, the as-obtained products are immersed into 120 mL of 2 M NaOH with stirring overnight at 80 ^{o}C to remove the silica template. After water and ethanol washing and drying, the sample is finally obtained by the second calcination at 900 ºC for 2 h under Ar atmosphere, which is denoted as ^{2}Fe/NHPC^{5AC} (thereafter superscripts “2” and “5AC” referred to as usage of Fe precursor and $(NH_4)_2CO_3$, respectively)

For the sake of comparison, a series of control samples are also prepared with identical synthetic route except for various usage of $(NH_4)_2CO_3$ (0 g, 0.5 g, 8 g) which are denoted as ^{2}Fe/HPC^{0AC}, ^{2}Fe/NHPC$^{0.5AC}$, ^{2}Fe/NHPC^{8AC}, respectively. Besides, control samples with addition of 0 g, 0.006 g, 0.1 g $FeCl_3 \cdot 6H_2O$ are also prepared with the same condition based on optimized addition amount of 5 g $(NH_4)_2CO_3$ which are denoted as NHPC^{5AC}, ^{1}Fe/NHPC^{5AC}, ^{3}Fe/NHPC^{5AC}, respectively. To investigate the effect $ZnCl_2$ and SiO_2 addition on catalytic performance. The ^{2}Fe/NHPC^{5AC}-w/o $ZnCl_2$, and ^{2}Fe/NC^{5AC}-w/o SiO_2 are also obtained without addition of $ZnCl_2$, without addition of SiO_2, respectively.

1.3 Materials and catalysts (Chapter 5- the synthesis of Fe/NMC-900 and control samples)

1.3.1 Materials

D-glucose [$C_6H_{12}O_6$, 100 %, MW: 180.16 g mol^{-1}] are provided by ACROS Organic™. Silica (SiO_2, fumed, 7 nm, MW: 60 g mol^{-1}) and ammonium chloride [NH_4Cl, MW: 53.5 g mol^{-1}] are obtained by Sigma-Aldrich. Iron (III) chloride hexahydrate ($FeCl_3 \cdot 6H_2O$; > 98 %, MW: 270.296 g mol^{-1}) and Nafion® (5 wt. % in isopropanol and water) are obtained from Alfa Aesar and Fluka, respectively. Unless otherwise stated, all reagents and solvents are used as provided by commercial suppliers without any further purification/treatment.

1.3.2 Preparation of catalyst

For a typical procedure, 2 g of Glucose (11.1 mmol), 5 g of NH_4Cl (93.5 mmol), 1.2 g of silica (20 mmol) are first dissolved in 25 mL ultrapure water (Veolia Ultra Analytique, 18.2 Mohm.cm, TOC < 2 ppb) under stirring until uniform liquid sol is obtained. Then, 0.05 g $FeCl_3·6H_2O$ (0.185 mmol) are dissolved into another 3 mL distilled water, followed by adding dropwise into above sol. After continuous stirring for 30 minutes, the mixture solution is transferred to oven for drying at 110 ^oC overnight. The dried solid is well crushed into fine powder and calcinated at different temperature (800, 900, 1000 ^oC, respectively) for 2 h under Ar atmosphere. Next, the as-obtained products are immersed into 120 mL of 2 M NaOH with stirring overnight at 80 ^oC to remove the silica template. After water and ethanol washing and drying, the samples are finally obtained by the second calcination at same temperature as the first thermal pyrolysis for another 1 h under Ar atmosphere, which are denoted as Fe/NMC-X (where "X" = 800, 900, 1000 ^oC, referred to pyrolysis temperature). The control sample NMC is also prepared under the identical condition at comparison without Fe precursor addition.

1.4 Materials and catalysts (Chapter 6 - the synthesis of $^{4.5}$Fe@NGC/CB and control sampels)

1.4.1 Materials

D-glucose [$C_6H_{12}O_6$, 100 %, MW: 180.16 g mol^{-1}], Urea [CH_4N_2O, high purity, MW: 60.06 g mol^{-1}], Carbon black (Vulcan XC-72) are provided by ACROS Organic^{TM}, VWR International, and Cabot corporation, respectively. Iron (III) chloride hexahydrate ($FeCl_3·6H_2O$ > 98%, MW: 270.30 g mol^{-1}) and Nafion$^{®}$ (5 wt. % in isopropanol and water) are obtained from Merck and Fluka, respectively. Unless otherwise stated, all reagents and solvents are provided by commercial suppliers without any further purification/treatment.

1.4.2 Preparation of catalysts

In a typical procedure, 0.2 g of carbon black, 0.2 g of glucose, 4 g of urea are well mixed together by grinding to obtain a uniform solid mixture. Afterwards, an incipient-wetness impregnation of iron chloride aqueous (0.05 g of $FeCl_3·H_2O$ is dissolved into 2.3 mL ultrapure water, Veolia Ultra Analytique, 18.2 Mohm.cm, TOC < 2 ppb) is employed on the mixture to form a black slurry followed by drying overnight at 80 ^{o}C. The obtained mixture is ground into powder, followed by annealing at 900 ^{o}C for 2 h under argon atmosphere. Eventually, the $^{4.5}$Fe@NGC/CB hybrid is directly collected without any other post-treatment, where superscript is denoted as mass loading of Fe determined by inductively coupled plasma-atomic emission spectroscopy (ICP-AES). For the sake of comparison, the variable amounts of Fe precursor (0 g, 0.01 g and 0.25 g $FeCl_3 \cdot H_2O$) are also used for the fabrication of NGC/CB, $^{1.15}$Fe@NGC/CB, $^{16.2}$Fe@NGC/CB, respectively, with identical synthetic route as described above. Fe@NCB and Fe@C/CB are prepared without addition of glucose and urea at comparison to gain insight into the role played by secondary graphene-like carbon phase and N-doped effect, respectively.

2. Catalysts characterization

Scanning Electron Microscopy (SEM) analyses are carried out on a Zeiss 2600F with a resolution of 5 nm. Samples are deposited onto a double face graphite tape in order to avoid charging effects during the measurements.

The loading amount of Fe of as-prepared catalyst is determined by *inductively coupled plasma-atomic emission spectroscopy* (*ICP-AES*, Plasma-Spec-II spectrometer).

The *Raman spectra* is recorded using a LabRAM ARAMIS Horiba Raman spectrometer equipped with a Peltier cooled CCD detector. A laser line (532 nm/100 mW (YAG) with Laser Quantum MPC600 PSU) is used to excite sample.

The *temperature-programmed desorption-mass spectra (TPD-MS)* is conducted on a Micromeritics ASAP-2100 setup equipped with a multichannel mass spectrometer: In a typical procedure, 50 mg of the samples is loaded in the reactor and then flushed with He (50 mL min^{-1})

at 50 °C for 1 h. Afterward, the temperature is raised from 50 to 1000 °C at a heating rate of 5 °C min^{-1}. The evolved species are monitored with intensities of m/e.

Thermogravimetric analyses (TGA) are performed under A_r or air (25 mL min^{-1}) atmosphere on an EXSTAR thermogravimetric analyzer (TG/DTA) Seiko 6200, the temperature is raised from room temperature to 900 ^{o}C with a heating rate of 10 ^{o}C min^{-1}.

Fourier transform infrared (FTIR) measurements were carried out using a Nicolet iS10 FTIR spectrometer (Thermo Scientific) equipped with a Smart Diamond attenuated total reflection (ATR) accessory in the spectral range of 400 - 4000 cm^{-1}.

Transmission electron microscopy (TEM) is carried out on a JEOL 2100F working at 200 kV accelerated voltage, equipped with a probe corrector for spherical aberrations and a point-to-point resolution of 0.2 nm. The sample is dispersed by ultrasounds in an ethanol solution for 5 min and a drop of the solution is deposited on a copper grid covered with a holey carbon membrane for observation.

X-ray photoelectron spectroscopy (XPS) measurements are carried out in an ultrahigh vacuum (UHV) spectrometer equipped with a VSW Class WA hemispherical electron analyzer. A monochromatic Al Kα X-ray source (1486.6 eV) is used as incident radiation. Survey and high-resolution spectra are recorded in constant pass energy mode (90 and 50 eV, respectively).

X-ray diffractograms (XRD) is recorded using Cu Kα radiation (40 mA, 45 kV) in the 10–80^{o} 2θ range, using step size and step time of 0.05^{o} and 80 s, respectively.

The pore structural property of the different samples is determined by *N_2 adsorption/desorption isotherms* at 77 K with a Micromeritics Tristar II instrument (Micromeritics GmbH, Munich, Germany). Before measurement, the sample is outgassed at 200 ^{o}C under vacuum overnight.

X-ray adsorption spectroscopy (XAS) measurements is carried out in fluorescence mode at the BL14W1 station of the Shanghai Synchrotron Radiation Facility (SSRF, 3.5 GeV, 250 mA in maximum, Si (311) double crystals). IFEFFIT software packages are used to process the data. The extended X-ray absorption fine structure (EXAFS) contributions is separated from different coordination shells using a Hanning window (dk = 1.0 Å^{-1}).

3. Preparation of electrode and oxygen reduction reaction (ORR)

In order to prepare working electrode, various catalyst loadings are investigated, and the optimal catalyst loading for ink preparation in four works are described as following:

(1) for the first work (Chapter 3), 6 mg catalyst is first dispersed in mixture solution containing 100 μL ethanol, 300 μL ultrapure water and 15 μL Nafion solution (5 wt. % in isopropanol and water), followed by sonicating for 30 min to form a homogeneous ink. Then, 10 μL ink is drop-casted on the surface of glassy carbon rotating (ring) disk electrode (RDE(RRDE) Metrohm, 5 mm in diameter), followed by naturally drying in room temperature. The dried electrode is used as working electrode with a catalyst loading of 0.75 mg cm^{-2};

(2) for the second work (Chapter 4), the 5 mg catalyst is first dispersed in mixture solution containing 750 μL ultrapure water, 250 μL isopropanol and 80 μL Nafion solution (5 wt. % in isopropanol and water), followed by sonicating for 30 min to form a homogeneous ink. Then, 16 μL ink is drop-casted on the surface of glassy carbon rotating (ring) disk electrode (RDE/RRDE Metrohm, 5 mm in diameter), followed by naturally drying in room temperature. The dried electrode is used as working electrode with a catalyst loading of 377 μg cm^{-2};

(3) for the third and fourth works (Chapter 5 and 6), 5 mg of catalyst powder are dispersed in a 1 mL solution including 250 μL of ethanol and 750 μL of ultrapure water. 50 μL of a Nafion® solution (5 wt. % isopropanol and water) are added to above solution. The obtained mixture solution is then ultrasonically treated for 30 min until uniform ink formed. 16 μL ink is drop-casted on the surface of glassy carbon rotating (ring) disk electrode (RDE/RRDE, Metrohm, 5 mm in diameter), followed by naturally drying in room temperature. The dried electrode is used as working electrode with a catalyst loading of 388 μg cm^{-2};

Ag/AgCl electrode and graphite rod as reference and counter electrode respectively, all of the potentials are calibrated to reversible hydrogen electrode (RHE) according to following equation: $E_{\mathrm{RHE}} = E_{\mathrm{Ag/AgCl}} + 0.197 + 0.0592$ pH. All measurements are performed in three-electrode cell with compartments of working and counter electrode separated by porous glass membrane to exclude any transfer of possible products of processes on CE to WE compartment. Electrochemical measurements are performed with Bio-Logic SP-300 potentiostat by using EC-Lab 11.32 software. Linear sweep voltammetry (LSV) is conducted in O_2-saturated 0.1 M KOH electrolyte with a scan rate of 10 mV s^{-1} at a rotating rate of 1600 rpm. For comparison, the standard Pt loading amount of 20 μg cm^{-2} is used for the Pt/C (Vulcan carbon XC-72, 20 wt. %, E-TEK, Inc. USA) sample. The accelerated durability tests (ADT) are measured by cycling the catalysts between 0.6 and 1.0 V at scan rate of 50 mV s^{-1} under O_2 atmosphere. The chronoamperometry response is collected by polarizing the catalyst with a rotating speed of 1600 rpm at 0.65 V (vs. RHE). The methanol poisoning experiment is performed in O_2-saturated 0.1 M KOH with addition of 1 % (*v* : *v*) MeOH. The number of electrons involved in oxygen reduction reaction (ORR) is determined by the Koutecky-Levich equation as follow:

$$\frac{1}{J}=\frac{1}{J_L}+\frac{1}{J_K}=\frac{1}{B\omega^{1/2}}+\frac{1}{J_K} \quad (1)$$

$$B=0.62nFC_OD_O{}^{2/3}\upsilon^{-1/6} \quad (2)$$

where J is the measured current density per electrode geometric surface area, J_K and J_L are the kinetic and diffusion-limiting current densities respectively, ω is the angular velocity (rad s^{-1}), n is a number of electrons in ORR reaction, F is the Faraday constant (96485 C mol^{-1}), C_o is the bulk concentration of O_2 (1.2×10^{-6} mol cm^{-3}), D_o is the diffusion coefficient of O_2 in 0.1 M KOH (1.9×10^{-5} cm^2 s^{-1}), and υ is the kinetic viscosity of the electrolyte (0.01 cm^2 s^{-1}).

For rotation ring-disk electrode (RRDE) tests, the working electrode (PINE AFE6R2GCPT, glassy carbon disk with a diameter of 5 mm, Pt ring with inner diameter of 6.5 mm and outer diameter of 7.5 mm) is prepared with the same catalyst loading as RDE test, the ring potential is kept at 1.2 V vs. RHE. The number of electron transfer and HO_2^- yield are evaluated by following equations:

$$X_{HO_2^-}=\frac{200\ I_r/N}{I_d+I_r/N} \quad (3)$$

$$n_{e^-}=\frac{4\ I_d}{I_d+I_r/N} \quad (4)$$

wherein I_r and I_d are the ring and disk current, respectively, and N (0.25) is the ring collection efficiency.

The electrochemical double layer capacitances (C_{dl}) of catalysts are calculated by the use of simple CV method. A potential range of 1.02 - 1.12 V *vs.* RHE is selected for the capacitance measurements. Then, the average capacitive currents derived from difference of anode and cathode current at potential of 1.07 V *vs.* RHE are plotted as a function of the CV scan rate of 5, 10, 15, 20, 25, 30 mV s^{-1}. These data are then fit to a line, the slope of which is used as C_{dl} value.

Chapter 3

An Open Gate for High-Density Metal Ions in N-doped Carbon Networks: Powering Fe-N-C Catalyst Efficiency in Oxygen Reduction Reaction

Abstract

Non-noble metal catalysts displaying catalytic activity for Oxygen reduction Reaction (ORR) comparable or even superior to that of the commercial Pt/C catalyst are of high interest for the development of a mature fuel cells technology. Fe-N-C moieties exhibit excellent performance in the ORR although a synthetic strategy for their production still remains a challenging matter. Herein, an original and general protocol for the preparation of high-density and discrete Fe-N-C-based atomically dispersed catalysts on carbon-based matrix has been proposed. The catalysts were produced starting from cheap and food-grade raw components which significantly contributes to the reduction of energy incentive treatment after the synthesis step. The rational combination of chelating citrate ions with the ancillary monodentate SCN^- ligand has established as an “open gate” for water soluble iron ions to be accommodated in the form of Fe-N-C moieties within final C-N networks. NH_3 post thermo-chemical treatment further introduces the highly basic N-terminated groups, as well as enhancing the exposure of active sites by creating more abundant porosity. Although recent findings in the field of electrocatalysis have pointed out the often-beneficial synergistic action between isolated and metallic iron species or iron carbides and their protecting C-N shells, the poor selectivity on the nature of the final Fe-species in N-doped C-networks remains matter of debate and does not contribute to shed light on the effective nature of the active species in the process. The highly metal-loaded catalysts in the form of atomically dispersed Fe-N-C moieties prepared with the synthetic protocol described in this chapter have been tested as electrocatalysts in the oxygen reduction reaction (ORR), showing excellent electrocatalytic performance under alkaline environment. Detailed study suggested that the high catalytic activity observed can be ascribed to the optimal porous structure, surface chemical composition as well as

specific active site of FeN_x moieties, generated between iron oxyhydroxide and N-doped graphitic C network.

1. Introduction

In order to keep with the relentless pace in the development of H_2-O_2 fuel cells (PEMFC, AFC), the kinetically sluggish oxygen reduction process (ORR) is among the most investigated reactions with both metal-[244] and metal-free [245, 246] catalysts.[247] On this regard, the last years have witnessed impressive progresses in the development of innovative synthetic methodologies for the straightforward preparation of efficient (electro)catalysts from cheap and non-critical components with a special attention to the replacement of scarce and costly platinum-group metals (PGMs) [248, 249]. In addition, Numerous researches have been devoted in controlling the shape and reducing the size of the active phases from a nanometer scale down to few-atoms cluster-sized and finally, to single atomic site catalysts (SACs). Such an effort has been dictated by the need of reducing the active-phase amount, maximizing the atom utilization and optimizing the metals microenvironment by improving their stabilization with appropriate donor atom sets. In other words, all this work has been focused on the improvement of catalysts performance in key (electro)catalytic processes [250-254]. Although reducing nanocatalysts sizes down to atomically dispersed metal systems still represents a challenging matter and especially for medium-to-high metal loading [255], it is commonly recognized that the control of both electronic and geometric structural features of metal sites is the key tool to get catalysts exhibiting unique and improved electro(catalytic) performance [256-258].

In our previous work we have proposed a green and versatile synthetic method for the preparation of N-enriched mesoporous carbon-based materials starting from cheap and food-grade raw building blocks [259-261]. Such an approach was successfully used to translate powdered catalyst into hierarchically 3D foam catalyst structures [259, 260] and organic-inorganic composites [262-264] to be employed as effective, stable and single-phase metal-free systems for catalyzing a relatively wide number of industrially relevant transformations. At odds with more conventional methods to produce N-rich carbon networks, *i.e.* the chemical-vapor-deposition (CVD) technique, C and N sources employed for the synthesis of these novel materials were selected from commonly available solid feedstock to be simply dissolved in water. D-glucose ($C_6H_{12}O_6$) was selected as C-source, a leavening agent [*i.e.* ammonium carbonate $(NH_4)_2CO_3$)] as N-source and citric acid ($C_6H_8O_7$) as a sacrificial carrier for harvesting and conveying NH_3 released from the carbonate decomposition under the form of ammonium citrate [$HO-C_3H_4(COO)_3H_x(NH_4)_{3-x}$)] (x = 0 - 3). Successive and controlled material thermal treatments have led to mesoporous carbon networks featuring with relatively high specific surface areas (*i.e.* 150 $m^2 g^{-1}$) and N-contents up to 5 wt.%.

The presence of a potentially tridentate chelating agent (*i.e.* citrate ions) prompted us to reconsider our original metal-free scheme as a protocol for the preparation of highly dispersed and atomically sized metal-based catalysts. Indeed, citrates are known to act as chelating agents towards a variety of transition metals, forming relatively stable and water-soluble complexes. Accordingly, their generation can be regarded as an “open gate” for water soluble metal ions to be accommodated and stabilized within final C-N networks.

Although in the past few years’ huge efforts have been devoted to power single-atom catalysts technology within light-heterodoped nanocarbon networks, their large-scale production with a high metal-active site density, avoiding the generation of inhomogeneous metal agglomerates or the co-generation of less active metal species, remains a challenging task to be properly addressed.

Seminal works from two independent teams have recently shed light on the role of thiocyanate (SCN^-) as a sacrificial ancillary ligand for Fe-metal ions in the synthesis of atomically dispersed Fe-N-C composites with superior electrocatalytic activity [265, 266]. In particular, Wu et al. have demonstrated the role of sulfur ligands addition (in the form of SCN^-) to a mixture of 2,2-bipyridine and $FeCl_3$ on the ultimate composition of an acid-washed CNT-coating layer obtained from the materials pyrolysis at 900 °C [265]. They found that S-salt addition to the mixture during pyrolysis resulted in the formation of Fe-sulfides mainly instead of the more acid-resistant Fe carbides. Given the higher solubility of the former in acidic media, the large excess of Fe not present in the form of Fe-N_x coordinated ions was easily etched and removed during the washing treatment, leaving behind atomically dispersed Fe-N_x species [267]. Wei, and co-workers proposed another intriguing example for the control of SACs in Co-N/C systems through the pyrolysis of an urea and glucose mixture in the presence of SCN^- as the counterion for a Co^{2+} salt precursor [268]. They found that SCN^- addition reduced the temperature at which Co-rich particles grew respect to the temperature at which their C-shell encapsulation occurred. Accordingly, their removal along with other various impurities was easily accomplished by a simple acid washing while preserving the SA-Co-N/C active phases only.

On the other hand, it is well known that the Fe-N-C catalysts derived from pyrolysis in NH_3 possess relatively high ORR activity but limited durability [174, 269]. Zitolo et al. [183] claimed the formation of the same Fe-center moieties in both Ar pyrolysis and NH_3 post-treatment by the use of XANES and Mössbauer spectra, and attributed the much higher activity, after NH_3 post-treatment, to the change of the chemical-physical properties of support. Subsequently Kramm et al. [113] fabricated Fe-N doped carbon with exclusive presence of FeN_4-type sites taking advantage of N_2/H_2 treatment of Fe/N/C followed by acid leaching. They came to the conclusion that the second N_2/H_2 treatment allowed one to increase the surface area of the catalyst whereas the inorganic Fe species migrate to the surface that is easier to be washed out by acid treatment. Hence, an enhanced surface area and better utilization of active sites is at the origin of higher ORR activity after purification. Although recent advances have significantly improved Fe-N-C catalytic performance by NH_3 treatment, but the role of such post-synthesis NH_3 thermal treatment on the modification of the active sites still remains a problem to be resolved.

Herein, we report a novel and effective approach towards the preparation of highly dispersed Fe-N-C frameworks, starting from the chelating ability of the tridentate citrate ion with a Fe^{3+} salt as metal precursor, followed by two thermal pyrolysis steps in different atmosphere (Ar and NH_3). The simultaneous entering of the monodentate thiocyanate (SCN^-) ion in the metal coordination sphere was found to be highly beneficial for the ultimate preparation of a Fe-N-C composite. Indeed, the excess of iron which was not stabilized in the form of Fe-N-C nuclei throughout the high-temperature pyrolysis, was preferably converted into iron sulfide species on the outer surface of carbon matrix which can be easily etched and removed compared to iron carbides upon the sample acid washing. Although any mechanistic consideration on the Fe-coordinated SCN^- ion(s) during the material pyrolysis remains merely speculative, our outcomes leave no doubts that catalysts prepared without the addition of SCN^- ions lead to a more inhomogeneous Fe-containing samples with the evident formation of iron-carbide nanoparticles to a markedly higher extent. The NH_3 post thermo-chemical treatment also plays a crucial role of improvement of ORR activity and its activation effect is also well unveiled. The as-prepared Fe-N-C catalysts, with and without SCN^- and NH_3 treatment, were thoroughly characterized and evaluated for the ORR process under alkaline environment. The optimal catalyst Fe/NSMC-SHT exhibiting highly graphitic porous C networks structure enriched with high density FeN_x moieties in the interface between N-doped carbon basal plane and Fe oxyhydroxide, shows outstanding electrocatalytic performance.

2. Results and discusses

D-glucose, citric acid, ammonium carbonate are cost-effective and non-toxic naturally carbon/nitrogen-containing chemicals, which have been intensively employed in food-processing industries. Integration these cheap and abundance components into the synthesis procedure of specific catalysts affords a great progress toward renewable energy technology. The use of these basic materials in the synthesis of the Fe-N-C catalyst, atomically dispersed on the surface of the catalyst, allows one to demonstrate the high efficiency of nitrogen doping with $(NH_4)_2CO_3$ as an inorganic precursor. Typically, a mixture of D-glucose, citric acid, KSCN and $(NH_4)_2CO_3$ are dissolved in deionized water to get a homogeneous solution followed by a dropwise addition of an aqueous solution containing Fe precursor. A subsequently drying process at 110 ^{o}C under air induces the formation of gelation accompanied by a series of complex transformations (condensations, acid-base reactions, decompositions). Particularly, this process results in the complete decompositions of ammonium carbonate $[(NH_4)_2CO_3 \rightarrow 2\ NH_3 + CO_2 + H_2O]$ and subsequent trapping of ammonia (NH_3) in the form of basic ammonium citrate [15]. Attenuated total reflectance-Fourier transform infrared spectroscopy (ATR-FTIR) is conducted to figure out the coordination state of Fe cation existed in the precursor phase. As can be seen in Figure 1A, the peaks at 1710 cm^{-1}, 1657 cm^{-1}, 1562 cm^{-1}, 1390 cm^{-1}, 1185 cm^{-1} and 1072 cm^{-1} can be ascribed to COOH, C=O, N-H, O-H, C-N, C-O characteristics vibration mode of different function groups present in the precursor material, respectively [270, 271]. Notably, the presence of both SCN$^-$ adsorption peak, located at 2062 cm^{-1} [272] for KSCN solution and Fe/NSMC precursor while its absence in Fe(SCN)$_3$ solution imply that Fe^{3+} ions are preferentially coordinated with citric acid or glucose rather than free SCN$^-$ anions, albeit strong binding force between Fe^{3+} and SCN$^-$. Furthermore, the solution color (Figure 1B) is subjected to an immediate change from blood-red to yellow upon Fe(SCN)$_3$ solution is added into mixture solution of D-glucose, citric acid and (NH$_4$)$_2$CO$_3$, indicting the stronger binding strength of Fe^{3+} cations toward citric acid/glucose with respect to SCN$^-$ anions. Most likely, the Fe^{3+} cation preferences to chelate with citric acid due to its improved complexation capacity in comparison to D-glucose and SCN$^-$ under the action of dative bonds derived from vacant electron orbits of Fe^{3+} ions and the lone pair electrons of O existed in the form of -COO$^-$ groups [273].

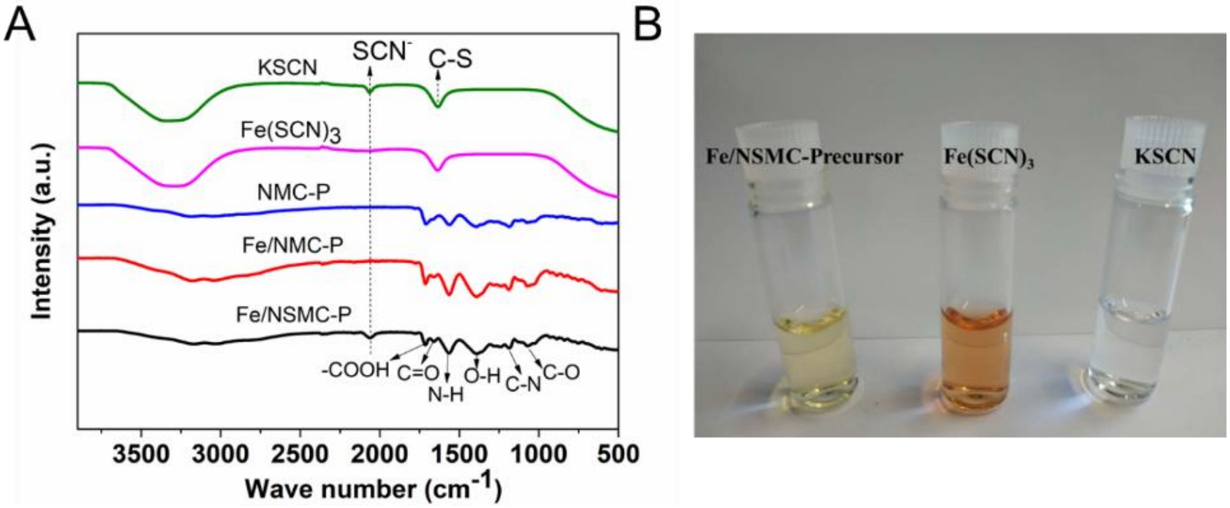

Figure 1 (A) ATR-FTIR spectra of Fe/NSMC, Fe/NMC and NMC precursor gel after 110 ^{o}C drying as well as KSCN and Fe(SCN)$_3$ aqueous solution; (B) Digital photos of Fe/NSMC precursor, Fe(SCN)$_3$ and KSCN aqueous solution.

The phase structure and composition are detected by X-ray diffraction (XRD) for as-prepared catalysts. As shown in Figure 2, without addition of KSCN, Fe and FeC$_x$ crystalline phases are formed which are hardly removed by acid leaching, demonstrating that the Fe-related species have been coated by highly anti-acid protective carbon layer. Instead, FeS_x and Fe big particle are generated with addition of KSCN, which can be washed out more easily as a consequence of their improved dissolution in acidic medium. Thus, it can be deduced that the position for these species is probably located at out of carbon surface and not encapsulated by carbon layer. Furthermore, the stronger peaks intensity and positive shift of position (from 24° shift up to 26° assigned to (002) peaks of amorphous carbon and graphitized carbon, respectively) for KSCN-free catalysts verify again that Fe-related species are coated by carbon layer. It is well known that the Fe species surrounded by carbon layer have a significantly enhancement toward graphitization [274]. No apparent peaks regarding Fe particles or other impurities are detected after second heating treatment in NH_3 atmosphere for Fe/NSMC-W, indicating the Fe atoms probably are confined into carbon matrix in highly dispersed form.

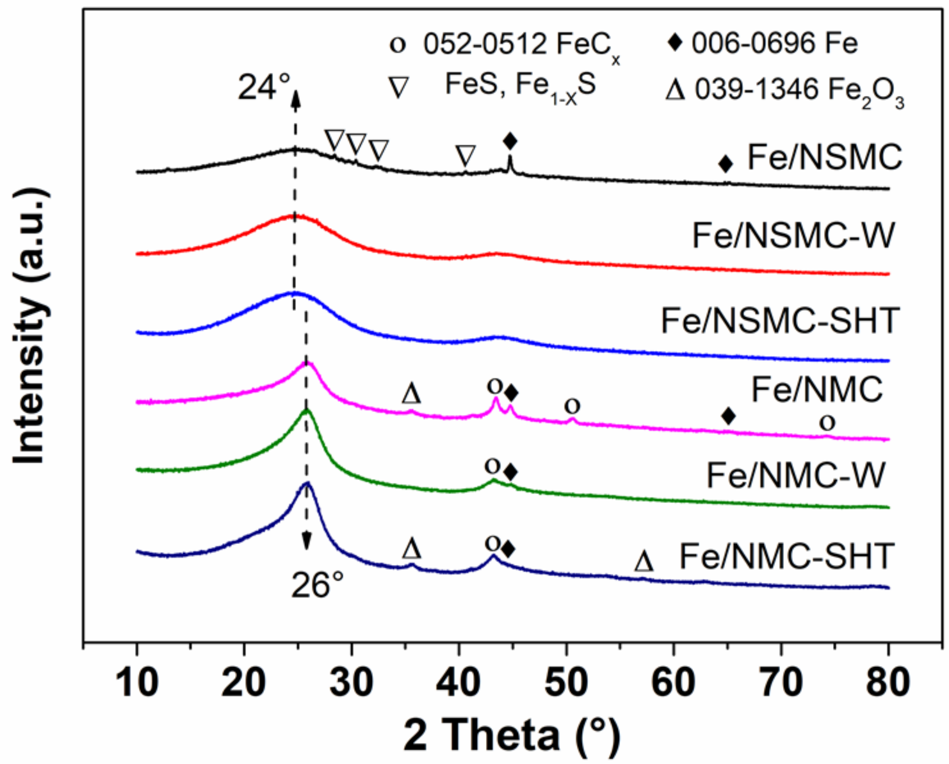

Figure 2. XRD patterns of the different as-prepared iron-based catalysts after calcination.

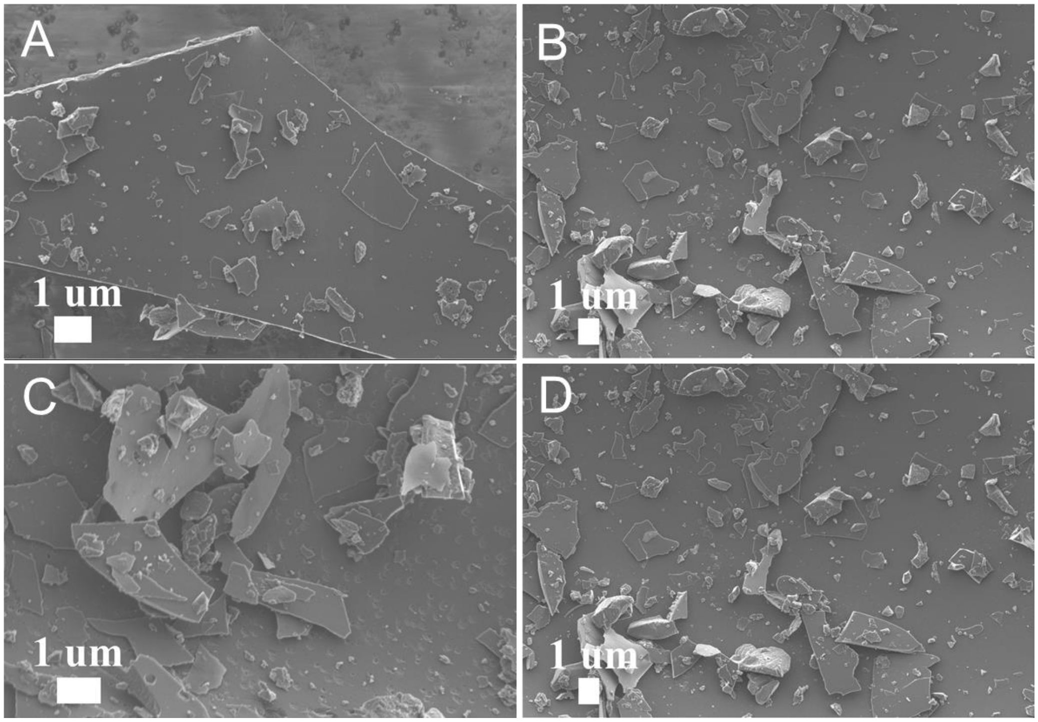

Figure 3. FESEM images at low magnification of (A) Fe/NSMC-SHT, (B) NSMC-SHT, (C) Fe/NMC-SHT, (D) Fe/NSMC-W.

Scanning electron microscope (SEM) is employed to investigate the morphology of the as-prepared catalysts. The similar morphologies of Fe/NSMC-SHT, NSMC-SHT, Fe/NMC-SHT and Fe/NSMC-W at low magnification (Figure 3) indicate that the addition of Fe and S- source as well as the second NH_3 treatment have a negligible effect on the overall morphology. As can be seen in Figure 4A, the nanosheet-like architectures, with thickness varied between 70 and 310 nm, are observed for Fe/NSMC-SHT. Interestingly, there are significant differences on the surface of control catalysts. As shown in Figure 4E, some holes with an average diameter of 100 nm can be clearly found on the outer surface of Fe/NSMC-W, which are caused by acid-washing of large FeS_x and metal Fe particles. On the contrary, a large number of small nanoparticles with mean size of 20 nm coated by carbon layers along with bulge are observed in Fe/NMC-W presented in Figure

4F, which could be well preserved by the protection of carbon layer even with such a severe condition of acid medium.

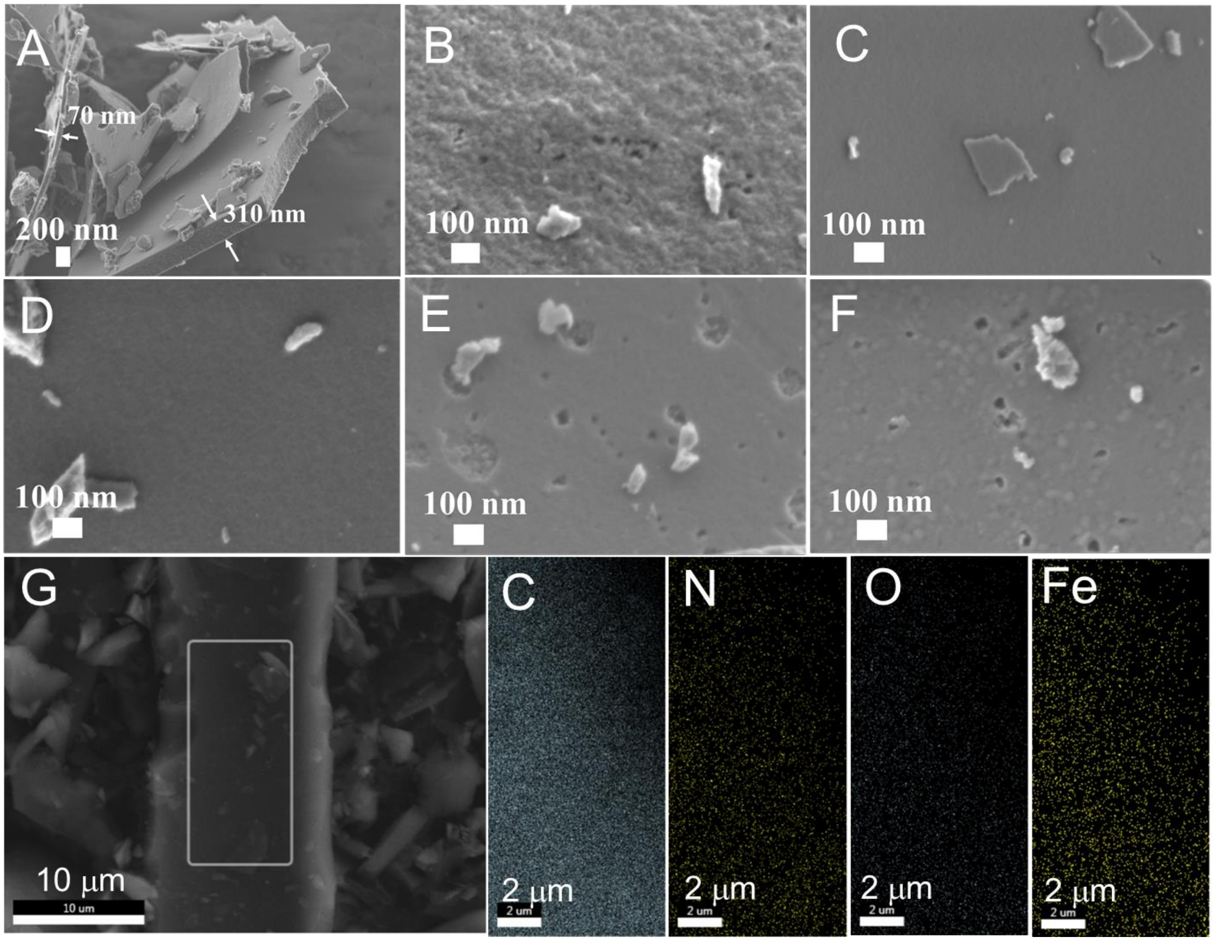

Figure 4. FESEM images of (A) Fe/NSMC-SHT at low magnification, of which high magnification images (B), and corresponding images of (C) Fe/NMC-SHT, (D) NSMC-SHT, (E) Fe/NSMC-W, (F) Fe/NMC-W, as well as energy-dispersive x-ray (EDX) mapping (G) of Fe/NSMC-SHT.

The findings unambiguously illustrate that SCN^- serves as surface mediator which can "catch" Fe atoms by S segments formed by the decomposition of SCN^- during high annealing temperature thus devoid of the encapsulation of Fe species by carbon layer. After the second NH_3 treatment, the surface of the Fe/NSMC-SHT catalysts become more porous (Figure 4B) while only solid surface is found for Fe/NMC-SHT which can be ascribed to improved graphitization against NH_3 etching (Figure 4C). Accordingly, NSMC-SHT shows moderate porous structure (Figure 4D), suggesting the addition of Fe promotes the formation of porous structure. It can also be inferred that such puffed porous configuration of Fe/NSMC-SHT will facilitate the exposure of active sites and reactant accessibility, thus enabling the enhancement of electrochemical catalytic performance as compared with that of monolithic nanosheets with lower porosity and accessibility. The energy-dispersive X-ray (EDX) mapping and the spectra of the different elements for Fe/NSMC-SHT (Figure 4G) confirm that the homogeneous distribution of C, N, O, Fe within the material. It is worth noting that there is no S signal observed on the analyzed catalysts, which could be attributed to the chemical reaction between S and NH_3 in the second NH_3 treatment at 900 ^oC as follow: $3\ S + 2\ NH_3 = 3\ H_2S + N_2$ [222].

The detailed microstructure is investigated by transmission electron microscope (TEM) and the results are presented in Figure 5A. The result shows that Fe/NSMC-SHT presents sheet-like morphology with no obvious large nanoparticles aggregation. Hierarchical porous structure with the presence of meso and micropores in the Fe/NSMC-SHT sample can be clearly observed at high resolution TEM image (Figure 5B). It is expected that such porous combination could greatly increase the wettability which thus contributes to the improvement of the mass transport of proton and O_2 molecules in bulk solution to FeN_x actives sites. High-angle annular dark-field scanning transmission electron microscope (HAADF-STEM) images (Figure 5C-D) reveal that both single atom Fe sites and prevalent Fe nanoclusters are presented in Fe/NSMC-SHT sample. On the other hand, a large number of nanoparticles are found in Fe/NMC-SHT, which can be assigned to Fe-related species (Figure 5E-F). These findings are in good agreement with the XRD results on the different samples. As revealed by XRD and TEM results, the Fe/NMC-SHT shows enhanced graphitization degree with respect to Fe/NSMC-SHT, resulting from the Fe-related species (especially for FeC_x species) catalyzed graphitization mechanism. In turn, the improved graphitization degree is detrimental to obtain high density active FeN_x active sites due to loss of nitrogen in high graphitization carbon matrix [275]. Moreover, the well-developed porous structure will significantly enhance exposure of FeN_x active sites for Fe/NSMC-SHT, contributing to higher ORR activity than that of Fe/NMC-SHT and NH_3 treatment-free Fe/NSMC-W.

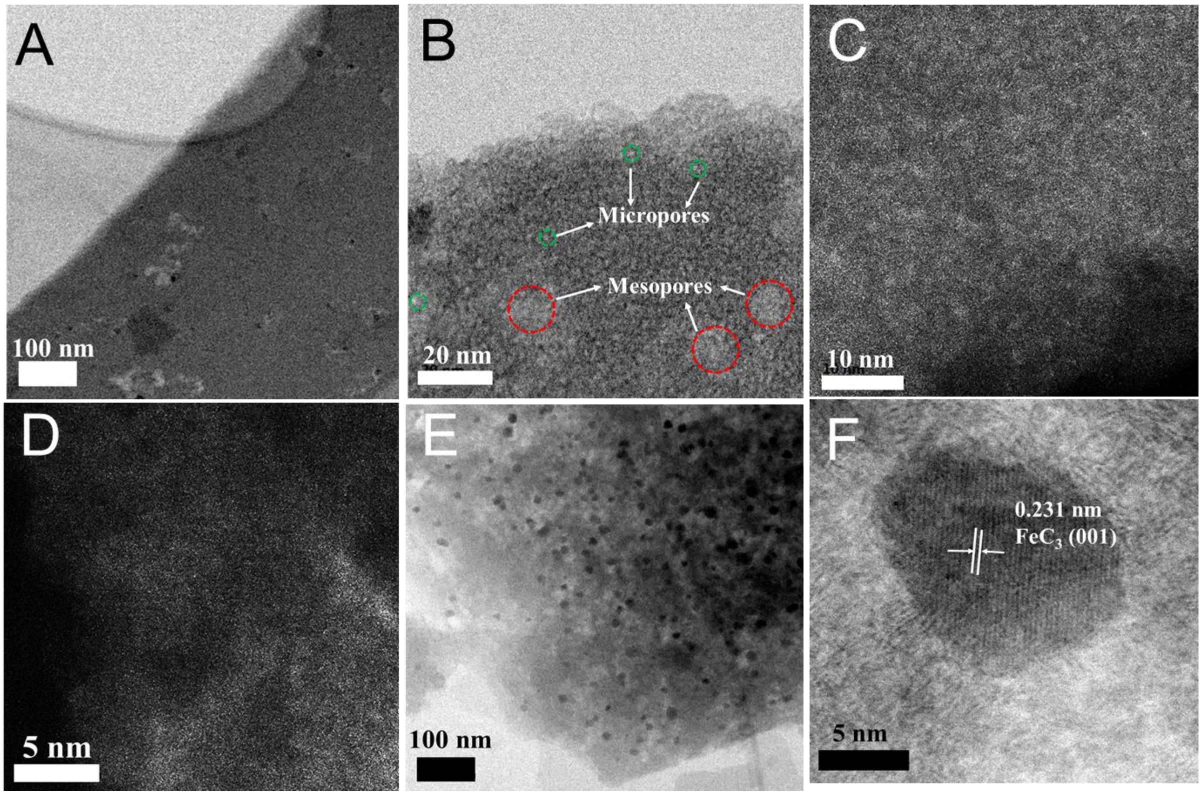

Figure 5. TEM (A-B) and (C-D) HAAF-STEM images of Fe/NSMC-SHT and TEM images (E-F) of Fe/NMC-SHT.

TGA/DTG are conducted in Ar atmosphere at a ramp of 5 ^{o}C min^{-1} to investigate the carbonization process of control samples. As shown in Figure 6, the TGA spectra for three precursor samples present almost the same thermal behavior at a moderate temperature decomposition range (below 600 ^oC) which can be associated to the dehydration of the precursors, condensation and thermal decomposition of D-glucose and citric acid. It is worthy to note that significant differences on DTA curves occur in the high temperature region with and without addition of KSCN to the synthesis process. Two peaks located at 692 ^oC and 799 ^oC in the Fe/NSMC-P can be observed (top spectrum in Figure 6) while only one broad peak centered at 866 ^oC is visible for Fe/NMC-P. The peak at higher temperature for both samples is attributed to the carbon deposition showing that carbon deposition for Fe/NSMC-P occurred at lower temperature compared to that of precursor with no addition of KSCN [276]. The discrepancy can be ascribed to the introduction of S which increase the disorder of carbon lattice thus decreasing the carbon deposition temperature. Besides, the extra peak at 692 ^oC for Fe/NSMC-P can be assigned to the generation of Fe-related species such as FeS_x and metal Fe. The absence of such typical peak in Fe/NMC-P illustrates the simultaneous occurrence of Fe species (metal Fe and FeC_x in this case) and carbon deposit which lead to the direct formation of carbon layer coated Fe species resistant to acid leaching. Combined with the TGA results, the formation temperature for large FeS_x and metal Fe precedes that of carbon deposition. Such phenomenon gives rise to the incomplete encapsulation of Fe species, thereby the atomically dispersion Fe can be generated by "top-down" process. Herein, single Fe atoms can escape at high temperature from the uncoated large Fe particles across the discontinuous carbon layers and eventually coordinate with N to form FeN_x moiety with high thermodynamically stability. In sharp contrast, a large number of small Fe-related particles coated by carbon layer are obtained due to its formation in parallel to carbon deposition without addition of KSCN.

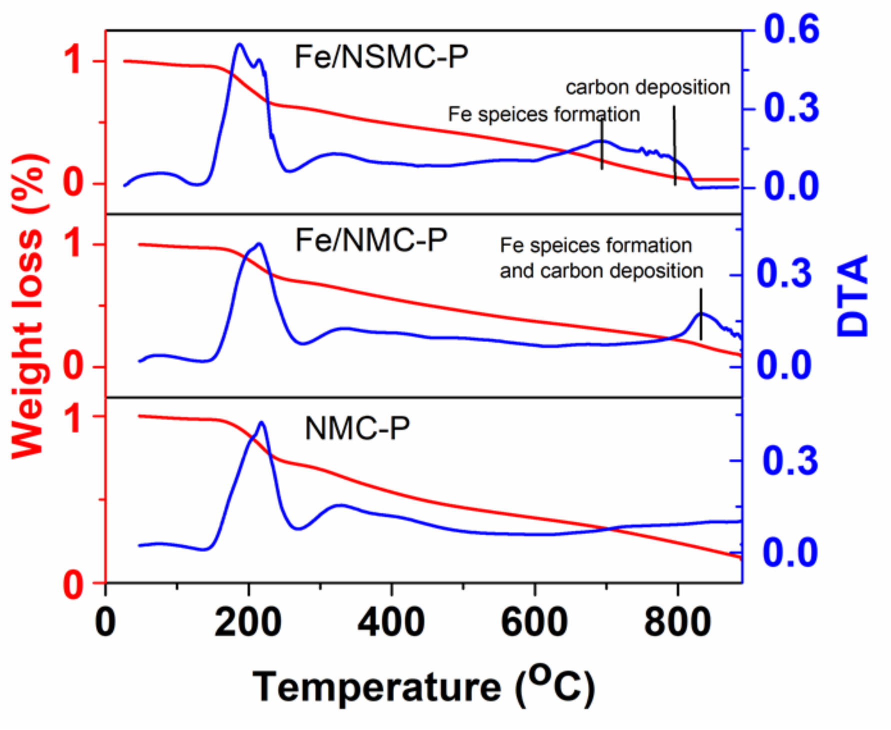

Figure 6. TGA and DTG curves of Fe/NSMC, Fe/NMC and NMC precursor gel.

The X-ray photoelectron spectroscopy (XPS) is conducted to investigate the surface elemental composition and electronic structure of the as-prepared samples. The different surface elemental compositions determined by XPS analysis are summarized in Table 1. The doped N content of Fe/NSMC-SHT is amounted to 6.1 at. %, higher than that of Fe/NMC-SHT (4.6 at.%), indicating that the introduction of S into the sample can be at the origin of the increase of N content in the catalyst. The origin of enhanced N-doping should be ascribed to the lower graphitization degree induced from S addition. The higher graphitization degree results in loss of N-doped level, which fails to form high active FeN_x for ORR process. Owning to the etching effect of NH_3, the N and Fe content for Fe/NSMC-SHT are evidently improved with respect to those of Fe/NSMC-W. Deconvolution of high-resolution spectra at their N 1s core regions accounted for five distinct N-components whose relative % (before and after the NH_3 thermo-chemical treatment) were used to fix the materials composition (Table 1).

Table 1 Selected chemico-physical and morphological properties of catalysts and precursors.

Entry	Sample	SSA^a ($m^2 g^{-1}$)	Total pore volume ($cm^3 g^{-1}$) ^{b}	t-plot micropore volume ($cm^3 g^{-1}$) ^{c}	Fe wt.% ^{d}	Fe at.% ^{e}	XPS data, N-species (%)^f					
							N at.% ^{e}	Pyridinic	Fe-N	Pyrrolic	Graphitic	Oxidized
1	Fe/NSMC-W	220	0.125	0.084	n.d.	0.8	3.7	21.8	25.9	30.3	17.4	4.6
2	Fe/NSMC-SHT	622	0.346	0.235	2.54	1.7	6.1	21.9	31.1	19.8	20.8	6.4
3	Fe/NMC-W	260	0.268	0.015	n.d.	0.5	4.3	26.7	23.3	29.9	17.9	2.2
4	Fe/NMC-SHT	461	0.406	0.058	1.67	0.9	4.6	26.8	25.4	20.1	20.5	7.2
5	NSMC-SHT	618	0.318	0.251	-	-	6.8	51.4	-	36.5	9.3	2.9

[a] Brunauer-Emmett-Teller (BET) specific surface area (SSA) measured at T = 77 K. [b] Total pore volume determined using the adsorption branch of N_2 isotherm at $P/P_0 = 0.98$. [c] Determined by t-plot method. [d] Determined by ICP analysis on the properly digested samples. [e] Determined by XPS analysis. [f] Determined by high resolution XPS N 1s core region and its relative peak deconvolution.

An appreciable increase of the components at 399.9 eV, conventionally ascribed to iron-coordinated N sites [64, 277], are found in NH_3 treated samples (Fe/NSMC-SHT and Fe/NMC-SHT) (Figure 7). On the other hand, the amount of pyridinic N and graphitic N are also enhanced. Both of these two sites have been well documented to be highly active for ORR [127, 278]. It can be well expected that Fe/NSMC-SHT will display best electrochemically activity among all other catalysts. The actual weight fraction of Fe in the Fe/NSMC-SHT and Fe/NMC-SHT is 2.54 wt. % and 1.67 wt. % by inductively coupled plasma atomic emission spectroscopy (ICP-AES) analysis. Sample with a relatively high metal loading in the Fe/NSMC-SHT strengthens the role of SCN^- for the preparation of atomically dispersed Fe-N-C nuclei. The high resolution of Fe 2p spectrum

(Figure 8) of Fe/NSMC-SHT can be deconvoluted into five peaks. The binding energy at 710.9 eV and 724.0 eV are assigned to Fe^{2+} $2p_{3/2}$ and Fe^{2+} $2p_{1/2}$ peaks, respectively. While the peaks at 714.8 eV and 727.3 eV correspond to Fe^{3+} $2p_{3/2}$ and Fe^{3+} $2p_{1/2}$ peaks [182]. Besides, the satellite peak at 719.0 eV further demonstrates the co-existing of mixture valence of Fe^{2+} and Fe^{3+} [279]. No zero valence of metallic Fe is observed in Fe/NSMC-SHT, which is consistent with most reported atomically dispersed FeN_x catalysts [100, 280]. Unfortunately, it is difficult to deconvolute Fe 2p spectra in the Fe/NSMC-W and Fe/NMC-SHT due to its relative weak signal resulted from low Fe surface concentration.

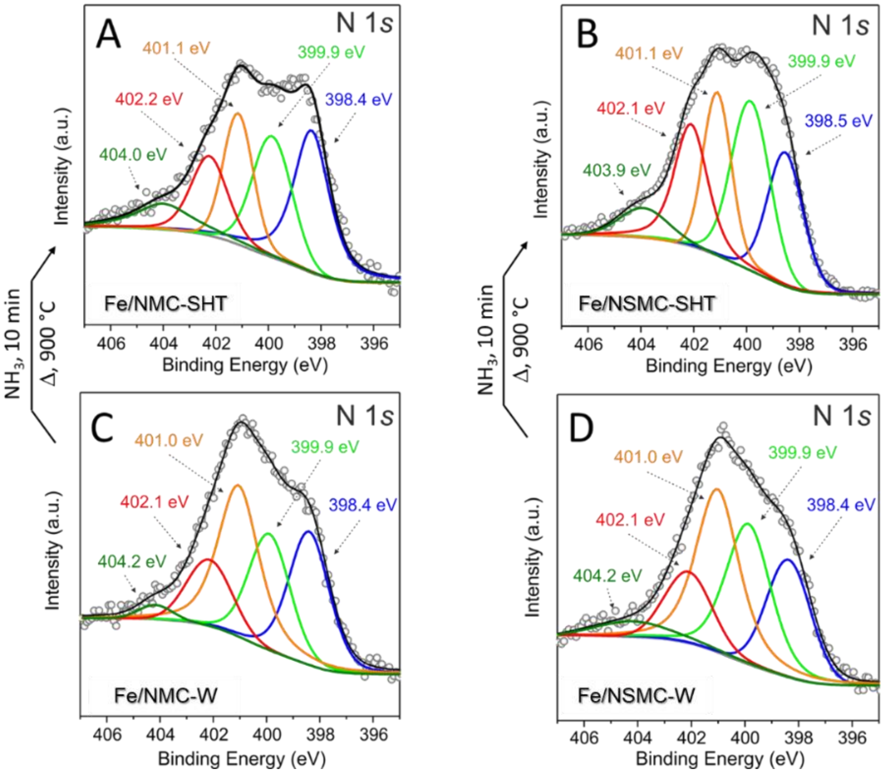

Figure 7. High resolution XPS N *1*s core level region of samples Fe/NSMC-W, Fe/NMC-W (D and C) and Fe/NSMC-SHT, Fe/NMC-SHT (B and A) along with the respective curve fittings. The vertical view of these spectra C vs. A and D vs. B accounts for the N *1*s profile changes recorded upon neat-NH_3 treatment of samples at 900 °C for 10 min.

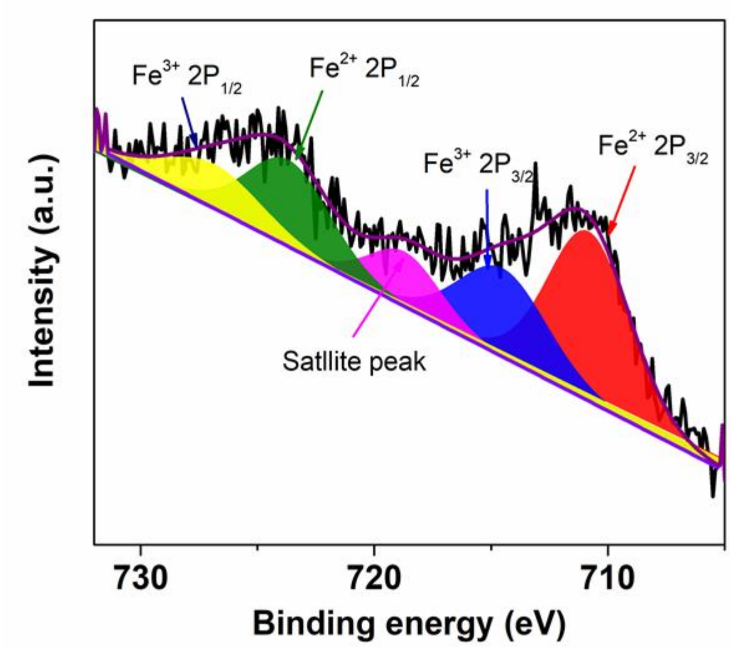

Figure 8. The deconvolution spectra of high-resolution Fe 2p for Fe/NSMC-SHT.

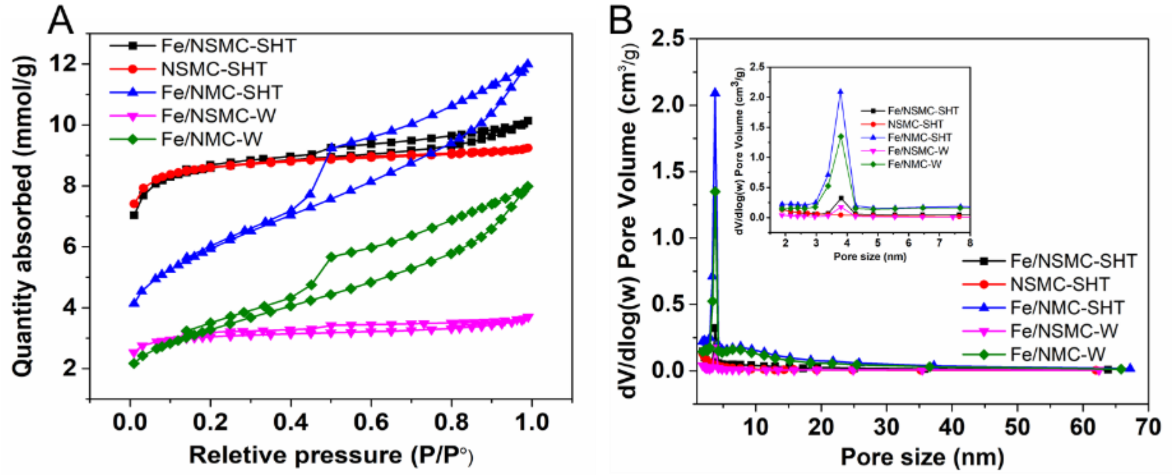

Figure 9. (A) N_2 absorption-desorption isotherms curves recorded at 77 K, and (B) respective pore size distribution curves with Barrett-Joyner-Halenda (BJH) method based on desorption branches of representative samples.

N_2 adsorption-desorption isotherms curves shown in Figure 9A exhibit type IV isotherm character with pronounced hysteresis loop implying the existence of mesoporous of all representative samples. Obviously, the N_2 uptakes significantly increase after the second NH_3

treatment, suggesting the improved specific surface area. As listed in Table 1, Fe/NSMC-SHT and Fe/NMC-SHT deliver specific surface area of 622 and 460 m^2/g, respectively, much higher than that of Fe/NSMC-W (220 m^2/g) and Fe/NMC-W (260 m^2/g). The improved specific surface area is attributed to partly gasification of the carbon support by NH_3 etching, giving rise to the generation of micropore as well as mesopore [281]. At odds with the pore size distribution of prevailing mesopores with the narrow 3-5 nm range in Fe/NMC-W, Fe/NSMC-W presents predominant micropores density (Figure 9A-B), as further evidenced by much larger micropore volume for Fe/NSMC-W with respect to Fe/NMC-W (Table 1). As a result, the Fe/NSMC-W exhibits slight lower total specific surface area than Fe/NMC-W (220 vs. 260 m^2/g), which is different from those conclusions reported by most other works that S-doping can enhance specific surface area of carbon-based catalysts thus boosting catalytic activity [282-284]. However, the enhancement of specific surface area for Fe/NSMC-W is more prominent (from 220 to 622 m^2/g) than that of Fe/NMC-W (from 260 to 460 m^2/g) after the second NH_3 heat treatment, in agreement with SEM observations. The result demonstrates that addition of KSCN result in the generation of more disorder carbon enriched defect and partial collapse of mesopores. The disorder carbon phases react much faster with NH_3 and are preferentially gasified [174, 285, 286], eventually creating a larger amount of micropores and small mesopores due to the interconnected pore channels. The generated hierarchical porous structure is well agreement with the result observed in TEM. It is believed that the micropore is more beneficial to increase the number of active sites thus boosting ORR activity.

To get additional details on the effective nature of the iron species in Fe/NSMC-SHT, and to address properly the nature of their coordination sphere and fix the nature of the metal-active sites engaged in ORR (*vide infra*), the model catalyst is investigated by X-ray adsorption spectroscopy

(XAS). Figures 10A-B refers to the X-ray absorption near edge structure (XANES) spectra at the Fe K edge of model catalyst along with that of common iron oxides and metallic iron as reference samples at comparison.

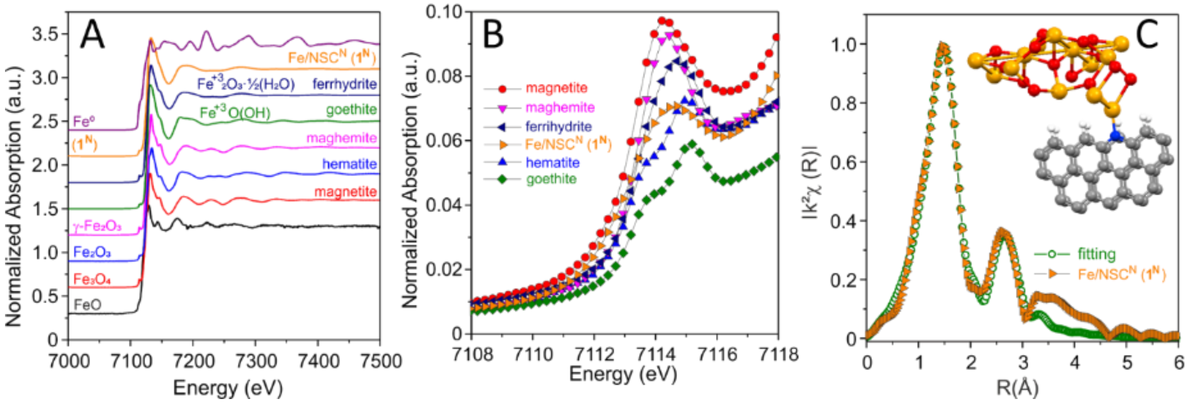

Figure 10. A) Normalized XANES spectra for model catalyst (1^N is referred to as Fe/NSMC-SHT for the sake of convenience) and more common iron oxide samples or metallic iron. B) Magnification section of Figure 10A dealing with the absorption pre-edge (1s → 3d) resonances. C) k^2 weighted Fourier transform of EXAFS data of model catalyst and related fit. Color codes for the inset: C = gray, H = white, N = blue, Fe = orange, O = red

A careful analysis of Figure 10A reveals a striking match between ferrihydrite (*Fh*) [287] and our sample Fe/NSMC-SHT. Even if the former may be present in several forms and crystallinity, all of them share similar structural features such as the prevalence of six coordinated Fe^{III} centers and distinct Fe-Fe second and third shells distributed around 3.0 and 3.4 Å. A closer look to the pre-edge peak (1s → 3d transition) in Figure 10B confirms that Fe/NSMC-SHT contains prevalently Fe^{III}. While the positions of the absorption pre-edge (1s → 3d) as well as that of the edge peak (1s → 4p transition) resonances are sensitive to the iron oxidation state, the intensity of the 1s → 3d transition depends on the site symmetry. In particular, the lower the transition intensity the higher the symmetry of the Fe sites. Therefore, intense pre-edge peaks will account for tetrahedral or distorted octahedral geometries while octahedral coordination environments give rise to less intense signals. As Figure 10B shows, the pre-edge resonance in Fe/NSMC-SHT well align with maghemite (γ-Fe_2O_3) and ferrihydrite ($Fe_2O_3 \cdot ½H_2O$, *Fh*) with a peak intensity [288] evidently lower than that of other partially four coordinated compounds. This feature clearly suggests a prevalent six coordination sphere around the metal center. Finally, a quantitative evaluation of the local structure has been performed by fitting the Fe K edge EXAFS signal (see Figure 10C) and structural data are reported in Table 2.

Table 2. Structural data from the fitting of Fe/NSMC-SHT sample Fe K-edge EXAFS signal.

Path	Coord. Numb.	R(Å)[a]	σ^2 (10^{-2} Å^2)[b]	ΔE_0 [c]	R-factor [d]
Fe-O(N)	6.2 (6)	1.957 (7)	1.2 (1)	-5 (1)	0.007
Fe-Fe (1)	1.3 (3)	3.00 (1)	-	-	-
Fe-Fe (2)	1.6 (4)	3.45 (2)	-	-	-

[a] Interatomic distance. [b] Debye-Waller factor. [c] Difference in the threshold Fermi level between data and fit. [d] Goodness of fit parameters

If the signal fitting establishes a coordination very close to that expected for ferrihydrite (*Fh*) [287], with a *hcp* form of Fe oxyhydroxide, where Fe^{III} cations are coordinated with O atoms and terminal OH species, Fe-Fe(1,2) coordination numbers are appreciably lower (1.3 and 1.6, respectively) than those expected for bulk ferrihydrite [287] or crystallized goethite [289] whose Fe-Fe(1) and Fe-Fe(2) values are roughly estimated in 4 and 6, respectively. This structural features found a pretty good match between data recorded for Fe/NSMC-SHT and previously reported data on N-coordinated iron sites (Fe-N-C) as single atoms or polyatomic species at the interface between iron oxyhydroxide and a nitrogen-doped carbon network [258]. In their seminal contribution, Arrigo et al. concluded on the structural nature of their N-coordinated iron sites and their catalytic performance in the CO_2 electrochemical reduction (CO_2RR) by the combination of operando XAFS analysis and *in-silico* studies. These authors demonstrated that their iron active-sites were not directly embedded in nitrogen doped C-network but they were present as small *Fh*-FeOOH clusters or Fe single atoms at the edge of N-doped graphitic frameworks (*inset* Figure 10C). This is particular true for our present work that Fe nanocluster and single Fe atoms are co-existed in the catalytic system reflected from the HAADF-STEM (Figure 5C-D). It should be stressed that EXAFS cannot establish if N or O are mixed in the first shell, since scattering amplitudes and phases are very similar. Anyhow, a fit with only N-coordinative sites would result in a too large coordination number. According to XPS evidences for the presence of a Fe-N component in the fitting of the N 1s high resolution peak (see Figure 7) and the last NH_3 thermo-chemical treatment Fe/NSMC-W underwent, it can be inferred that active iron sites of the latter possess a mixed N, O coordination environment. The Debye Waller factor reported in Table 2 is enough large as to confirm a distribution of distances in the octahedron ($0.01Å^2$). However, the introduction of two distinct Fe-O, N sub shells does not improve the fit at all: the octahedron is deformed, but the contributions cannot be resolved.

All these data taken together confirm the role of KSCN in the starting mixture to get highly dispersed Fe-N-C nuclei at the interface between an iron oxyhydroxide nanostructure and a nitrogen-doped carbon network almost exclusively in the final composite. The addition of SCN^- ions was found to prevent the generation of iron carbides to a larger extent, while favoring the conversion of the excess of iron (not present as dispersed Fe-N-C nuclei of the type described above) into iron sulfides [265] that were leached and easily removed upon the acid washing step.

Based on systematic analysis above, the formation mechanism toward model Fe/NSMC-SHT catalysts are put forward. As shown in Figure 11, the Fe ions/atoms tend to coordinate with citric acid in precursor solution/gel, during which SCN^- anions are dispersed in precursor/gel in the form of dissociation. The gelation under 110 ^oC is involved in a series of chemical reactions such as the decomposition of $(NH_4)_2CO_3$ followed by acid-basic chemical reaction. The first thermal treatment at 900 ^oC under Ar atmosphere induces polymerization/condensation/aromatic processes, where D-glucose represents main carbon source while as-generated basic ammonium citrate plays double role of N-reservoir and pore-forming agents during first thermal treatment. As the temperature increasing, the added SCN^- will be decomposed into sulfide and cyanide along with the incorporation of S into carbon matrix. The resultant sulfide subsequently serves as surface mediator to “catch” Fe by the formation of large FeS_x and metal Fe nanoparticles prior to carbon deposition, thus preventing the formation of carbon coating layer. Simultaneously, the FeN_x sites are created gradually by the top-down process, where atomically dispersed Fe can be obtained via direct transformation of Fe metal into Fe atom induced by high thermal treatment followed by trapping of atoms powered by N capture. After acid leaching, the composite of atomically dispersed Fe specie is finally obtained. The second thermal treatment (SHT) under NH_3 are executed to develop porosity as well as activate the FeN_x sites, during which more basic N-containing groups (pyridinic N and graphitic N) are in-situ introduced. Resultantly, the densely accessible FeN_x active sites coupled to Fe oxyhydroxide with high basic N-containing groups supported carbon nanosheets are achieved. As a comparison, a large number of Fe nanoparticles coated by carbon layer are visible when no additional SCN^- introduced. Taken together, during the first Ar annealing stage, the addition of KSCN (i) mediates surface reaction by the formation of S-related Fe species, preventing the formation of carbon coated Fe-related species. (ii) leads to lower graphitization degree, hosting more active FeN_x sites. (iii) induces the formation of prevailing micropores, thus indirectly help improving FeN_x active sites. On the other hand, the following NH_3 treatment (i) introduces more abundant pore structure by gasifying amorphous carbon. (ii) creates more basic N-containing groups by in-situ doping. All these compelling benefits drive us to explore its further application in ORR.

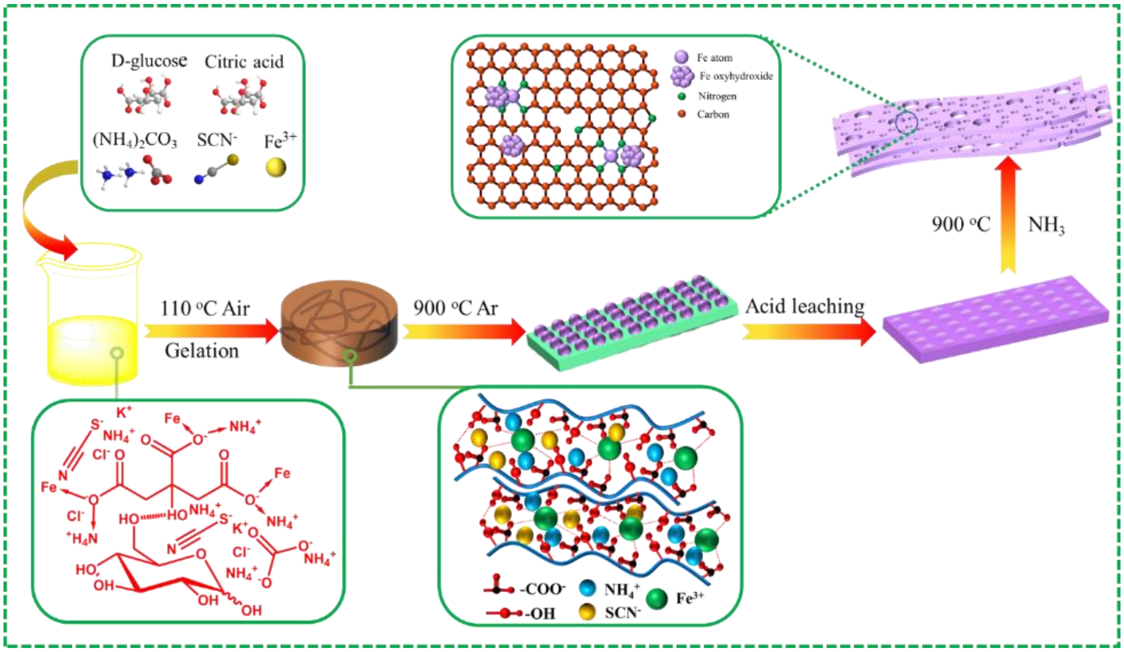

Figure 11. The proposed schematic illustration for synthetic route of Fe/NSMC-SHT

The electrocatalytic ORR performance of catalyst is investigated in O_2-saturated 0.1 M KOH solution by a typical three-electrode system. For the sake of comparison, commercial Pt/C (20% Pt/C), a series of control samples are also evaluated. As shown in Figure 12A-B, the Fe/NSMC-SHT exhibits the superior ORR activity with onset potential (1.14 V) and half-wave potential ($E_{1/2}$) of 0.87 V, which is highest amongst all investigated samples including commercial benchmark catalyst.

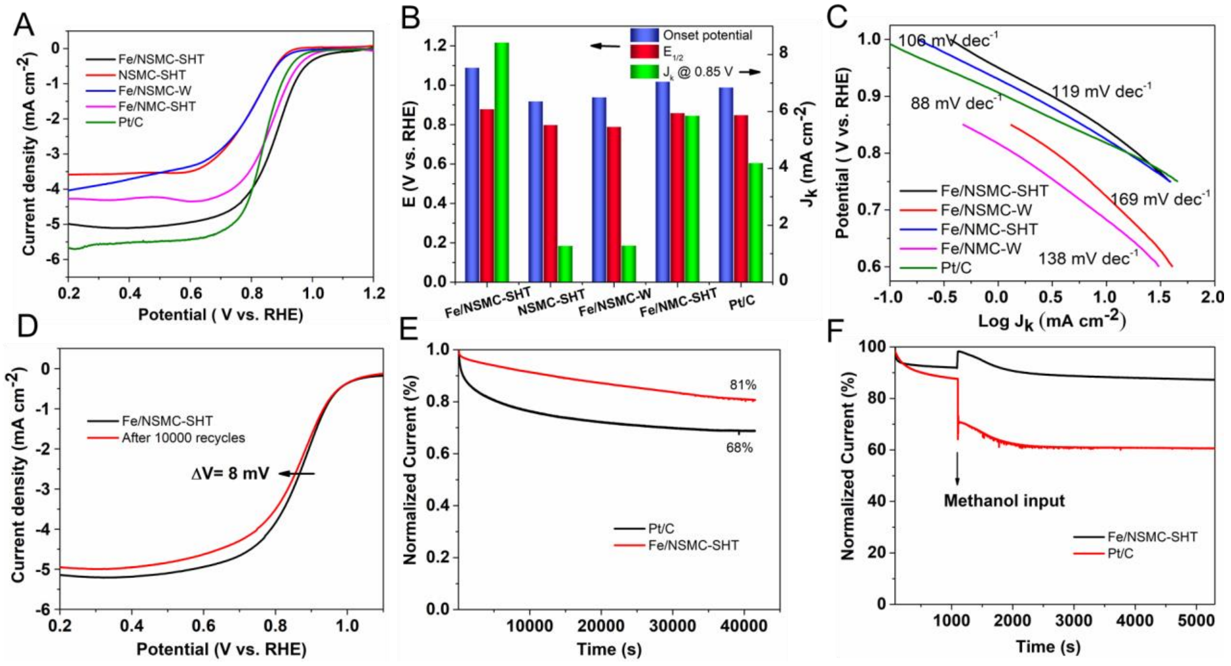

Figure 12. (A) ORR polarization curves, (B) Onset Potential, half-wave potential ($E_{1/2}$) and kinetic current density (J_k) for different catalysts, (C) Tafel slop for as-prepared catalysts, (D) Accelerated durability test (ADT) for Fe/NSMC-SHT, (E) CA response for Fe/NSMC-SHT, (F) methanol tolerance test for Fe/NSMC-SHT.

Furthermore, the kinetic current density (J_k) of Fe/NSMC-SHT reaches 8.43 mA cm^{-2} at 0.85 V, which is higher than those for other samples and twice higher than 4.19 mA cm^{-2} for Pt/C. The ORR performance for the desired catalyst also outperforms reported most Fe-based atomically dispersed electrocatalysts. The Tafel slope (Figure 12C) of Fe/NSMC-SHT is determined to be 92 mV dec^{-1}, comparable with that of Pt/C (89 mV dec^{-1}), and much lower than those of Fe/NMC-SHT (106 mV dec^{-1}), NSMC-SHT (119 mV dec^{-1}) and Fe/NSMC-W (169 mV dec^{-1}), indicating Fe/NSMC-SHT electrocatalyst manifests accelerated ORR kinetic and similar reaction mechanism with Pt/C catalyst. The limited diffusion current density (J_L) for Fe/NSMC-SHT is measured to be 5.08 mA cm^{-2}, far outperforming those for Fe/NSMC-W (3.65 mA cm^{-2}), NSMC-SHT (3.57 mA cm^{-2}), Fe/NMC-SHT (4.35 mA cm^{-2}), albeit a slightly lower value than commercial Pt/C (5.5 mA cm^{-2}). The higher value of J_L for Fe/NSMC-SHT compared with controlled catalysts can be attributed to efficient four electron transfer process resulted from abundant hierarchical porous featured with larger specific surface area for efficient O_2 diffusion and transportation as well as the more FeN_x active sites [81, 290].

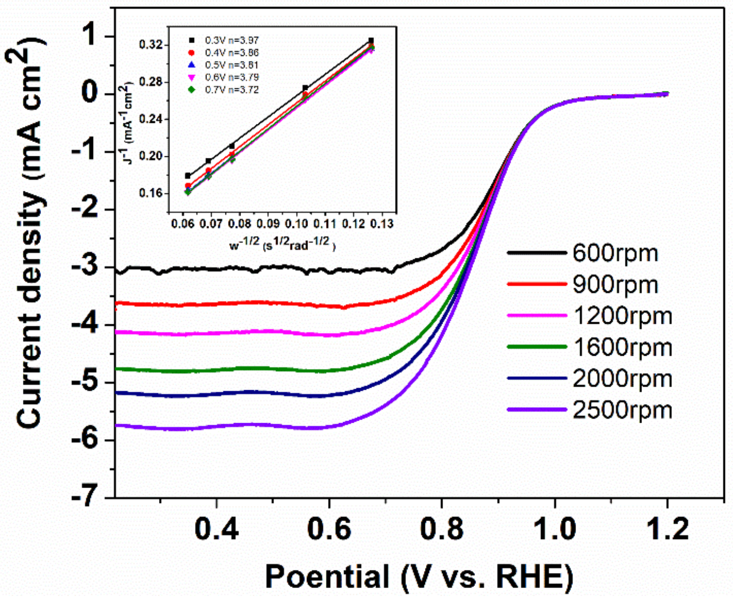

Figure 13. Polarization curve at different rotation speed for Fe/NSMC-SHT.

To further explore the ORR kinetics, the rotating disk electrode (RDE) measurements with different rotation speeds are performed and corresponding Koutecky-Levich (K-L) plots are presented in Figure 13, the increase of limited-diffusion current with increasing of rotation speeds suggests the diffusion-controlled oxygen reduction process in alkaline electrolyte [291]. The linear and almost parallel K-L plots at different applied potential indicate the first-order reaction kinetics toward the concentration of dissolved oxygen [292]. The electron transfer number is determined to 3.86 at applied potential of 0.4 V, demonstrating Fe/NSMC-SHT favors four-electron oxygen reduction process [293]. The electrocatalytic durability is key criterion for practical application of fuel cell. We conducted accelerated durability test (ADT) for Fe/NSMC-SHT, as shown in Figure 12D, after continuous 10,000 cyclic voltammetry (CV) scans between 0.6 V to 1.0 V at a rate of 50 mV s^{-1} under O_2 atmosphere, the $E_{1/2}$ for Fe/NSMC-SHT only decrease by 8 mV, exhibiting superb long-term stability in alkaline electrolyte. Besides, chronoamperometric (CA) response curves are also conducted to evaluate the stability and methanol tolerance at applied potential of 0.6 V. As displayed in Figure 12E, the current density of Fe/NSMC-SHT retain up to 81% of its initial current density, while only 68% current density retention is obtained for Pt/C under the same experimental condition after testing more than 40,000 seconds. In comparison with the dramatic decrease of current density for Pt/C after injecting 1% (v/v) methanol, the current density for Fe/NSMC-SHT remains negligible decay. All above results disclose remarkable stability and methanol tolerance of Fe/NSMC-SHT (Figure 12F). Several important factors should be responsible for the superb electrochemical performance toward ORR for Fe/NSMC-SHT in comparison to other catalysts: (1) The hierarchical porous structures with dominating micropore resulting from KSCN surface mediator effect greatly foster mass-transport during electrochemical reaction on the premise of ensuring abundant FeN_x active sites, which can significantly enhance the ORR activity. (2) NH_3 heat treatment improves the exposure of FeN_x active sites by producing slacker surface configuration, which increases the accessible active FeN_x active sites and result in enhanced ORR activity. (3) more basic N-containing groups introduced by NH_3 post-treatment especially for pyridinic N and graphitic N can afford extra active sites. These active sites can also contribute more activity for ORR. (4) On the basis of existing literature, the co-existing Fe nanoclusters (Fe oxyhydroxide) probably play a crucial role for improved intrinsic activity of single FeN_x site by optimization of reaction oxygenated intermediates over FeN_x active sites, although a lack of more convincible evidence like DFT simulation for the comparison between exclusively atomically dispersed FeN_x sites and FeN_x/Fe oxyhydroxide mix sites in present work.

3. Conclusions

In summary, we have described an effective and general strategy to the clean production of highly metal charged Fe-based composites containing discrete FeN_x moieties at the interface of iron oxyhydroxide sub-nanometric structures and N-doped carbon network through the combination of chelating citrate ions with the ancillary monodentate SCN^- ligand. The control of the metal ion donor atom set originates an ideal “open gate” for water soluble iron ions to be accommodated in the form of Fe-N-C moieties within final C-N networks. A rational exploitation of their thermo-chemical and washing sequences has finally provided an effective and durable electrocatalyst for promoting the kinetically sluggish oxygen reduction reaction. Besides the general synthetic scheme that may apply to a variety of water-soluble transition-metal based salts, the protocol is a cost-effective path to the clean production of iron-composites containing catalytically active Fe-N-C moieties for the electrochemical process. The as-prepared highly metal-loaded catalyst has shown excellent electrocatalytic performance under alkaline environment. Studies devoted to the preparation and characterization of different transition metal SACs based on the functional protocol described in the paper are currently on-going in the lab and will be reported elsewhere in combination with different catalytic applications.

Chapter 4

Atomic Fe-decorated N-doped Hierarchical Porous Carbon for Oxygen Electroreduction

Abstract

The preparation of atomically dispersed Fe on N-doped carbon (Fe-N-C) using separate metal precursor, N and C sources enables better flexibility of the synthesis and control on the structure and composition of the final product towards next generation viable fuel cell or metal-air batteries technologies, but remains a huge challenge to face. In this featured work, atomic Fe decorated N-doped hierarchical porous carbon (Fe/NHPC) is successfully synthesized through the use of $(NH_4)_2CO_3$ as single N source, citric acid as C source, and $FeCl_3$ as metal precursor. Combined with template-assisted strategy, the formation mechanism of Fe/NHPC on the basis of gas-solid interfacial reactions is proposed. To the best of knowledge, this is the first time that inorganic N-containing compound is employed as exclusive N source involving in the synthesis of Fe-N-C catalyst. Owing to this compelling feature of completely separated precursor, N-doped level can be finely tuned by adapting the amount of $(NH_4)_2CO_3$ and the dependence of electrochemical activity of prepared catalysts in ORR on N-doping is observed. Detailed investigation reveals that both single Cl-FeN_4 sites and pyridinic N are the active sites with Cl-FeN_4 moieties being the most active sites, while Fe/Fe_3O_4 nanoparticles show no activity for ORR in alkaline condition. The optimized catalyst presents high ORR activity with a half-wave potential ($E_{1/2}$) of 0.88 V, large kinetic current density (109.6 A g^{-1} normalized by catalyst loading at 0.8 V vs. RHE) along with outstanding stability, outperforming commercial Pt/C catalyst. This work affords a completely new route for the rational design of cost-effective highly active ORR electrocatalysts.

1. Introduction

The sluggish kinetics of electrocatalytic oxygen reduction reaction (ORR) is one of the main obstacles in large scale commercialization of the next-generation energy storage and conversion devices such as fuel cell, metal-air batteries [23, 294]. Presently, Pt group metal (PGM) is the most efficient and viably ORR catalysts, while the problem of its high cost and availability has stimulated extensively searches for alternative cost-effective PGM-free catalysts [34, 295]. The exploitation of highly active, robust PGM-free catalysts especially for non-precious metal catalysts (NPMCs) with comparable or even better performance in ORR with respect to commercial Pt/C remains a challenging research topic nowadays.

The metal-nitrogen coordination sites embedded into carbon matrix catalysts (M-N-C, M = Fe, Co, Mn, etc.) have been typically regarded as promising alternative to PGM catalysts [165, 174, 296]. Four milestones can be outlined in the development of M-N-C catalysts. The first important step was an observation of cobalt phthalocyanine capable of catalyzing the ORR in an alkaline medium, reported by Jasinski [38]. Followed by this pioneering work, other M-N_4 macrocycles were also found to be active towards ORR in both alkaline and acid mediums [297]. The second important step was the discovery that high temperature treatment (400-1000 ^{o}C) in inert atmosphere of M-N_4 macrocycles could significantly increase their activity and stability [298-300]. The nature of active sites generated by thermal decomposition of M-N_4 macrocycles has ever since been debated. Currently it is widely believed that M-N_4 moiety inherited from parent configuration of macrocycles survived pyrolysis is most likely active site towards ORR [153]. The third breakthrough made by Yeager et al. was a synthesis of NPMCs using metal salts, N-containing precursor and high surface area carbon. This approach opened a new avenue for preparation of M-N-C electrocatalyst independent on M-N_4 macrocycles molecule [41], suggesting that high temperature synthesis of M-N-C catalyst was typically involved in the simultaneous presence of metal salt, N, and C sources. Afterwards extensive efforts have been followed to the developments of highly active and durable M-N-C catalysts by this route, in particular Fe-N-C electrocatalysts due to its best ORR activity [290, 301, 302]. Of note is that in all these works, MOF-based [233, 234, 303], N-containing organic small molecule [304, 305] and/or polymers [306, 307], were primarily utilized as a simultaneous N and C sources. The fourth significant breakthrough was achieved by Dodelet's group, who demonstrated that for the synthesis of Fe-N-C catalyst, the transition metal, N, C could be separately introduced by the use of reactive gas NH_3 or CH_3CN as exclusive N source [308, 309]. Subsequent numerous studies have been devoted to improving catalytic activity and stability of NH_3-treated Fe-N-C catalysts [223, 225, 226]. However, high temperature NH_3 treatment is a highly dangerous and hardly controllable procedure, hindering intensive development of Fe-N-C ORR catalysts. The preparation of Fe-N-C with high ORR performance using a single N source such as inorganic N-containing compound rather than NH_3 presents a desirable but yet challenging progress. On the other hand, the fabrication strategy for Fe-N-C catalysts relies mainly on error and trial process due to the complexity of chemical nature of as-prepared catalysts arising from high temperature pyrolysis as well as precursor species. The utilization of simple precursor molecules with well-defined chemical structure will lead to better control on the properties of prepared Fe-N-C electrocatalysts.

The identification of ORR active site is of great importance for the rational design of high ORR performance electrocatalyst. Actually, the real active sites which are responsible for operating the ORR process on Fe-N-C catalysts have been debated since relatively long time due to possible formation of multiple active species upon high temperature pyrolysis. For instance, the metallic Fe [310, 311], oxidative Fe_xO_y [312-314], carbide Fe_xC [147, 315] as well as nitride Fe_xN [223, 316, 317] nanoparticles encapsulated into N-doped carbon layer have been proposed either as an active site itself or as co-catalyst exerting synergistic effect together with FeN_x active sites. Existence of the multiple possible coordination of N-sites, such a pyridinic N and graphitic N, which are active toward ORR particularly in alkaline media, further complicates the analysis of the nature of active site. Although the controversy still exists in regards to a relative activity of Fe-based species, the FeN_x moiety is commonly considered to be most active sites with highly efficient 4-electron oxygen reduction [113, 114]. The activity of FeN_x moiety can be further altered by tuning d-electron density of Fe center through heteroatom doping (e.g. O, S, B) [283, 318, 319] or by changing carbon sp^2-plane size [320]. Alternatively, the most intuitive approach is to increase Fe loadings which enriches the total density of FeN_x active sites. Zhao et al [321] prepared Fe-N-C catalyst with a metal loading up to 12.1 wt % using cascade anchoring strategy. The as-prepared Fe–N-C catalyst shows a superior ORR activity with a half-wave potential of 0.90 V in 0.1 M KOH. However, in many cases, the excess Fe loadings inevitably generate less active metallic and/or carbide particles with possible deterioration of ORR activity, thus optimal Fe loading has to be optimized. Moreover, Kucernak's group revealed that even in the case of Fe almost exclusively dispersed into FeN_x sites, only a small proportion (less than 5 %) of these sites was actually involved in the ORR process [322], assuming that majority of sites may be hidden within the bulk of carbon and inaccessible for electrolyte/reactants. On this regard, increasing of exposure of FeN_x sites is another viable strategy of improvement of ORR activity. Lee et al [323] investigated systematically the roles of macro and mesopore on the ORR performance of Fe-N-C. They found that mesopores serve as a channel for reaction medium accessibility into active sites, while macropores significantly decrease mass transport resistance of the electrocatalyst. Hence, the rational design of hierarchical porous structure with interconnected macro, meso, and micropores not only affords high surface area for hosting more underlying active sites but also facilitate the ORR kinetic due to the improved exposure of active sites and facile mass (reactant/product) transfer.

In our last work we have reported an original and general synthetic route for atomically dispersed Fe-N-C catalysts with aid of ancillary monodentate thiocyanate ligand [324]. The synthesis allowed fine control on the composition of the final product, but required a step of high temperature annealing in NH_3 atmosphere to develop a carbon structure optimal for ORR electrocatalyst. In this present work, a modified strategy is reported, allowing to avoid NH_3 annealing at high temperature by using inorganic salt $(NH_4)_2CO_3$ as single nitrogen precursor and citric acid as only carbon precursor. With the aid of silica template, the as-prepared catalyst presents favorable hierarchical porous structure containing interconnected micropores, bimodal mesopores and macropores with tunable pore distribution. Importantly, N-doping level can be finely tuned using separated sources for carbon and nitrogen in this synthesis and respective formation mechanism of atomic Fe-decorated hierarchical porous carbon is proposed. To our best knowledge, this is the first example of a synthesis of Fe-N-C catalyst by the use of separated N and C source instead of using gas phase N resource (NH_3, etc.). As a result, the optimal catalyst exhibits outstanding ORR activity and stability as well as methanol tolerance, outperforming commercial Pt/C catalyst. Moreover, the ORR reactivity dependence on the level of N-doping is observed. Systematic investigation reveals that both porphyrin-like single Cl-FeN_4 sites and pyridinic N are active sites in ORR with Cl-FeN_4 moieties being the most active sites, and Fe/Fe_3O_4 metal nanoparticles show no activity for ORR in alkaline media. This work highlights the great promises of cost-effective Fe-N-C in electrocatalysis and offers a completely new route for the synthesis of Fe-N-C catalyst. Last but not least, this work also presents a general strategy for the synthesis of other single metal atom catalysts with superior performance for other applications.

2. Results and discussion

2.1 The formation mechanism of Fe/NHPC catalyst

Ammonium carbonate ($(NH_4)_2CO_3$), one of the cheapest inorganic ammonium salts, has been extensively applied in the field of fertilizer industry. Utilization of this abundant and ecofriendly inorganic feedstock in the synthesis of atomically dispersed Fe-N-C electrocatalyst is challenging, especially due to its low decomposition temperature (as low as 60 ^oC). We propose a synthesis route for atomic dispersed Fe decorated N-doped hierarchical porous carbon employing silica template-assisted strategy with citric acid as single carbon source, and $(NH_4)_2CO_3$ as single N-precursor. The entire synthetic procedure takes full advantage of strong coordination of citric acid with cations (Zn^{2+}, Fe^{3+} and NH_4^+).

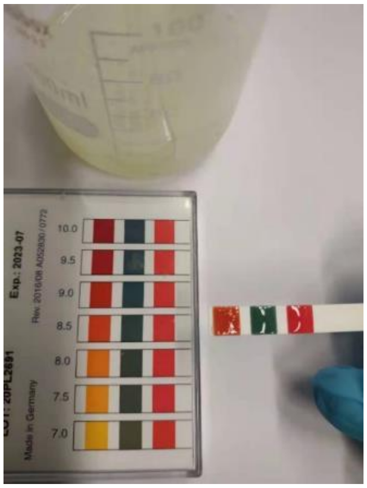

Figure 1. The digital picture of pH value for precursor sol solution of model catalyst.

First of all, the mixture of citric acid, $(NH_4)_2CO_3$, silica nanosphere powder are dissolved into deionized water to form uniform liquid sol, during which $(NH_4)_2CO_3$ is subjected to initial hydrolysis accompanied by release of CO_2 gas and the formation of large number of NH_4^+ in the aqueous solution. After adding metal salts, Zn^{2+} and Fe^{3+} cations can be readily complexed by citrate ion due to the strong coordination interaction [325]. The total contents of metal cations (1.87 mmol) are much lower than that of carboxylate ion (31.23 mmol based on addition amount of citric acid) giving rise to the formation of ammonium citrate [14, 15]. The pH of sol precursor solution is measured to be about 8.5 (Figure 1), higher than isoelectric point (pH = 2.5) of SiO_2 aqueous solution, implying that the surface of silica nanosphere is negatively charged. Hence, excess NH_4^+ ions are presumably adsorbed at surface of silica nanosphere. After drying at 110 ^{o}C a solid deposit is obtained. Upon pyrolysis under Ar at 900 ^{o}C, the black power is formed. After silica template removal by NaOH etching, the atomic Fe decorated hierarchical porous carbon, referred to as ^{2}Fe/NHPC^{5AC} is finally produced by the second thermal treatment in Ar at 900 ^{o}C. On the contrary, the viscous gel-like substance is formed after drying the solution of citric acid, ammonium carbonate, and metal salts, when no silica template particles are added. After pyrolysis under Ar at 900 ^{o}C, the silver-gray foam product is obtained which is also subjected to second thermal treatment in Ar at 900 ^{o}C (Figure 2).

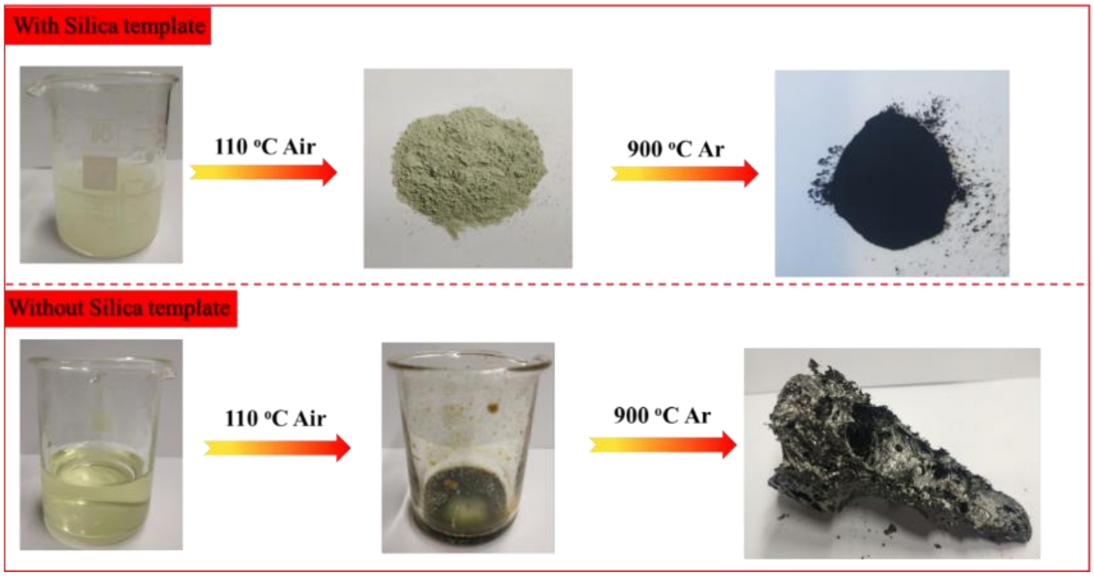

Figure 2. The digital picture of synthetic procedure of model catalyst ^{2}Fe/NHPC^{5AC} (above), and control sample ^{2}Fe/NC^{5AC}-w/o SiO_2 (below).

In order to understand the processes of pyrolysis of precursors mixture and formation mechanism of atomic Fe decorated N-doped hierarchical porous carbon, TPD-MS experiment of precursor powder of ^{2}Fe/NHPC^{5AC} obtained after 110 °C dryness are first conducted. As Figure 3 shows, the main mass loss occurs with the temperature range from 100 °C to 500 °C along with generation of considerable amount of H_2O (m/z = 18), CO_2 (m/z = 44), NH_3 (m/z = 17) and small portion of H_2 (m/z = 2), O_2 (m/z = 32), CO (m/z = 28). This process is attributed to the dehydration along with thermal decomposition of citrate ions and NH_4^+ in the precursor mixture. The process results in the formation of citraconic anhydride and itaconic anhydride [326], during which the evolved NH_3 reacts with oxygen-containing functional groups of carbon network resulting in the in-situ N-doping. At the temperature above 500 °C, a significant amount of H_2 is gradually released, along with generation of small amount CO, which can be attributed to dehydrogenation carbonization process with formation of amorphous carbon and decomposition of more thermal-resistant oxygen function groups [327]. As pyrolysis temperature increases, Fe atoms are reduced by amorphous carbon and trapped by N atoms, leading to the formation of highly stable FeN_x active sites incorporated into carbon matrix. When pyrolysis temperature reaches up to 900 °C, the metal Zn is vaporized and leave micropore channel, which is highly beneficial for hosting more FeN_x active sites thus improvement of ORR activity.

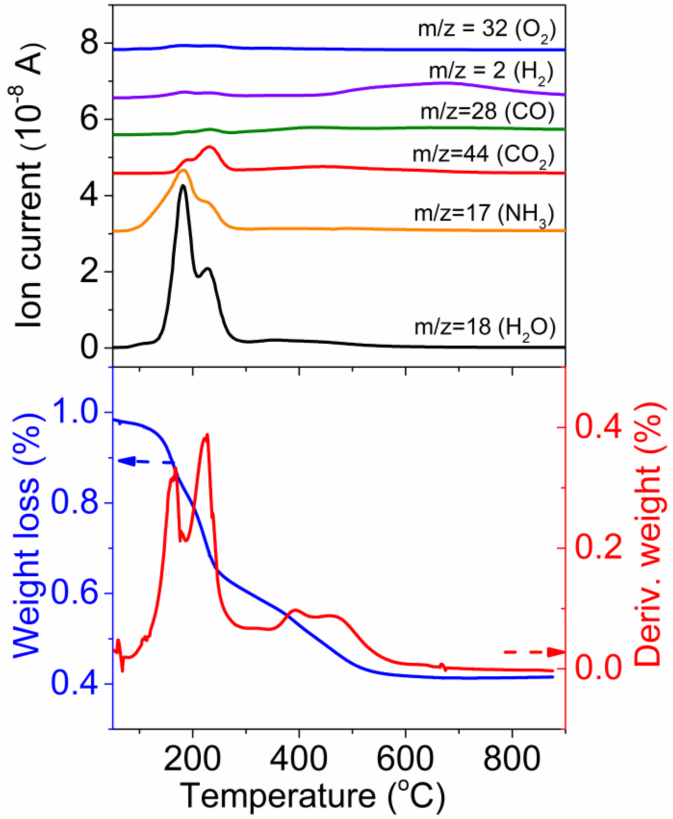

Figure 3. TPD-MS (above) and corresponding TGA plots (below) of precursor powder of ^{2}Fe/NHPC^{5AC} after a drying step at 110 °C.

N_2 adsorption isotherms for catalysts prepared with different amount of $(NH_4)_2CO_3$ are then measured to get an insight into the formation of porous structure containing atomic Fe catalyst. As Figure 4A shows, all investigated samples display type IV isotherm profiles with markedly type-

H3 hysteresis loop, a typical characteristic of mesoporous carbon structure [328]. Dependencies of BET specific surface area (SSA) and relative pore volume on the amount of $(NH_4)_2CO_3$ are presented in Figure 4B. The SSA of catalyst prepared in the absence of $(NH_4)_2CO_3$ is 931 m^2 g^{-1}. An introduction of small amount of $(NH_4)_2CO_3$ (0.5 g) induces a slight decrease in surface area (840 m^2 g^{-1}). However, further increase of $(NH_4)_2CO_3$ amount results in increase in SSA to 925 m^2 g^{-1} for $^2Fe/NHPC^{5AC}$ and 1036 m^2 g^{-1} for $^2Fe/NHPC^{8AC}$. The relative volumes of micro-, meso-, as well as total pore volume monotonically increase with the increasing of amount of $(NH_4)_2CO_3$. In order to better understand the role of $(NH_4)_2CO_3$ in the formation of the catalyst porous structure, we analyze the dependence of relative surface area and volume of micro-, meso- and macropores as function of the added amount of $(NH_4)_2CO_3$, for detail see Figure 4B and Table 1. Compared with N-free catalyst, addition of small amount of $(NH_4)_2CO_3$ (0.5 g) results in significant increase in surface area and micropores volume. However, a decrease in surface area of mesopores is observed, while their relative volume is increased. This can be rationalized by the fact that the total length of mesopores becomes slightly shorter but their average diameter increases as $(NH_4)_2CO_3$ is introduced. Therefore, the surface area, proportional to the product of length and diameter, is decreasing, while their volume, proportional to product of length and square of diameter, is increasing. Indeed, an average pore diameter, estimated from the ratio of volume to area (Table 1), is increasing from ca. 7.8 nm to ca. 12.8 nm with addition of $(NH_4)_2CO_3$. We can speculate that NH_3 evolution produces a large number of micropores by etching carbon matrix during pyrolysis, and hardly contributes new mesopores which results in shortening/broadening of mesopores formed by silica template. Further increase in $(NH_4)_2CO_3$ amount (5 g) results in a slight increase in average diameter of mesopores (13.3 nm), and gradual increase in both pores volume and surface area, while for larger amount of $(NH_4)_2CO_3$ added (8 g) a slight decline in average pore diameter is detected (12.7 nm). In this case, mesopores surface area improves sharply while the micropores surface area and pores volume reach up to saturation and shows limited improvement. The observation suggests that an excess amount of NH_3 probably forms bubbles, enabling the formation of new mesopores. The conclusion is further verified by analysis of pore size distribution.

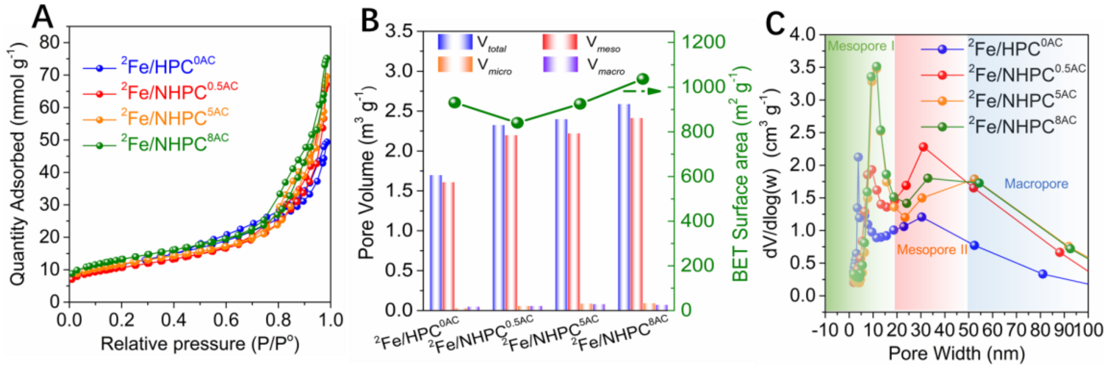

Figure 4. (A) N_2 adsorption-desorption isotherm plots for samples with different amount of $(NH_4)_2CO_3$ recorded at 77 K; (B) The correlation plots of specific surface area (SSA) and pore volume as function of addition of $(NH_4)_2CO_3$; (C) The respective pore size distribution using the desorption branch of N_2 isotherms (BJH method, the data recorded with a pore width from 1.7 nm to 100 nm).

As shown in Figure 4C, all samples show hierarchical porous features with two apparent mesopore regions along with a small amount of macropores. The bimodal mesopore contains two domains: with low pore diameter region (Mesopore I) mostly presented by silica template-derived mesopores, and larger mesopores region with broad diameter distribution (Mesopore II) mostly formed consecutively by gas (CO_2, CO, H_2, NH_3) generation during pyrolysis. Without addition of $(NH_4)_2CO_3$, the main peaks in region I is centered at ca.7 nm, well in accordance with the size of silica template (7 nm). The peak gradually positively shifts to 9.5 nm for ^{2}Fe/NHPC$^{0.5AC}$, 11.5 nm for both ^{2}Fe/NHPC^{5AC} and ^{2}Fe/NHPC^{8AC}, respectively.

Table 1. Textural properties of as-obtained catalysts

Sample	Total SSA^a (m^2 g^{-1})	SSA$_{micro}$ (m^2 g^{-1})	SSA$_{meso}$ (m^2 g^{-1})	Total V ^{b} (cm^3 g^{-1})	V$_{micro}$ ^{c} (cm^3 g^{-1})	V$_{meso}$ (cm^3 g^{-1})	Average pore size ^{d} (nm)
^{2}Fe/HPC^{0AC}	931	85	831	1.70	0.03	1.61	7.8
^{2}Fe/NHPC$^{0.5AC}$	840	141	661	2.33	0.06	2.20	12.8
^{2}Fe/NHPC^{5AC}	925	205	677	2.40	0.09	2.23	13.3
^{2}Fe/NHPC^{8AC}	1036	213	785	2.59	0.10	2.42	12.7
NHPC^{5AC}	1158	293	809	2.93	0.14	2.01	13.9
w/o ZnCl$_2$	828	196	591	2.28	0.09	2.12	14.0

[a] Brunauer-Emmett-Teller (BET) specific surface area (SSA) measured at T = 77 K. [b] Total pore volume determined using the adsorption branch of N_2 isotherm at P/P_0 = 0.98. [c] Determined by t-plot method. [d] Determined by BJH desorption average pore width (4V/A).

Table 2. Chemical composition properties of as-obtained catalysts

Sample	XPS data							
	Element composition ^{a} (at. %)^c			N species (at. %) ^{b}				
	Carbon	Oxygen	Nitrogen	Pyridinic	Pyrrolic	Graphitic	Oxidized	Fe-N
^{2}Fe/HPC^{0AC}	96.21	3.79	-	-	-	-	-	-
^{2}Fe/NHPC$^{0.5AC}$	88.90	6.24	4.85	1.74	1.37	0.82	0.3	0.64
^{2}Fe/NHPC^{5AC}	88.59	5.07	6.35	1.96	1.47	1.18	0.6	1.13
^{2}Fe/NHPC^{8AC}	88.04	4.30	7.66	3.30	2.28	1.17	0.36	0.55
NHPC^{5AC}	88.86	5.09	6.05	2.69	2.31	0.60	0.45	-
w/o ZnCl$_2$	89.20	3.96	6.84	1.95	2.03	1.44	0.66	0.78

[a] Determined by XPS analysis. [b] Determined by high resolution XPS N 1s core region and the product of relative deconvoluted peak and total nitrogen content on each sample.

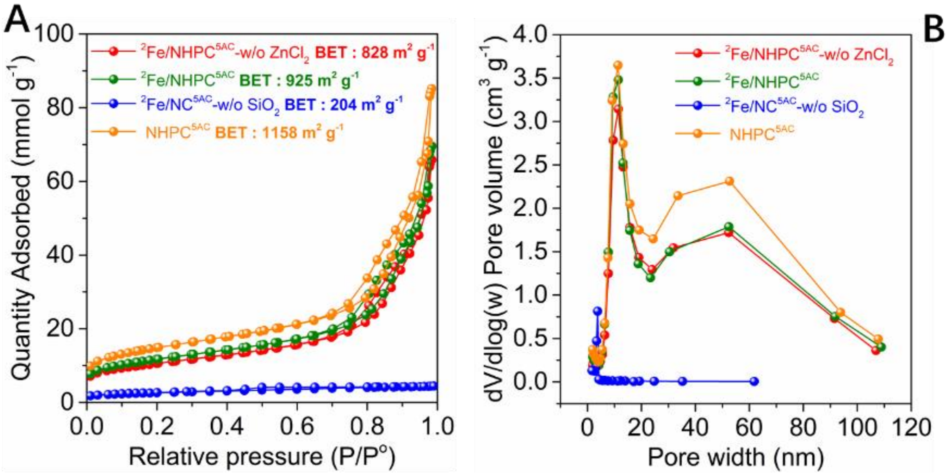

Figure 5. A) N_2 adsorption-desorption isotherm linear plot of ^{2}Fe/NHPC^{5AC}, ^{2}Fe/NHPC^{5AC}-w/o $ZnCl_2$, ^{2}Fe/NC^{5AC}-w/o SiO_2, and NHPC^{5AC} recorded at 77 K and respective pore size distribution determined by BJH method using the desorption branch of N_2 isotherm (the data recorded with a pore width from 1.7 nm to 100 nm).

Likewise, in the region II, the density of large mesopores (ca. 31 nm) increases with addition of 0.5 g $(NH_4)_2CO_3$. The further increase in amount of $(NH_4)_2CO_3$ leads to an increase of pores density, both small (11.5 nm) and large mesopores with wider pore size dimension (ca. 52 nm), which could be induced by the formation of NH_3 which is at the origin of pore expansion and formation of new mesopores. It can be also mentioned that the macropores in samples prepared with $(NH_4)_2CO_3$ have larger relative pore volume and surface area as compared to N-free samples. It is still believed that macropores play a critical role for the improved electrochemical performance due to kinetic accessibility of active sites during electrocatalytic reaction [323]. N_2 adsorption isotherms for ^{2}Fe/NC^{5AC}-w/o SiO_2 and ^{2}Fe/NHPC^{5AC}-w/o $ZnCl_2$ have also been performed to investigate the $ZnCl_2$ and silica template effects on the textural nature. The BET surface area of sample prepared without silica template is 204 m^2 g^{-1} (Figure 5A), much lower than that of ^{2}Fe/NHPC^{5AC}, suggesting the pivotal role of silica for the formation of porous structure. The introduction of $ZnCl_2$ does not significantly affect micropore surface area with only slight enhancement of mesopore surface area compared to that on ^{2}Fe/NHPC^{5AC}-w/o $ZnCl_2$ (Table 1). Similar pore size distribution (Figure 5B) for both ^{2}Fe/NHPC^{5AC} and ^{2}Fe/NHPC^{5AC}-w/o $ZnCl_2$ further confirms the introduction of $ZnCl_2$ indeed has a negligible contribution for the generation of micropores and the change of pore structure. The observation differs from often reported conclusions that $ZnCl_2$ can serve as micropore-forming agent due to its “escape pore” after evaporation at high temperature. In present work, the generation of micropore is governed by NH_3 evolution as aforementioned, and $ZnCl_2$ is likely positive beneficial to improvement of ORR activity in different manner. For instance, the Zn atoms can also be acted as isolator to enlarge distance between Fe atoms, which prevents the aggregation of Fe atoms at high pyrolysis temperature and consequently promotes the FeN_x active sites density [329]. Further evidences on this hypothesis will be given in the following part.

Based on the results discussed above, the schematic illustration of the formation mechanism of atomic Fe decorated hierarchical porous carbon is proposed in Figure 6. The strong coordination ability of citric acid results in interaction between citrate ion and metal cations as well as NH_4^+ ions, while the excess NH_4^+ is adsorbed on the surface of silica nanosphere due to electrostatic interaction. The gas-solid interfacial reaction occurred on the rigid outer surface of silica nanosphere, resulting in decomposition of precursors, in-situ N-doping, carbonization, and formation of FeN_x active sites. To be specific, as the temperature of pyrolysis increases, the decomposition of citrate complexes and NH_4^+ result in generation of a large amount of gas. Gases issued from decomposition of citrate, i.e. CO, CO_2, H_2O, etc., primary escape from precursor matrix, forming large mesopores and small portion of macropores with wide pore size distribution.

On the other hand, NH_3 formed from the decomposition of NH_4^+ on the surface of silica nanoparticles, produces a large number of escape channels. These escape channels further enlarge the pore size of small mesopores derived from silica etching. Simultaneously, the escaping NH_3 readily reacts with carbon matrix and O-containing functional groups of carbon precursor [330], along solid-gas interface, leading to the formation of micropores and in-situ N-doping at relatively low temperature. As pyrolysis temperature increases, Fe atoms are trapped by N atoms and FeN_x active sites are formed along the channel walls, in which rigid interface plays an important role in suppressing the aggregation of Fe atoms and consequently prevent the formation of large Fe particles. As temperature reaches up 900 ºC, the metal Zn reduced by carbon is volatilized due to its relatively low boiling point, which enables the achievement of more densely FeN_x active sites due to the effect of steric hindrance (the presence of Zn atoms enlarging the distance between Fe atoms). Finally, the atomic Fe decorated N-doped hierarchical porous carbon consisting of interconnected micropores, bimodal mesopores and macropores is obtained. Such a hierarchical structure significantly facilitates fast mass transport and offers efficient utilization of FeN_x sites. More importantly, the porosity of as-prepared catalysts can be easily tuned ranging from micro- to macro pores scale by adjusting the addition amount of $(NH_4)_2CO_3$. All of these compelling features are highly beneficial for an electrochemical process.

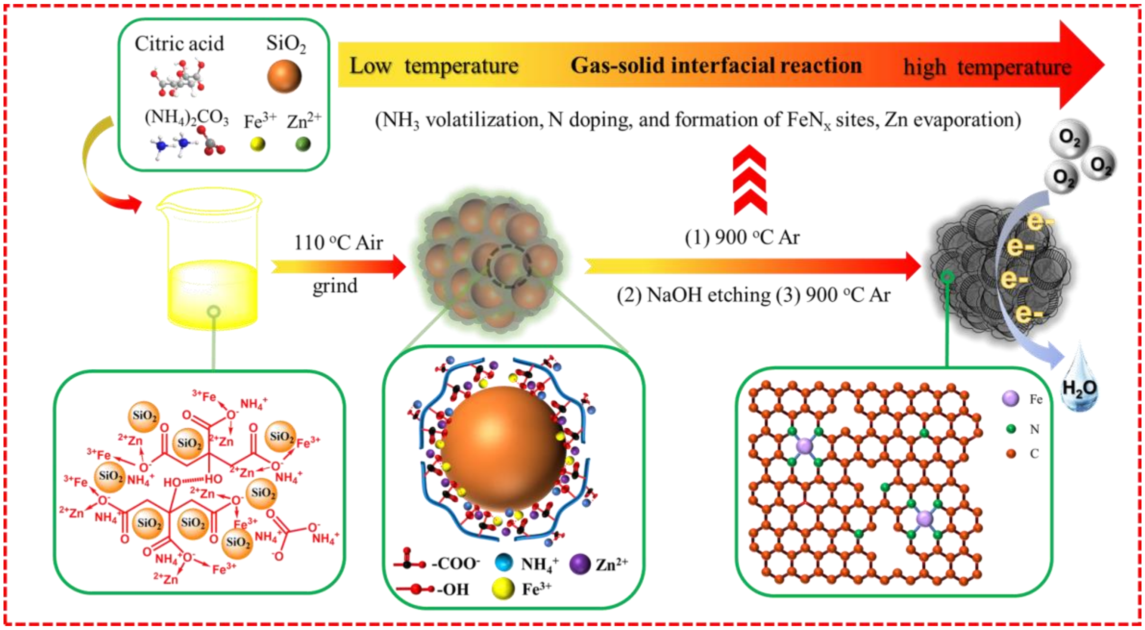

Figure 6. The proposed schematic illustration for the formation of atomic Fe decorated N-doped hierarchical porous carbon.

2.2 Structural characterization of as-prepared catalysts

X-ray diffraction (XRD) patterns (Figure 7A) of as-prepared catalysts shows the formation of Fe_3C nanoparticles in absence of SiO_2 template. Well defined peak at 26° of this sample suggests the enhanced graphitization in the ^{2}Fe/NC^{5AC}-w/o SiO_2 in comparison to samples prepared with silica template. On the contrary, when silica template is used, only Fe metallic phases, and no Fe_3C, are found, even though no $(NH_4)_2CO_3$ is added. This result indicates that SiO_2 template plays critical role in suppressing the formation of Fe_3C phase. All samples with simultaneous presence of $(NH_4)_2CO_3$ and SiO_2 template exhibit two broad peaks located at 24.4° and 44°, which can be assigned to (002) and (100) planes of graphitic carbon, respectively. No other peaks associated with Fe metal phase are observed, suggesting that Fe is predominantly atomically dispersed into single site within the carbon matrix.

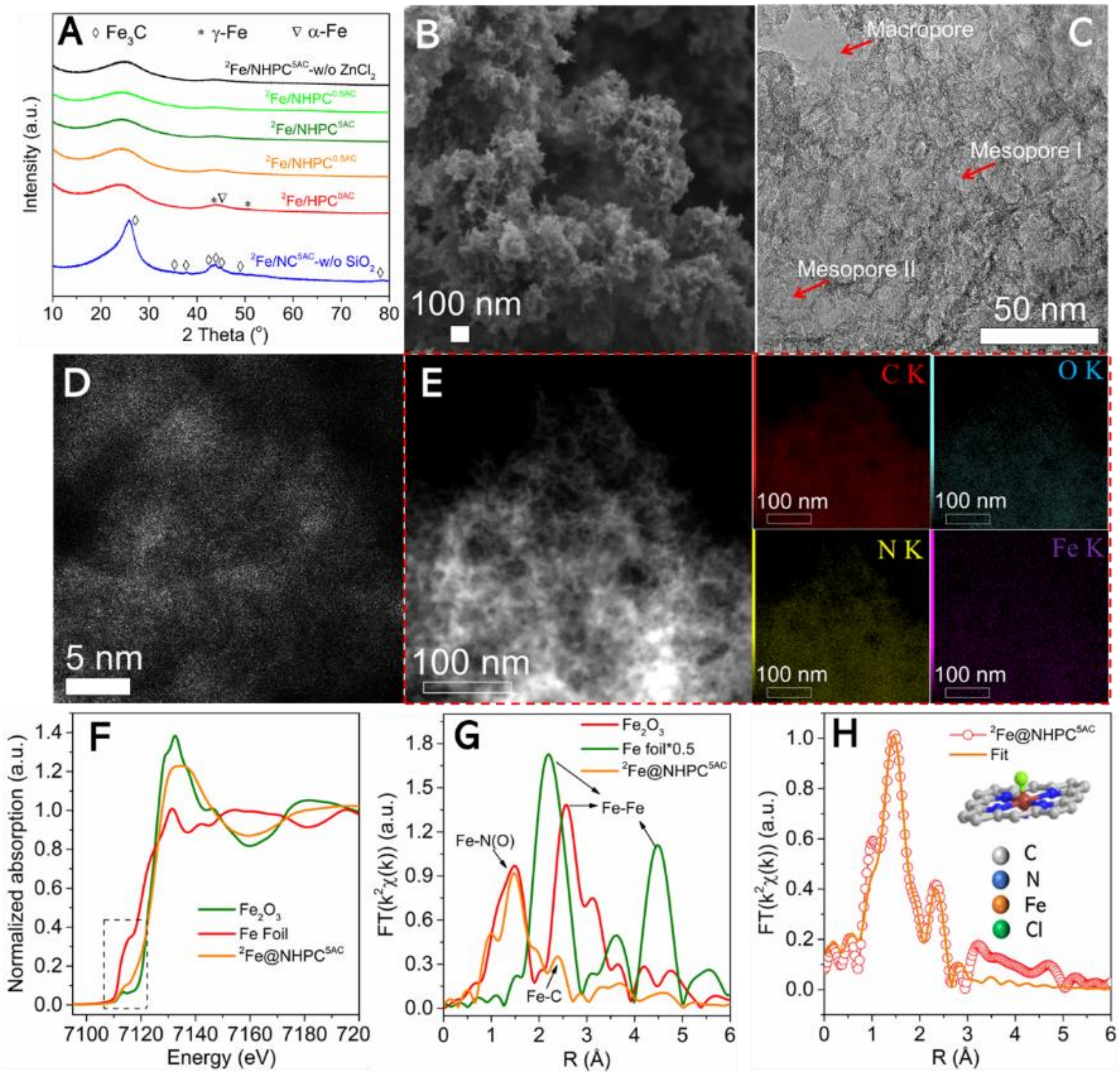

Figure 7. (A) XRD profile of as-prepared catalysts; (B) representative SEM image; (C) TEM image; (D) HAADF-STEM image, and (E) EDX elemental mapping at a selected region of model catalyst ^{2}Fe/NHPC^{5AC}; (F) The normalized XANES spectra at the Fe K-edge of ^{2}Fe@NHPC^{5AC} and respective Fe foil and Fe_2O_3 reference samples; (G) The k^{2}-weighted Fourier transform spectra of ^{2}Fe@NHPC^{5AC} catalyst as well as reference samples; (H) The corresponding EXAFS fitting curves of the ^{2}Fe@NHPC^{5AC} with Cl-Fe-N_4 model.

Scanning electron microscope (SEM) in Figure 7B reveals the flower-like morphology with highly developed pore structure and open carbon network framework of model catalyst ^{2}Fe/NHPC^{5AC}. In a sharp contrast, only solid bulk carbon with poor porosity is found for the sample prepared without silica-template (Figure 8A-B), demonstrating a key role of silica template in the formation of highly developed porous structure. Transmission electron microscopy (TEM) at low magnification with different selected region (Figure 9A-C) showing an overview of microscopic nature of model catalyst, suggests that almost no nanoparticle is present and Fe atoms probably exist in atomically dispersed form. The high-resolution TEM image (Figure 7C) shows a hierarchical porous structure with distinctive pore size scale spanning from meso- to macropore forming interconnected networks, in line with the observation by BET and SEM analysis. HAADF-STEM image (Figure 7D) shows a number of bright spots assigned to heavier Fe atoms that are observed across the carbon framework, unambiguously suggesting the formation of single Fe atoms. The energy-dispersive X-ray (EDX) mapping (Figure 7E) has presented a homogeneous distribution of Fe and N along with C, O elements, further confirming the formation of atomically dispersed FeN_x moieties over N-doped porous carbon.

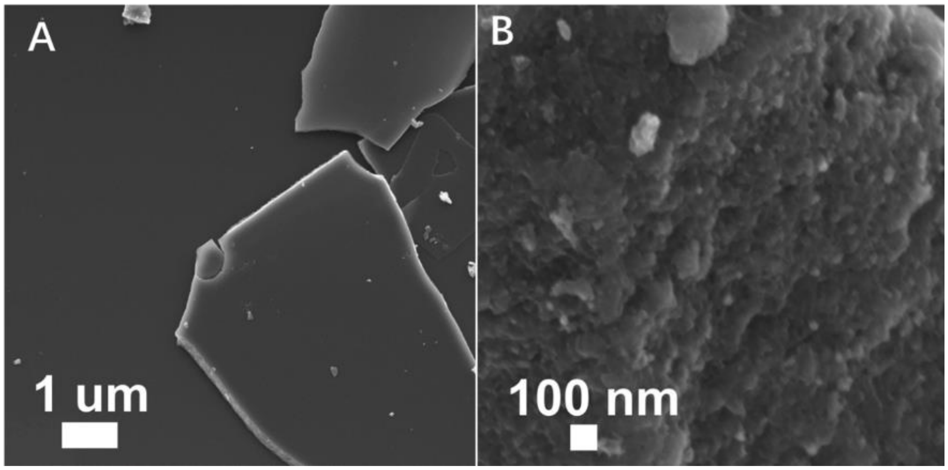

Figure 8. SEM images of ^{2}Fe/NC^{5AC}-w/o SiO_2 at low (A) and high (B) magnification, respectively.

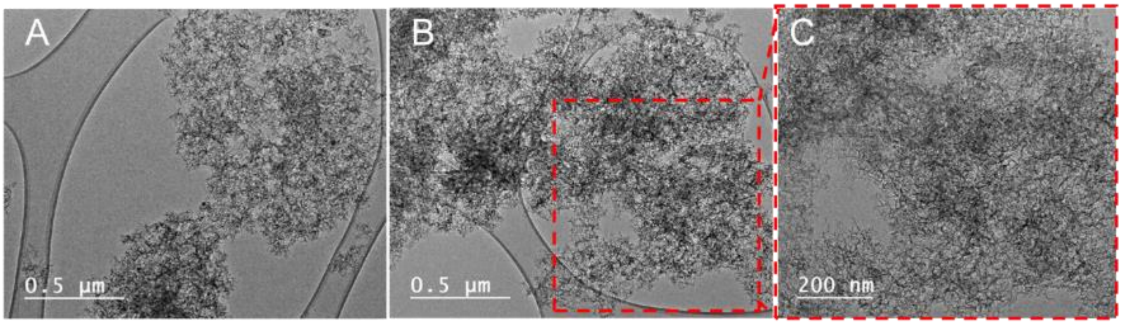

Figure 9. The overview of low-magnification TEM images at different selected region (A and B) and corresponding high-resolution image (C).

To better identify active site structure of FeN_x sites, X-ray absorption spectroscopy (XAS) is performed to obtain more coordination information. Figure 7F shows X-ray absorption near edge structure (XANES) spectra at the Fe K edge of model catalyst. The absorption pre-edge peak at 7118 eV assigned to 1s – $4p_z$ shakedown transition (e.g. typical FePc structure) is of no presence for $^2Fe@NHPC^{5AC}$, revealing the broken D4h symmetry [183]. In this case, an absorption pre-edge peak appeared at 7113.6 eV whose peak intensity lies between Fe_2O_3 and Fe foil, suggesting that the tetrahedral or distorted octahedral geometries feature is dominated in our system [331]. The finding further suggests that the Fe single atom is probably coordinated in the form of Fe-N_4 moiety with porphyrin-like structure [332]. Of note is that the absorption edge (1s - 4p transition) of model catalyst is nearly superimposed on the Fe_2O_3 reference sample, which demonstrates the valence state of Fe^{3+} is prevalent in the sample $^2Fe@NHPC^{5AC}$. This result is different from most usually report on single Fe atom supported carbon carrier with mixture chemical valence of + 2 and + 3. In this case, the Fe ions is oxidized from + 2 to + 3 during the pyrolysis, which is closely associated with involvement of more electronegative heteroatoms [333]. The Fourier-transformed (FT) k^2-weighted extended X-ray absorption fine structure (EXAFS) is further conducted to get more insight into coordination structure of sample. As Figure 7G shows, the pronounced Fe-Fe backscattering signals can be found at 2.20 Å and 2.58 Å in the Fe foil and Fe_2O_3 samples, respectively [334]. On the contrary, the sample ^{2}Fe@NHPC^{5AC} exhibits a prominent peak at 1.47 Å, assigned to Fe-N(O) in the first coordination shell, while another peak at 2.39 Å can be ascribed to Fe-C distance of the second neighbor shell [147]. No Fe-Fe bonds signal is detected, indicating the single metal Fe is incorporated into carbon matrix in the sample. The observation is consistent with results obtained by the XRD and HAADF-STEM techniques. The curve-fitting result of FT-EXAFS (Figure 7H and Table 3) on the model catalyst reveals that the average coordinated number of Fe-N contribution is ca. 3.4, suggesting conventional Fe-N_4 moiety structure. Interestingly, the additional Fe-Cl contribution in the first coordination shell with coordination number of ca. 1 is also observed, in which Cl atom is primarily originated from the $ZnCl_2$ in the starting precursor.

Table 3. Structural data from the fitting of Fe K-edge EXAFS signal in the ^{2}Fe@NHPC^{5AC}.

Path	Coord. Numb.	R(Å)[a]	σ^2 (10^{-2} Å^2)[b]	ΔE_0 [c]	R-factor [d]
Fe-N	3.4 ± 0.2	1.97 ± 0.01	2.9 ± 0.9	-2.8 ± 0.4	0.009
Fe-Cl	1.0 ± 0.1	2.32 ± 0.01	2.7 ± 1.2	4.6 ± 0.9	-
Fe-C	4.8 ± 0.6	2.90 ± 0.01	3.8 ± 1.9	-2.8 ± 0.4	-

[a] Interatomic distance. [b] Debye-Waller factor. [c] Difference in the threshold Fermi level between data and fit. [d] Goodness of fit parameters.

Therefore, the nature of active sites can be proposed as Fe-N_4 center axially coordinated with one chloride anion, make it a Cl-FeN_4 configuration (see picture in inset of Figure 7H). Indeed, the existence of Fe-Cl coordination shall be responsible for the predominant chemical state of Fe^{3+} revealed in the XANES analysis, further reinforcing the accuracy of fitting results. Worthy of note, such active site structure is similar to porphyrin-based macrocycle compound

(Iron(tetraphenylporphyrinato) chloride (FeTTPCl)) which is known to be high active toward ORR albeit with the unsatisfied durability [335, 336]. Such an active sites structure similar to macrocycle molecular catalyst presents two compelling benefits: I) the unique nature of active site inherits advantage of high ORR activity of macrocycle compound molecular catalyst; II) at odds with conventional macrocycle compounds which are known to be less stable in ORR process, the single FeN_4Cl site is strongly stabilized in inert carbon matrix consequently giving rise to much enhanced durability toward ORR. All of these advantages make such carbon-based single-phase system ideal candidates to act as efficient electrocatalyst toward ORR with high active and stability.

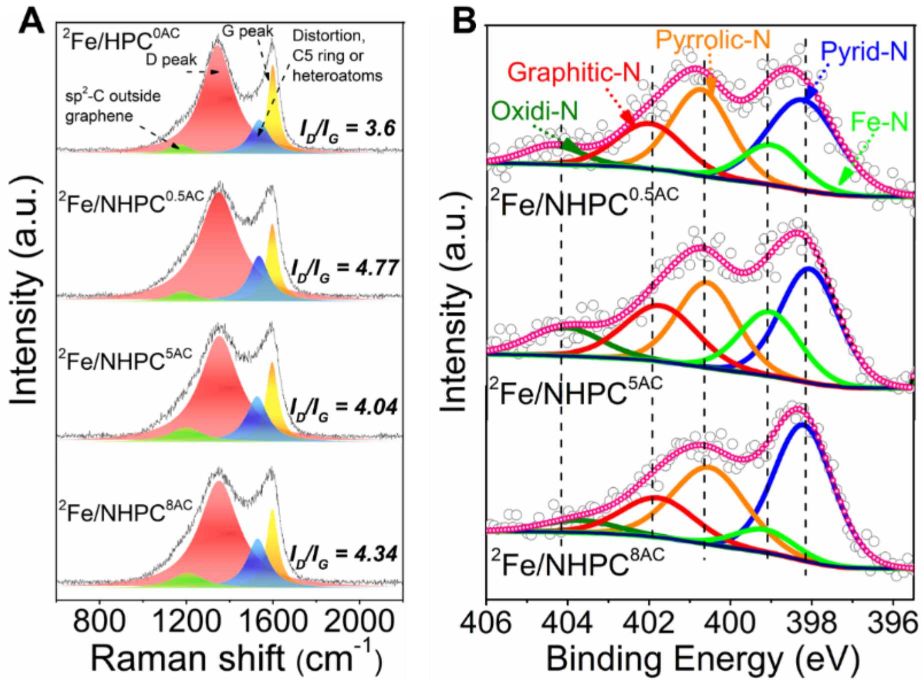

Figure 10. (A) Raman spectra of samples using various amount of $(NH_4)_2CO_3$; (B) XPS spectra of high-resolution N 1s core region in the N-containing catalysts.

Raman measurements are carried out to get a deeper insight into carbon structure information of catalysts prepared with different amount of $(NH_4)_2CO_3$. As shown in Figure 10A, the spectra of all samples are well fit by four Lorentzian peaks. The dominating peaks at 1596 cm^{-1} and 1352 cm^{-1} are ascribed to G and D bands of carbon material, typically characteristic resonance of sp^2-hybridized carbon atoms within ideal graphene layer and carbon atoms close to edge of graphene sheet or structural defect, respectively [337]. The intensity ratio of D band and G band can be used as indicator for a density of defects of specific carbon-based materials. The calculated I_D/I_G values for ^{2}Fe/NHPC$^{0.5AC}$, ^{2}Fe/NHPC^{5AC}, ^{2}Fe/NHPC^{8AC} are 4.77, 4.04, 4.34, respectively, higher than that of N-free sample (3.6), indicating the introduction of N increases the more edge defects and disorder carbon. The two weak peaks centered at 1200 cm^{-1} and 1526 cm^{-1} are attributed to carbon atoms outside of perfectly planar graphene networks associated with aliphatic and amorphous carbon, and distortion carbon structure related to five-members or heteroatoms, respectively [338]. Both of these two peaks proportion gradually improve as the increase of $(NH_4)_2CO_3$ (Table 4), suggesting that more N heteroatoms are introduced into carbon matrix.

Table 4. Raman fitting results for samples prepared by using different amount of $(NH_4)_2CO_3$

Sample	Deconvoluted results ^{a} (Area. %)					
	Sp^2 carbon Outside	D peak	Distortion C5 ring Heteroatom	G peak	^{b} I_D/I_G	^{c} L_a (nm)
^{2}Fe/HPC^{0AC}	3.77	65.63	12.36	18.24	3.60	5.34
^{2}Fe/NHPC$^{0.5AC}$	4.00	67.38	14.48	14.13	4.77	4.03
^{2}Fe/NHPC^{5AC}	7.00	62.36	15.19	15.43	4.04	4.76
^{2}Fe/NHPC^{8AC}	7.16	62.53	15.92	14.40	4.34	4.43

^{a} fitting by Lorentz method, ^{b} determined by the area ratio between D peak and G peak, ^{c} calculated by the general equation proposed by Cançado et al [339]: L_a (nm) = $(2.4\times10^{-10})\ \lambda^4\ (I_D/I_G)^{-1}$, where λ is referred to wave length of laser (532 nm).

Table 5. N1s deconvoluted results of as-prepared catalysts

Sample	N species (at. %)				
	Pyridinic N	Pyrrolic N	Graphitic N	Oxidized N	Fe-N_x
^{2}Fe/NHPC$^{0.5AC}$	35.81	28.16	16.82	6.11	13.10
^{2}Fe/NHPC^{5AC}	30.83	23.30	18.64	9.47	17.77
^{2}Fe/NHPC^{8AC}	43.09	29.71	15.21	4.75	7.24
NHPC^{5AC}	44.45	38.20	9.99	7.36	0
^{2}Fe/NHPC^{5AC}-w/o $ZnCl_2$	28.47	29.69	20.98	9.60	11.34

XPS measurements are carried out to elucidate the effect N-doping on the electronic structure of the different samples. The relative elemental compositions determined by semi-quantitative analysis for various catalysts are summarized in Table 2. The Fe signal is invisible due to its low loading (the mass loading of ^{2}Fe/NHPC^{5AC} is determined to be 0.4 wt. % by ICP-AES measurement). It is found that much higher carbon content (96.2 %) are obtained for ^{2}Fe/HPC^{0AC} respect to that of N-containing catalysts, demonstrating the improvement of the carbonization and graphitization degree. Once $(NH_4)_2CO_3$ is added, the carbon content is significantly decreased. The N contents gradually increase with increasing the amount of $(NH_4)_2CO_3$ from 4.85, 6.35 to 7.66 % for ^{2}Fe/NHPC$^{0.5AC}$, ^{2}Fe/NHPC^{5AC} and ^{2}Fe/NHPC^{8AC}, respectively. On the contrary, oxygen contents decrease accordingly as a function of $(NH_4)_2CO_3$ addition. Noteworthy, the total amount of N and O species remains unchanged, indicating that the introduction of N is mostly linked by a reaction between NH_3 and oxygen functional groups. At odds with all of results reported for the Fe-N-C catalysts, the N-doping level can be carefully tuned by changing the amount of solid N precursor. The high-resolution N 1s spectra for N-containing samples is further analyzed to reveal the more details of N-doping species. As presented in Figure 10B, a deconvolution of high-resolution spectra at their N 1s core regions accounted for five distinct N-components, where the peaks at ca. 398.0 eV, 400.6 eV, 401.8 eV, 404.1 eV are assigned to pyridinic N, pyrrolic N, graphitic N and oxidized N respectively. The additional peak at 399.1 eV is conventionally ascribed to the contribution of Fe-N sites (Cl-FeN$_4$ moiety in this case) [146, 340]. The relative fraction of N-species and the amount of nitrogen species calculated on a basis of total nitrogen content and its fraction on each sample has been summarized (Table 2 and Table 5). It is worth noting that the ^{2}Fe/NHPC^{5AC}-w/o ZnCl$_2$ shares similar elemental composition and almost the same N-doped content to that of ^{2}Fe/NHPC^{5AC} (Table 2). However, at odds with predominant pyridinic N-doping of ^{2}Fe/NHPC^{5AC}, the graphitic N is main contributor for the ZnCl$_2$-free catalyst with much lower Cl-FeN$_4$ content (Figure 11, Table 2). The observation suggests that ZnCl$_2$ plays important role of generation of more densely Cl-FeN$_4$ active sites during pyrolysis.

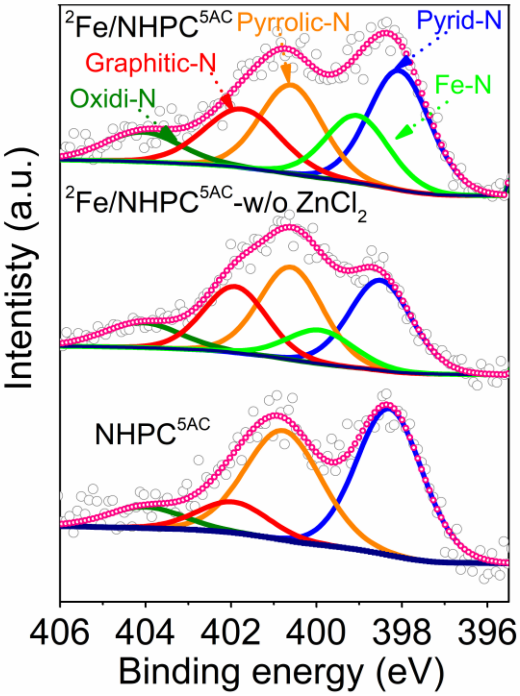

Figure 11. High resolution XPS N 1s core level region of ^{2}Fe/NHPC^{5AC}, ^{2}Fe/NHPC^{5AC}-w/o ZnCl$_2$, and NHPC^{5AC}.

2.3 The influence of different precursors on ORR activity

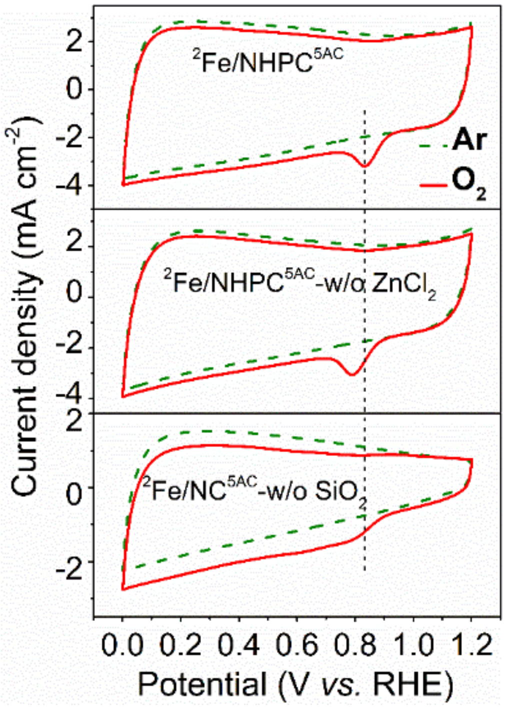

Figure 12. Cyclic voltammetry (CV) curves under Ar and O_2- saturated 0.1 M KOH solution at scan rate of 50 mV s^{-1} for ^{2}Fe/NHPC^{5AC}, ^{2}Fe/NHPC^{5AC}-w/o $ZnCl_2$, and ^{2}Fe/NC^{5AC}-w/o SiO_2.

The ORR electrocatalytic performance of model catalyst ^{2}Fe/NHPC^{5AC} along with counterparts prepared without addition of $ZnCl_2$ and silica template are evaluated. Figure 12 presents the CV curves of various catalyst in Ar-saturated and O_2-saturated 0.1 M KOH electrolyte with a scan rate of 50 mV s^{-1}. The distinct reduction peaks are observed only in O_2-saturated electrolyte, confirming that all the catalysts possess the capacity to catalyze oxygen reduction. The most positive reduction peak position for ^{2}Fe/NHPC^{5AC} suggests its highest onset potential and the best ORR activity. The polarization curve and calculated onset potential (E_{on}), half wave potential ($E_{1/2}$) as well as kinetic current density at applied potential of 0.8 V (J_k@0.8 V) are displayed in

Figure 13A and Table 6. ^{2}Fe/NC^{5AC}-w/o SiO$_2$ shows the much lower ORR activity compared to catalysts prepared with silica template irrespectively of addition of ZnCl$_2$, indicating the indispensable role of silica addition for the generation of catalysts with improving ORR activity.

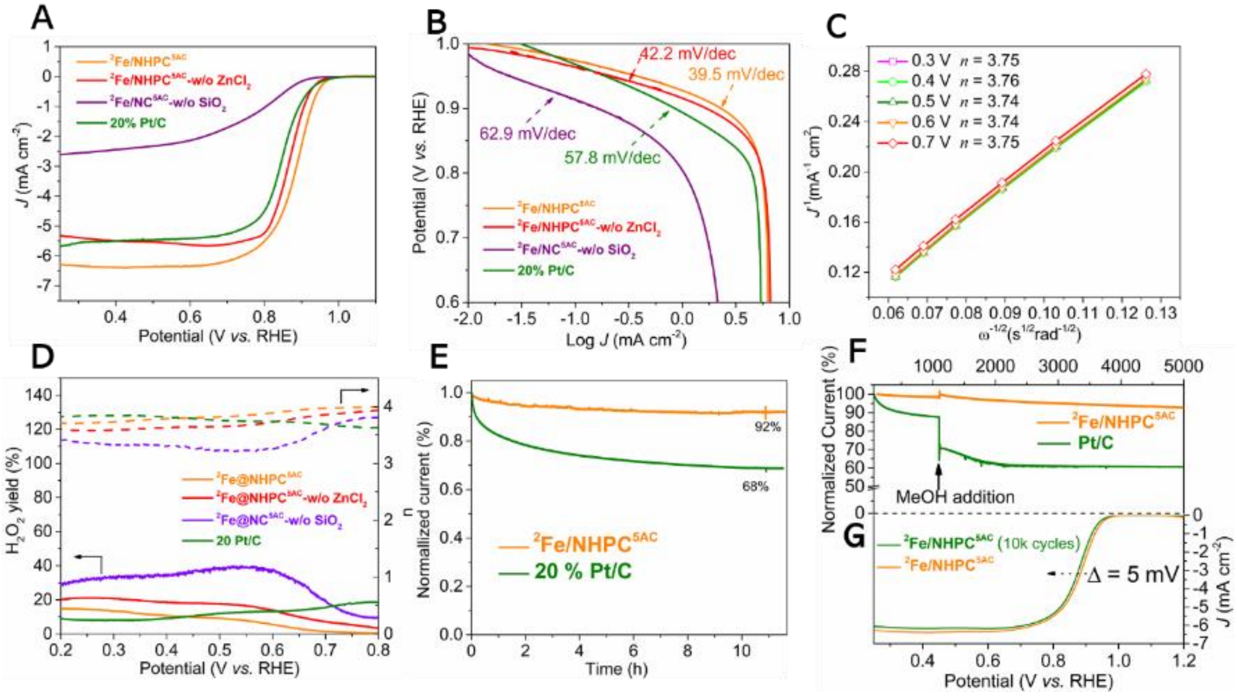

Figure 13. (A) Linear sweep voltammograms (LSVs) curves of model catalyst along with control samples recorded in an O$_2$-saturated 0.1M KOH electrolyte solution at a scan rate of 10 mV s^{-1} at a rotating speed of the working electrode of 1600 rpm; (B) corresponding Tafel plots; (C) K-L plots of ^{2}Fe/NHPC^{5AC} as obtained from the respective LSVs at 0.3 - 0.7 V; (D) The plots of electron transfer number and H$_2$O$_2$ yield of all concerned samples based on RRDE measurements at rotation speed of 1600 rpm with scan rate of 10 mV s^{-1} in O$_2$-saturated 0.1 M KOH solution; (E) Chronoamperometric (CA) responses of ^{2}Fe/NHPC^{5AC} and 20% Pt/C catalyst at applied potential of 0.65 V with a rotating speed of 1600 rpm under O$_2$ atmosphere; (F) Methanol poisoning and (G) durability tests.

The silica template-boosting catalytic activity can be attributed to: (1) the sharply enhanced specific surface area along with developed pore structure, which significantly facilitates the mass transfer during electrocatalytic process, (2) prevention of the formation of Fe_3C particles and increased density of single atom Fe active sites. The model catalyst ^{2}Fe/NHPC^{5AC} shows superior ORR activity with E_{on} of 0.97 V and $E_{1/2}$ of 0.88 V, outperforming that of ^{2}Fe/NHPC^{5AC}-w/o $ZnCl_2$ (E_{on} = 0.96 V, $E_{1/2}$ = 0.86 V). The result demonstrates that the $ZnCl_2$ also plays an important role for further improved ORR activity. In light of the similar textural properties for both catalysts with/without addition of $ZnCl_2$, the improved ORR activity can be rationalized by the formation of denser FeN_x active sites. The calculated kinetic normalized by electrode geometric area and catalyst loading, respectively, which are the highest value over all investigated samples. Note of worthy, the ORR activity for ^{2}Fe/NHPC^{5AC} surpasses that of commercial Pt/C (E_{on} = 0.97 V, $E_{1/2}$ = 0.85 V) catalyst, suggesting its great potential as a promising alternative to the commercial Pt-based catalysts.

Table 6. Electrochemical performance of all samples in ORR

Entry	Catalyst	E_{on} ^{a} (V)	$E_{1/2}$ ^{b} (V)	J_L ^{c} (mA cm^{-2})	Tafel slope (mV dec^{-1})	J_k ^{d} (mA cm^{-2})
1	^{2}Fe/HPC^{0AC}	0.93	0.84	4.60	47.20	12.75
2	^{2}Fe/NHPC$^{0.5AC}$	0.96	0.87	5.70	37.60	29.96
3	^{2}Fe/NHPC^{5AC}	0.97	0.88	6.35	39.50	41.31
4	^{2}Fe/NHPC^{8AC}	0.97	0.884	5.87	39.50	40.12
5	NHPC^{5AC}	0.90	0.80	4.60	40.0	4.93
6	^{2}Fe/NC^{5AC}-w/o SiO_2	0.91	0.77	2.45	62.9	1.8
7	^{2}Fe/NHPC^{5AC}-w/o $ZnCl_2$	0.96	0.86	5.56	42.2	19.05
8	^{1}Fe/NHPC^{5AC}	0.95	0.85	5.72	39.7	23.84
9	^{3}Fe/NHPC^{5AC}	0.96	0.87	5.52	44.0	33.84
10	Pt/C	0.97	0.85	5.44	57.8	25.98

^{a} Onset and ^{b} half-wave potential values reported *vs*. RHE, ^{c} limited diffusion current density, ^{d} Kinetic current density calculated from K-L equation at 0.80 V *vs*. RHE.

The Tafel slope is closely linked surface reaction mechanism and can give insights into rate-determining steps towards ORR process. As shown in Figure 13B, the Tafel slopes are calculated to be 62.9, 42.2, 39.5, 57.8 mV dec^{-1} for ^{2}Fe/NC^{5AC}-w/o SiO_2, ^{2}Fe/NHPC^{5AC}-w/o $ZnCl_2$, ^{2}Fe/NHPC^{5AC}, and Pt/C catalysts, respectively. The lowest Tafel slope for model catalyst further confirms the most superior ORR reaction kinetic amongst all samples. From the mechanism viewpoint, the Tafel slope of 39.5 mV dec^{-1} suggests the first order reaction towards OH^-, which corresponds to Fe^{III}-OH / Fe^{II} redox transition. Simultaneously, the rate-determining step (RDS) is proposed to be the formation of superoxide (O_2^-) character on the surface of Fe^{2+} without concerted proton transfer [89]. The electron transfer numbers based on polarization curves of model catalysts at different rotation speeds are determined to ca. 3.75 at applied potential of 0.3 - 0.7 V according to Koutecky-Levich (K-L) plots, suggesting the model catalyst follows ideally four-electron reduction process (Figure 13C, Figure 14A). The kinetic study on the basis of rotating ring disk electrode (RRDE) tests (Figure 13D, Figure 14B) further reveals the low H_2O_2 yield of less than 10 % with approximately 4-electron transfer numbers across the whole potential range on the model catalyst. It is worth noting that the H_2O_2 yield for model catalyst is even slightly lower than that measured on Pt/C in the higher potential region of 0.45 - 0.8 V, suggesting the preferentially inner-sphere electron transfer (ISET) mechanism is dominant in the model catalyst during ORR. On the contrary, the Pt/C catalyst prefers to follow outer-sphere electron transfer (OSET) where specifically adsorbed OH^- on the oxidized-Pt surface as bridge for electron transfer giving rise to the formation of H_2O_2 at higher potential region [93]. On the other hand, the $ZnCl_2$-free and SiO_2-free samples show markedly higher H_2O_2 yield of approx. 20 % and 40 % respectively, strengthening the key role of both silica template and $ZnCl_2$ in enhancing four-electron selectivity toward ORR. The chronoamperometry (CA) response (Figure 13E) at applied potential of 0.65 V in O_2 atmosphere is carried out to confirm the stability of model catalyst. After 12 h continuous operation, the 92 % retention respect to initial current density is obtained, much higher than that of commercial Pt/C catalyst (68%), manifesting much enhanced stability of ^{2}Fe/NHPC^{5AC}. Accelerated durability tests (ADT) shows that the $E_{1/2}$ of ^{2}Fe/NHPC^{5AC} exhibits minor degradation with only 5 mV negatively shift after 10000 continuous potential cycles at a scan rate of 50 mV s^{-1} in the potential range of 0.6 - 1 V, further indicating outstanding long-term durability (Figure 13G).

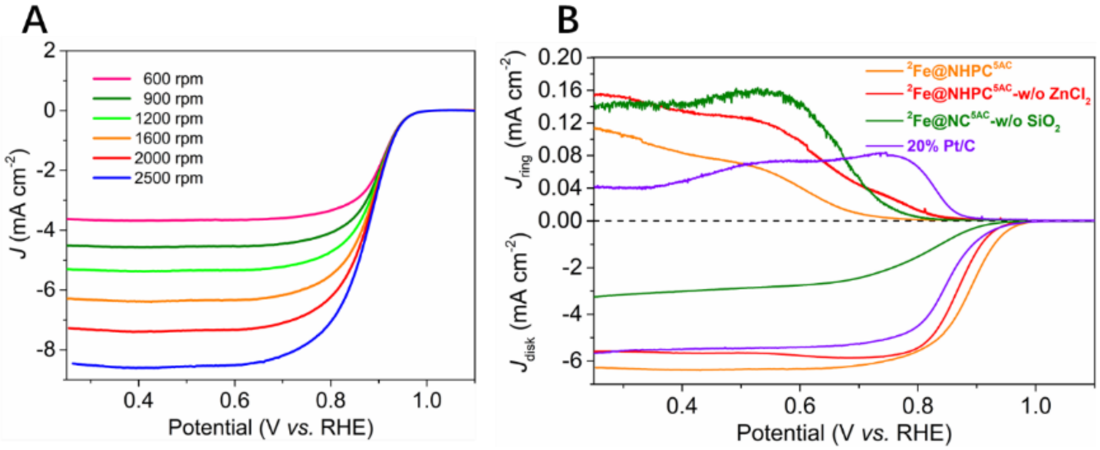

Figure 14. (A) Linear sweep voltammograms (LSVs) for ORR in O_2-saturated 0.1 M KOH solution for ^{2}Fe/NHPC^{5AC} at variable spin rates. Scan rates: 10 mV s^{-1}; (B) RRDE current-potential curves of ^{2}Fe/NHPC^{5A} and respective control samples as well as Pt/C catalyst at 293 K for ORR in O_2 saturated 0.1 M KOH solution recorded at the Pt-ring potential of 1.2 V (*vs.* RHE). All ring currents have been measured at an angular rotation rate (ω) of 1600 rpm.

As an additional trial, the tolerance of the best performing electrocatalyst towards alcohol poisoning has been investigated, which is known to critical consideration for practical application of fuel cell. As displayed in (Figure 13F), after introducing methanol, the dramatic decrease of current density is detected for commercial Pt/C catalyst. In contrast, no pronounced response can be observed for model catalyst at identical operation condition, demonstrating its superior tolerance towards methanol crossover. All these measurement results indicate the model catalyst ^{2}Fe/NHPC^{5AC} possesses remarkable catalytic activity, durability and methanol tolerance toward ORR, which hold great promise for the development of fuel cell with cost-effective, and high efficiency.

2.4 The influence of N-content in precursor mixture on ORR activity

The ORR activity for catalysts prepared with various amount of $(NH_4)_2CO_3$ are systematically investigated. As shown in Figure 15A, the evident dependence of ORR activity on usage of $(NH_4)_2CO_3$ is observed. More detailed electrochemical activity parameters are presented in Table 6. The catalyst ^{2}Fe/HPC^{0AC} shows relatively low ORR activity with E_{on} of 0.93 V and $E_{1/2}$ of 0.84 V, along with low limited current density of 4.6 mA cm^{-2}. After introduction of $(NH_4)_2CO_3$, the catalytic activity for ^{2}Fe/NHPC$^{0.5AC}$ is markedly improved, indicating that the N doping is indispensable to the construction of active sites. The enhanced catalytic activity is closely linked with the formation of N-containing active sites especially for atomically dispersed Cl-FeN$_4$ sites. As the amount of $(NH_4)_2CO_3$ increase, the optimal catalytic ORR activity is obtained for ^{2}Fe/NHPC^{5AC}. Further increasing amount of $(NH_4)_2CO_3$ results in unchanged E_{on} and slightly higher $E_{1/2}$ but with significant decreased of the limited current density.

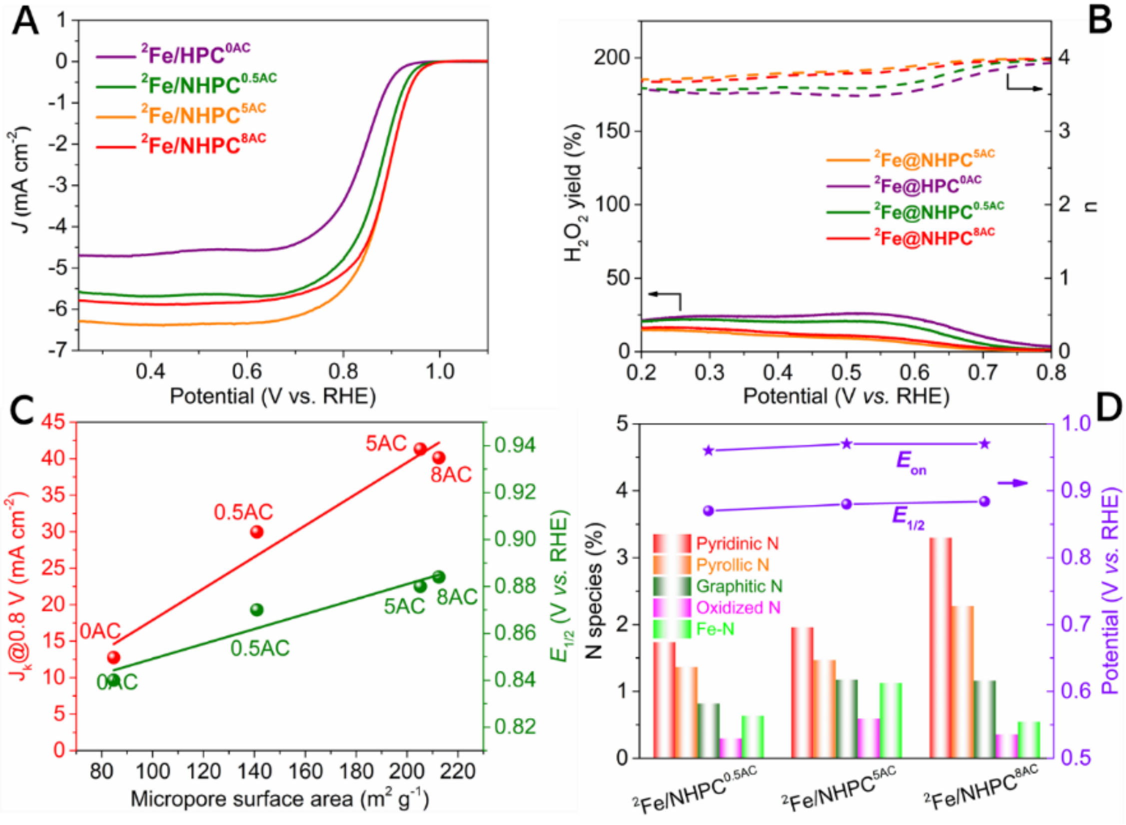

Figure 15. (A) The LSV curves of various catalysts prepared with different addition of $(NH_4)_2CO_3$ at O_2-saturated 0.1 M KOH solution at a scan rate of 10 mV s^{-1}; (B) The plots of electron transfer number and H_2O_2 yield of samples prepared by various $(NH_4)_2CO_3$ addition based on RRDE measurements at rotation speed of 1600 rpm with scan rate of 10 mV s^{-1} in O_2-saturated 0.1 M KOH solution; (C) the correlation plots between ORR activity (J_k@0.80 V) and micropore surface area; (D) The correlation between ORR activity (E_{on} and $E_{1/2}$) and N-species.

RRDE measurement further is carried out for the kinetic analysis on investigated samples. As shows in Figure 15B and Figure 16, the significant advance in generation of H_2O_2 products on ^{2}Fe@HPC^{0AC} respect to that of N-containing samples reveals the probably mixture between ISET and OSET reaction mechanism. The generation of OSET reaction mechanism is ascribed to the introduction of Fe nanoparticles on ^{2}Fe@HPC^{0AC}, which in turn verifies the N-doped is highly required to build Cl-FeN_4 active sites with higher 4-electron selectivity by ISET reaction mechanism. In addition, the trend on H_2O_2 yield and electron transfer numbers of all N-containing samples are consistent with apparent ORR activity with the lowest H_2O_2 yield and the highest electron transfer numbers obtained on ^{2}Fe@NHPC^{5AC}.

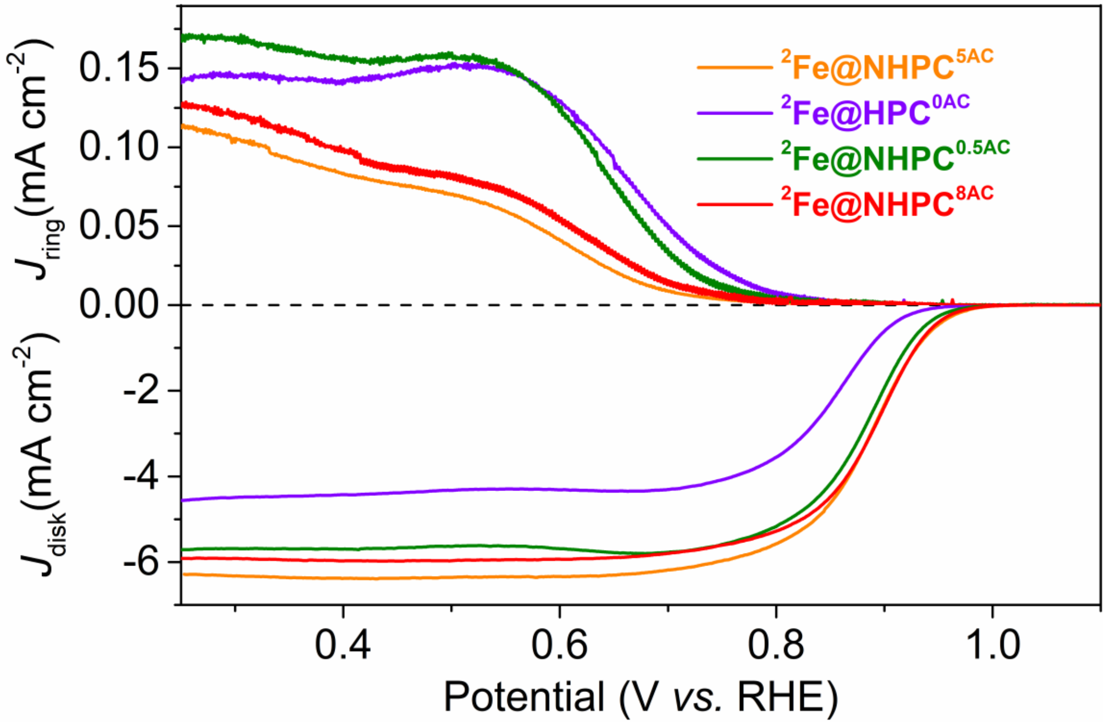

Figure 16. RRDE current-potential curves of samples prepared by different $(NH_4)_2CO_3$ addition at 293 K for ORR in O_2 saturated 0.1 M KOH solution recorded at the Pt-ring potential of 1.2 V (*vs.* RHE). All ring currents have been measured at an angular rotation rate (ω) of 1600 rpm.

To get the deeper insight into the origin of the dependence of ORR activity on N-doping, the correlation between textural property and activity is established. As Figure 15C shows, the ORR activity is clearly correlated with micropore surface area, as both are increasing with the amount of $(NH_4)_2CO_3$. The finding indicates the active sites are mainly hosted in micropores created by NH_3 evolution, in well agreement with reported conclusion [227, 228].

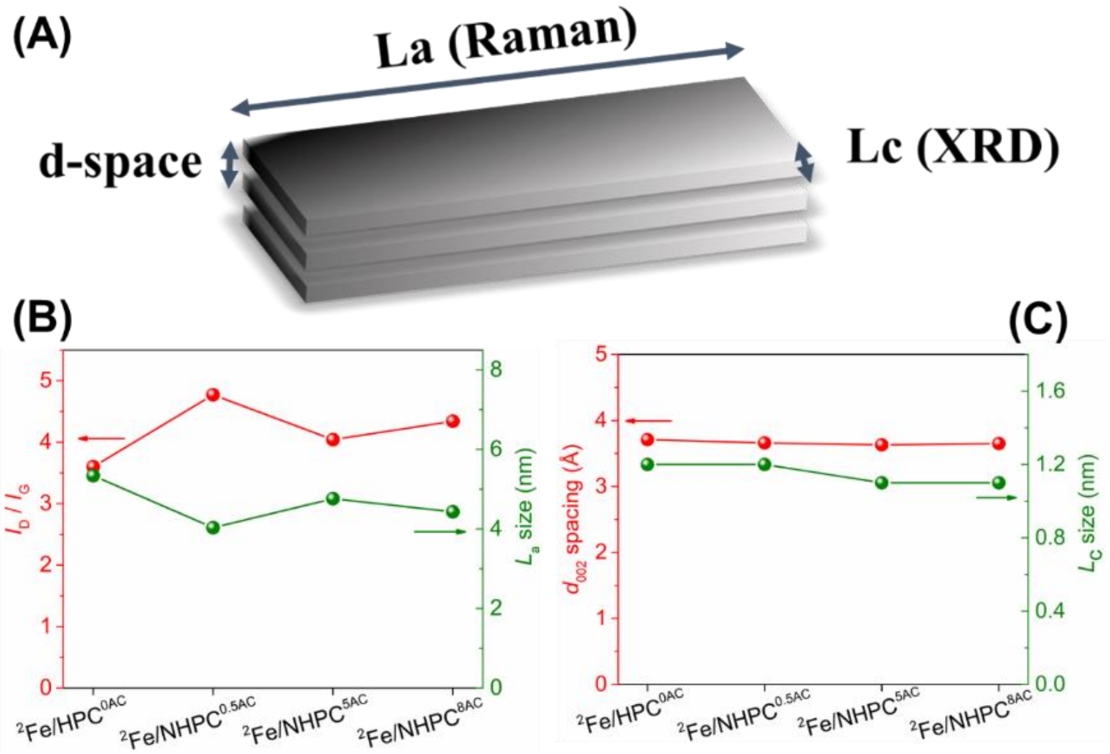

Figure 17. (A) The proposed model of carbon structure; (B) I_D/I_G values and L_a sizes obtained from Raman spectra; and (C) the d spacing values and L_c sizes from XRD analysis as function of addition amount of $(NH_4)_2CO_3$.

The intrinsic activity of Fe-N-C catalyst can be regulated by carbon plane size due to distinct electron-withdrawing/donating effects. A larger carbon plane size with electron-enriched π-band results in the higher electron density of FeN_x moieties due to electron-donating effect of carbon plane. The higher charge density of FeN_x moiety is responsible for stronger affinity between Fe center and oxygen-containing species, thus reducing the ORR activity, and *vice versa* [320]. To quantitatively evaluate the carbon crystallite size arising from different N-doping, the L_a sizes are obtained from Raman spectrum according to the general equation proposed by Cançado et al. [339], the L_c sizes and d-spacing value are calculated by XRD pattern. The corresponding model structure of carbon crystallite is presented as Figure 17A. It is found that the L_a sizes for all investigated catalysts show comparable value, and similar L_a size along with d-spacing value are also observed (Figure 17B-C). The result indicates that the change of carbon plane size is not responsible for N doping dependence on ORR activity.

The correlation between ORR activity and N-doped composition are further established to give a deeper insight into N doping-dependent ORR activity. As Figure 15D shows, the contents of pyridinic N and graphitic N as well as Fe-N sites are simultaneously enhanced with the increase of $(NH_4)_2CO_3$ addition from 0.5 g to 5 g, which gives rise to a significant increase of both E_{on} and $E_{1/2}$. The further increasing amount of $(NH_4)_2CO_3$ results in decreased Fe-N sites (1.13 % for ^{2}Fe/NHPC^{5AC} to 0.55 % for ^{2}Fe/NHPC^{8AC}), along with a pronounced increase in the densities of pyridinic N and unchanged graphitic N. Accordingly, the ORR activity for ^{2}Fe/NHPC^{8AC} does not show significantly improve, with similar E_{on} and $E_{1/2}$ and even lower J_L compared to those of ^{2}Fe/NHPC^{5AC} (see Figure 15A, Table 6). Hence, in this case of ^{2}Fe/NHPC^{8AC}, the comparable ORR activity respect to that on ^{2}Fe/NHPC^{5AC} is primary due to the enhancement of pyridinic N content, in spite of decreased density of FeN_x sites. In light of the underlying active sites (pyridinic N, graphitic N and FeN_x sites) documented by most studies in alkaline media [129, 132]. It can be well suggested that both pyridinic N and Cl-FeN_4 sites are actual active sites with Cl-FeN_4 sites being the most active for ORR in present work (the latter statement stems from the fact that the decrease in the density of Cl-FeN_4 sites is much lower than the increase in the density of pyridinic N). To further verify the conclusion, the study of surface specific double-layer capacitance (C_{dl}) of electrocatalyst, a characteristic value proportional to electrochemically active surface area (ECSA) [341], is performed. The calculated C_{dl} values obtained from cyclic voltammetry measurements are 24.99, 26.62, 27.81, 31.45 mF cm^{-2} for ^{2}Fe/HPC^{0AC}, ^{2}Fe/NHPC$^{0.5AC}$, ^{2}Fe/NHPC^{5AC}, ^{2}Fe/NHPC^{8AC}, respectively (Figure 18). The gradual increase in C_{dl} with the amount of N precursor suggests the enhanced N doping level. The higher C_{dl} value of ^{2}Fe/NHPC^{8AC} compared to that of ^{2}Fe/NHPC^{5AC} further confirms that pyridinic N indeed serves as active sites. All taken together, the improved activity with increase of N doping is originated from the increased density of active sites associated with pyridinic N and Cl-FeN$_4$ moieties, with Cl-FeN$_4$ being the most active sites.

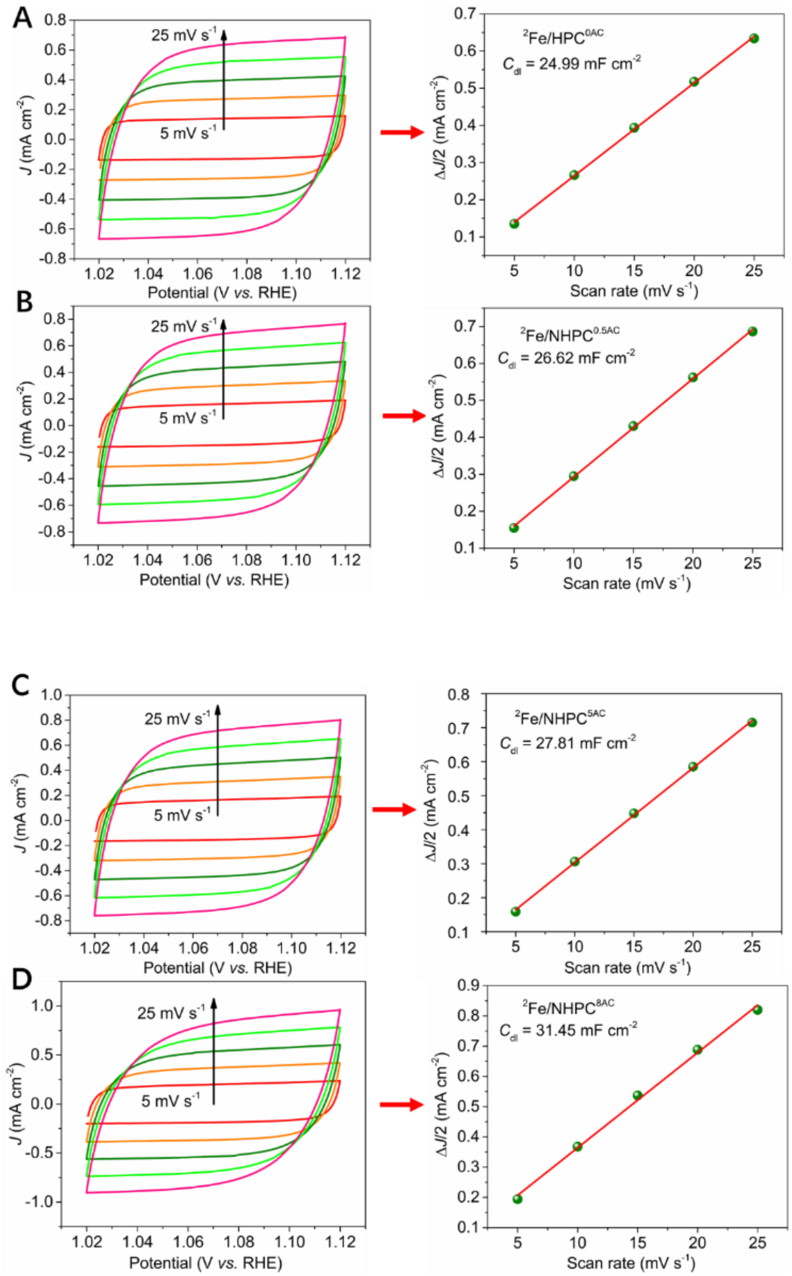

Figure 18. The CV curves in the potential range of 1.02-1.12 V vs. RHE with various scan rates in N_2-saturated 0.1 M KOH solution and corresponding linear fitting of the capacitive currents *vs.* scan rates for (A) ^{2}Fe/HPC^{0AC}; (B) ^{2}Fe/NHPC$^{0.5AC}$; (C) ^{2}Fe/NHPC^{5AC}; (d) ^{2}Fe/NHPC^{8AC}.

2.5 The influence of Fe content on Fe-N-C activity in ORR

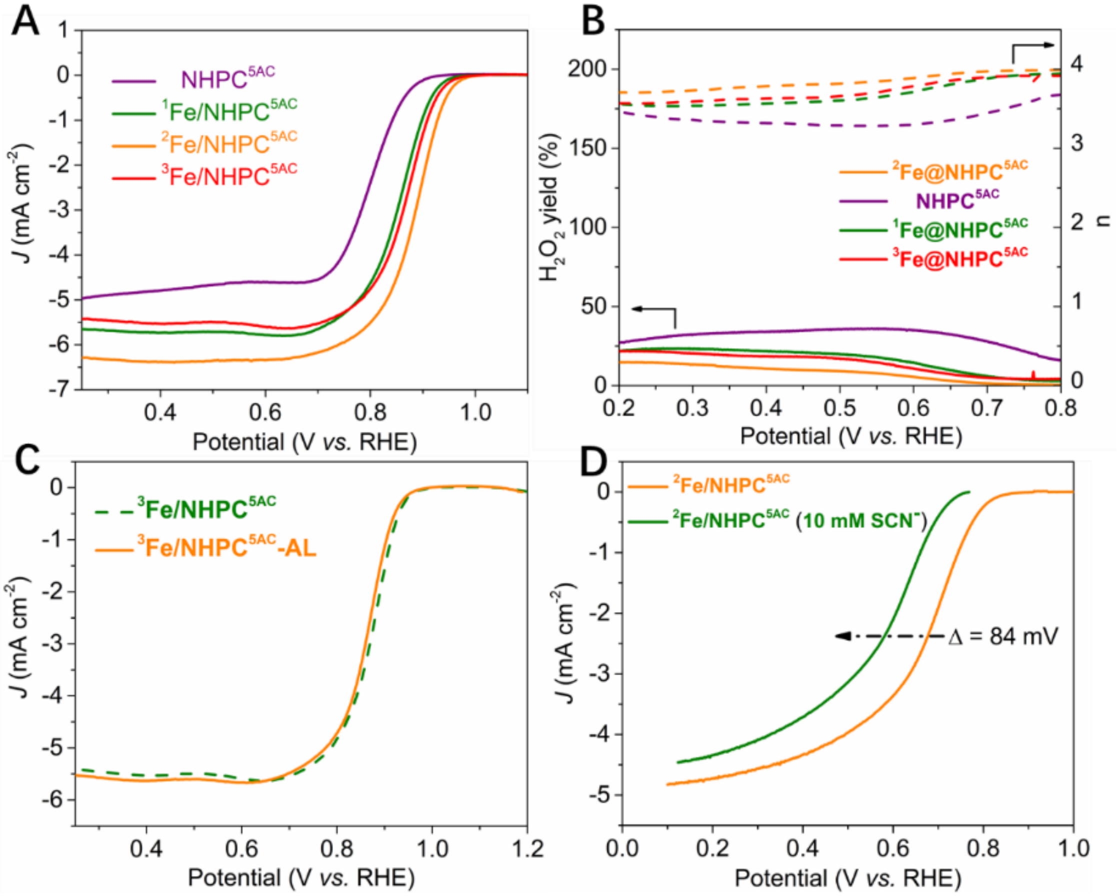

Figure 19. (A) The LSV curves of various catalysts prepared with different addition of Fe precursor at O_2-saturated 0.1 M KOH solution at a scan rate of 10 mV s^{-1}; (B) The plots of electron transfer number and H_2O_2 yield of samples prepared by various Fe precursor addition based on RRDE measurements at rotation speed of 1600 rpm with scan rate of 10 mV s^{-1} in O_2-saturated 0.1 M KOH solution; (C) The LSV curves of ^{3}Fe/NHPC^{5AC} and ^{3}Fe/NHPC^{5AC}-AL at O_2-saturated 0.1 M KOH solution at a scan rate of 10 mV s^{-1}; (D) The LSV curves of ^{2}Fe/NHPC^{5A} in O_2-saturated 0.5 M H_2SO_4 solution at a scan rate of 10 mV s^{-1} with/without 10 mM KSCN.

The catalysts with various loading of Fe precursor based on the optimal addition of $(NH_4)_2CO_3$ are ultimately investigated to get insight into nature of active site in ORR. The Fe loadings are determined to be 0.0714 wt.%, 0.4 wt.%, 5.27 wt.% using inductively coupled plasma-atomic emission spectroscopy (ICP-AES) for ^{1}Fe/NHPC^{5AC}, ^{2}Fe/NHPC^{5AC}, ^{3}Fe/NHPC^{5AC}, respectively. The polarization curve and corresponding E_{on}, $E_{1/2}$ as well as J_k@0.80 V are presented in Figure 19A and Table 6. Without introduction of Fe, NHPC^{5AC} displays relatively poor activity with an E_{on} of 0.9 V and $E_{1/2}$ of 0.80 V respect to those of Fe-containing catalysts. The much higher H_2O_2 yield and lower electron transfer number in whole potential range compared to those of Fe-containing samples demonstrates Fe doping is indispensable for high ORR activity (Figure 19B and Figure 20). It can be attributed to the formation of more active Cl-FeN_4 sites compared with CN_x sites [161]. The ORR activity is greatly dependent on the Fe loadings. As increase in the Fe loading from 0.0714 % to 0.4 %, the $E_{1/2}$ and E_{on} gradually shift positively, accompanied by significant decrease of H_2O_2 yield and enhanced electron transfer number, approaching optimal values (Figure 19B). This can be attributed to higher density of Cl-FeN_4 active sites. Further increase in Fe loading (5.27 %) leads to decreased ORR activity with E_{on} of 0.96 V and $E_{1/2}$ of 0.87 V and increased H_2O_2 yield and declined four-electron selectivity. Similar tendency is also observed in regards to J_k at applied potential of 0.80 V with various Fe loading. This decrease in ORR activity is likely due to the severe aggregation of excessive Fe atoms (Figure 19A-B). XRD pattern and TEM images (Figure 21A-B) confirms the generation of Fe and Fe_3O_4 phase for ^{3}Fe/NHPC^{5AC}. As a matter of fact, the specific role of Fe-based nanoparticles towards ORR is strongly debated to date. For example, Jiang et al. [147] reported the Fe/Fe_3C nanoparticles encapsulated N-doped carbon layer boost activity of FeN_x sites by altering the charge density of central Fe atom in FeN_x configuration. Kramm et al. claimed [148] excessive Fe/Fe_3C

nanoparticles lead to disintegration of FeN_4 centers, thus degrading ORR activity. On the other hand, Zhang et al. [342] claimed that the synergistic effect between Fe_3O_4 and single FeN_x sites contributes to the enhanced ORR activity. Tylus et al. [63] proposed that FeN_4 moiety underwent single site $2e^-$ ∗ $2e^-$ mechanism with no involvement of adjacent Fe/Fe_xO_y nanoparticles in alkaline electrolyte, while these nanoparticles serve as secondary active sites for reduction of intermediates in acidic medium.

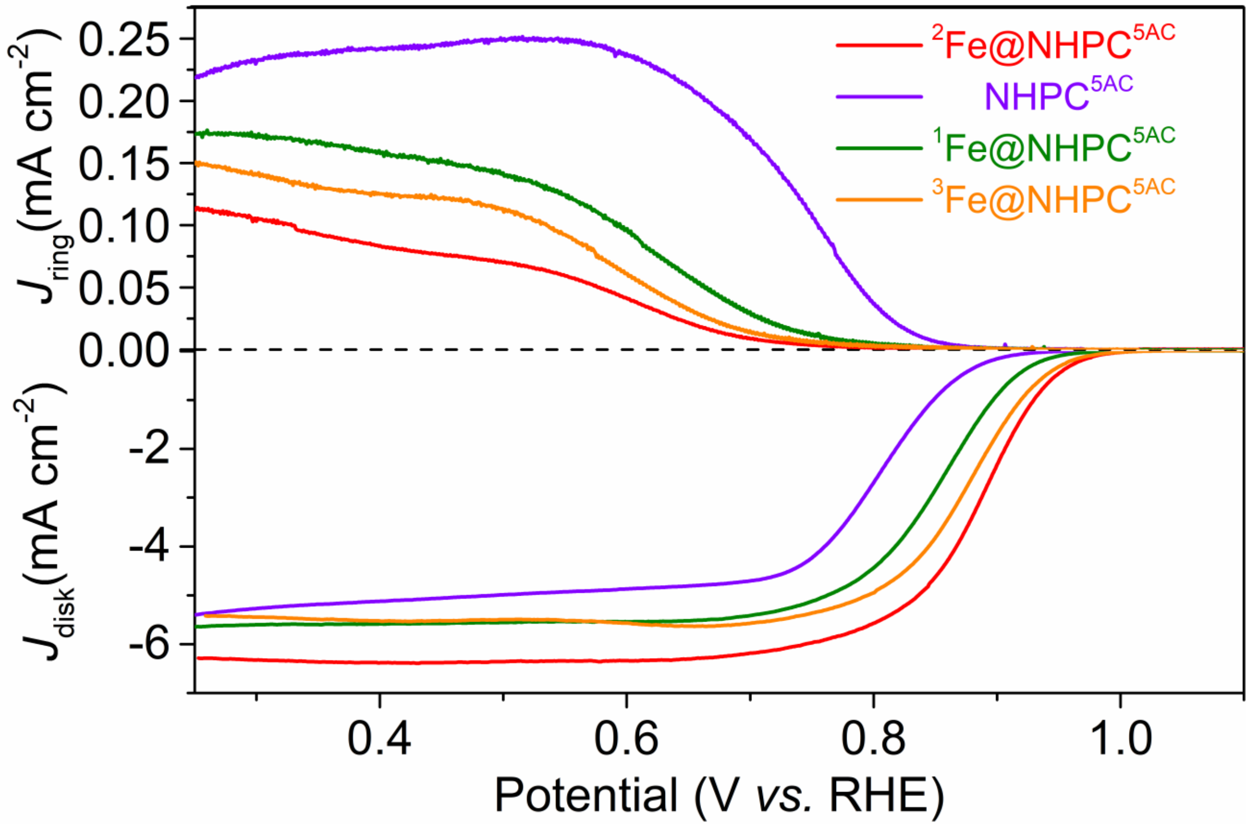

Figure 20. RRDE current-potential curves of samples prepared by different Fe addition at 293 K for ORR in O_2 saturated 0.1 M KOH solution recorded at the Pt-ring potential of 1.2 V (*vs.* RHE). All ring currents have been measured at an angular rotation rate (ω) of 1600 rpm.

In this present work, the formation of Fe/Fe_3C coated by carbon layer is prevented by silica-protect strategy and only Fe/Fe_3O_4 nanoparticles are formed. These nanoparticles are easily washed out by acidic solution thus simplifying the identification of active sites. In order to further verify active sites, control experiment is conducted: catalyst ^{3}Fe/NHPC^{5AC} is leached by 0.5 M H_2SO_4 solution at 80 ^{o}C for 8 h to remove metal Fe/Fe_3O_4 nanoparticles (referred as ^{3}Fe/NHPC^{5AC}-AL). XRD results (Figure 21C) demonstrates that no metal crystallite phase is observed, and TEM images (Figure 21D) further confirms nearly no nanoparticles are found after acid leaching. Accordingly, the polarization curve (Figure 19C) exhibits ^{3}Fe/NHPC^{5AC}-AL shows negligible activity deterioration compared with pristine ^{3}Fe/NHPC^{5AC}. The observation suggests that Fe/Fe_3O_4 nanoparticles do not display appreciable catalytic activity towards ORR. It is well known that the SCN^- could be used as a probe to identify the active site of FeN_x moiety due to the interaction between Fe metal center and SCN^- ion [147, 302]. To precisely elucidate the role of Cl-FeN_4 moiety, the poison test is further carried out under acidic media due to the more stable adsorption of SCN^- on Cl-FeN_4 moiety (Figure 19D). It is clearly found that the $E_{1/2}$ shifts negatively by 80 mV after addition of SCN^- along with significantly decrease of E_{on} and J_L with respect to that on ^{3}Fe/NHPC^{5AC}, demonstrating the Cl-FeN_4 moiety is actual active site towards ORR. Taken together, these control experiments unambiguously corroborate the Cl-FeN_4 sites should be responsible for highly efficient ORR process and Fe-based nanoparticles show no activity in alkaline medium.

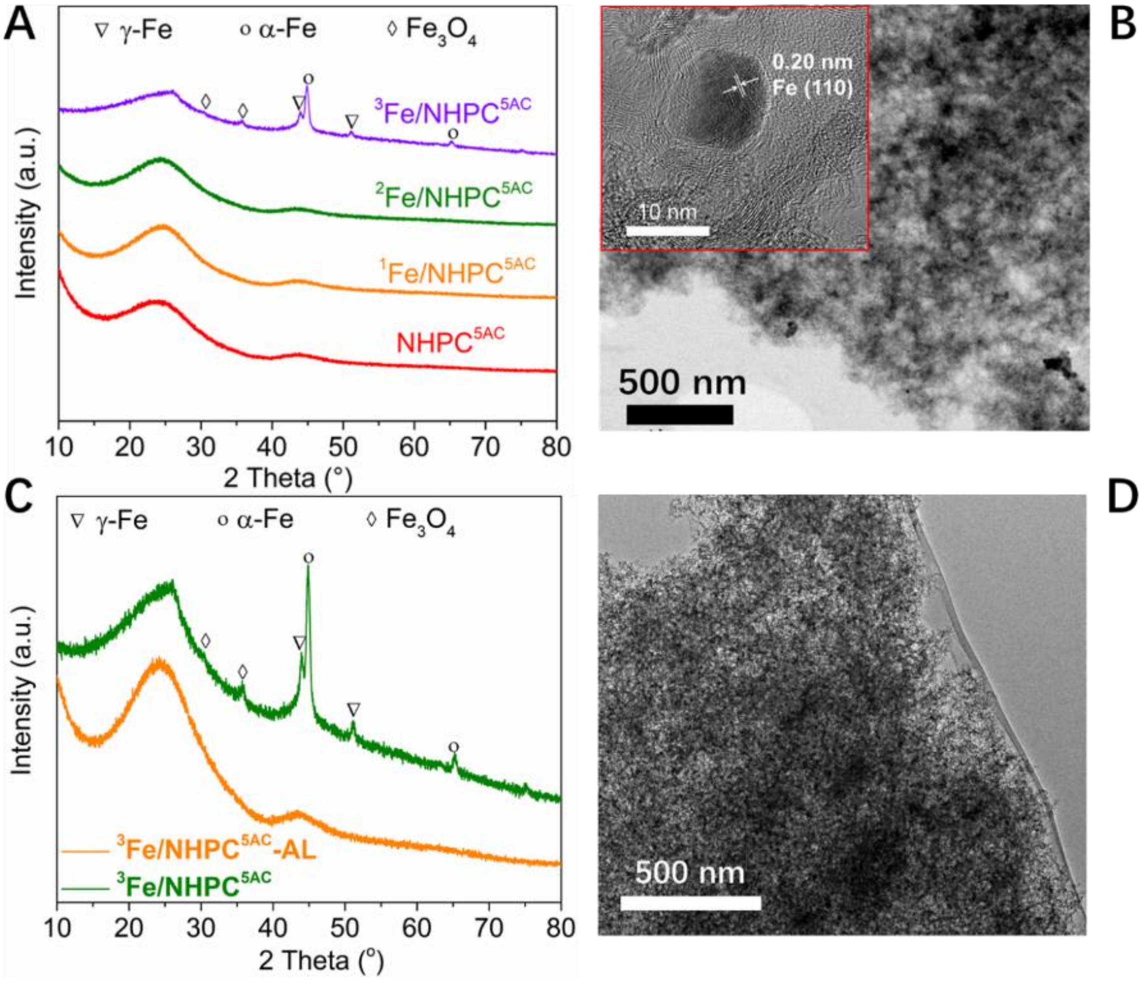

Figure 21. (A) XRD patterns of as-obtained catalysts using different amount of Fe precursor; (B) TEM image of ^{3}Fe/NHPC^{5AC} (HRTEM shown in the inset); (C) XRD patterns of ^{3}Fe/NHPC^{5AC} and ^{3}Fe/NHPC^{5AC}-AL; (D) TEM image of ^{3}Fe/NHPC^{5AC}-AL.

3. Conclusion

In summary, highly active Fe-N-C catalysts are developed via silica template-assisted strategy using inorganic $(NH_4)_2CO_3$ as exclusive N source, citric acid as carbon source and $FeCl_3$ and $ZnCl_2$ as metal precursor. Accounting for the strong coordination and hard-template effect of silica, the formation mechanism of atomically dispersed Fe catalyst based on gas-solid interfacial reaction is proposed. The as-prepared catalyst shows hierarchical porous structure with interconnected micropores, bimodal mesopores and macropore size distributions. More importantly, the geometry of pore structure and N-doped level can be easily tuned by the in-situ doping of NH_3 during pyrolysis leading to the formation of catalysts with N doping-dependent ORR activity.

The systematic investigation demonstrates that ORR activity is gradually improved with the increase of $(NH_4)_2CO_3$ added to the precursor, which is attributed to the formation of higher density of ORR active sites. However, the excess amount of $(NH_4)_2CO_3$ also contributes to the formation of largest surface area (as high as 1036 m^2 g^{-1}), but exerts adverse effect on ORR activity. Additionally, silica template effect and $ZnCl_2$ role on the catalyst preparation and ORR measurement are also scrutinized, both of them play crucial role for the achievement of high density of single Fe active sites and optimization of ORR activity. Finally, the identification of active site conducted by a series of control experiments and poisoning tests confirms that both of Cl-FeN_4 moiety and pyridinic N are active sites. Cl-FeN_4 moieties are concluded to be most active site, while Fe-based nanoparticles show no activity in alkaline condition.

Our work opens a new path for the preparation of single site Fe-N-C by using separated N, C, and metal sources, which shed a light on the understanding of the nature of active sites and rational design of Fe-N-C catalyst. Most importantly, this work also represents a universal approach for the synthesis of other single metal atom catalysts for numerous downstream applications.

Chapter 5

Fe-N-C Electrocatalyst with High ORR Performance: Assessment of Fabrication Procedure.

Abstract

Fe-N-C electrocatalyst has recently received a great deal of research interests due to its potential alternative to the commercial Pt/C catalyst towards oxygen reduction reaction. A deep understanding and optimization of fabrication process is necessary for the development of Fe-N-C catalyst to step forward practical availability. In this work, a novel fabrication strategy is adopted by means of hard template with glucose as only carbon source, inorganic NH_4Cl as solely nitrogen source, and $FeCl_3$ as metal precursor. The effect of pyrolysis temperature on ORR activities is scrutinized by establishing the correlation between structure and performance from geometric and electronic insights. Resultantly, the study emphasizes the importance on the trend-off between the number of FeN_x active sites and intrinsic activity of FeN_x site as well as conductivity of materials. A pyrolysis temperature at 900 ^oC is found to be optimal temperature due to good balance of both relative high number of active sites, excellent intrinsic activity and electron conductivity. Along with a desire hierarchical porous structure composed of micropore pore, bimodal mesopore and macropore, the resulting Fe/NMC-900 exhibits high ORR activity, stability and methanol tolerance in both alkaline and acidic media, comparable with or even outperforms the commercial Pt/C catalyst. The work provides a comprehensive understanding of structure- performance relationship for rational design of Fe-N-C based on high temperature pyrolysis methodology.

1. Introduction

The main obstacle for the widespread commercialization of hydrogen fuel cell electric vehicles is the lack of highly efficient, cost-effective, durable cathode catalyst toward oxygen reduction reaction (ORR) [23]. The current commercial cathode catalyst based on Pt group metal (PGM) makes up over 40 % of stack costs [343]. Over the past decade, there is consensus among researchers on the priority of decreasing PGM content, such as the use of alloy with 3d transition metal [344], and the modification of electrocatalyst morphology [345, 346]. Although both of performance improvement and reduction of Pt usage are obtained, there still is urgency on the investigation of PGM-free ORR electrocatalyst because these Pt-based catalysts contribute to most of cost of fuel cell stack resulted from the scarcity and limited global reserves. The development of PGM-free catalyst with comparable ORR activity and durability to those of low-PGM catalyst represents a reliable key to large-scale manufacturing of fuel cell with good cost competitiveness.

M-N-C (M = Fe, Co, Mn, Zn etc.) catalysts have recently been extensively studied due to their excellent ORR activity, comparable with commercial PGM-based catalyst [176, 290, 347, 348]. Specifically of an Fe-based catalyst (Fe-N-C) is emerged as most reliant electrocatalytic ORR materials due to its highest intrinsic activity amongst these 3d transition metals. Initial investigation on Fe catalyst is mainly concentrated on molecule catalyst on the basis of Fe macrocyclic complexes [3-5]. The performance can be further improved by pyrolysis of metal precursor, carbon and nitrogen source, called Fe-N-C [7, 64]. In spite of enhanced ORR activity on these pyrolysis-derived material, ration design of Fe-N-C electrocatalyst toward practical application is still impeded by insufficient cognition of nature of active sites due to multiplicity of potential active sites. One widespread opinion on such material for nature of active site is FeN_4 moiety incorporated into carbon matrix, which is claimed to be responsible for the ORR activity in both acidic and basic medium. To maximum electrochemistry activity of Fe-N-C material, two strategies are taken into account: 1) increase the site density of FeN_x moiety. Very recently, Jiao et al [210] successfully synthesized Fe-N-C catalyst with recorded site density of 1.92×10^{20} and 100 % site utilization of FeN_x on the basis of non-contact chemical vapour deposition of $FeCl_3$ to Zn-N-C substrate at relatively low temperature at 750 ^{o}C, which exhibited unprecedented ORR activity very close to commercial Pt/C in the condition of fuel cell. It is worth noting that the site utilization of FeN_x can be further enhanced by design of porous structure particularly for construction of hierarchical porous structure [323]. 2) increase intrinsic activity (or Turnover frequency, TOF) in single FeN_x moiety. The coordination environment of Fe center [162], degree of π-electron delocalization [95], and heteroatom doping (S, P, B etc.) [319, 320, 349] surrounding FeN_x significantly change the intrinsic activity of Fe center. The ORR activity is mainly realized by regulation of adsorption energy of O intermediates on FeN_x moiety during ORR. Pyrolysis atmosphere effect has been widely investigated and confirmed to be of importance for the fabrication of high active Fe-N-C particularly in NH_3 [340, 350]. However, of note is that the pyrolysis temperature plays also a pivotal role especially because the formation of active sites is closely related to pyrolysis temperature [351, 352]. The most studies on influence of pyrolysis temperature on ORR activity mainly focus on geometric property of as-prepared catalyst [353, 354]. A comprehensive understanding on both geometric and electronic properties of pyrolytic material should be paid more attention to obtain overall activity descriptor in ORR while remain hitherto no well explored.

Our previous work has reported a novel strategy for the fabrication of single Fe-N-C catalyst using separate carbon and nitrogen source on the basis of gas-solid interfacial reaction, which could be used as highly efficient electrocatalyst towards O_2 reduction reaction. However, the influence of pyrolysis temperature on ORR activity has yet been optimized because the limitation of preparation condition. In present work, a modified method is adopted by the using of glucose as only carbon source, inorganic NH_4Cl as nitrogen source and $FeCl_3$ as metal precursor. With the aid of silica template, an atomic Fe decorated N-doped mesopore carbon electrocatalyst is obtained. Likewise, the final catalyst shows a desirable micropore, bimodal mesopore and macropore structure, which serves a requisite for high mass transfer and more electrochemically available active sites. On the other hand, it is found that pyrolysis temperature has significantly influence on ORR activity. By means of establishing structure-performance relationship, the pyrolysis temperature dependent ORR activity is well clarified in terms of geometric and electronic properties, which is a result from trend-off between site density and intrinsic activity as well as electron conductivity. The optimal catalyst obtained with a pyrolysis temperature of 900 ^{o}C exhibits an excellent ORR activity ($E_{1/2}$ = 0.86 V) and durability as well as methanol tolerance which outperforms the commercial Pt/C catalyst in alkaline media. In acidic media, the Fe/NMC-900 presents also decent ORR activity with $E_{1/2}$ of 0.63 V and good stability. Our work emphasizes the importance of pyrolysis temperature on ORR activity, not only in geometric property, but also more in electronic structure.

2. Results and discussion

2.1 Preparation and characterization of Fe/NMC electrocatalyst.

In our previous work, we proposed a synthesis route of atomic-decorated hierarchical porous carbon using $(NH_4)_2CO_3$ and citric acid as only N source and carbon source respectively, to be applied for efficient O_2 electroreduction. Inspired by such unique design strategy, modified approach is deployed for the development of atomic dispersed Fe supported N-doped mesopore carbon (Fe/NMC) catalyst. In this work, D-glucose, a non-toxic and earth abundance component, is used as only carbon source. In addition, glucose is also known to serve as an excellent chelating agent for the anchorage of the metal cation (Fe^{3+} ions here) in the precursor solution [19, 20]. More importantly, the higher carbonization yield of glucose respect to that of citric acid enables more practicality and the large-scaled production. Ammonia chloride (NH_4Cl) acts as an optimal N source throughout entire preparation process. The feature of C-free for NH_4Cl makes the N-doped level more controllable, which is critical for the development of highly efficient electrocatalytic materials. The adopted approach for the synthesis of Fe/NMC is based on gas-solid interfacial reaction proposed on our previous work. Firstly, glucose dissolved into water interacts strongly with Fe cation in the precursor gel solution while NH_4^+ ions are adsorbed on the surface of silica nanoparticles. The gel solution is then dried directly in an oven overnight at 110 ^{o}C. Afterwards, the first annealing treatment of obtained power is carried out at different pyrolysis temperature under Ar atmosphere for carbonization and graphitization. As pyrolysis temperature increases, the glucose is subjected to carbonization and NH_4Cl is gradually also decomposed into NH_3 and HCl at relative low temperature range. The generated NH_3 reacts easily with oxygenated group in carbon intermediate framework leading to N-doped into carbon matrix. Meanwhile, the evaporated NH_3 and HCl gas act as pore-expansion reagent in micro- and mesoscopic level which is conducive of the formation of hierarchical porous structure. Such structure has been intensively confirmed to be high desired toward electrocatalytic O_2 reduction. As the further temperature increases, the Fe atoms is trapped N atoms induced by high temperature ultimately giving rise to the formation of Fe-N_x moieties. The obtained sample is followed by NaOH leaching to remove silica template. The final catalyst is collected by second thermal treatment in Ar with identical temperature as the first heat-treated step. Such a post heat-treatment is necessary because it is thought to be critical for the improvement of ORR performance due to the elimination of adverse oxygenated groups created by NaOH etching as well as possible formation of vacancy defects [355]. The preparation conditions of electrocatalysts are optimized by changing pyrolysis temperature (800, 900, 1000 ^oC), which are denoted as Fe/NMC-800, Fe/NMC-900, Fe/NMC-1000, metal-free N-doped mesopore carbon (NMC) is also fabricated with the same process as Fe/NMC-900 except for the addition of Fe precursor.

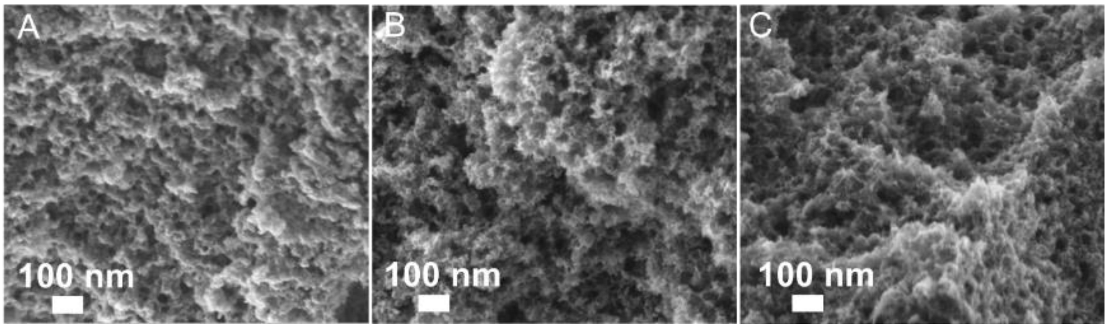

Figure 1. SEM microscopic images for (A) Fe/NMC-800, (B) Fe/NMC-900, (C) Fe/NMC-1000, respectively.

The morphology of as-prepared samples with different pyrolysis temperature is firstly measured by means of scanning electron microscopy (SEM). As shown in Figure 1A-C, all investigated samples exhibit almost the same geometric morphology with highly interconnected porous structure, which leads to developed open carbon network framework. Such a structure extremely facilitates mass transport in the catalyst layer, thus enhancing the ORR activity.

XRD pattern shown in Figure 2A reveals two distinct broad peaks at 24 ^oC and 43 ^oC, corresponding to (002) and (100) plane of typical amorphous carbon. Notably, Fe_3O_4 phase related to is observed as the pyrolysis temperature approaching to 1000 ^oC, demonstrating that Fe metal atoms begin to aggregate. The generation of Fe nanoparticles potentially results in the decrease of active FeN_x moieties, which in turn diminishes the ORR activity.

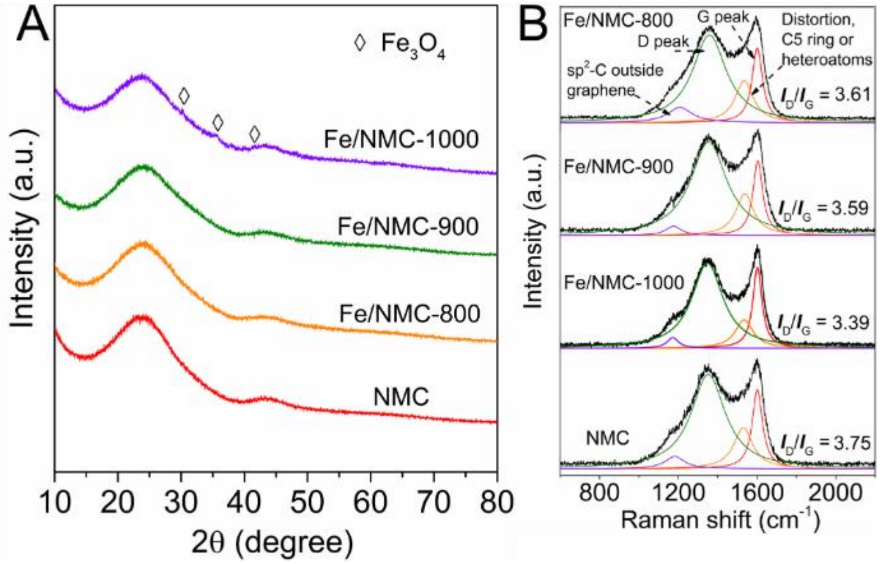

Figure 2. (A) XRD pattern and (B) Raman spectra of as-prepared catalyst.

Raman measurement is then carried out to get details on carbon structure. As shown in Figure 2B and Table 1, the spectra of all samples are well deconvoluted into four components, where the peaks located at ca. 1350 and 1600 cm^{-1} can be attributed to D band related to structural disorder or defect and G band associated with in-plane tangential stretching vibration mode (E2g) of the graphite sheet [356]. The graphitization degree determined by I_D/I_G is calculated to be 3.75, 3.61, 3.59, 3.39 for NMC, Fe/NMC-800, Fe/NMC-900, Fe/NMC-1000, respectively. This result indicates the increased pyrolysis temperature leads to higher graphitization degree. Generally, higher graphitization degree implies better conductivity which is beneficial for the enhancement of ORR. Besides, the additional peak at ca. 1530 cm^{-1} for Fe-containing samples, a characteristic peak assigned to five-member or heteroatoms in graphene-sheet structure [198], gradually decreases in portion as the pyrolysis temperature increases. This result indirectly implies the higher pyrolysis temperature is detrimental for the N doping of final materials.

Table 1 Raman fitting results for all samples

Sample	Deconvoluted results [a] (Area. %)					
	Sp^2 carbon Outside	D peak	Distortion C5 ring Heteroatom	G peak	[b] I_D/I_G	[c] L_a (nm)
NMC	4.78	62.79	15.68	16.75	3.75	5.12
Fe/NMC-800	7.69	59.81	15.94	16.56	3.61	5.32
Fe/NMC-900	2.93	64.00	15.24	17.82	3.59	5.48
Fe/NMC-1000	3.13	64.93	12.79	19.15	3.39	5.67

[a] fitting by Lorentz method, [b] determined by the area ratio between D peak and G peak, [c] calculated by the general equation proposed by Cançado et al [339]: L_a (nm) = $(2.4\times10^{-10})\ \lambda^4\ (I_D/I_G)^{-1}$, where λ is referred to wave length of laser (532 nm).

The XPS spectra is further conducted to obtain more elemental composition and N doping details. No obvious Fe signal is visible due to the low Fe loadings. The Fe loading amount are determined to be 0.43 wt. %, 0.52 wt. %, and 1.42 wt.% for Fe/NMC-800, Fe/NMC-900, Fe/NMC-1000, respectively, based on ICP-AMS measurement. As show in Table 2, it is found that the carbon content gradually increases as the pyrolysis temperature increases, which confirms the improved graphitization degree induced by high temperature as consistent with Raman analysis. Accordingly, N-doped contents show pronounced decrease, from 8.56 at. % for Fe/NMC-800 to 6.26 at. % for Fe/NMC-900, finally decreasing to only 2.86 at. % for Fe/NMC-1000. This indicates the heat treatment at higher temperature leads to the loss of N content.

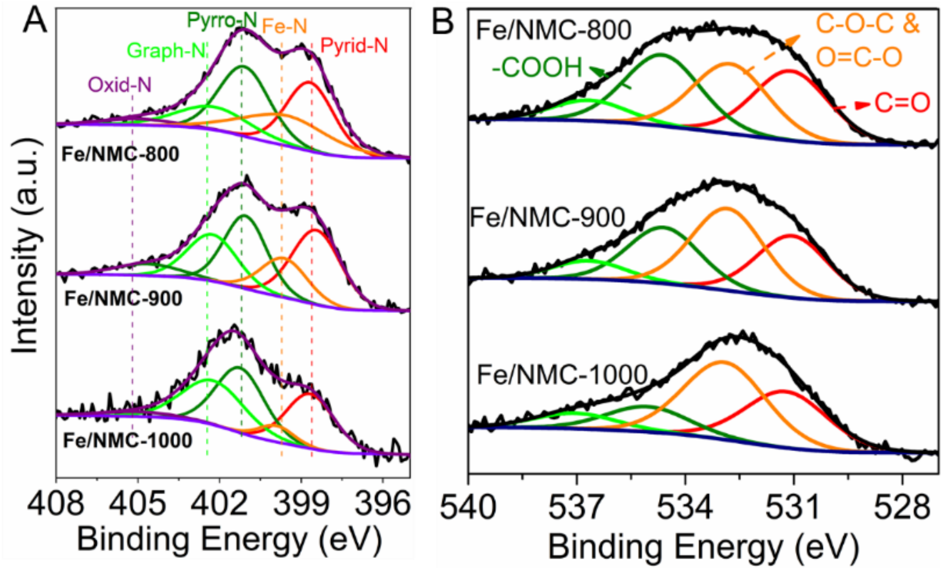

Figure 3. (A) High resolution spectra of N1s core level and O1s (B) for Fe/NMC-800, Fe/NMC-900, Fe/NMC-1000.

Table 2. Relative elementary content of samples on the basis of XPS analysis.

Sample	XPS element analysis (at. %)		
	C	N	O
NMC	89.61	6.58	3.81
Fe/NMC-800	85.86	8.58	5.55
Fe/NMC-900	89.14	6.26	4.60
Fe/NMC-1000	93.17	2.86	4.00

The high resolution N1s spectra for Fe-contained samples can be deconvoluted into five components (Figure 3A). The peak at ca.398.5, 401.2, 402.6, 405.2 eV are assigned to pyridinic N, pyrrolic N, graphitic N and oxidized N respectively while the peak at 399.7 eV can be conventionally attributed to Fe-N moieties [200]. The relative content of such five species is present in Table 3 on the base of deconvolution fitting results. The relative content of pyridinic N remains negligible change while the graphitic N shows significantly increase as the pyrolysis temperature increase. It is reasonable that graphitic N possesses higher thermal stability as comparison to that of edge-located pyridinic- and pyrrolic- N species and thus graphitic N is typically predominant on higher pyrolysis temperature. Notably, the Fe-N content undergoes a gradually decrease as the pyrolysis temperature increases, which is believed to exert an important influence on ORR activity. On the other hand, an appreciable decrease in overall O content has also been observed ranging from 5.55 at. %, 4.6 at. % to 4.0 at. % for Fe/NMC-800, Fe/NMC-900, Fe/NMC-1000, respectively.

Table 3. XPS fitting results of N1s spectra. (The values shown in the brackets refer to the absolute values of N species determined by the production of overall N content and relative content of N specie on each sample)

Sample	Content of N species (at. %), XPS				
	Pyridinic N	Pyrrolic N	Fe-N	Graphitic N	Oxidized N
NMC	40.64(2.67)	38.75(2.55)	0	18.18(1.20)	2.43(0.16)
Fe/NMC-800	28.34(2.43)	30.42(2.61)	22.89(1.96)	14.62(1.25)	3.73(0.32)
Fe/NMC-900	31.28(1.96)	26.68(1.67)	15.58(0.98)	19.95(1.25)	6.50(0.41)
Fe/NMC-1000	27.85(0.79)	33.03(0.93)	6.11(0.17)	29.25(0.83)	3.76(0.11)

The deconvoluted results of O1s high resolution spectra (Figure 3B) are assigned to four components, namely ketonic groups (-C=O, 531.1 eV), ether groups and/or lactone, anhydride (C-O-C, 532.8 eV), carboxylic groups (-COOH, 534.6 eV), and satellite structure of the spectrum or adsorbed oxygen-containing molecules (H_2O/O_2, 536.6 eV) [357, 358]. It is worth noting that the relative content of -COOH subjected to distinctly decrease as increase of pyrolysis temperature, as a result of low thermally stability respect to those of ketonic groups or ether groups [357]. The further analysis of effect of oxygen species on ORR activity is discussed in the following parts.

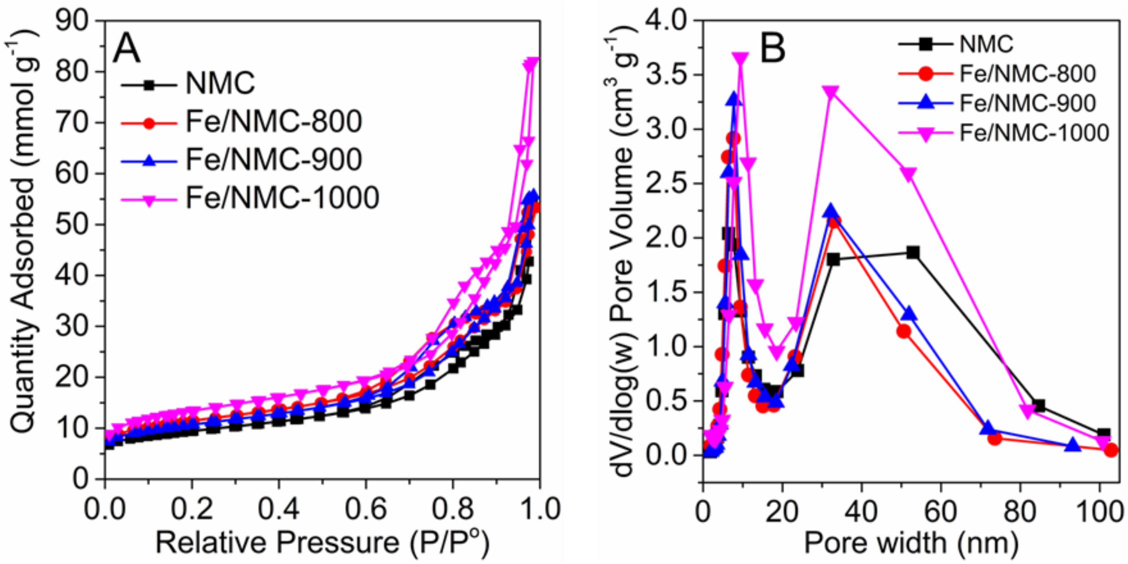

Figure 4. (A) N_2 adsorption/desorption isotherm plots for as-prepared catalysts recorded at 77 K; and (B) respective pore size distribution curves using desorption branch of isotherms for all samples (BJH method, the data recorded with a pore width from 1.7 nm to 100 nm).

The texture properties of all as-samples are further revealed using N_2 isotherms. As Figure 4A shows, the curves show type IV isotherms with pronounced type H3 hysteresis loop, a typically characteristic of mesopore structure [359]. The corresponding structural parameter is summarized in Table 4. The specific surface area (SSA) values are 725, 886, 829, 1041 m^2 g^{-1} for NMC, Fe/NMC-800, Fe/NMC-900, Fe/NMC-1000, respectively, with mesopore pore being mainly contributor of SSA. Pore size distribution (Figure 4B) exhibits that all samples feature two-modal mesopore, with small pore region located at ca. 7 to 10 nm, a characteristic pore arising from silica template removal. Another large pore region is derived from gas-expansion effect. (NH_3, CO_2, HCl etc.). Moreover, the average pore size gradually increases as pyrolysis temperature increases. Such hierarchical pore structure composed of micropore (not shown in N_2 isotherms), interconnected bimodal mesopore and macropore (shown in PSD with size of lager than 50 nm) is known to favor the electrochemically accessibility into active sites [323], thus enhancement of electrocatalytic ORR performance.

Table 4. Texture property of as-prepared catalysts.

Sample	SSA[a] (m^2/g)	S_{micro}[b] (m^2/g)	$S_{external}$ (m^2/g)	V[c] (cm^3/g)	V_{micro} (cm^3/g)	PSD[d] (nm)
NMC	725.36	236.04	492.86	1.361	0.112	13.35
Fe/NMC-800	885.67	273.82	611.85	1.548	0.131	10.67
Fe/NMC-900	829.18	250.07	579.11	1.603	0.118	11.62
Fe/NMC-1000	1040.99	288.92	752.07	2.146	0.136	14.47

[a] Brunauer-Emmett-Teller (BET) specific surface area (SSA) measured at T = 77 K. [b] Determined by t-plot method. [c] Total pore volume determined using the adsorption branch of N_2 isotherm at $P/P_0 = 0.98$. [d] Determined by BJH desorption average pore width (4V/A).

2.2 Electrochemical performance of as-prepared catalysts

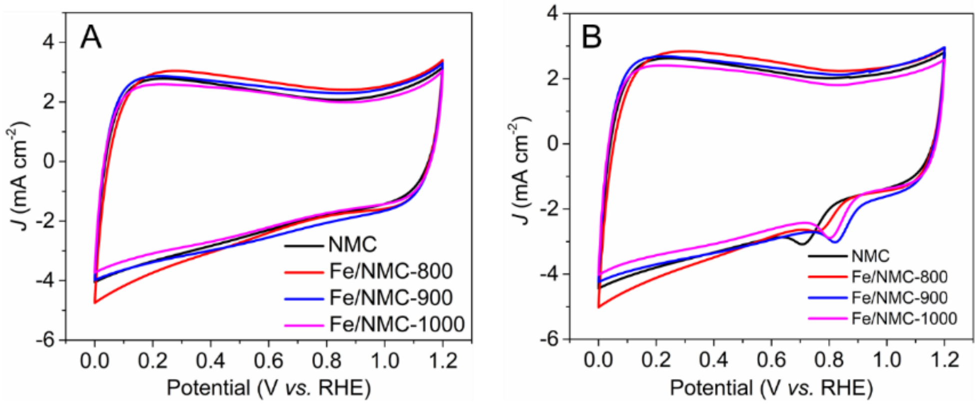

Figure 5. (A) Cyclic voltammetry of as-prepared catalyst under N_2-saturated and O_2-saturated (B) 0.1 M KOH solution at scan rate of 50 mV s^{-1}.

The electrochemical oxygen reduction activities of various catalysts prepared at different pyrolysis temperature is firstly evaluated at 0.1 M KOH. Figure 5 presents the cyclic voltammetry (CV) curves recorded at N_2 and O_2 saturated 0.1 M KOH electrolyte. In N_2 saturated electrolyte, all samples exhibit similar quasi-rectangular pattern, demonstrating negligible faradic process occurs on the electrode surface with charging/discharging process of double layer current being predominant. The area of rectangle gradually decreases as following order: Fe/NMC-800 > Fe/NMC-900 = NMC > Fe/NMC-1000, indicating Fe/NMC-800 possesses highest electrochemical active surface area. In O_2-saturated electrolyte, well-defined O_2 reduction peaks are observed in all samples. Previous studies [89, 190] have pointed out that the peak is closely linked to Fe^{3+}-OH/Fe^{2+} redox transition, and the more positive the potential is, the better the electrochemical performance is. Clearly, the Fe/NMC-900 shows the most positive oxygen reduction potential, implying that the most superior electrochemical performance is obtained among all samples.

Table 5. ORR performance and respective electrochemical parameters in O_2-saturated 0.1 M KOH solution.

Entry	Catalyst	E_{on} ^{a} (V)	$E_{1/2}$ ^{b} (V)	J_L ^{c} (mA cm^{-2})	Tafel slope (mV dec^{-1})	J_k ^{d} (mA cm^{-2})
1	NMC	0.87	0.77	4.09	62	0.20
2	Fe/NMC-800	0.91	0.82	4.68	57	1.53
3	Fe/NMC-900	0.96	0.86	5.28	54	9.36
4	Fe/NMC-1000	0.944	0.85	5.68	54	6.68
5	Pt/C	0.97	0.85	5.44	68	25.98

[a] Onset and [b] half-wave potential values reported *vs*. RHE, [c] limited diffusion current density, [d] Kinetic current density calculated from K-L equation at 0.80 V *vs*. RHE.

RRDE measurement are next carried out to evaluate the ORR activity for samples obtained in different pyrolysis temperature. Detailed electrochemical parameters have been summarized in

Table 5. The metal-free sample exhibits an ORR activity with half-wave potential ($E_{1/2}$) of only 0.77 V along with onset potential (E_{on} of 0.87 V) and limiting diffusion current (J_L of 4 mA cm^{-2}), much lower respect to that of Fe-containing samples, suggesting that the Fe is indispensable for the construction of FeN_x active sites. It is noted that the ORR activity gradually increases with the pyrolysis temperature increases, with optimal performance being obtained for Fe/NMC-900 (Figure 6A). The high $E_{1/2}$ of 0.86 V even outperforms that of commercial Pt/C (0.85 V), showing the potential commercial availability in the fuel cell application.

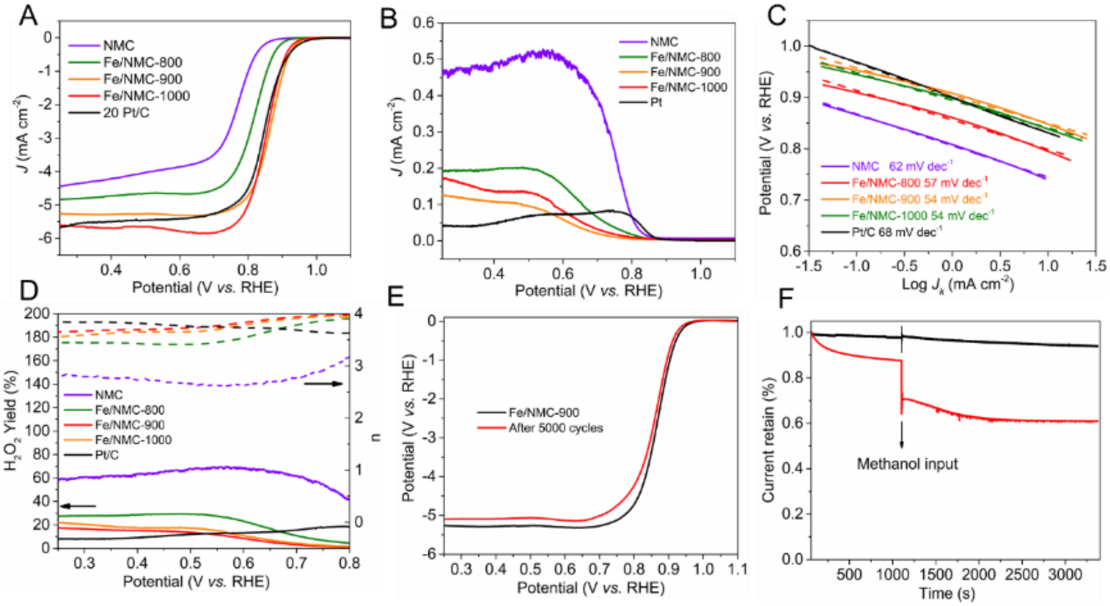

Figure 6. (A) LSVs curves of disk current for all as-prepared catalysts recorded at O_2 saturated 0.1 M KOH at rotation speed of 1600 rpm, along with commercial Pt/C catalysts at comparison, and (B) respective ring current curves, the ring potential is fixed at 1.2 V vs. RHE; (C) The Tafel slope for all as-prepared catalysts; (D) H_2O_2 yield and exchanged electron transfer number of all samples; (E) Durability test for sample Fe/NMC-900 and (F) Methanol tolerance test for Fe/NMC-900 and Pt/C.

It is worth noting that H_2O_2 generation for Fe-containing samples occurs at much lower potential range than corresponding onset potential of ORR, which differs from the case in the commercial Pt/C that (see ring current curves in Figure 6B). This observation suggests different ORR mechanism between Fe-containing samples and Pt/C. Briefly, the ORR process on Fe-containing samples initialized on single Fe center of Fe-N_x moieties by reaction as following: N_x-Fe^{3+}-OH + e^- - N_x-Fe^{2+} + OH^-, which leads to a direct O_2 adsorption on Fe^{2+} center within inner Helmholtz plane (IHP) to favor inner sphere electron transfer process (ISET) [93]. In sharp contrast, the ORR starts on Pt/C is dominated by out-sphere electron transfer (OSET) (or parallel inner and outer sphere electron transfer mechanism) process in alkaline media due to the block effect of Pt surface by oxide species in high potential range, the oxide species on the surface of Pt serves as bridge for electron transfer from electrode surface to solvated O_2 for the generation of H_2O_2. The all samples show similar Tafel slope (Figure 6C) and are found to fall within the range of 54 - 68 mV dec^{-1}, indicating the first electron transfer is rate-determining step (RSD) for all samples. The H_2O_2 yield and electron transfer number for all investigated samples are present in Figure 6D. For metal-free NMC sample, a high H_2O_2 yield (as high as 70 % at maximum) is found. And the average electron transfer number is 2.6, implying a predominant two-electron pathway with H_2O_2 as mainly products. With the same pyrolysis temperature, the introduction of Fe significantly alters the reaction pathway which enables change from two-electron to four-electron (approximately 10 % H_2O_2 yield and almost completely four-electron pathway for Fe/NMC-900). This result further verifies the ORR process on single FeN_x center prefers to direct $4e^-$ pathway or indirect 2 * 2 e^- pathway with H_2O as main products. The H_2O_2 yield on Fe-containing samples shows similar trend to that in the LSVs curves. The H_2O_2 yield of Fe/NMC-900 decreases significantly respect to that of Fe/NMC-800, further increasing pyrolysis temperature contrarily results in increase of H_2O_2

yield. Therefore, a proper pyrolysis temperature is also of paramount importance for the optimization of electrode materials. To evaluate durability of Fe/NMC-900, cyclic voltammetry in O_2-saturated atmosphere at a potential range of 0.6 - 1 V with rotation speed of 1600 rpm is carried out. After continuous 5000 recycles, the electrocatalytic performance exhibits negligible change with a slight decrease of limiting current density, demonstrating Fe/NMC-900 possesses excellent stability in alkaline media. An additional methanol poison trail is further conducted to ensure the practical availability in anti-crossover effect fuel cell. As shown in Figure 6F, the current significantly decreases once adding methanol on commercial Pt/C. In contrast, nearly no current change is observed for sample Fe/NMC-900, suggesting its superior methanol-resistance property.

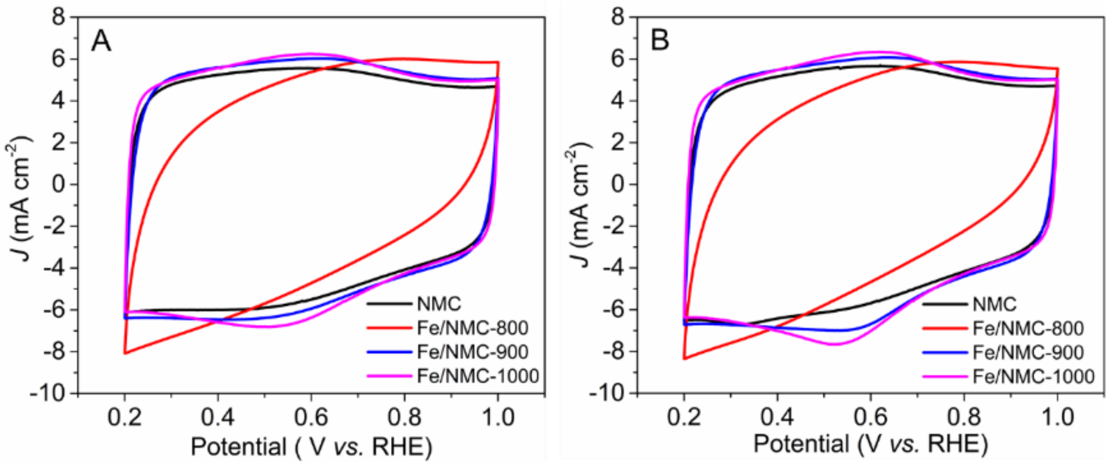

Figure 7. Cyclic voltammetry of as-prepared under N_2-saturated (A) and O_2-saturated (B) 0.5 M H_2SO_4 solution at scan rate of 50 mV s^{-1}.

Further assessment of electrocatalytic O_2 reduction in acidic electrolyte (0.5 M H_2SO_4) is also carried out for all catalysts. Cyclic voltammetry behaviors in N_2 and O_2 atmosphere are firstly analyzed for all as-prepared samples (Figure 7). At odds with electrochemical behavior under N_2 displayed in basic electrolyte, the CV curves exhibit well-defined redox peaks with two broad peaks, the cathodic peak is in the potential range of 0.8 - 0.3 V and another anodic peak is located in the range of 0.4 - 0.8 V for NMC, Fe/NMC-900, Fe/NMC-1000. The reversible redox peaks at almost the same peak position for these three samples are acknowledge to result from the oxidation/reduction of hydroquinone-/quinone-like groups on the carbon surface [104, 360]. Under O_2 atmosphere, the distinct O_2 reduction peaks occur at slightly more positive potential respect to that observed at N_2 atmosphere for Fe/NMC-900 and Fe/NMC-1000 while the reduction peak is suppressed for Fe-free NMC sample, which is associated with Fe^{3+}-OH/Fe^{2+} redox transition, similar to CV behavior found in basic media. Of note is that the less pronounced redox peaks are found on Fe/NMC-800 in both N_2 and O_2 atmosphere, which is correlated with surface properties of carbon surface (the enriched surface functional groups).

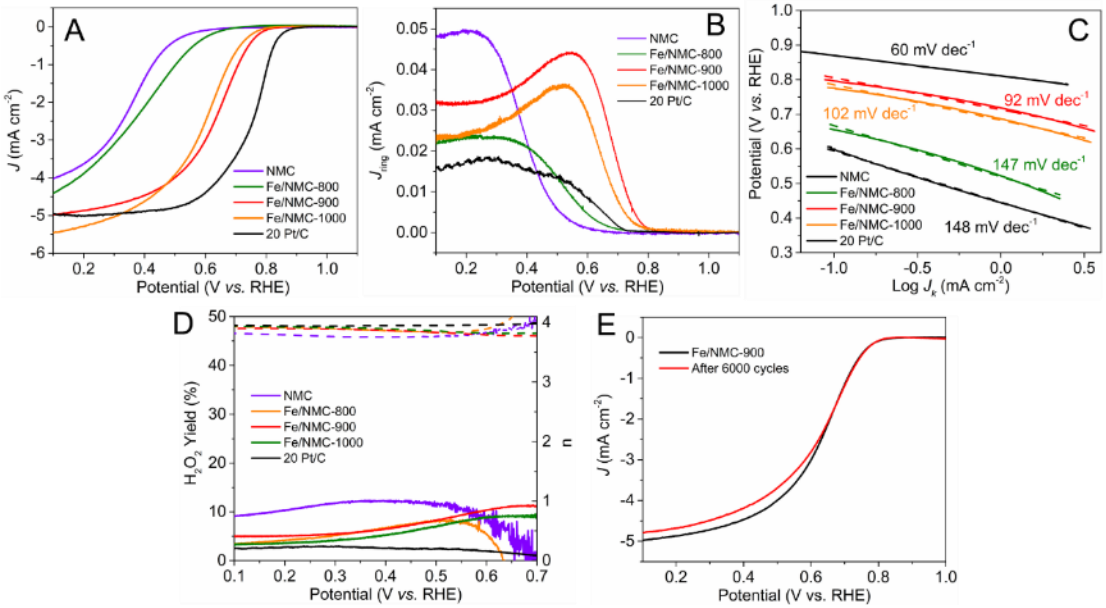

Figure 8. (A) LSVs curves of as-prepared along with commercial Pt/C catalyst at comparison recorded at O_2-saturated 0.5 M H_2SO_4 solution at a scan rate of 10 mV s^{-1} with rotation speed of 1600 rpm; (B) Respective ring current density curves; (C) Tafel slope extracted by LSVs curves in the disk electrode; (D) H_2O_2 yield and electron transfer number derived from RRDE measurement; (E) The durability test for Fe/NMC-900.

The RRDE measurement of as-prepared samples along with commercial Pt/C catalyst are then conducted in O_2-saturated 0.5 M H_2SO_4 solution to evaluate the ORR activity and corresponding electrochemical parameters are present in the Table 6. As Figure 8A, the dependence on pyrolysis temperature is also found. As expected, the ORR activity for all samples on acidic media is much less than that of alkaline media. The Fe-free sample shows negligible ORR activity with an onset potential (E_{on}) of 0.6 V and limited half potential ($E_{1/2}$) of 0.39 V. Once Fe introduced, the ORR activity shows a visible improvement. Noteworthy, the Fe/NMC-800 exhibits a limited enhancement of ORR activity respect to NMC, the increased pyrolysis temperature results in dramatically increase in ORR activity. The optimal catalyst (Fe/NMC-900) shows a decent E_{on} of 0.80 V and $E_{1/2}$ of 0.63 V, although lower than that of commercial Pt/C with loading of 40 μg Pt cm^{-2}. Further increase of pyrolysis temperature results in a slight decrease of ORR activity. As Figure 8B presents, the potential of H_2O_2 generation for Fe-containing samples is the same with onset potential of oxygen reduction. The observation suggests the reaction mechanism for these materials prefers to follow 2 * 2 e^- pathway with successive generation and reduction of H_2O_2 on Fe-N moieties in acidic media. Meanwhile, this result further reveals the instable binding of generated H_2O_2 on Fe^{2+} active sites thus giving rise to desorption and/or decomposition of H_2O_2 intermediates into bulk electrolyte [93]. On contrary, the generation of H_2O_2 on Pt/C occurs at much lower potential range, demonstrating a dominant inner-sphere electron transfer mechanism in acidic media. Tafel slopes (Figure 8C) are determined to be 92, 102, 147, 148 mV dec^{-1} for Fe/NMC-900, Fe/NMC-1000, Fe/NMC-800, NMC, respectively. This finding demonstrates the first electron transfer is rate-determining step as following reaction: $Fe^{2+}\text{-}OH_2 + O_2 + e^- \rightarrow Fe^{2+} - O_2^- + H_2O$ [89]. The quantitatively of H_2O_2 yield and electron transfer number (Figure 8D) shows that all samples present almost complete four-electron reaction with similar H_2O_2 yield of lower than 10 % over a wide potential range except for NMC sample (ca. 13 % yield of H_2O_2). Further durability test shown in Figure 8E present an excellent stability with the same onset potential and kinetic-diffusion region besides the slight decrease of limiting current density at harsh acidic media for Fe/NMC-900 after 6000 recycles.

Table 6. ORR performance and respective electrochemical parameters in O_2-saturated 0.5 M H_2SO_4 solution.

Entry	Catalyst	E_{on} ^{a} (V)	$E_{1/2}$ ^{b} (V)	J_L ^{c} (mA cm^{-2})	Tafel slope (mV dec^{-1})	J_k ^{d} (mA cm^{-2})
1	NMC	0.60	0.39	4.01	148	0.013
2	Fe/NMC-800	0.65	0.61	4.40	147	0.024
3	Fe/NMC-900	0.80	0.63	4.98	92	0.088
4	Fe/NMC-1000	0.78	0.59	5.46	102	0.031
5	Pt/C	0.87	0.76	5.0	60	1.51

^{a} Onset and ^{b} half-wave potential values reported *vs*. RHE, ^{c} limited diffusion current density, ^{d} Kinetic current density calculated from K-L equation at 0.80 V *vs*. RHE.

2.3 Discussion of activity dependence on pyrolysis temperature.

To reveal the origin of ORR activity trend on samples prepared by different pyrolysis temperature. The correlations between structure and performance are established (The ORR activity obtained at alkaline media is taken as a sample for comparison due to the same ORR activity trend in both acidic and alkaline medium). In general, a large specific surface area (SSA) particularly micropore-prevailing carbon materials is known to host higher number of FeN_xC_y moieties thus positively contributing to enhanced ORR activity. However, no pronounced correlation is observed between ORR activity (in terms of $E_{1/2}$) and total surface area as well as micropore surface area (Figure 9), illustrating that the specific surface area is not main decisive factor for the ORR activity. In other words, the high SSA is sufficient to host all available FeN_x

moieties into carbon matrix, and adverse effect especially for Fe/NMC-800 resulted from diffusion limitation is not true in this case due to developed hierarchical porous structure.

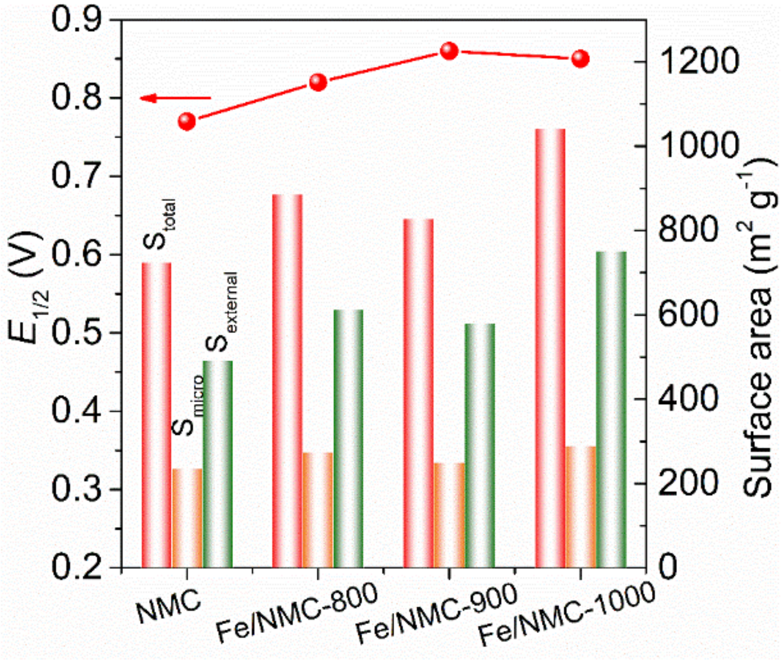

Figure 9. The correlation between texture property and ORR activity in alkaline media.

It is well acknowledged that the π-electron delocalization of carbon basal plane exerts a significant effect on d-orbital charge density of Fe center on FeN_x, which thus affects the ORR activity due to different binding energy between O species and Fe atom. The degree of π-electron delocalization of carbon plane can be described quantitatively by C 1s full-width at half maxima (FWHM). A narrow FWHM of C1s indicates a higher degree of π-electron delocalization and stronger electron-donating capacity, and *vice versa* [95]. The C1s spectrums for three samples showing in Figure 10 are deconvoluted into three components, the peaks located at 284.7, 285.9, 289.0 eV are assigned to be graphitic carbon, C bonded to heteroatoms, and a high energy satellite plasmon peak [95]. A gradually decrease of C-heteroatoms content as the increase of pyrolysis temperature are observed, indicating the loss of heteroatoms induced by high temperature pyrolysis. This result is well agreement with conclusion in previous elemental composition analysis of XPS. However, it is noted that FWHM values of graphitic carbon remain negligible change as the increase of pyrolysis temperature. Consequently, in combination with similar size of carbon crystallite (L_c and L_a, see Table 1 and 7), the activity differences of samples derived from change of π-electron delocalization are thus ruled out.

Table 7. The *d*-spacing and L_c value obtained by XRD pattern.

Sample	*d*-spacing	L_c
NMC	3.71	10
Fe/NMC-800	3.71	10
Fe/NMC-900	3.72	9
Fe/NMC-1000	3.73	9

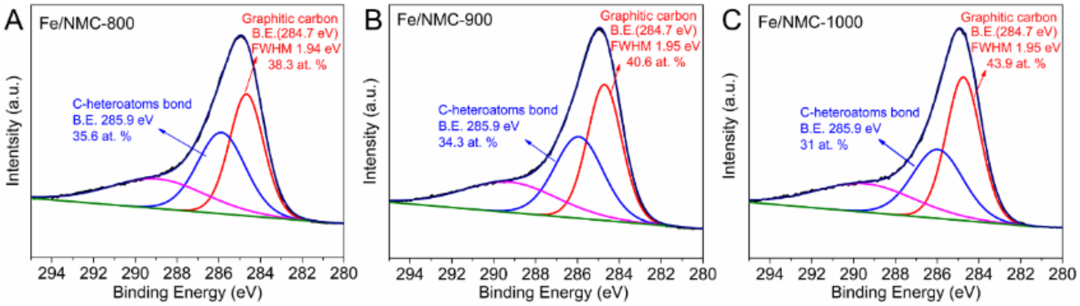

Figure 10 The high resolution C1s spectra for samples prepared at 800 °C (A), 900 °C (B), 1000 °C (C).

The ORR activity in terms of $E_{1/2}$ is then plotted as a function of N doping. As shown in Figure 11A, the Fe/NMC-900 exhibits the highest ORR activity with moderate overall N content and FeN_x relative moieties. Further increasing the pyrolysis temperature leads to a significant drop of overall N content as well as FeN_x relative content. The loss N content probably results in number of insufficient active FeN_x sites or change of nature of FeN_x active sites [361], which in turn decreases the ORR activity. However, it is surprised that the Fe/NMC-800 exhibits the worst ORR activity, although possessing both of the highest overall N doping content and Fe-N_x relative contents. Hence, we come to conclusion that the low ORR activity of Fe/NMC-800 is not dictated by the number of active FeN_x moieties, but the intrinsic ORR activity (Turnover frequency in single Fe sites). Preceding analysis has shown that the π-electron delocalization of various catalysts prepared by different pyrolysis temperature has a negligible effect on ORR activity. In fact, the nature of O doping significantly affects the electronic structure of atomic Fe center in FeN_x moieties. Ni' et al [318] emphasized the critical role of carbonyl group next to FeN_4 moieties on the enhanced ORR activity, which was mainly ascribed to the reduced formation barrier of *OOH and facilitation in reduction of *OH intermediates. However, for most cases, the higher O content is detrimental for ORR by four-electron pathway (prefer to two-electron pathway with H_2O_2 production), which is generally attributed too weak binding force between O-contained intermediates and electron-poor Fe atom center induced by excess of O-bearing groups in the carbon matrix [362, 363]. To reveal electron effect of O species on Fe center of FeN_x moieties, the correlation between O composition and ORR activity is established (Figure 11B). It is worth note that the content of O specie is retained at large extent in relative low pyrolysis temperature especially for carboxyl group with low thermal stability. The carboxyl groups are subjected to a significantly decrease as pyrolysis temperature increases, which in turn leads to a gradually improvement of ORR activity. Given the electron withdrawing characters of carboxyl groups, it can be rationalized that much more positive charge state in single atom Fe center diminishes the interaction between the O species and Fe center. The too weak binding of O species on Fe center makes the first adsorption step of O_2 difficult, thus resulting in low onset potential and activity of Fe/NMC-800. Indeed, the specific shape of CV curve with high polarization and irreversible redox peaks feature for Fe/NMC-800 in N_2-saturated acidic media (see Figure 7A) is additional hint for the enriched electron of surface property, which imparts adverse effect on ORR activity. On the other hand, the higher graphitization degree and conductivity are usually found at higher temperature which is beneficial for the enhanced electrocatalytic activity due to improved electron transport. Thus, the inferior electrocatalytic performance of FeNMC-800 respect to those observed in Fe/NMC-900 and Fe/NMC-1000 is partially attributed to the poor conductively arising from high heteroatom dopants. Taken together, an appropriate trend-off between N-doped level (FeN_x moiety) and graphitization degree (electron conductivity) as well as proper O-doped level (electron effect on FeN_x moiety) should be paid more attention for the optimization of ORR activity.

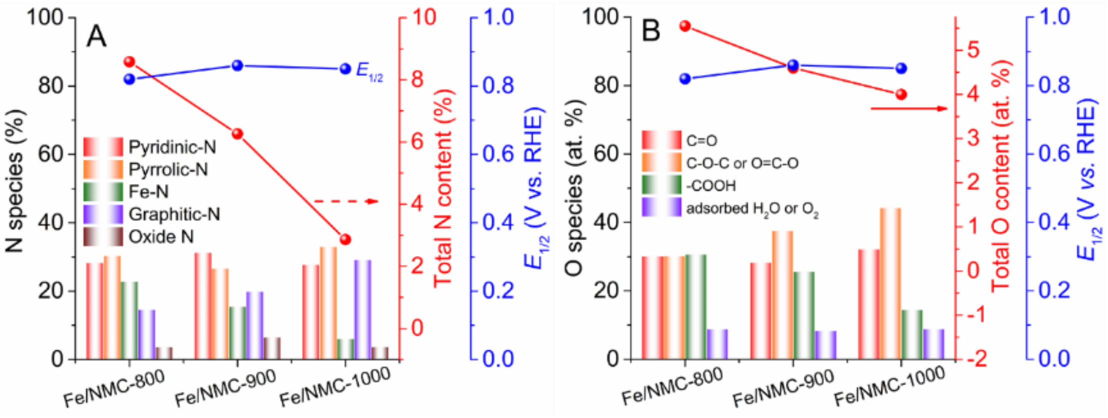

Figure 11 (A) Correlation between nitrogen composition and ORR activity; (B) correlation between oxygen composition and ORR activity.

3. Conclusion

In this work, an active and durable single atom Fe catalyst toward ORR over both alkaline and acid media is developed based on pyrolysis approach using silica as hard template, glucose as carbon source, NH_4Cl as nitrogen source, and $FeCl_3$ as metal precursor. The ORR activity is found to be greatly dependent of pyrolysis temperature, with 900 ^{o}C being the optimal temperature. The obtained optimal catalyst Fe/NMC-900 exhibits an excellent ORR activity ($E_{1/2}$ = 0.86 V) and durability as well as methanol tolerance which outperforms the commercial Pt/C catalyst in alkaline media. In acidic media, the Fe/NMC-900 shows also decent ORR activity with $E_{1/2}$ of 0.63 V and good stability, although inferior than those of Pt/C. No direct correlation between ORR activity and total specific surface area and micropore surface area as a function of pyrolysis temperature is found because the sufficient surface area for host almost all Fe active sites. Further analysis discloses that both overall nitrogen and oxygen content undergo significantly decrease as increasing of pyrolysis temperature. Too high pyrolysis temperature (1000 ^{o}C) leads to the aggregation of Fe atoms and generation of Fe-based nanoparticle, as well as dramatic decrease of N content, which avoidably deteriorate ORR activity due to lower density of FeN_x active sites. On the other hand, although N-content and active FeN_x moieties are retained at largest extent under a relative low pyrolysis temperature (800 ^{o}C), the ORR activity is still limited by low electron conductivity and the highest oxygen content. The high oxygen content especially for carboxylic groups with electron-withdrawing property is detrimental for ORR activity due to the too weak binding force between single Fe atom center and O intermediates during ORR arising from decreased electron-density of Fe center. An improved pyrolysis temperature (900 ^{o}C) decreases the overall N content and FeN_x moieties, but intrinsic activity of FeN_x moiety is significantly enhanced due to optimized electron structure of Fe center associated with decreased amount of oxygen groups. In combination of higher graphitization degree, the Fe/NMC-900 exhibits highest ORR activity. This work emphasizes the importance on the trend-off between the number of FeN_x active sites and intrinsic activity of FeN_x site as well as conductivity of materials and it also affords an extra way for the fundamental insights into temperature dependent ORR activity.

Chapter 6.

Fe_3O_4/Fe_3C nanoparticles coupled with single Fe atoms on hierarchical porous graphene-like carbon nanosheet/carbon black hybrid

Abstract

The synthesis of Fe-N-C catalyst, for oxygen reduction process, showing comparable and even better performance with respect to Pt-based catalyst via simple and high-efficient strategy is still a challenge for the next-generation clean and sustainable energy technologies like fuel cell and metal-air batteries. This chapter describes a straightforward and easy-scale-up methodology for the fabrication of Fe, N co-doped graphene-like carbon nanosheet/carbon black hybrid featuring Fe_3C/Fe_3O_4 nanoparticles wrapped by graphitic carbon layer. The catalysts were prepared via one-step thermal pyrolysis, starting from incipient wet impregnation of Fe salt aqueous solution of a mixture of cost-effective raw components. Such a heterostructure allows synchronous construction of open porous network and high density exposure of single FeN_x active sites, leading to an enhanced electrocatalytic ORR performance, outperforming the benchmarked Pt/C catalyst. Importantly, in-depth investigation on hybrid material have unambiguously unraveled that FeN_x moieties are real active sites for ORR and less acid-resistant Fe_3O_4 itself does not serve as active site but exert promotion effect on activity of FeN_x site. This work not only clarifies the origin of high catalytic performance of Fe-N-C catalysts, but also affords a simple and large-scale synthetic strategy toward high performance ORR catalyst.

1. Introduction

Addressing the concerns related to massive depletion of fossil fuels and increasing environmental and climate changes are becoming urgent priority of modern chemistry. The next generation of energy conversion devices, such as fuel cells have been receiving a great mark of interest as a part of clean and renewable energy systems, which represent a viably scheme for tackling the upcoming energy crisis due to its compelling merits of zero-carbon emissions along with high energy conversion efficiency [25, 364]. The high cost and scarcity of platinum group metal-based (PGM) electrocatalyst at the cathode to be applied for driving oxygen reduction reaction (ORR) with sluggish kinetic have been considered as a heart issue to be reckoned with [117]. Therefore, the exploitation employing non-critical components like cost-effective PGM-free catalyst with improved catalytic performance and high robustness is highly expected but remains quite challenging research topic.

The recent years have witnessed a real boom in the development of innovation synthetic strategy for the preparation of PGM-free electrocatalyst. A variety of novel PGM-free catalyst have been explored, including heteroatom-doped nanocarbons [365, 366], metal oxides [367, 368], and metal coordinated with N doped carbon materials (M-N-C, M = Fe, Co, Mn etc.) [37, 369]. Specifically, the atomically dispersed Fe-N-C catalysts have recently been extensively investigated due to its excellent ORR activity comparable to or even better than commercial Pt/C catalyst. Numerous efforts have been devoted to improving electrocatalytic intrinsic activity of single atom Fe-N-C catalytic by optimization of geometric and electronic structure as well as Fe coordination chemical state [89, 317, 370]. On the other hand, a structural design with higher density of exposed active sites ensuring the reactants/electrolyte availability provides an access for the improvement of ORR activity. A carbon scaffold (*e.g.* carbon black) not only provides high population of single atom Fe active sites arising from large surface but also afford a soft self-template to avoid the aggregation of Fe atoms during high temperature pyrolysis. The carbon black has been widely employed especially on preliminary exploration as support of metal macrocycle compounds [371-373].

Recently, graphene or graphene-like two-dimensional carbon nanosheet has emerged as a new-generation carbon carrier because of its outstanding electrical conductivity, high surface area, and excellent chemical stability. More importantly, the flexible surface chemical structure can be readily regulated by introduction of light-heteroatoms (nitrogen, sulfur, boron, etc.) to stabilize metal atoms in the form of atomically dispersed dopants [374]. Compared with conventional post-functionalization of as-existed graphene oxides, a “Top-down” strategy on the basis of high temperature pyrolysis is preferentially required for simultaneous construction of graphene framework and active atomically dispersed Fe sites [375]. However, the low carbonization yields particularly derived from small molecular carbon and/or nitrogen source, hinder its fabrication at large-scale production for practical application. On this regard, the preparation of hybrid network composed of cheap carbon black as primary phase and in-situ generated graphene-like material as secondary carbon phase afford a synergistic advantage with both high-production and abundant single atom Fe sites. Moreover, the presence of carbon black phase is thought to play a crucial role for the separation of two-dimension graphene/graphene-like carbon sheets thus enhanced accessibility of electrolyte and O_2 molecule [366, 376]. Indeed, the combination benefit based on N- doped mesopore carbon phase coupling with other flexible substrates toward challenging industrial application have been reported recently by our groups [15, 377-382], which further prompts us to explore a novel hybrid electrocatalyst with high catalytic activity by simple and scalable strategy.

Another key step for further improvement of Fe-N-C catalytic performance is to increase the density of FeN_x active sites, as well they accessibility, within a specific carbon support. Unfortunately, simple increase in the quantity of Fe precursor leads to Fe-based nanoparticles (oxides, carbide) or nanoclusters co-generation along with FeN_x sites. In particular, excessive Fe loading (> 10 wt. %) inevitably leads to the formation of larger size Fe-based nanoparticles coated with carbon layers upon high temperature pyrolysis. Previous studies have demonstrated that metal Fe [310, 311], Fe_3C [315, 383], oxidative FeO_x [313, 384-386] nanoparticles encapsulated into N-doped carbon show high and stable ORR activity. All these works come to the conclusion that the electronic interaction between Fe-based nanoparticle and N-doped carbon layer is mainly responsible for excellent electrocatalytic activity and durability. However, in most cases, the formation of FeN_x sites is not taken into account, it is worth noting that actually single atom Fe coordinated N site is easily formed in concert with Fe-based nanoparticles which underlying contribute to catalytic activity. On the contrary, from high active single atom Fe viewpoint, these less-active Fe-based nanoparticles are typically removed by acid leaching in most works in attempt to achieve exclusive atomically dispersed Fe specie [113, 282]. Noteworthy, recent studies have also revealed that these Fe-based nanoparticles play a crucial role of enhanced ORR activity through synergistically cooperation effect with FeN_x moiety. Wei and co-workers reported the interaction between Fe/Fe_3C nanocrystals and FeN_4 sites favored the adsorption of oxygen molecule, which significantly boosted the activity of $Fe\text{-}N_x$ sites [147]. Yang and co-workers revealed the FeN_x moieties played a critical role for ORR activity and the co-existed Fe_2N nanoparticles could further improve activity of FeN_x by weakening the adsorption of ORR intermediates on active sites [317]. Zhang’s group [342] and Xiang’s group [314] have disclosed that the synergistic effects between the Fe_3O_4 nanoparticles and the atomically dispersed $Fe\text{-}N_x$

resulted in enhanced ORR activity. Contrarily, Li et al. claimed that metallic Fe/Fe_3C promoted ORR activity on FeN_x sites while Fe_3O_4 nanoparticles exerted an adverse effect on FeN_x sites [387]. These disputable results along with multiple active components besides Fe-N_x coordination further complicates the identification of exact activity origin of Fe-N-C electrocatalysts in catalyzing the ORR process. Hence, a viably experimental proof for action mechanism of each component toward ORR is highly desired but still challenging.

Herein, we report a facile and easily-scalable strategy for the preparation of highly active Fe-N-C hybrid catalyst based on one-step thermal pyrolysis starting from cheap and non-toxic raw components. The as-obtained hybrid catalyst exhibits a unique hierarchical structure consisting of carbon black as primary carbon phase and in-situ generated graphene-like carbon nanosheet as secondary carbon phase, along with the generation of highly porous structure. With appropriate amount of Fe precursor addition, the optimal catalyst not only possesses the highest content of single atom FeN_x active sites, which plays a decisive role for the most superior ORR activity amongst all investigated samples, but also generates acid-resistance graphitic onion-like nanocarbon-shells wrapped Fe_3C nanoparticles in concert with less acid-tolerance Fe_3O_4 nanoparticles. Interestingly, in-depth investigation based on a series of control trials have unambiguously shown that the Fe_3O_4 nanocrystals significantly boost the electrocatalytic activity of adjacent FeN_x sites for ORR while themselves show negligible activity. The synergistic effect between FeN_x active sites and Fe_3O_4 nanocrystals is claimed to be responsible for the enhanced ORR activity. As a result, the optimal catalyst ($^{4.5}$Fe@NGC/CB) displays a superior ORR performance with an onset potential of 1.0 V and half-wave potential of 0.87 V along with outstanding durability and methanol tolerance, outperforming the commercial Pt/C catalyst and most reported non-precious catalyst. This present work provides a simple and large-scale materials fabrication strategy using cheap raw components. More importantly, this finding shed light on the activity origin of high-performance Fe-N-C catalyst toward ORR, and affords a new cognition for rational design of high active ORR electrocatalysts.

2. Results and discussions

2.1 The Synthesis of Fe@NGC/CB catalyst

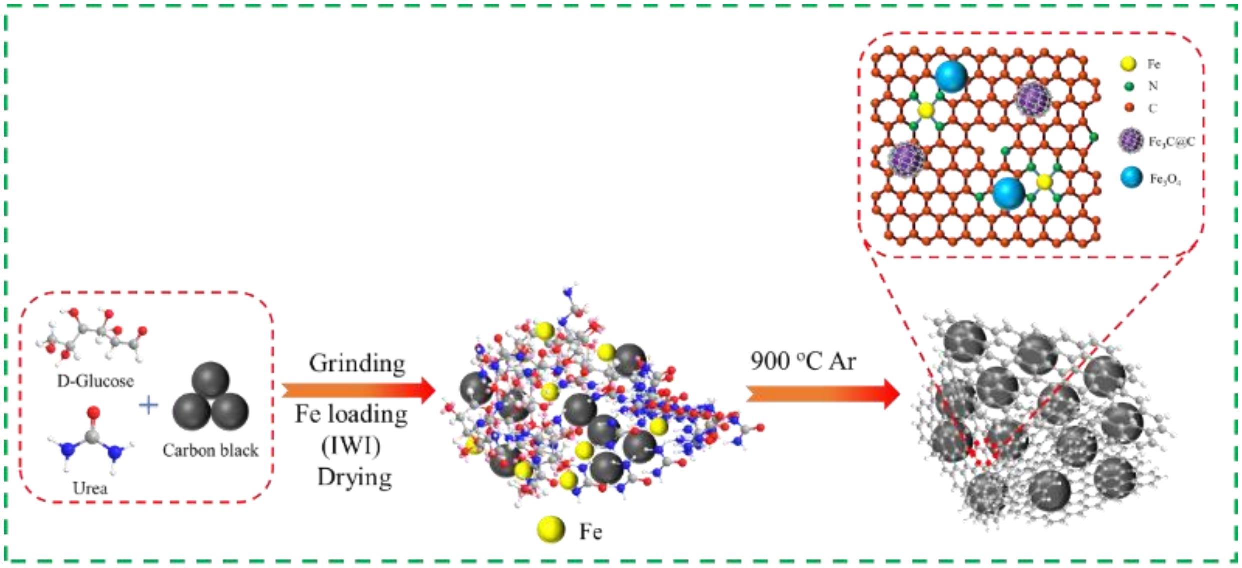

Figure 1. Schematic illustration of fabrication procedure of $^{4.5}$Fe@NGC/CB hybrid electrocatalyst.

Figure 1 illustrates the adopted synthetic methodology of Fe@NGC/CB hybrid. Carbon black (Vulcan XC-72, Cabot) is used as a “standing scaffold” (primary carbon phase) for the accommodation of porous N-doped graphene-like nanosheets (secondary carbon phase) to enable the host of graphitic carbon layer encapsulated Fe_3O_4/Fe_3C along with high densely atomic Fe-N_x nuclei. The physical mixture of three raw components starting from carbon black, D-glucose, urea is firstly subjected to incipient wetness impregnation with control concentration (0, 0.016, 0.08, 0.4 M) of iron chloride precursor solution, hereafter referred to as NGC/CB, $^{1.15}$Fe@NGC/CB,

$^{4.5}$Fe@NGC/CB, $^{16.2}$Fe@NGC/CB, respectively). In contrast to conventional solid phase synthesis from direct physical mixtures of N and C-contained components and Fe precursor powder, the impregnated phase with an aqueous Fe-based solution allows a uniform distribution of metal cations where Fe^{3+} can be firmly bound to deprotonated alcoholic hydroxyl groups in the glucose molecule due to its strong chelating ability [20]. The impregnated samples after dryness are then annealed at 900 ^{o}C under argon atmosphere without any post-treatment (e.g., acid/basic leaching, the second NH_3/N_2 thermal treatment). During annealing process, urea is first thermally polymerized into layered graphitic carbon nitride (g-C_3N_4) at around 550 ^{o}C which then assists the directed formation of two-dimension carbon nanosheet on the carbon black scaffold [388]. Specifically, the in-situ formed layered g-C_3N_4 acts as space-limited self-sacrificial template to confine the patches of aromatic carbon derived from decomposition of glucose-metal complex, while N sites in the g-C_3N_4 is thought to be an ideal nucleation and stabilization sites for Fe atoms. Above 750 ^{o}C, the thermally unstable layered g-C_3N_4 is completely decomposed accompanied with evolution of N-containing gases and graphene-like carbon nanosheet, with defects, is then liberated [389]. Together with NH_3 generated from urea at relatively low temperature range, N-doping and pore structure are created by reaction between N-containing gases and oxygen function group in the glucose/carbon intermediate/carbon black and subsequently substitution of carbon atom at elevated temperature. Simultaneously, the Fe atoms are moved into carbon matrix and then trapped by N- species giving rise to the formation of atomically dispersed FeN_x sites at a relatively high temperature range. Some of Fe atoms are not coordinated to N sites, resulting in the formation of graphitic carbon layer encapsulated Fe-based nanoparticles through thermal-induced carbon diffusion inside/outside crystalline lattice of Fe [147, 390]. Eventually, Fe-based nanoparticles encapsulated by graphitic carbon layer are coupled with FeN_x moieties and supported on porous N-doped graphene-like carbon nanosheet/carbon black hybrid (Fe@NGC/CB).

2.2 Characterization of Fe@NGC/CB catalysts.

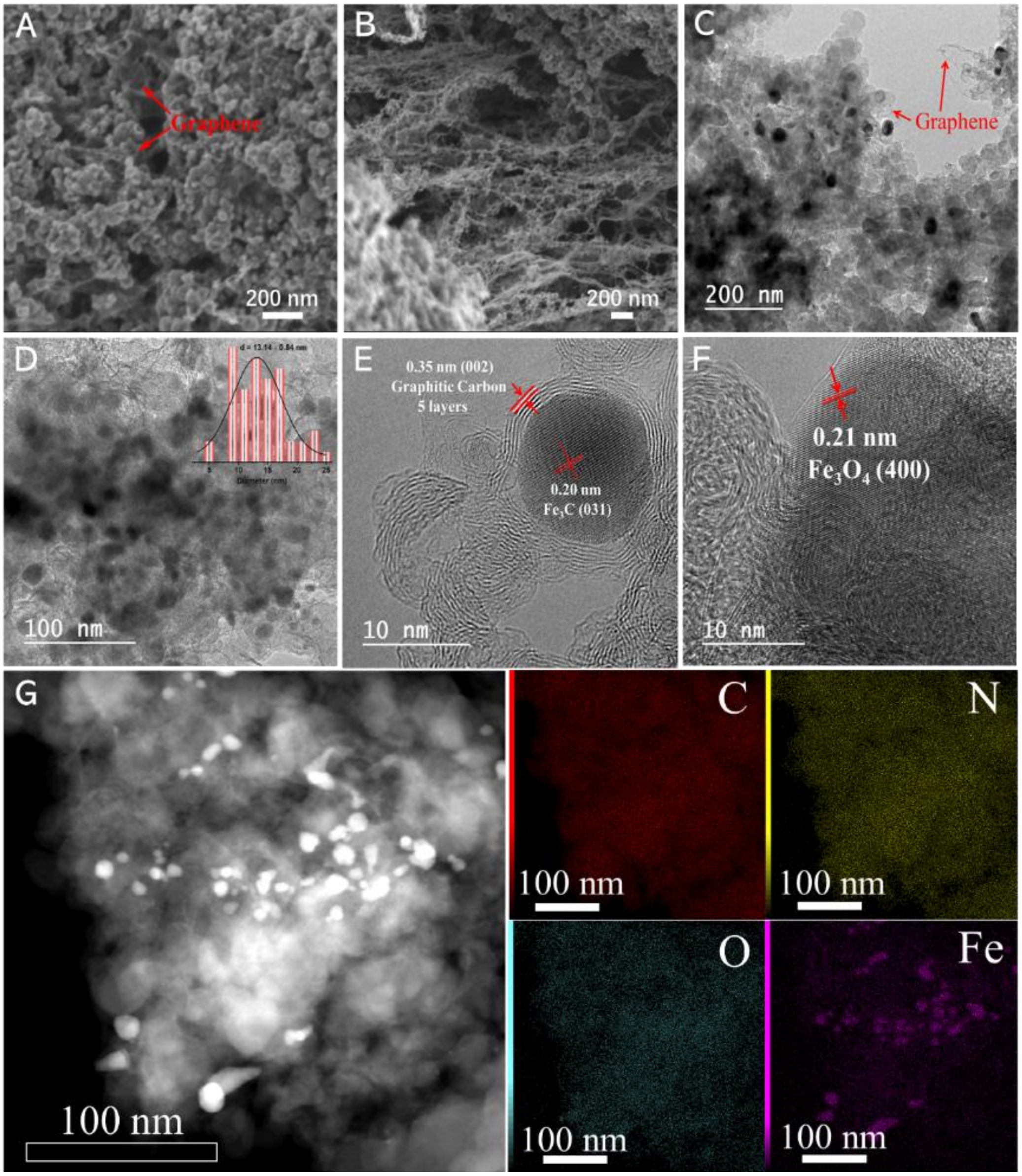

Figure 2. The SEM micrographs at different selected region (A-B), low-resolution (C-D) TEM images (inset in Figure D showing the nanoparticle size distribution), high-resolution (HRTEM) images (E-F), and energy-dispersive-X ray (EDX) mapping images (G).

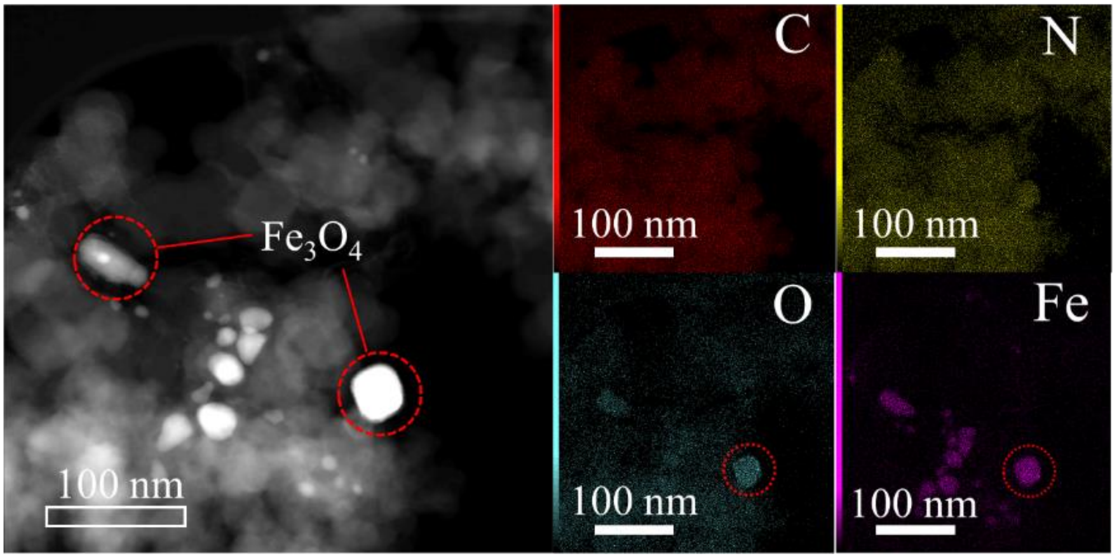

Figure 3. Energy-dispersive-X-ray (EDX) mapping on the $^{4.5}$Fe@NGC/CB.

The selected representative micrographs (SEM) recorded for $^{4.5}$Fe@NGC/CB sample reveal hierarchal structure with carbon black nanoparticles as mainly carbon phase and ultra-thin, highly crumpled nanosheets as secondary carbon phase (Figure 2A-B). The entangled layered carbon structures on the carbon black grains give rise to the formation of open network framework and well-developed meso-macro scale pore structure of as-prepared electrocatalyst. The open network framework with abundant porous structure is thought to play an important role in the ORR process as it provides an easily accessibility of the reactant to the active sites.

Transmission electron microscopy (TEM) image (Figure 2C) further displays ultrathin characteristic of transparent carbon nanosheet localized on the edge of carbon grains which might be (-in part at least-) attributed to graphene. Indeed, several works in regard to the use of glucose and N-containing small molecules to be employed for the fabrication of N-doped graphene nanosheet-based materials have been documented [374, 375]. An overview of $^{4.5}$Fe@NGC/CB

(Figure 2D) reveals the presence of some nanoparticles with mean size of ca. 13 nm, while a close look at high resolution image (HR-TEM) shown in Figure 2E-F unveils that these nanoparticles are composed of Fe_3C nanoparticle encapsulated by onion-like graphitic carbon nano-shells with around 5 layers, along with less carbon layers coated Fe_3O_4 nanocrystal. In light of the similar interplanar distance (0.21 nm) for (400) plane of Fe_3O_4 and (211) plane of Fe_3C, the direct evidence for the presence of Fe_3O_4 phase with less carbon layers encased is further validated by energy-dispersive-X-ray (EDX) mapping (Figure 3). A more representative region selected on this sample has explicitly shown a co-existence of homogeneous distribution of atomic Fe nuclei sites and Fe-based nanoparticles along with N and O elements over the entire carbon hybrid carrier (Figure 2G).

X-ray diffraction (XRD) patterns of samples prepared with distinctive amount of Fe precursor along with respective control samples are present in Figure 4A. The broad diffraction peaks at $2\theta = 24.7^o$, 43.8^o for $^{1.15}$Fe@NGC/CB, ascribed to (002), (100) planes of amorphous carbon, share almost the same pattern with sample obtained without Fe precursor (NGC/CB), indicating the highly dispersed Fe are presumably incorporated into carbon hybrid framework. As the amount of Fe precursor increases, the distinctive reflection peaks associated with Fe_3O_4 and Fe_3C crystalline phase are observable for $^{4.5}$Fe@NGC/CB, in agreement with the results shown in TEM analysis. Further increase of Fe precursor amount ($^{16.2}$Fe@NGC/CB) leads to sharper diffraction peaks of Fe_3C phases, corresponding to the formation of larger size of Fe_3C nanoparticles, while the Fe_3O_4 nanoparticles are no longer detected and a new crystalline phase related to $Fe_{0.945}O$ starts to appear. The control catalysts are also reproduced with the same synthetic procedure as $^{4.5}$Fe@NGC/CB but without the use of glucose, urea as to afford Fe@NCB, Fe@C/CB samples for comparison, respectively. Apart from as-existed Fe_3O_4 and Fe_3C crystalline phases, the additional metallic Fe phase (γ-Fe) are clearly observed for Fe@NCB. As for Fe@C/CB, the sharp peaks regarding metallic Fe phase occur while Fe_3C phase could not be found. These outcomes disclose that both urea and glucose play a crucial role for the transformation of crystal phase, while the distinctive composition of Fe-based phases might be responsible for the apparent variability in activity towards ORR.

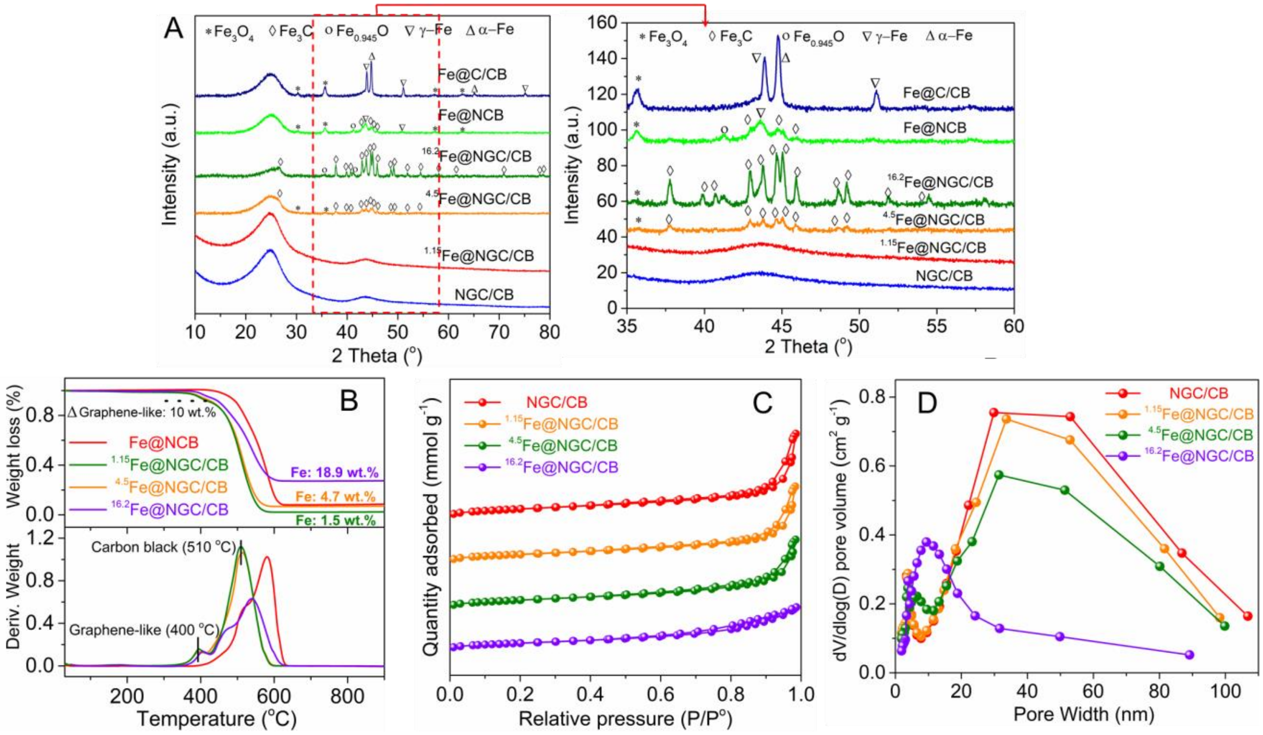

Figure 4. (A) The XRD profiles of all as-prepared catalysts; (B) The TGA (above) and DTG (below) curves of $^{1.15}$Fe@NGC/CB, $^{4.5}$Fe@NGC/CB, $^{16.2}$Fe@NGC/C, and Fe/NCB; (C) N_2 adsorption-desorption isotherm plots of samples with variable Fe addition recorded at 77 K along with (D) the respective pore size distributions (BJH method) based on desorption branch.

Thermogravimetric analysis (TGA) is conducted (from r.t. to 900 ^{o}C with a heating rate of 10 ^{o}C min^{-1} under air atmosphere) to further reveal the composition of catalysts synthesized with variable amount of Fe precursor together with Fe/NCB at comparison. As shown in Figure 4B, the weak peak at ≈ 400 ^{o}C observed on the $^{1.15}$Fe@NGC/CB, $^{4.5}$Fe@NGC/CB, $^{16.2}$Fe@NGC/CB samples, which is not present in Fe/NCB, can be attributed to the decomposition of graphene-like carbon nanosheet. The mass fraction of the graphene-like carbon phase in the hybrid carbon framework account for roughly 10 wt. % on the basis of weight loss at low temperature range. The broad peak located at relatively high temperature region (510 °C) for $^{1.15}$Fe@NGC/CB, $^{4.5}$Fe@NGC/CB arising from the carbon black-relevant degradation, shifts up to higher temperature range for $^{16.2}$Fe@NGC/CB and Fe/NCB. The higher decomposition temperature of carbon black is closely associated with enhanced graphitization degree. Based on the analysis of Fe_2O_3 phase residues in the final product, the mass loadings of Fe are calculated to be 1.5, 4.7, 18.9 wt. % for the $^{1.15}$Fe@NGC/CB, $^{4.5}$Fe@NGC/CB, $^{16.2}$Fe@NGC/CB, respectively, basically consistent with outcomes of ICP-AES measurement.

Table 1. Textural properties of as-obtained catalysts

Sample	SSA^{a} (m^2 g^{-1})	SSA$_{micro}$ (m^2 g^{-1})	SSA$_{external}$ ^{b} (m^2 g^{-1})	V ^{c} (cm^3 g^{-1})	V$_{micro}$ ^{d} (cm^3 g^{-1})	Mean pore size ^{e} (nm)
NGC/CB	286	85	201	0.482	0.040	13.8
$^{1.15}$Fe@NGC/CB	258	64	194	0.452	0.030	12.8
$^{4.5}$Fe@NGC/CB	256	63	193	0.447	0.028	11.7
$^{16.2}$Fe@NGC/CB	218	47	171	0.343	0.022	8
Fe@C/CB	244	123	120	0.383	0.060	16.8
Fe@NCB	209	77	132	0.332	0.037	13.8
$^{4.5}$Fe@NGC/CB-AL	255	61	194	0.411	0.029	11.9

^{a} Brunauer-Emmett-Teller (BET) total specific surface area (SSA) measured at T = 77 K. ^{b} The total specific surface area of mesopore and macropore. ^{c} Total pore volume determined using the adsorption branch of N_2 isotherm at $P/P_0 = 0.98$. ^{d} Determined by t-plot method. ^{e} Determined by BJH desorption average pore width (4V/A).

Further textural properties for as-prepared samples are evaluated at N_2 adsorption isotherms (T = 77 K). All concerned catalysts present type IV isothermal profiles (Figure 4C and Figure 5A) with pronounced H3 - type hysteresis loop in the range of 0.4 - 1.0 P/P^0, a typical characteristic of mesopore carbon featuring with slit-shaped pore structure [328]. Notably, as Fe precursor amount increases, the hysteresis loop and N_2 adsorption amount (Figure 4C) at relatively high-pressure range ($P/P^0 > 0.9$) are gradually suppressed which could be linked to the decreasing of the external surface area (the total SSA of mesopores and macropores). The pore size distribution curve shown in Figure 4D exhibits two types of characteristic mesopores. The small mesopore region (ca. 5 nm) is originated from the N-doped graphene-like carbon phase, on which both of the use of glucose and urea play pivotal role in the formation of small mesopore (Figure 5B), and the pore size distribution at ca. 40 nm can be ascribed to the interstitial pores of carbon black particles. The smaller population of large mesopore range is found with the increase of Fe loading (Figure 4D), which is originated from the blockage of large mesopores by Fe-based nanoparticles due to agglomeration of excessive Fe. This conclusion is further verified by a lower mean pore size (Table 1). The quantitative results on the texture properties shown in Table 1 present a SSA of 256 $m^2 g^{-1}$ over $^{4.5}$Fe@NGC/CB, higher than that measured on Fe@NCB (210 $m^2 g^{-1}$), indicative of the contribution of secondary graphene-like carbon phase on the enhancement of SSA enabled by the use of glucose. Interestingly, in spite of the comparable SSA for both samples with and without the use of N-source (256 $m^2 g^{-1}$ for $^{4.5}$Fe@NGC/CB *vs.* 244 $m^2 g^{-1}$ for Fe@C/CB), the larger fraction of micropore (SSA_{micro} : 123 $m^2 g^{-1}$; V_{micro} : 0.06 $cm^3 g^{-1}$) for Fe@C/CB, twice higher respect to that of $^{4.5}$Fe@NGC/CB (SSA_{micro} : 60 $m^2 g^{-1}$; V_{micro} : 0.028 $cm^3 g^{-1}$) affords an evidence of the formation of Fe-N_x active sites due to the well-known micropore-hosted atomically dispersed FeN_x moieties in the $^{4.5}$Fe@NGC/CB. Indeed, the gradual decrease of micropore surface area is mainly responsible for smaller SSA as Fe loading increases (Table 1), which further enhances formation of FeN_x moieties even though the higher graphitization degree also results in inevitably the decrease of micropores. The as-formed FeN_x sites are thought to occupy a certain number of micropores, for sure the part of N-doped sites should also be considered as a contribution for the micropore loss. The observation exhibits that N-source is of paramount component for construction of essential active sites towards ORR process.

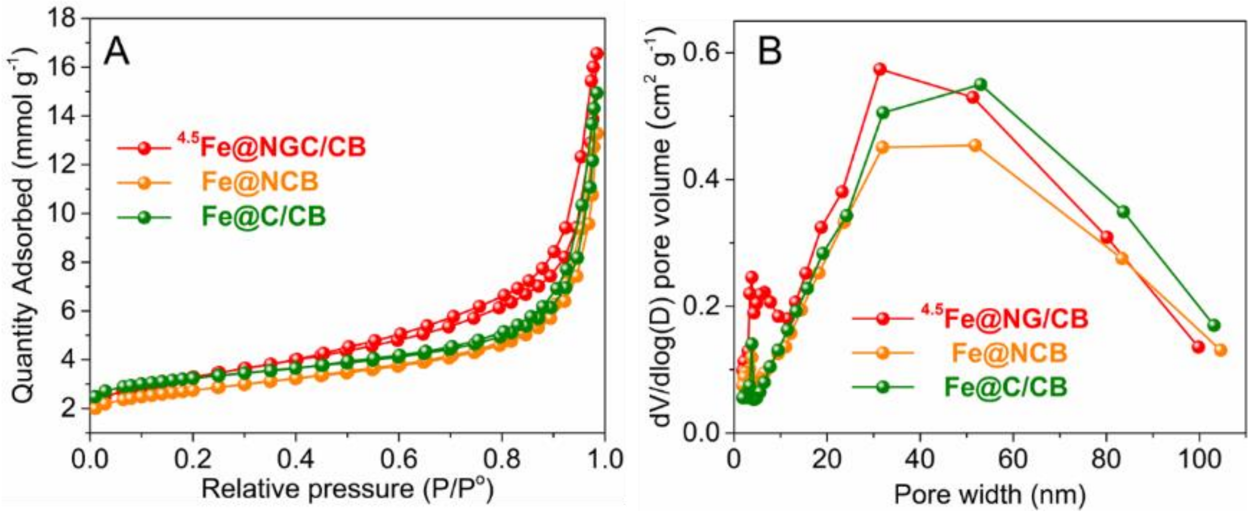

Figure 5. (A) N_2 adsorption-desorption isotherm plots of $^{4.5}$Fe@NGC/CB and control samples without using glucose (Fe@NCB), urea (Fe@C/CB) recorded at 77 K along with (B) the respective pore size distributions (BJH method) based on desorption branch.

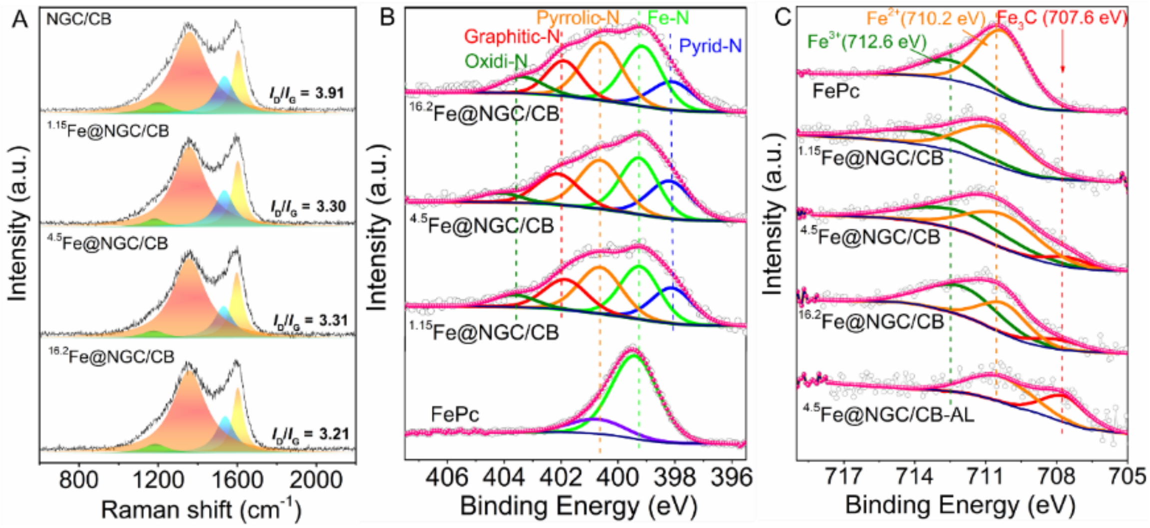

Figure 6. (A) The Raman spectra of samples prepared with different amount of Fe precursor; (B) XPS spectra of high-resolution N 1s core region in the samples containing variably Fe content along with FePc as reference sample at comparison; (C) XPS spectra of high-resolution Fe $2p_{3/2}$ core regions in all concerned samples.

To get more insights on carbon structure information, the Raman spectra is carried out for all investigated samples. All samples can be well fit into four Lorentz peaks (Figure 6A and Figure 7), and the respective fitting results are shown in the Table 2. The calculated intensity ratios of D and G band (I_D/I_G), typically used as indicator of graphitization degree on specific carbon materials, are 3.30, 3.31, 3.21 for $^{1.15}$Fe@NGC/CB, $^{4.5}$Fe@NGC/CB, $^{16.2}$Fe@NGC/CB, respectively, slightly lower respect to that on NGC/CB (3.91). This finding demonstrates that the introduction of Fe increases the graphitization degree of the sample. On the other hand, the I_D/I_G values for Fe@NCB and Fe@C/CB are accounted for 2.41, 2.37, respectively, significantly lower compared to the other samples (Figure 7 and Table 2). Given the fact that a relative low density of FeN_x sites are generated in high graphitized carbon due to the low nitrogen content in the graphitic matrix [275], the high graphitization degree of Fe@NCB and Fe@C/CB is mainly associated with a large number of Fe-based nanoparticles. The larger proportion of nanoparticles in turn results in decreased FeN_x active sites and subsequently lower ORR performance. This observation further strengthens the viewpoint that introduction of glucose and N-source plays important role in the improvement of FeN_x site density. Further effect on ORR catalytic activity will be unveiled in the following electrochemistry part.

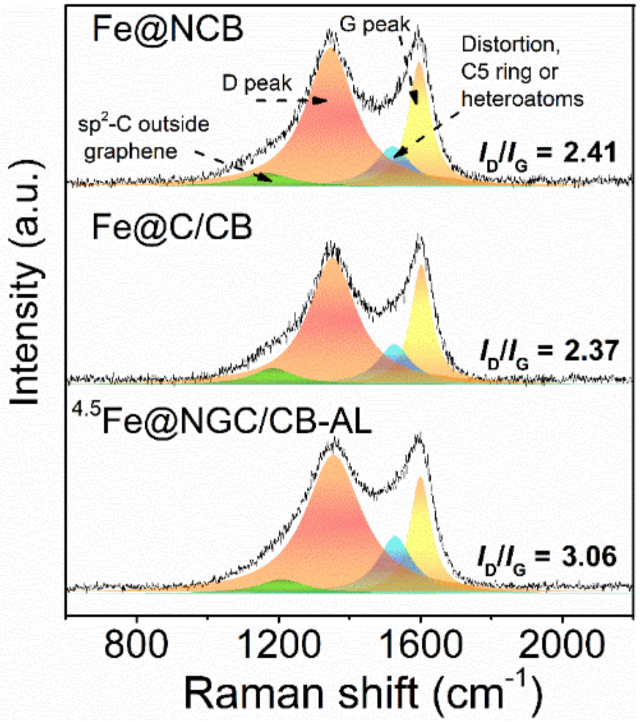

Figure 7. The Raman spectra of Fe@NCB, Fe@C/CB, and acid leached $^{4.5}$Fe@NGC/CB-AL samples (0.5 M H_2SO_4 at 80 ^{o}C for 8 h).

X-ray photoelectron spectroscopy (XPS) is further performed to gain more insight about the chemical composition of the as-synthesized samples. The pure FePc is used as a reference to precisely identify the assignment of chemical composition and bonding state of target elements. The relative elemental compositions on the different samples are displayed in Table 3. The N content of Fe-containing samples is significantly decreased compared to that of the counterparts without Fe addition, suggesting the Fe doping promotes the decomposition of N-configuration with weak thermostability [375]. The N1s core level spectrum of samples is further deconvoluted to gain more insight into the coordination state of N atom. As Figure 6B shows, the FePc reference sample shows main peak at 399.4 eV accompanied with a satellite at 400.7 eV, ascribed to four nitrogen coordinated with Fe atom (FeN_4 configuration) [147, 391]. Accordingly, the peak occurred at 399.21 eV in all Fe-containing samples confirms the presence of Fe-N_x moieties similar to FeN_4 configuration in FePc. Additional signals at around 398, 400.4, 401.8, 403.8 eV can be assigned to pyridinic N, pyrrolic N, graphitic N and oxidized N, respectively [7, 200]. According to the total nitrogen and respective fraction of N species on each sample based on the deconvolution results (Table 4), the N species contents are calculated and displayed in Table 3. The amount of FeN_x moiety is determined to be 1.06 % in $^{1.15}$Fe@NGC/CB, which further increases to 1.18 % with the increase of Fe content ($^{4.5}$Fe@NGC/CB), while the value decreases to 0.96 % in $^{16.2}$Fe@NGC/CB since the excessive additional of Fe gives rise to severe aggregation of Fe atoms during pyrolysis step. High-resolution Fe core level spectra (Fe 3/2p) is further deconvoluted to obtain deeper insight into the effect of Fe species change on electrocatalytic activity. As Figure 6C shows, the peaks at 710.2 eV, 712.6 eV shown in FePc reference sample can be ascribed to Fe^{2+}, Fe^{3+} in the macrocycle in the form of FeN_4 moiety with mostly being in he Fe^{II} state ($Fe^{2+} : Fe^{3+} = 3$, Table 5) [392, 393]. As for $^{1.15}$Fe@NGC/CB, the same feature peaks as that of FePc are found but with lower ration of Fe^{2+}/Fe^{3+} ($Fe^{2+} : Fe^{3+} = 2$), and the ratio gradually ecreases with increasing Fe precursor amount (Table 5), demonstrating the formation of Fe_3O_4 nanoparticles in all three samples. However, an additional peak occurred at 707.6 eV, which could be assigned to Fe_3C phase, is visible for both $^{4.5}$Fe@NGC/CB and $^{16.2}$Fe@NGC/CB, consistent with the XRD and TEM results. The relative fraction of Fe species and the amount of Fe species calculated on a basis of total Fe content and the fraction of Fe species has also been summarized (Table 5, Table 6).

Table 2. Raman fitting results for all samples

Sample	Deconvoluted results [a] (Area. %)				
	sp^2 carbon outside	D peak	Distortion C5 ring Heteroatom	G peak	[b] I_D/I_G
NGC/CB	6.62	61.6	16.03	15.76	3.91
$^{1.15}$Fe@NGC/CB	4.10	60.7	16.70	18.40	3.30
$^{4.5}$Fe@NGC/CB	4.11	62.6	14.34	18.95	3.31
$^{16.2}$Fe@NGC/CB	4.89	60.0	16.41	18.70	3.21
Fe@NCB	5.85	57.7	12.46	23.99	2.41
Fe@C/CB	6.29	56.8	12.87	24.02	2.37
$^{4.5}$Fe@NGC/CB-AL	5.06	59.9	15.43	19.60	3.06

[a] fitting by Lorentz method, [b] determined by the area ratio between D peak and G peak.

Table 3. Chemical composition properties of as-obtained catalysts

Sample	XPS data								
	Element composition [a] (at. %)[c]				N species (at. %) [b]				
	Carbon	Oxygen	Nitrogen	Iron	Pyridinic	Pyrrolic	Graphitic	Oxidized	Fe-N
NGC/CB	93.68	0.98	5.34	0	1.44	1.42	1.56	0.915	--
$^{1.15}$Fe@NGC/CB	93.94	1.97	3.75	0.33	0.75	1.01	0.66	0.27	1.06
$^{4.5}$Fe@NGC/CB	93.22	2.09	4.14	0.55	0.878	1.14	0.724	0.22	1.18
$^{16.2}$Fe@NGC/CB	93.0	3.15	3.22	0.63	0.497	0.97	0.5	0.29	0.962
Fe@C/CB	n.d.	n.d.	n.d.	n.d.	n.d.	n.d.	n.d.	n.d.	n.d.
Fe@NCB	n.d.	n.d.	n.d.	n.d.	n.d.	n.d.	n.d.	n.d.	n.d.
$^{4.5}$Fe@NGC/CB-AL	92.76	3.92	3.15	0.18	0.66	1.00	0.263	0.194	1.03

[a] determined by XPS analysis; [b] Determined by high resolution XPS N 1s core region and the product of relative deconvoluted peak and total nitrogen content on each sample.

Table 4. N1s deconvoluted results of as-prepared catalysts

Sample	N species (at. %)				
	Pyridinic N	Pyrrolic N	Graphitic N	Oxidized N	Fe-N_x
NGC/CB	27.0	26.52	29.21	17.13	-
$^{1.15}$Fe@NGC/CB	19.98	27.03	17.6	7.12	28.26
$^{4.5}$Fe@NGC/CB	21.21	27.55	17.49	5.33	28.42
$^{16.2}$Fe@NGC/CB	15.43	30.14	15.52	9.03	29.88
$^{4.5}$Fe@NGC/CB-AL	20.97	31.94	8.35	6.17	32.57

Table 5. Fe $2p_{3/2}$ deconvoluted results of as-prepared catalysts

Sample	Fe species			
	Fe_3C (at. %)	Fe^{2+} (at. %)	Fe^{3+} (at. %)	Fe^{2+}/Fe^{3+}
FePc	0	75.4	24.6	3.07
$^{1.15}$Fe@NGC/CB	0	68.2	31.8	2.14
$^{4.5}$Fe@NGC/CB	8.37	49.88	41.75	1.19
$^{16.2}$Fe@NGC/CB	11.7	35.3	53	0.67
$^{4.5}$Fe@NGC/CB-AL	35.54	64.46	0	-

Table 6. Fe composition based on production of Fe contents and respective fraction of Fe species on each sample.

Sample	Fe species		
	Fe_3C (at. %)	Fe^{2+} (at. %)	Fe^{3+} (at. %)
$^{1.15}$Fe@NGC/CB	0	0.201	0.129
$^{4.5}$Fe@NGC/CB	0.046	0.274	0.230
$^{16.2}$Fe@NGC/CB	0.074	0.222	0.334
$^{4.5}$Fe@NGC/CB-AL	0.064	0.116	0

2.3 Electrochemical properties of Fe@NGC/CB catalysts

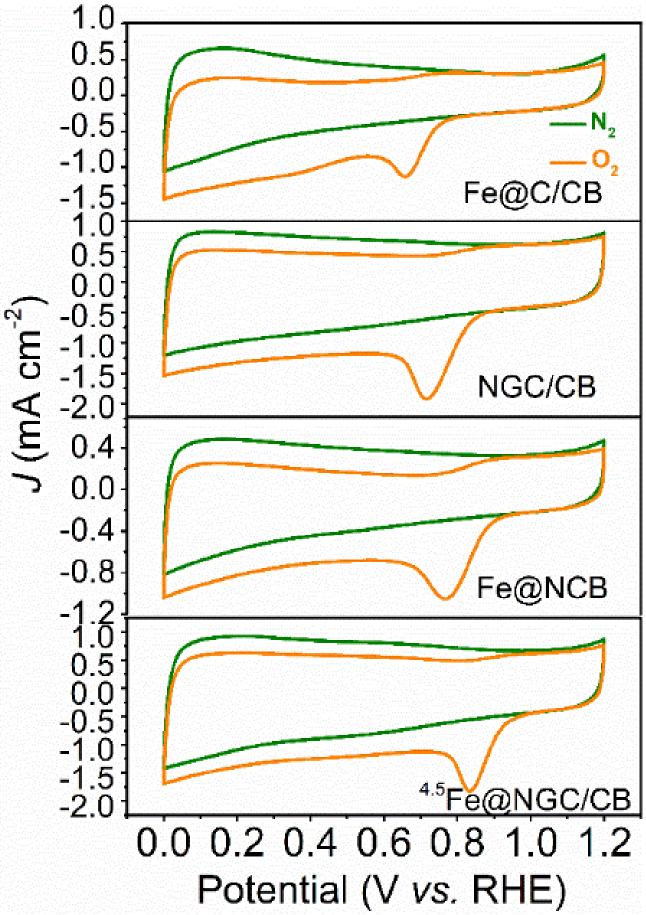

Figure 8. The CV curves of control samples at potential range of 0 - 1.2 V *vs.* RHE with a scan rate of 50 mV s^{-1} under N$_2$ and O$_2$- saturated 0.1 M KOH solution, respectively.

The ORR electrocatalytic activity of sample $^{4.5}$Fe@NGC/CB along with control catalysts without the use of glucose and urea are firstly evaluated. As Figure 8 shows, the CV curves recorded on N$_2$ and O$_2$-saturated 0.1 M KOH with a scan rate of 50 mV s^{-1} show pronounced reduction peaks in O$_2$ atmosphere for all concerned samples with the most positive potential observed in $^{4.5}$Fe@NGC/CB, indicating all samples display oxygen reduction ability with $^{4.5}$Fe@NGC/CB being the most active catalyst for ORR.

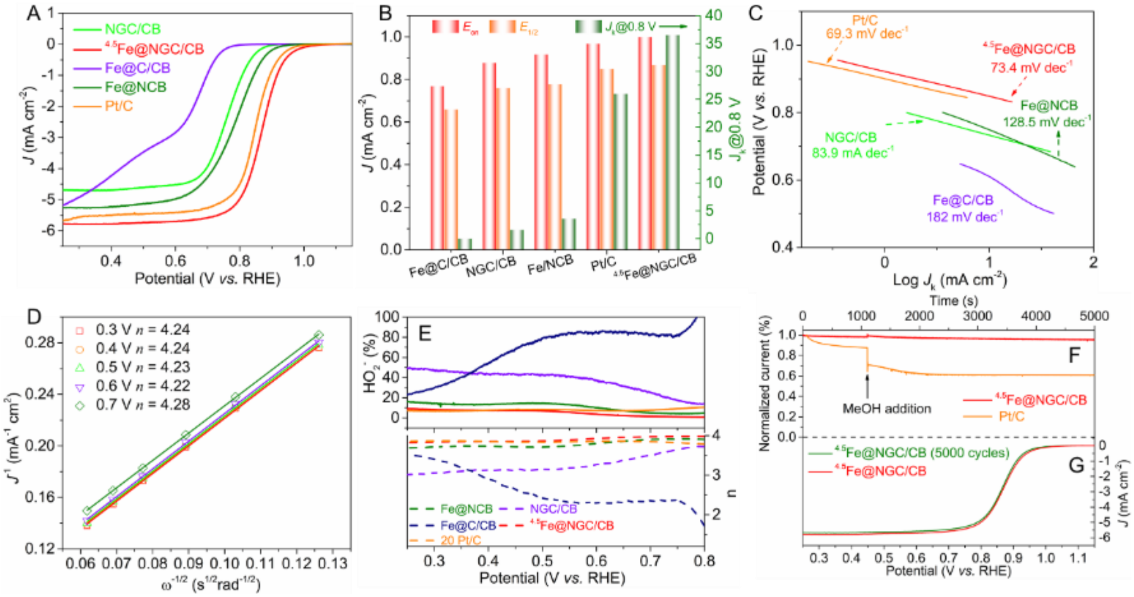

Figure 9. (A) Steady-state polarization curves of all control samples along with commercial Pt/C recorded in an O_2-saturated 0.1 M KOH electrolyte solution at a scan rate of 10 mV s^{-1} at a rotating speed of 1600 rpm and (B) corresponding electrochemical parameter (E_{on}, $E_{1/2}$, and kinetic current density at potential of 0.8 V, J_k@0.8 V); (C) Tafel plots for all control samples along with benchmarked Pt/C; (D) K-L plots for $^{4.5}$Fe@NGC/CB; (E) The H_2O_2 yield and electron transfer number for $^{4.5}$Fe@NGC/CB and control samples along with Pt/C derived from rotation disk-ring electrode (RRDE) measurement at a scan rate of 10 mV s^{-1} at a rotation speed of 1600 rpm in O_2-saturated 0.1 M KOH electrolyte; (F) Methanol poisoning and (G) durability tests.

The LSV curves and corresponding electrocatalytic parameter (onset potential (E_{on}), half-wave potential ($E_{1/2}$), and kinetic current density at applied potential of 0.8 V (J_k@0.8 V)) collected at rotation speed of 1600 rpm at scan rate of 10 mV s^{-1} are depicted in Figure 9A-B and Table 7. The control catalyst Fe@C/CB shows much lower ORR activity with a limited $E_{1/2}$ of 0.66 V and E_{on} of 0.77 V, indicating that Fe/Fe_3O_4 nanoparticles (see XRD result in Figure 4A) show negligible activity toward ORR and N doping is indispensable for the construction of active sites. However, the introduction of N-source alone (NGC/CB) leads to a limited enhancement of ORR activity ($E_{1/2}$ of 0.76 V and E_{on} of 0.88 V). Noteworthy, the presence of both Fe and N source ($^{4.5}$Fe@NGC/CB) dramatically boosts the ORR activity with optimal E_{on} of 1 V, $E_{1/2}$ of 0.87 V along with a highest limited current density (5.75 mA cm^{-2}). The finding reveals Fe and N synergistically contribute to enhanced ORR activity, implying the formation of FeN_x coordination configuration.

Table 7. Electrochemical performance of all samples in ORR

Entry	Catalyst	E_{on} ^{a} (V)	$E_{1/2}$ ^{b} (V)	J_L ^{c} (mA cm^{-2})	Tafel slope (mV dec^{-1})	J_k ^{d} (mA cm^{-2})
1	NGC/CB	0.88	0.76	4.66	83.9	1.59
2	$^{1.15}$Fe@NGC/CB	0.95	0.85	5.55	84.29	22.15
3	$^{4.5}$Fe@NGC/CB	1.0	0.87	5.75	73.40	36.56
4	$^{16.2}$Fe@NGC/CB	0.95	0.85	5.23	86.25	19.2
5	Fe@C/CB	0.77	0.66	3.78	182.0	0.026
6	Fe@NCB	0.92	0.78	5.2	128.5	3.59
7	$^{4.5}$Fe@NGC/CB-AL	0.97	0.85	5.36	-	25.20
8	20 Pt/C	0.97	0.85	5.44	69.3	25.98

^{a} Onset and ^{b} half-wave potential values reported *vs*. RHE, ^{c} limited diffusion current density, ^{d} Kinetic current density calculated from K-L equation at 0.80 V *vs*. RHE.

On the other hand, Fe@NCB presents an inferior ORR activity (E_{on} = 0.92 V, $E_{1/2}$ = 0.78 V) with respect to that of $^{4.5}$Fe@NGC/CB, indicating that the addition of glucose also plays important role for the improved ORR. In consideration to similar Fe content and crystal phase composition (see XRD and TGA results in Figure 4A-B) for $^{4.5}$Fe@NGC/CB and Fe@NCB, the enhanced electrocatalytic performance could be rationalized that N-doped graphene-like carbon nanosheet derived from glucose facilitate accommodation of larger portion of active sites due to higher total specific surface area and lower graphitic degree (Table 1, Figure 6A and Figure 7).

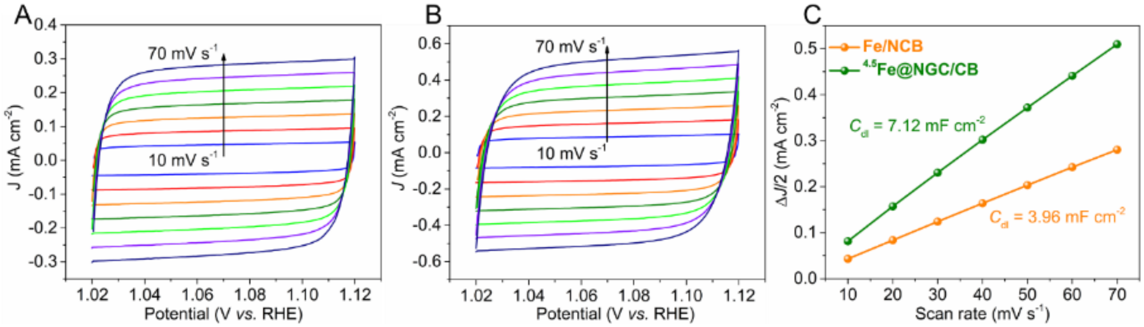

Figure 10. The CV curves of Fe@NCB (A) and ${}^{4.5}$Fe@NGC/CB (B) in the potential range of 1.02-1.12 V *vs.* RHE with various scan rates in N_2-saturated 0.1 M KOH solution and corresponding linear fitting of the capacitive currents *vs.* scan rates (C).

Indeed, the double-layer capacitance (C_{dl})- a parameter applied as a characteristic of electrochemically active surface area (ECSA) [341] - is calculated to be 3.96 mF cm^{-2} for Fe/NCB, nearly twice lower than that on ${}^{4.5}$Fe@NGC/CB (7.3 mF cm^{-2}) (Figure 10), further strengthening the pivotal role of glucose on the formation of higher active sites density for the electrocatalytic ORR process. More importantly, the improved electric conductivity and desired hierarchical open framework imparted by N-doped secondary carbon phase are important for both easily electron and mass transport. All of beneficial actions on the ${}^{4.5}$Fe@NGC/CB contribute to the eventually excellent ORR activity, which even outperforms the commercial Pt/C catalyst (E_{on} = 0.97 V, $E_{1/2}$ = 0.85 V) and most previously reported non-precious metal catalyst. The Tafel slope (Figure 9C) determined on ${}^{4.5}$Fe@NGC/CB exhibits a value of 73.4 mV dec^{-1}, lower than that of NGC/CB (83.9 mV dec^{-1}), Fe@NCB (128.5 mV dec^{-1}) and Fe@C/CB (182 mV dec^{-1}), demonstrating the fastest reaction kinetics over all control samples.

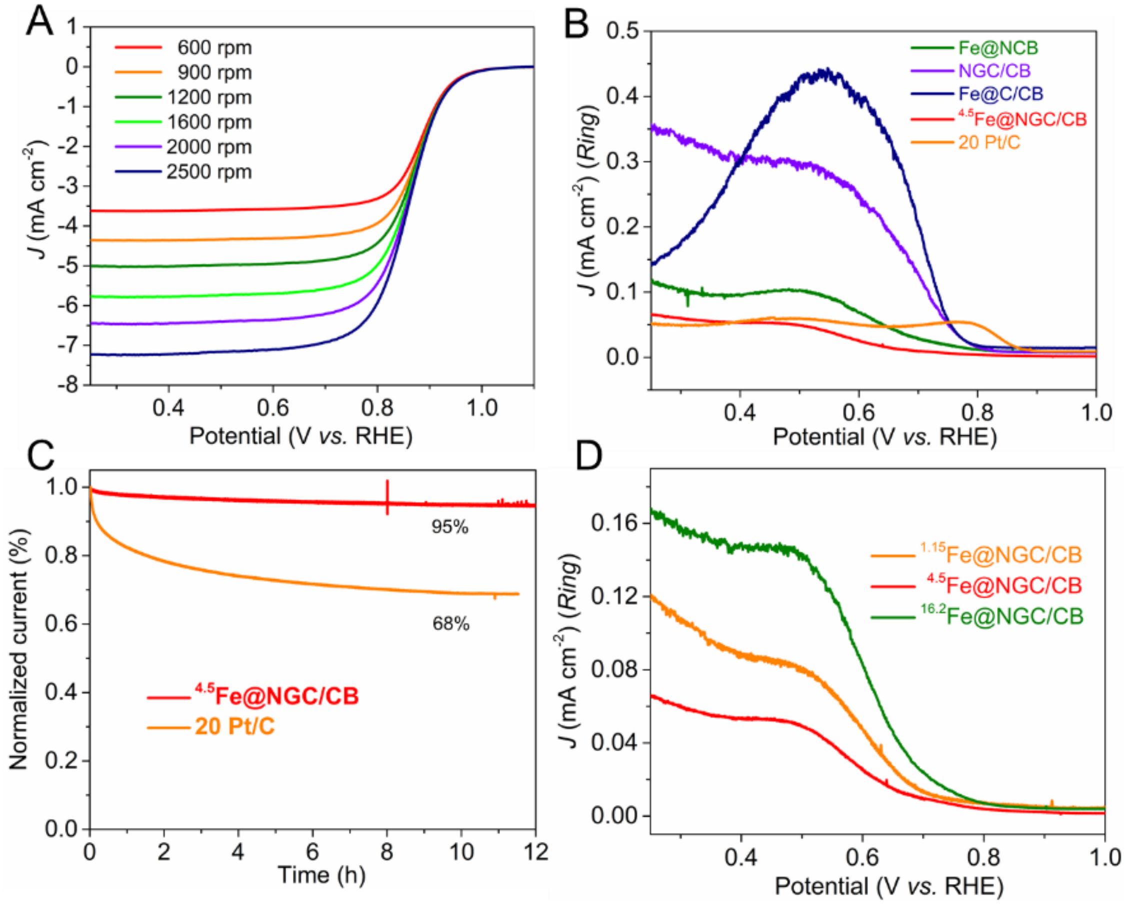

Figure 11. (A) Linear sweep voltammograms (LSVs) for ORR in O_2-saturated 0.1 M KOH solution for $^{4.5}$Fe@NGC/CB at variable rotation rates with a scan rate of 10 mV s^{-1}; (B) RRDE current-potential curves of $^{4.5}$Fe@NGC/CB and respective control samples as well as benchmarked Pt/C catalyst in O_2 saturated 0.1 M KOH solution recorded at the Pt-ring [A = 0.11 cm^2]. All ring currents have been measured at a rotation rate (ω) of 1600 rpm; (C) The chronoamperometric (CA) response curves of $^{4.5}$Fe@NGC/CB at a potential of 0.65 V *vs.* RHE with rotation speed of 1600 rpm in O_2-saturated 0.1 M KOH solution; (D) RRDE current-potential curves of samples prepared by variable Fe addition in O_2 saturated 0.1 M KOH solution recorded at the Pt-ring [A = 0.11 cm^2], and all ring currents have been measured at a rotation rate (ω) of 1600 rpm.

The LSV curves of $^{4.5}$Fe@NGC/CB at different rotation speeds are investigated and corresponding Koutecky-Levich (K-L) plots are present in Figure 9D and Figure 11A. The proportional increase of limited-diffusion current density with increasing rotation speeds (Figure 11A) implies a diffusion-controlled oxygen reduction process, and the good linearity of K-L plots at various applied potentials indicates the first-order reaction toward dissolved O_2. The average electron transfer number (n_E) based on K-L equation is calculated to be 4.2 in the range of 0.3-0.7 V (The value of n_E over 4 is ascribed to the deviation between theory parameter and practical parameter under operate condition), exhibits an ideally 4-electron transfer pathway.

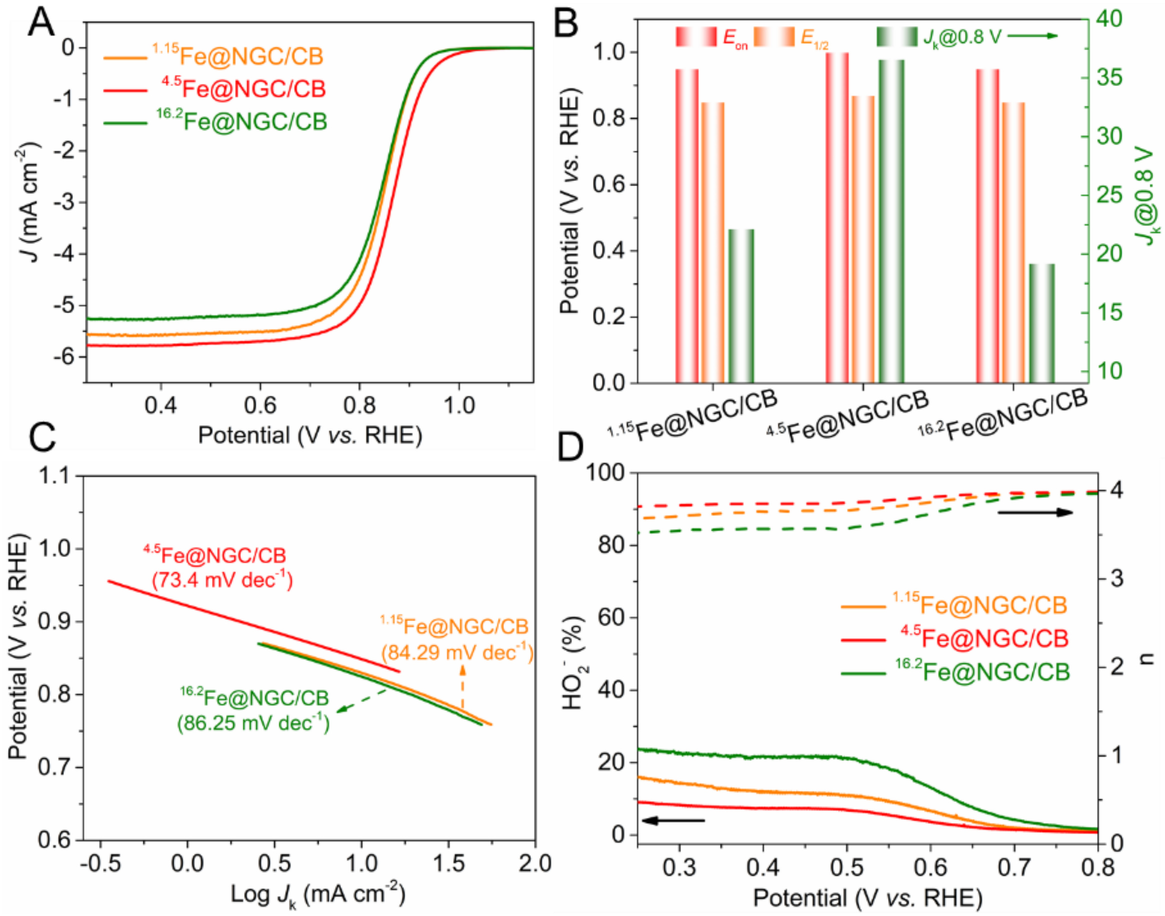

Figure 12. (A) Steady-state polarization curves of samples produced by the use of different Fe precursor and (B) respective electrochemical parameter (E_{on}, $E_{1/2}$, kinetic current density, J_k@0.8 V); (C) Tafel plots for samples prepared by variably addition of Fe; (D) The H_2O_2 yield and electron transfer number for samples with different Fe loadings derived from rotation disk-ring

electrode (RRDE) measurement at a scan rate of 10 mV s^{-1} at a rotation speed of 1600 rpm in O_2-saturated 0.1 M KOH electrolyte.

Rotation ring-disk electrode measurements (RRDE) are further performed to gain more understanding on kinetic behavior over all samples. As Figure 9E and Figure 11B show, the H_2O_2 yields of Fe@C/CB and NGC/CB are as high as 84.9 % and 37.5 %, corresponding to electron transfer number of 2.3 and 3.2 at applied potential of 0.6 V, respectively, exhibiting poor selectivity toward 4-electron transfer path. The simultaneously introduction of Fe and N (sample Fe@NCB) significantly decreases the H_2O_2 yields and increases the number of electron transfer, strengthening the beneficial role of FeN_x sites towards ideally 4- electron reduction process. The addition of glucose (sample $^{4.5}$Fe@NGC/CB) further improves the selectivity of reaction with H_2O_2 yield accounted for less than 10 % and almost full 4-electron path across the whole investigated potential range (H_2O_2 yield of as low as 3.72 % and electron transfer number of 3.93 at 0.6 V, even lower than those of benchmarked Pt/C). This result demonstrates the outstanding 4-electron selectivity of $^{4.5}$Fe@NGC/CB and the importance of secondary graphene-like carbon phase on the improvement of the ORR activity.

As an additional trial, the durability and methanol tolerance of the most active catalyst $^{4.5}$Fe@NGC/CB have also been investigated, which are considered to be fundamental prerequisite for the successful exploitation on the side of cathode at the heart of fuel cell. As shown in Figure 9G, the $E_{1/2}$ shows negligible degradation after 5000 continuous potential cycling in the range of 0.6 - 1 V at a scan rate of 50 mV s^{-1} under O_2 atmosphere, only with slight decrease of onset potential and limited-diffusion current density, thus demonstrating the excellent long-term stability of the catalyst. The additional chronoamperometric (CA) response curves are also performed to evaluate the stability and methanol tolerance at applied potential of 0.65 V. As Figure 11C shows, the current density for $^{4.5}$Fe@NGC/CB with respect to initial value retains up to 95 % after 12 h continuous operation, much higher than that measured on Pt/C (68 %). Furthermore, upon introduction of methanol (1 % v/v), a rapidly irreversible drop of current density is observed for Pt/C catalyst while no appreciable change is observed for $^{4.5}$Fe@NGC/CB under the identical operation condition (Figure 9F). All these measurement results unambiguously confirm $^{4.5}$Fe@NGC/CB presents superior stability and tolerance toward methanol crossover. Combined with high ORR activity along with facile, scalable fabrication methodology, the as-prepared hybrid holds great promise as non-precious metal catalyst for the replacement of Pt-based noble catalyst toward next generation of fuel cell.

The deeper insight into Fe loading effect on electrocatalytic activity and identification of active sites for as-prepared hybrid are further explored. As shown in Figure 12A-B and Table 7, the $^{1.15}$Fe@NGC/CB displays an E_{on} of 0.95 V and $E_{1/2}$ of 0.85 V, 50 mV and 20 mV lower than that on $^{4.5}$Fe@NGC/CB (E_{on} = 1 V, and $E_{1/2}$ = 0.87 V). Further increasing Fe content ($^{16.2}$Fe@NGC/CB) leads to a deteriorated of both E_{on} (0.95 V) and $E_{1/2}$ of (0.85 V), comparable electrocatalytic performance but with slightly lower limited-diffusion current density respect to that of $^{1.15}$Fe@NGC/CB. The highest kinetic current density (36.56 mA cm^{-2} calculated on a basis of K-L equation) at 0.80 V (Figure 12B, and Table 7) and lowest Tafel slope for $^{4.5}$Fe@NGC/CB (Figure 12C) verifies its most superior ORR activity among three samples. RRDE measurement (Figure 11D and Figure 12D) shows that $^{1.15}$Fe@NGC/CB catalyst presents moderate ORR selectivity respect to that of $^{4.5}$Fe@NGC/CB, while $^{16.2}$Fe@NGC/CB displays the worst selectivity among three samples in terms of highest yield of H_2O_2 and lowest electron transfer number throughout scanning region. This finding suggests an appropriate amount of Fe precursor is of great importance for the optimal activity and selectivity toward ORR.

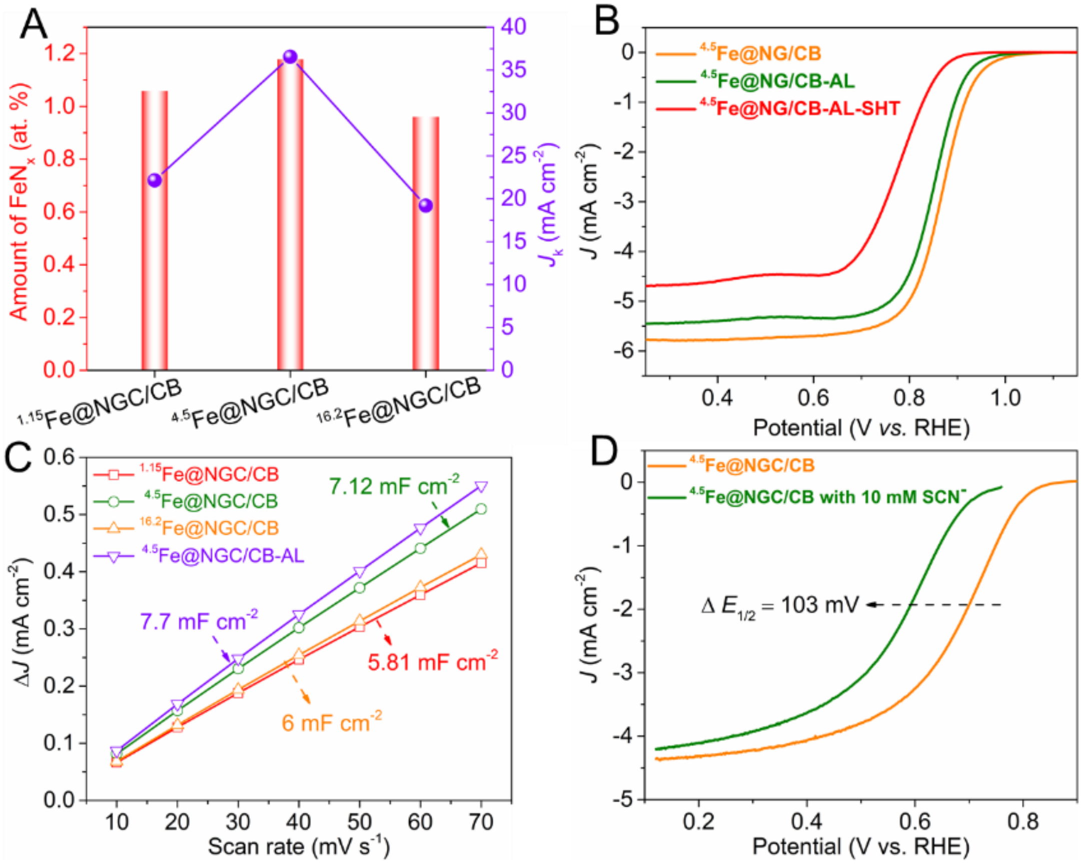

Figure 13. (A) The correlation plots between amount of FeN$_x$ moieties and ORR activity for samples with variable Fe loadings; (B) LSV curves of pristine $^{4.5}$Fe@NGC/CB, acid leached sample $^{4.5}$Fe@NGC/CB-AL, and subsequently second heating treatment sample $^{4.5}$Fe@NGC/CB-AL-SHT recorded at a rotation speed of 1600 rpm with scan rate of 10 mV s^{-1} in O_2-saturated 0.1 M KOH solution; (C) linear fitting plots of the capacitive currents *vs.* scan rates for samples with variable Fe loadings along with acid leached sample $^{4.5}$Fe@NGC/CB-AL; (D) LSV curves of sample $^{4.5}$Fe@NGC/CB before and after addition of 10 mM KSCN in O_2-saturated 0.5 M H_2SO_4 solution with scan rate of 10 mV s^{-1} at a rotation speed of 1600 rpm.

To unveil ORR activities trend on the samples with various amount of Fe contents, the correlation plot between the density of FeN_x sites based on XPS analysis and ORR activity is established. As shown in Figure 13A, the ORR activity is proportional to amount of FeN_x moieties. Given the fact that N-doped carbon with higher amount of pyridinic N and graphitic N (NGC/CB) exhibit much inferior activity compared to that measured on $^{4.5}$Fe@NGC/CB, the FeN_x is thought to be the most electrochemically active sites for ORR, as it is generally accepted [119, 394]. In light of possible role of nanoparticles existed in the form of Fe_3C and Fe_3O_4 in the electrocatalyst $^{4.5}$Fe@NGC/CB on enhanced electrochemical performances, some additional control experiments are conducted to gain deeper insight into potential synergism/promotion effect of Fe_3C/Fe_3O_4 and FeN_x active sites toward ORR. First of all, a conventional acid etching of $^{4.5}$Fe@NGC/CB, which is expected to remove the Fe-based nanoparticles (the leached sample is denoted as $^{4.5}$Fe@NGC/CB-AL), is employed and respective electrocatalytic activity is investigated. Of note is that the potential deconstruction on the carbon structure and generation of oxygen function groups induced by acid etching process should be took into account on the leached sample. These factors may significantly influence on the identification of active sites, and, unfortunately, nearly no study previously systematically reported on these impacts. Indeed, the oxygen contents have been significantly improved by approximately twice (3.92 at. % for $^{4.5}$Fe@NGC/CB-AL *vs.* 2.09 at. % for $^{4.5}$Fe@NGC/CB) after 0.5 M H_2SO_4 acid leaching at 80 ^{o}C for 8 h (Table 3), which in turn results in decrease of N relatively content. Hence, as an additional parallel trial, NGC/CB sample is also subjected to acid leaching with identical condition at comparison (referred as to NGC/CB-AL). As can be seen in Figure 14A, the ORR electrocatalytic activity of NGC/CB-AL almost retains the original level in terms of E_{on} and $E_{1/2}$ only with slightly drop of limited current density respect to that of sample before acid leaching (NGC/CB). In sharp contrast, a significantly decreased ORR activity with E_{on} of 0.97 V and $E_{1/2}$ of 0.85 V for $^{4.5}$Fe@NGC/CB-AL, 30 mV and 20 mV lower than that of $^{4.5}$Fe@NGC/CB, is observed (Figure 13B). This finding demonstrates that the increase of the oxygen content on the surface of carbon itself is not responsible for the decreased ORR activity. The similar texture properties (Table 1) and graphitization degree (Figure 7) for both $^{4.5}$Fe@NGC/CB and $^{4.5}$Fe@NGC/CB-AL also exclude the impact of potential destruction of carbon structure resulted from acid leaching on electrocatalytic activity.

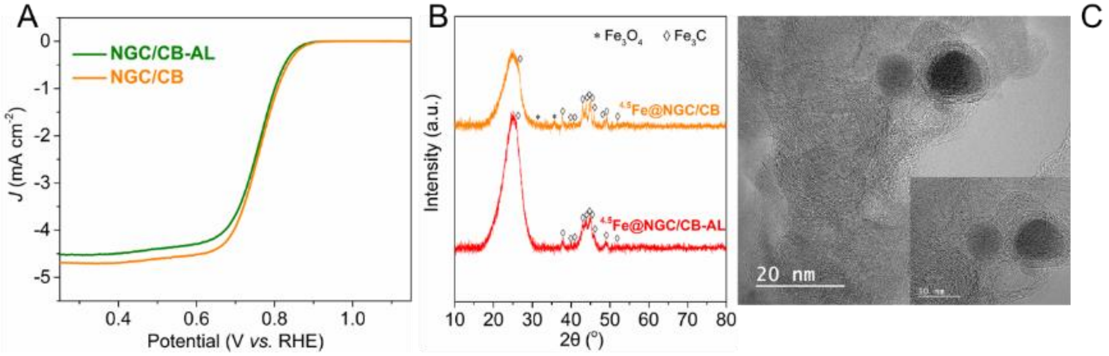

Figure 14. (A) LSVs for NGC/CB and respective acid-leached sample NGC/CB-AL; (B) The XRD patterns of $^{4.5}$Fe@NGC/CB and respective acid-leached sample $^{4.5}$Fe@NGC/CB-AL; (C) TEM images at different magnification for sample $^{4.5}$Fe@NGC/CB-AL.

To further eliminate the impact of protonation of basic N-groups and subsequent HSO_4^- adsorption during acid leaching, along with oxygen-containing groups generated on the carbon matrix, which results in a decreased turnover frequency of adjacent FeN_x sites for the ORR [106, 395], $^{4.5}$Fe@NGC/CB-AL is thermally treated at 900 °C for 1 h under Ar again to remove adsorbed anion ions and oxygen functional groups on the surface of carbon matrix, and the sample is labelled as $^{4.5}$Fe@NGC/CB-AL-SHT. Surprisingly, a dramatically decreased electrocatalytic ORR activity is observed after the thermal treatment at 900 °C (Figure 13B), with E_{on} of 0.9 V and $E_{1/2}$ of 0.78 V, both 70 mV lower than that of $^{4.5}$Fe@NGC/CB-AL, respectively, indicating that both protonation of N groups followed by anion adsorption and generation of oxygen-containing groups are not also responsible for the degradation of ORR activity after acid leaching. All above control trials imply that the removal of Fe_3O_4/Fe_3C nanoparticles existed in the $^{4.5}$Fe@NGC/CB during acid leaching is the only origin of the ORR activity loss. As Figure 14B shows, the distinctive reflection peaks ascribed to Fe_3C phase still present, while ones corresponding to Fe_3O_4 crystalline phase are no longer visible in the $^{4.5}$Fe@NGC/CB-AL. The result indicates that the Fe_3O_4 NPs are preferentially etched by acid washing, which is related to the insufficient carbon coating layers around Fe_3O_4 and easier acid etching. On the contrary, the Fe_3C NPs can survive the harsh acidic etching conditions due to the presence of robust carbon layer encapsulation which prevent contact with the acid medium. It is worthy to note that similar results have also been reported previously about the resistance of carbon encapsulated iron nanoparticles during the carbon nanotubes synthesis [396]. The TEM images (Figure 14C) of the $^{4.5}$Fe@NGC/CB-AL catalyst support the conclusion that there are indeed some graphitic carbon layers coated Fe_3C NPs preserved, and the intact scaffold buildings with integrated N-graphene and carbon blacks are also well maintained after acid leaching. From a quantitative viewpoint, the Fe mass loading of $^{4.5}$Fe@NGC/CB-AL deceases to 2.2 wt. %, approaching half of mass loss observed with respect to $^{4.5}$Fe@NGC/CB on the basis of ICP-AES measurements. The significant decline of surface Fe atom content has also been observed by XPS analysis (Table 3). Interestingly, there is still presence of Fe_3C phase with much higher proportion (Figure 6C and Table 5-6), while the peak related to Fe^{3+} is no longer detected for $^{4.5}$Fe@NGC/CB-AL, further confirming that acid etching preferentially eliminates Fe_3O_4 nanoparticles and Fe_3C nanoparticles are retained during acid leaching. Given the fact that FeN_x sites is known to be highly robust moieties which is difficult to be removed by acid leaching (the lower amount of FeN_x shown in Table 3 in $^{4.5}$Fe@NGC/CB-AL respect to that of pristine

$^{4.5}$Fe@NGC/CB is aroused from the introduction of O species during acid leaching procedure), all these systematically analysis unambiguously suggest the removal of Fe_3O_4 nanoparticles is responsible for the ORR activity loss after acid leaching. To figure out the promotion mechanism of Fe_3O_4 nanoparticles on ORR process, the ESCAs for various prepared electrocatalyst are further evaluated. The calculated C_{dl} values are 5.81, 7.12, 6, and 7.7 mF cm^{-2} for $^{1.15}$Fe@NGC/CB, $^{4.5}$Fe@NGC/CB, $^{16.2}$Fe@NGC/CB, and $^{4.5}$Fe@NGC/CB-AL, respectively (Figure 13C and Figure 15). The higher C_{dl} values for $^{4.5}$Fe@NGC/CB-AL respect to that of pristine $^{4.5}$Fe@NGC/CB evidence the loss of Fe_3O_4 nanoparticles do not lead to the decline of ESCA values. In fact, the enhanced ESCA values are probably attributed to the more exposed active sites located at the edge of Fe_3O_4 nanoparticles. This result indicates Fe_3O_4 nanoparticle itself does not serve as active site, which is well agreement with most inferior ORR activity on Fe@C/CB featuring Fe/Fe_3O_4 nanoparticles phase (Figure 4A, Figure 9A-B).

Taken together, it comes to the conclusion that these Fe_3O_4 nanoparticle indirectly boost ORR process on FeN_x sites via the beneficial electronic interaction, agreeing with some previously reports on Fe_3O_4-involved accelerated ORR reaction [384-386, 397, 398]. The poison experiment is finally carried out on sample $^{4.5}$Fe@NGC/CB to confirm the role of FeN_x sites on dominating ORR activity. As show in Figure 13D, the remarkably degradation of electrocatalytic activity (decreased by 103 mV in terms of $E_{1/2}$) after introduction of SCN^- is observed, which can be attributed to the block of FeN_x sites by SCN^-, indicating ORR process prefers to occur on the FeN_x active sites. The finding reinforces the point that FeN_x moieties are real active sites in catalyzing ORR, and Fe_3O_4 nanoparticles positively promote the ORR catalytic activity on FeN_x sites. It is worthy to note that we afford a clear-cut experimental proof on the role of Fe_3O_4 nanoparticles played in the hybrid electrocatalyst toward ORR process, which shed light on the real activity origin of multiple active sites with high complexity.

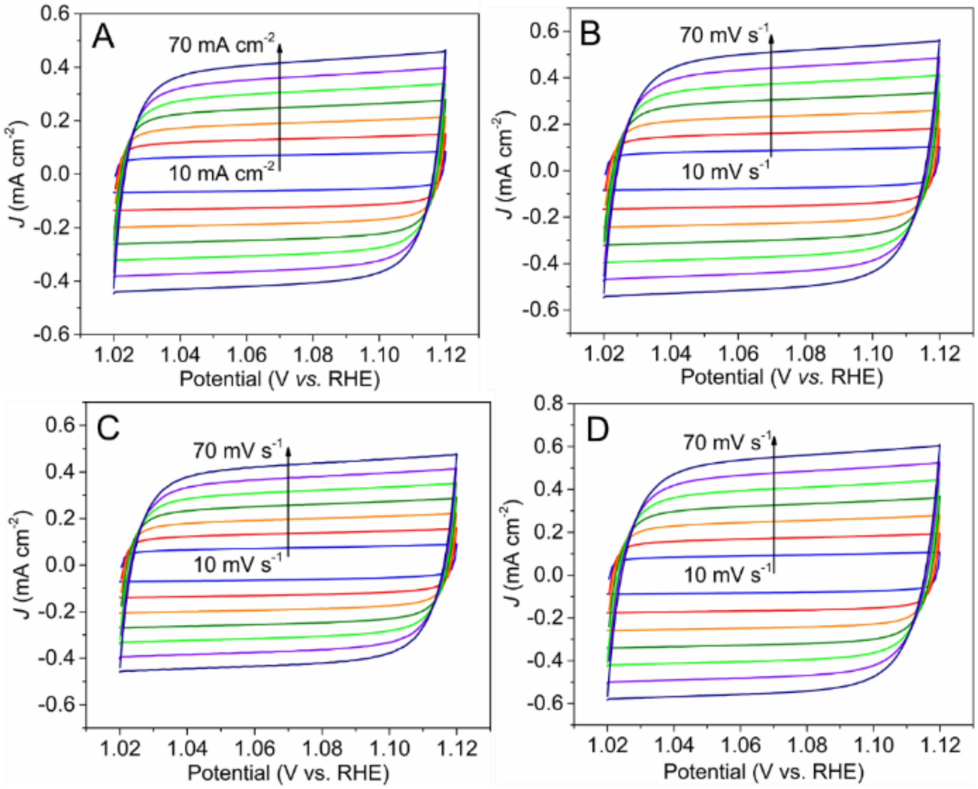

Figure 15. The CV curves in the potential range of 1.02-1.12 V *vs.* RHE with various scan rates in N_2-saturated 0.1 M KOH solution of (A) $^{1.15}$Fe@NGC/CB; (B) $^{4.5}$Fe@NGC/CB; (C) $^{16.2}$Fe@NGC/CB; (D) $^{4.5}$Fe@NGC/CB-AL

3. Conclusion

In summary, a facile and scalable strategy has been well developed for the preparation of hybrid catalyst enriched abundant FeN_x moieties coupling with highly graphitic carbon layer encapsulated Fe_3C/Fe_3O_4 nanoparticles. The synthesis is performed by an incipient wetness impregnation of Fe aqueous solution on physically mixture of glucose, urea, and carbon black, followed by one-step pyrolysis without any other post-treatment (e.g. acid leaching, NH_3 second treatment etc.). The as-prepared electrocatalyst exhibits an heterostructure composed of N-doped carbon black as primary carbon scaffold and interweaved N-doped graphene as secondary carbon phase, featuring hierarchical porous structure with micro, meso and macropores. The addition of glucose is responsible for the formation of N-doped graphene, which significantly increases specific surface area and is believed to host more active sites, thus exerting a positive effect on the ORR activity. Thanks to above compelling merits, the optimal catalyst with an appropriate amount of Fe addition ($^{4.5}$Fe@NGC/CB) displays a superior ORR performance.

A series of control experiments have unambiguously unraveled that FeN_x moieties are real active sites toward ORR and Fe_3O_4 nanoparticles endow positive promotion effect on activity of FeN_x sites via electronic interaction. Our present work affords a simple and cost-effective route for the rational design of highly performance ORR electrocatalyst. More importantly, this work systematically illustrates the real activity origin of electrocatalyst with high complicated multiple active sites toward ORR process, which would be a valuable guideline for the design of next generation non-precious metal Fe-based electrocatalyst.

Chapter 7

Conclusions and perspectives

7.1 Concluding remarks and respective perspectives

In summary, the contribution describes a general and original strategy for the fabrication of atomically dispersed Fe-N-C catalysts, using food-grade precursor as carbon source for C-networks, and inorganic ammonia salts as nitrogen source. The preparation condition and chemical composition of the as-prepared catalysts have been systematically investigated. Finally, the as-synthesized Fe-N-C catalysts are evaluated for the oxygen reduction reaction and the structure-performance relationship properties have also been established and discussed.

Chapter 3 focuses on the synthesis of highly metal charged Fe-N_x moieties located at the interface of iron oxyhydroxide sub-nanometric structures and a N-doped carbon network through the combination of chelating citrate ions with the ancillary monodentate SCN^- ligand. The role of SCN^- on the chemico-physical properties and composition of the final catalysts along with their respective electrocatalytic ORR performances are investigated in detail. The result evidences that the introduction of SCN^- is of great importance for the preparation of the atomically dispersed Fe-N-C active site configuration. The SCN^- plays a role of structural mediator to prevent the formation of the inactive carbides phase. Ammonia post thermo-chemical treatment further promotes the exposure of surface atomic Fe sites by introducing the formation of more abundant porosity and to introduce simultaneously the highly basic N-terminated groups. The optimal catalyst obtained displayed high electrocatalytic performance towards ORR in alkaline media. We attribute the high performance of such model catalyst to the combination effect of desired geometric properties and high density of proposed atomic sites, i.e. FeN_x located between Fe oxyhydroxide and N-doped C networks. However, the nature of the active sites on ORR is still needed to be unraveled from DFT calculation according to the proposed active sites configuration by EXAFS fitting results (FeN_x moiety between Fe oxyhydroxide and N-doped C networks), particularly in the aspect of electron structure. The stability of such unique active sites under operation should also be studied by in-situ XAS, which can be conducive for the understanding of the stability of the catalyst as a function of cycling tests. On the other hand, the ORR activity in acid media should be also optimized in our catalytic system. Lastly, the as-synthesized catalyst should be also evaluated in the membrane electrode assembly (MEA) such as anion-exchanged membrane fuel cell (AEMFC) for the consideration of future practical application. Indeed, regarding the future practical operation of such catalyst the problem of mass transfer should be assessed and benchmarked with that of the platinum-based catalysts.

Chapter 4 describes a modified strategy for the synthesis of highly N-doped hierarchical porous carbon networks decorated with single atom Fe sites without using high temperature NH_3 post thermo-treatment. Herein, the citric acid and ammonium carbonate are used as only carbon and nitrogen source, respectively. Thus, this methodology enables the flexible modulation on N-doped level by tuning in an independent way the amount of N-source. The addition of the third components (SiO_2 and $ZnCl_2$) also plays a crucial role on the modification of the physico-chemical properties of the as-synthesized active phase. The use of SiO_2 not only produces the prevalent mesopore but also allows the preferential generation of single Fe sites. Besides, the formation mechanism of single Fe sites based on the gas-solid interfacial reaction is proposed based on the use of SiO_2 as hard template. The $ZnCl_2$ addition is found to be also important for the improvement of the ORR activity. Nonetheless, at odds with conventional conclusion that $ZnCl_2$ usually acts as "porogen" to create micropore for hosting more FeN_x sites, the role of $ZnCl_2$ in our work is supposed to operate in other ways. Further, the Fe sites are proposed to exist in the form of Cl-FeN_4 moieties revealed by EXAFS fitting result. The control experiments reveal that both of Cl-FeN_4 moieties and pyridinic-N are active sites with Cl-FeN_4 being the most active sites and the

Fe-based nanoparticles shows no activity towards ORR in alkaline media. However, similar to the first work, the activity of Cl-FeN_4 moieties and its comparison analysis with pristine FeN_4 sites still need to be verified by DFT calculation. On the other hand, the role of Cl in axial orientation and its stability under operation are elusive, and corresponding XAS measurement of model catalyst after reaction should be further tested to reveal the reduction mechanism of O_2 at such active sites. Likewise, the ORR activity in acidic media and application in real condition like MEA are also required for further development.

Chapter 5 presents a simplified fabrication methodology for the synthesis of Fe-N-C hierarchical porous carbon networks using glucose as optimal carbon source, ammonium chloride as nitrogen source and SiO_2 as hard template for the construction of porous electrocatalyst. In this work, pyrolysis temperature has been investigated to obtain an optimal synthesis condition. The result suggests that the ORR activity is greatly dependent to the pyrolysis temperature, with 900 ^{o}C being the optimal one. Indeed, the excessive pyrolysis temperature (1000 ^{o}C) will lead to aggregation of Fe atom and the loss of N contents (FeN_x moieties) which compromise the ORR activity. While the high N content and FeN_x moieties are retained with low pyrolysis temperature (800 ^{o}C) compared with those of sample prepared in 900 ^{o}C, the ORR activity is still inferior with respect to those of other samples. Systematical studies reveal that too high oxygen content, especially for that belonging to carboxyl groups, with strong electron withdrawing property and low electron conductivity, are mainly responsible for the low ORR activity. The too strong effect of electron withdrawing results in the reduction of TOF on the Fe center, thus decreasing the ORR activity. This work sheds light on the importance of trend-off between the exposure density of FeN_x active sites and its intrinsic activity as well as the whole conductivity of the samples. However, there still are some prospective investigations for the development of this work. First of all, the precise nature of the samples prepared with different pyrolysis temperature should be analyzed by XAS analysis and HAADF-STEM images. In fact, there have been precedents regarding the role of pyrolysis temperature on tailoring the coordination number of FeN_x (X = 1, 3, 4, 5, 6) [162, 351]. Once the nature of the active sites is identified, corresponding DFT calculation is required to confirm the reactivity of different FeN_x moiety. In this end, the structure-performance might be resized in our present work. Secondary, the site density (SD) of single Fe sites on different samples, prepared with different pyrolysis temperature, should be evaluated by nitrite stripping voltammetry as to determine the corresponding TOF. Further comparison on TOF of various samples allows more directly and convinced establishment of structure-performance relationship. Lastly, although optimal catalyst shows a decent ORR activity in alkaline media, the performance in acidic media still needs to be further improved.

Chapter 6 reports a new catalytic system which allows facile one-step thermal pyrolysis using carbon black as primary carbon source and backbone structure, glucose as secondary carbon source, and urea as nitrogen source. The use of carbon black not only significant increases the yield of the final production of the catalyst, but also acting as soft template to facilitate the dispersion of secondary carbon phase and Fe-based species. The resulting material presents a desired hierarchical porous structure with co-existence of FeN_x moieties and Fe-based metal compounds. Specifically, the Fe-based metal phases are composed of high carbon-coated Fe_3C phase and low carbon-coated Fe_3O_4 phase, which afford a great chance for the selective removal of single Fe_3O_4 phase by post-synthesis acid leaching step. A series of control experiments suggest that FeN_x moieties are the actual active sites while Fe_3O_4 itself is inactive but exerts an electron synergistic effect on FeN_x moieties for improving ORR activity. This work unravels the ORR activity origin on Fe-N-C catalyst with high complicated multiple active sites, which would be a valuable guideline for the design of next generation non-precious metal Fe-based electrocatalysts. However, direct evidence for the existence of FeN_x moieties needs to be verified by HAADF-STEM and XAS is required to get more insight into coordination information of Fe. In addition, the DFT calculation is also required to reveal the electron interaction between FeN_x moiety and Fe_3O_4 nanoparticles which is expected to be at the origin of the ORR activity in alkaline medium. Further MEA should also be evaluated for the assessment of the ORR performance in view of practical application.

The results obtained from this work confirm that single FeN_x sites are active sites for performing ORR process with full 4-electron selectivity. The results also confirm that Fe_3O_4 nanoparticles shows no activity toward ORR in alkaline but the synergistic effect between Fe_3O_4 nanoparticles and FeN_x moiety might exist which is dependent of different catalytic systems. There are still additional works remain to complete the investigation such as stability degradation mechanism for the proposed catalytic active sites (FeN_x moiety at interfacial between Fe oxyhydroxide and N-doped C networks, and Cl-FeN_4 active sites) in the alkaline medium. Finally, it is worth noting that this work also represents a universal approach for the synthesis of other single metal atom catalysts such as Co-N-C, Mn-N-C, Ni-N-C, Cu-N-C etc., which can be further applied in numerous applications of interest, i.e. CO_2 electroreduction, N_2 electroreduction; Li-sulfur battery etc. Besides, such single site catalysts could also be used as heterogeneous catalysts and not only to the field of electrocatalysis.

Annex: Publications, oral presentations

1. Publications

[1] **Xiong. Zhang**, Lai. Truong-Phuoc, Xuemei. Liao, Giulia. Tuci, Emiliano. Fonda, Vasiliki. Papaefthymiou, Spyridon. Zafeiratos, Giuliano. Giambastiani, Sergey. Pronkin, Cuong. Pham-Huu, An Open Gate for High-Density Metal Ions in N-Doped Carbon Networks: Powering Fe–N–C Catalyst Efficiency in the Oxygen Reduction Reaction, ***ACS Catalysis***, 11 (2021) 8915-8928.

[2] **Xiong Zhang**, Lai Truong-Phuoc, Xuemei Liao, Vasiliki Papaefthymiou, Matteo Pugliesi, Giulia Tuci, Giuliano Giambastiani, Sergey Pronkin, Cuong Pham-Huu, Inducing Atomically Dispersed Cl-FeN_4 Sites for ORR in the SiO_2-Mediated Synthesis of Highly Mesoporous N-enriched C-networks, ***Journal of Materials Chemistry A***, 2021, DOI: 10.1039/D1TA09519F.

[3] Giulia Tuci, Andrea Rossin, **Xiong Zhang**, Cuong Pham-Huu, and Giuliano Giambastiania, Chemically Functionalized Carbon-Based Networks as Catalysts for Electrochemical Syntheses, ***Current Opinion in Green and Sustainable Chemistry***, 2021, DOI: 10.1016/j.cogsc.2021.100579.

[4] **Xiong Zhang**, Lai Truong-Phuoc, Tristan Asset, Sergey Pronkin, Cuong Pham-Huu, Is Fe-N-C an Alternative to Pt-based Electrocatalysts for the Next Generation of Proton Exchange Membrane Fuel Cells? ***To be submited.***

[5] **Xiong Zhang**, Lai Truong-Phuoc, Vasiliki Papaefthymiou, Giulia Tuci, Giuliano Giambastiani, Sergey Pronkin, Cuong Pham-Huu, Fe_3O_4/Fe_3C nanoparticles coupled with single Fe atoms on hierarchical porous graphene-like carbon nanosheet/carbon black hybrid for electrocatalytic oxygen reduction reaction. ***In preparation.***

2. Oral presentations

[1] Atomic Fe decorated N-doped porous carbon electrocatalysts with high performance in oxygen electroreduction, **Xiong Zhang**, Lai Truong-Phuoc, Giuliano Giambastiani, Sergey Pronkin, Cuong Pham-Huu, 29th Topical Meeting of the International Society of Electrochemistry 18 - 21 April 2021 Online Meeting - Mikulov, Czech Republic

[2] Fe_3O_4/Fe_3C nanoparticles coupled with single Fe atoms on hierarchical porous graphene-like carbon nanosheet/carbon black hybrid for electrocatalytic oxygen reduction reaction, **Xiong Zhang**, Lai Truong-Phuoc, Vasiliki Papaefthymiou, Giulia Tuci, Giuliano Giambastiani, Sergey Pronkin, Cuong Pham-Huu, 6th Indo-French Symposium “Functionalized MATerials for Sustainable CATalytic and Related Applications” 26 - 28 October 2021 - Strasbourg, France.

References

[1] Z.F. Huang, J. Wang, Y. Peng, C.Y. Jung, A. Fisher, X. Wang, Design of efficient bifunctional oxygen reduction/evolution electrocatalyst: recent advances and perspectives, Advanced Energy Materials, 7 (2017) 1700544.

[2] F.T. Wagner, B. Lakshmanan, M.F. Mathias, Electrochemistry and the future of the automobile, The Journal of Physical Chemistry Letters, 1 (2010) 2204-2219.

[3] G. Faubert, G. Lalande, R. Cote, D. Guay, J. Dodelet, L. Weng, P. Bertrand, G. Denes, Heat-treated iron and cobalt tetraphenylporphyrins adsorbed on carbon black: physical characterization and catalytic properties of these materials for the reduction of oxygen in polymer electrolyte fuel cells, Electrochimica Acta, 41 (1996) 1689-1701.

[4] M.-S. Liao, S. Scheiner, Electronic structure and bonding in metal porphyrins, metal = Fe, Co, Ni, Cu, Zn, The Journal of chemical physics, 117 (2002) 205-219.

[5] H. Schulenburg, S. Stankov, V. Schünemann, J. Radnik, I. Dorbandt, S. Fiechter, P. Bogdanoff, H. Tributsch, Catalysts for the oxygen reduction from heat-treated iron (III) tetramethoxyphenylporphyrin chloride: structure and stability of active sites, The Journal of Physical Chemistry B, 107 (2003) 9034-9041.

[6] E. Proietti, F. Jaouen, M. Lefèvre, N. Larouche, J. Tian, J. Herranz, J.-P. Dodelet, Iron-based cathode catalyst with enhanced power density in polymer electrolyte membrane fuel cells, Nature communications, 2 (2011) 1-9.

[7] F. Jaouen, J. Herranz, M. Lefevre, J.-P. Dodelet, U.I. Kramm, I. Herrmann, P. Bogdanoff, J. Maruyama, T. Nagaoka, A. Garsuch, Cross-laboratory experimental study of non-noble-metal electrocatalysts for the oxygen reduction reaction, ACS applied materials & interfaces, 1 (2009) 1623-1639.

[8] T. Asset, P. Atanassov, Iron-nitrogen-carbon catalysts for proton exchange membrane fuel cells, Joule, 4 (2020) 33-44.

[9] B. Singh, V. Sharma, R.P. Gaikwad, P. Fornasiero, R. Zboril, M.B. Gawande, Single - Atom Catalysts: A Sustainable Pathway for the Advanced Catalytic Applications, Small, 17 (2021) 2006473.

[10] M.B. Gawande, P. Fornasiero, R. Zbořil, Carbon-based single-atom catalysts for advanced applications, ACS Catalysis, 10 (2020) 2231-2259.

[11] S.K. Kaiser, Z. Chen, D. Faust Akl, S. Mitchell, J. Pérez-Ramírez, Single-atom catalysts across the periodic table, Chemical Reviews, 120 (2020) 11703-11809.

[12] Z. Kou, W. Zang, Y. Ma, Z. Pan, S. Mu, X. Gao, B. Tang, M. Xiong, X. Zhao, A.K. Cheetham, Cage-confinement pyrolysis route to size-controlled molybdenum-based oxygen electrode catalysts: from isolated atoms to clusters and nanoparticles, Nano Energy, 67 (2020) 104288.

[13] Y. Chen, S. Ji, C. Chen, Q. Peng, D. Wang, Y. Li, Single-atom catalysts: synthetic strategies and electrochemical applications, Joule, 2 (2018) 1242-1264.

[14] H. Ba, Y. Liu, L. Truong-Phuoc, C. Duong-Viet, X. Mu, W.H. Doh, T. Tran-Thanh, W. Baaziz, L. Nguyen-Dinh, J.-M. Nhut, A highly N-doped carbon phase "dressing" of macroscopic supports for catalytic applications, Chemical Communications, 51 (2015) 14393-14396.

[15] H. Ba, Y. Liu, L. Truong-Phuoc, C. Duong-Viet, J.-M. Nhut, D.L. Nguyen, O. Ersen, G. Tuci, G. Giambastiani, C. Pham-Huu, N-doped food-grade-derived 3D mesoporous foams as metal-free systems for catalysis, ACS Catalysis, 6 (2016) 1408-1419.

[16] H. Ba, J. Luo, Y. Liu, C. Duong-Viet, G. Tuci, G. Giambastiani, J.-M. Nhut, L. Nguyen-Dinh, O. Ersen, D.S. Su, Macroscopically shaped monolith of nanodiamonds@ nitrogen-enriched mesoporous carbon decorated SiC as a superior metal-free catalyst for the styrene production, Applied Catalysis B: Environmental, 200 (2017) 343-350.

[17] C. Duong-Viet, J.-M. Nhut, T. Truong-Huu, G. Tuci, L. Nguyen-Dinh, Y. Liu, C. Pham, G. Giambastiani, C. Pham-Huu, A nitrogen-doped carbon-coated silicon carbide as a robust and highly efficient metal-free catalyst for sour gas desulfurization in the presence of aromatics as contaminants, Catalysis Science & Technology, 10 (2020) 5487-5500.

[18] C. Duong-Viet, J.-M. Nhut, T. Truong-Huu, G. Tuci, L. Nguyen-Dinh, C. Pham, G. Giambastiani, C. Pham-Huu, Tailoring Properties of Metal-Free Catalysts for the Highly Efficient Desulfurization of Sour Gases under Harsh Conditions, Catalysts, 11 (2021) 226.

[19] L. Nagy, T. Gajda, J. Kürti, K. Schrantz, K. Burger, Spectroscopic studies of iron (III) complexes of D-saccharose and D-glucose in the solid state and in solution, Journal of radioanalytical and nuclear chemistry, 209 (1996) 225-234.

[20] L. Nagy, K. Burger, J. Kürti, M. Mostafa, L. Korecz, I. Kiricsi, Iron (III) complexes of sugar-type ligands, Inorganica chimica acta, 124 (1986) 55-59.

[21] Y. Jiao, Y. Zheng, M. Jaroniec, S.Z. Qiao, Design of electrocatalysts for oxygen-and hydrogen-involving energy conversion reactions, Chemical Society Reviews, 44 (2015) 2060-2086.

[22] W. Zhang, W. Lai, R. Cao, Energy-related small molecule activation reactions: oxygen reduction and hydrogen and oxygen evolution reactions catalyzed by porphyrin-and corrole-based systems, Chemical reviews, 117 (2017) 3717-3797.

[23] M.K. Debe, Electrocatalyst approaches and challenges for automotive fuel cells, Nature, 486 (2012) 43-51.

[24] X. Wang, Z. Li, Y. Qu, T. Yuan, W. Wang, Y. Wu, Y. Li, Review of metal catalysts for oxygen reduction reaction: from nanoscale engineering to atomic design, Chem, (2019).

[25] C. Wan, X. Duan, Y. Huang, Molecular Design of Single‐Atom Catalysts for Oxygen Reduction Reaction, Advanced Energy Materials, 10 (2020) 1903815.

[26] G. Wu, P. Zelenay, Nanostructured nonprecious metal catalysts for oxygen reduction reaction, Accounts of chemical research, 46 (2013) 1878-1889.

[27] D. Banham, S. Ye, Current status and future development of catalyst materials and catalyst layers for proton exchange membrane fuel cells: an industrial perspective, ACS Energy Letters, 2 (2017) 629-638.

[28] X. Huang, Z. Zhao, L. Cao, Y. Chen, E. Zhu, Z. Lin, M. Li, A. Yan, A. Zettl, Y.M. Wang, High-performance transition metal–doped Pt_3Ni octahedra for oxygen reduction reaction, Science, 348 (2015) 1230-1234.

[29] L. Chong, J. Wen, J. Kubal, F.G. Sen, J. Zou, J. Greeley, M. Chan, H. Barkholtz, W. Ding, D.-J. Liu, Ultralow-loading platinum-cobalt fuel cell catalysts derived from imidazolate frameworks, Science, 362 (2018) 1276-1281.

[30] C. Cui, L. Gan, M. Heggen, S. Rudi, P. Strasser, Compositional segregation in shaped Pt alloy nanoparticles and their structural behaviour during electrocatalysis, Nature materials, 12 (2013) 765-771.

[31] C. Wang, H. Daimon, Y. Lee, J. Kim, S. Sun, Synthesis of monodisperse Pt nanocubes and their enhanced catalysis for oxygen reduction, Journal of the American Chemical Society, 129 (2007) 6974-6975.

[32] N. Marković, R. Adžić, B. Cahan, E. Yeager, Structural effects in electrocatalysis: oxygen reduction on platinum low index single-crystal surfaces in perchloric acid solutions, Journal of Electroanalytical Chemistry, 377 (1994) 249-259.

[33] L. Zhang, L.T. Roling, X. Wang, M. Vara, M. Chi, J. Liu, S.-I. Choi, J. Park, J.A. Herron, Z. Xie, Platinum-based nanocages with subnanometer-thick walls and well-defined, controllable facets, Science, 349 (2015) 412-416.

[34] C.W. Bezerra, L. Zhang, K. Lee, H. Liu, A.L. Marques, E.P. Marques, H. Wang, J. Zhang, A review of Fe–N/C and Co–N/C catalysts for the oxygen reduction reaction, Electrochimica Acta, 53 (2008) 4937-4951.

[35] X.X. Wang, M.T. Swihart, G. Wu, Achievements, challenges and perspectives on cathode catalysts in proton exchange membrane fuel cells for transportation, Nature Catalysis, 2 (2019) 578-589.

[36] L. Yang, D. Cheng, H. Xu, X. Zeng, X. Wan, J. Shui, Z. Xiang, D. Cao, Unveiling the high-activity origin of single-atom iron catalysts for oxygen reduction reaction, Proceedings of the National Academy of Sciences, 115 (2018) 6626-6631.

[37] M. Chen, Y. He, J.S. Spendelow, G. Wu, Atomically dispersed metal catalysts for oxygen reduction, ACS Energy Letters, 4 (2019) 1619-1633.

[38] R. Jasinski, A new fuel cell cathode catalyst, Nature, 201 (1964) 1212-1213.

[39] P. Gouerec, M. Savy, J. Riga, Oxygen reduction in acidic media catalyzed by pyrolyzed cobalt macrocycles dispersed on an active carbon: The importance of the content of oxygen surface groups on the evolution of the chelate structure during the heat treatment, Electrochimica Acta, 43 (1998) 743-753.

[40] R. Franke, D. Ohms, K. Wiesener, Investigation of the influence of thermal treatment on the properties of carbon materials modified by N_4-chelates for the reduction of oxygen in acidic media, Journal of electroanalytical chemistry and interfacial electrochemistry, 260 (1989) 63-73.

[41] S. Gupta, D. Tryk, I. Bae, W. Aldred, E. Yeager, Heat-treated polyacrylonitrile-based catalysts for oxygen electroreduction, Journal of applied electrochemistry, 19 (1989) 19-27.

[42] M. Yuasa, A. Yamaguchi, H. Itsuki, K. Tanaka, M. Yamamoto, K. Oyaizu, Modifying carbon particles with polypyrrole for adsorption of cobalt ions as electrocatatytic site for oxygen reduction, Chemistry of Materials, 17 (2005) 4278-4281.

[43] V. Nallathambi, J.-W. Lee, S.P. Kumaraguru, G. Wu, B.N. Popov, Development of high performance carbon composite catalyst for oxygen reduction reaction in PEM Proton Exchange Membrane fuel cells, Journal of Power Sources, 183 (2008) 34-42.

[44] T. Schilling, M. Bron, Oxygen reduction at Fe–N-modified multi-walled carbon nanotubes in acidic electrolyte, Electrochimica Acta, 53 (2008) 5379-5385.

[45] J. Baschuk, X. Li, Carbon monoxide poisoning of proton exchange membrane fuel cells, International Journal of Energy Research, 25 (2001) 695-713.

[46] S. Yasuda, A. Furuya, Y. Uchibori, J. Kim, K. Murakoshi, Iron ‐ nitrogen ‐ doped vertically aligned carbon nanotube electrocatalyst for the oxygen reduction reaction, Advanced Functional Materials, 26 (2016) 738-744.

[47] Z. Li, J. Yang, G. Xu, S. Wang, Non-precious cathode electrocatalyst for magnesium air fuel cells: activity and durability of iron-polyphthalocyanine absorbed on carbon black, Journal of power sources, 242 (2013) 157-165.

[48] Y. Sun, L. Han, P. Strasser, A comparative perspective of electrochemical and photochemical approaches for catalytic H 2 O 2 production, Chemical Society Reviews, 49 (2020) 6605-6631.

[49] H. Yan, B. Xu, S. Shi, C. Ouyang, First-principles study of the oxygen adsorption and dissociation on graphene and nitrogen doped graphene for Li-air batteries, Journal of Applied Physics, 112 (2012) 104316.

[50] L. Ou, F. Yang, Y. Liu, S. Chen, First-principle study of the adsorption and dissociation of O_2 on Pt (111) in acidic media, The Journal of Physical Chemistry C, 113 (2009) 20657-20665.

[51] J.K. Nørskov, J. Rossmeisl, A. Logadottir, L. Lindqvist, J.R. Kitchin, T. Bligaard, H. Jonsson, Origin of the overpotential for oxygen reduction at a fuel-cell cathode, The Journal of Physical Chemistry B, 108 (2004) 17886-17892.

[52] A. Damjanovic, M. Genshaw, J.O.M. Bockris, Distinction between intermediates produced in main and side electrodic reactions, The Journal of Chemical Physics, 45 (1966) 4057-4059.

[53] H.S. Wroblowa, G. Razumney, Electroreduction of oxygen: a new mechanistic criterion, Journal of Electroanalytical Chemistry and Interfacial Electrochemistry, 69 (1976) 195-201.

[54] A. Muthukrishnan, Y. Nabae, T. Okajima, T. Ohsaka, Kinetic approach to investigate the mechanistic pathways of oxygen reduction reaction on Fe-containing N-doped carbon catalysts, ACS Catalysis, 5 (2015) 5194-5202.

[55] A. Bonakdarpour, M. Lefevre, R. Yang, F. Jaouen, T. Dahn, J.-P. Dodelet, J. Dahn, Impact of loading in RRDE experiments on Fe–N–C catalysts: two-or four-electron oxygen reduction?, Electrochemical and Solid-State Letters, 11 (2008) B105-B108.

[56] M. Bron, S. Fiechter, P. Bogdanoff, H. Tributsch, Thermogravimetry/Mass Spectrometry Investigations on the Formation of Oxygen Reduction Catalysts for PEM Fuel Cells on the Basis of Heat‐Treated Iron Phenanthroline Complexes, Fuel Cells, 2 (2002) 137-142.

[57] M. Inaba, H. Yamada, J. Tokunaga, A. Tasaka, Effect of agglomeration of Pt/C catalyst on hydrogen peroxide formation, Electrochemical and solid-state letters, 7 (2004) A474-A476.

[58] M.O. Davies, M. Clark, E. Yeager, F. Hovorka, The Oxygen Electrode I. Isotopic investigation of electrode mechanisms, Journal of The Electrochemical Society, 106 (1959) 56-61.

[59] I. Morcos, E. Yeager, Kinetic studies of the oxygen—peroxide couple on pyrolytic graphite, Electrochimica Acta, 15 (1970) 953-975.

[60] P. Fischer, J. Heitbaum, Mechanistic aspects of cathodic oxygen reduction, Journal of Electroanalytical Chemistry and Interfacial Electrochemistry, 112 (1980) 231-238.

[61] J. Park, Y. Nabae, T. Hayakawa, M.-a. Kakimoto, Highly selective two-electron oxygen reduction catalyzed by mesoporous nitrogen-doped carbon, ACS Catalysis, 4 (2014) 3749-3754.

[62] F. Jaouen, J.-P. Dodelet, O_2 reduction mechanism on non-noble metal catalysts for PEM fuel cells. Part I: Experimental rates of O_2 electroreduction, H_2O_2 electroreduction, and H_2O_2 disproportionation, The Journal of Physical Chemistry C, 113 (2009) 15422-15432.

[63] U. Tylus, Q. Jia, K. Strickland, N. Ramaswamy, A. Serov, P. Atanassov, S. Mukerjee, Elucidating oxygen reduction active sites in pyrolyzed metal–nitrogen coordinated non-precious-metal electrocatalyst systems, The Journal of Physical Chemistry C, 118 (2014) 8999-9008.

[64] K. Artyushkova, A. Serov, S. Rojas-Carbonell, P. Atanassov, Chemistry of multitudinous active sites for oxygen reduction reaction in transition metal–nitrogen–carbon electrocatalysts, The Journal of Physical Chemistry C, 119 (2015) 25917-25928.

[65] A.B. Anderson, T.V. Albu, Ab initio determination of reversible potentials and activation energies for outer-sphere oxygen reduction to water and the reverse oxidation reaction, Journal of the American Chemical Society, 121 (1999) 11855-11863.

[66] A.B. Anderson, J.m. Roques, S. Mukerjee, V.S. Murthi, N.M. Markovic, V. Stamenkovic, Activation energies for oxygen reduction on platinum alloys: Theory and experiment, The Journal of Physical Chemistry B, 109 (2005) 1198-1203.

[67] A.B. Anderson, T.V. Albu, Catalytic effect of platinum on oxygen reduction an ab initio model including electrode potential dependence, Journal of The Electrochemical Society, 147 (2000) 4229-4238.

[68] A.B. Anderson, Y. Cai, R.A. Sidik, D.B. Kang, Advancements in the local reaction center electron transfer theory and the transition state structure in the first step of oxygen reduction over platinum, Journal of Electroanalytical Chemistry, 580 (2005) 17-22.

[69] T.V. Albu, A.B. Anderson, Studies of model dependence in an ab initio approach to uncatalyzed oxygen reduction and the calculation of transfer coefficients, Electrochimica Acta, 46 (2001) 3001-3013.

[70] T. Zhang, A.B. Anderson, Oxygen reduction on platinum electrodes in base: Theoretical study, Electrochimica Acta, 53 (2007) 982-989.

[71] M.J. Janik, C.D. Taylor, M. Neurock, First-principles analysis of the initial electroreduction steps of oxygen over Pt (111), Journal of the Electrochemical Society, 156 (2009) B126-B135.

[72] Y. Sha, T.H. Yu, B.V. Merinov, P. Shirvanian, W.A. Goddard III, Oxygen hydration mechanism for the oxygen reduction reaction at Pt and Pd fuel cell catalysts, The Journal of Physical Chemistry Letters, 2 (2011) 572-576.

[73] M.-h. Shao, P. Liu, R.R. Adzic, Superoxide anion is the intermediate in the oxygen reduction reaction on platinum electrodes, Journal of the American Chemical Society, 128 (2006) 7408-7409.

[74] A.S. Bondarenko, I.E. Stephens, H.A. Hansen, F.J. Pérez-Alonso, V. Tripkovic, T.P. Johansson, J. Rossmeisl, J.K. Nørskov, I. Chorkendorff, The Pt (111)/electrolyte interface under oxygen reduction reaction conditions: an electrochemical impedance spectroscopy study, Langmuir, 27 (2011) 2058-2066.

[75] J.K. Nørskov, T. Bligaard, J. Rossmeisl, C.H. Christensen, Towards the computational design of solid catalysts, Nature Chemistry, 1 (2009) 37.

[76] B. Hammer, J.K. Norskov, Why gold is the noblest of all the metals, Nature, 376 (1995) 238-240.

[77] A. Nilsson, L. Pettersson, B. Hammer, T. Bligaard, C.H. Christensen, J.K. Nørskov, The electronic structure effect in heterogeneous catalysis, Catalysis Letters, 100 (2005) 111-114.

[78] M. Mavrikakis, B. Hammer, J.K. Nørskov, Effect of strain on the reactivity of metal surfaces, Physical Review Letters, 81 (1998) 2819.

[79] V. Stamenkovic, B.S. Mun, K.J. Mayrhofer, P.N. Ross, N.M. Markovic, J. Rossmeisl, J. Greeley, J.K. Nørskov, Changing the activity of electrocatalysts for oxygen reduction by tuning the surface electronic structure, Angewandte Chemie International Edition, 45 (2006) 2897-2901.

[80] J. Greeley, J.K. Nørskov, Combinatorial density functional theory-based screening of surface alloys for the oxygen reduction reaction, The Journal of Physical Chemistry C, 113 (2009) 4932-4939.

[81] X. Ge, A. Sumboja, D. Wuu, T. An, B. Li, F.T. Goh, T.A. Hor, Y. Zong, Z. Liu, Oxygen reduction in alkaline media: from mechanisms to recent advances of catalysts, ACS Catalysis, 5 (2015) 4643-4667.

[82] W. Xia, A. Mahmood, Z. Liang, R. Zou, S. Guo, Earth‐abundant nanomaterials for oxygen reduction, Angewandte Chemie International Edition, 55 (2016) 2650-2676.

[83] G. Chen, P. Liu, Z. Liao, F. Sun, Y. He, H. Zhong, T. Zhang, E. Zschech, M. Chen, G. Wu, Zinc‐Mediated Template Synthesis of Fe‐N‐C Electrocatalysts with Densely Accessible Fe‐Nx Active Sites for Efficient Oxygen Reduction, Advanced Materials, (2020) 1907399.

[84] N. Daems, X. Sheng, I.F. Vankelecom, P.P. Pescarmona, Metal-free doped carbon materials as electrocatalysts for the oxygen reduction reaction, Journal of Materials Chemistry A, 2 (2014) 4085-4110.

[85] H.A. Gasteiger, S.S. Kocha, B. Sompalli, F.T. Wagner, Activity benchmarks and requirements for Pt, Pt-alloy, and non-Pt oxygen reduction catalysts for PEMFCs, Applied Catalysis B: Environmental, 56 (2005) 9-35.

[86] J. Zhang, PEM fuel cell electrocatalysts and catalyst layers: fundamentals and applications, Springer Science & Business Media2008.

[87] P. Hu, Y. Song, L. Chen, S. Chen, Electrocatalytic activity of alkyne-functionalized AgAu alloy nanoparticles for oxygen reduction in alkaline media, Nanoscale, 7 (2015) 9627-9636.

[88] J.S. Spendelow, A. Wieckowski, Electrocatalysis of oxygen reduction and small alcohol oxidation in alkaline media, Physical Chemistry Chemical Physics, 9 (2007) 2654-2675.

[89] J.H. Zagal, M.T. Koper, Reactivity descriptors for the activity of molecular MN_4 catalysts for the oxygen reduction reaction, Angewandte Chemie International Edition, 55 (2016) 14510-14521.

[90] U. Paulus, T. Schmidt, H. Gasteiger, R. Behm, Oxygen reduction on a high-surface area Pt/Vulcan carbon catalyst: a thin-film rotating ring-disk electrode study, Journal of Electroanalytical Chemistry, 495 (2001) 134-145.

[91] Y.-L. Tsai, K.-L. Huang, C.-C. Yang, J.-S. Ye, L.-S. Pan, C.-L. Lee, Preparation and cyclic voltammetric dissolution of core–shell–shell Ag–Pt–Ag nanocubes and their comparison in oxygen reduction reaction in alkaline media, International journal of hydrogen energy, 39 (2014) 5528-5536.

[92] M. Tarasevich, O. Korchagin, Electrocatalysis and pH (a review), Russian Journal of Electrochemistry, 49 (2013) 600-618.

[93] N. Ramaswamy, S. Mukerjee, Fundamental mechanistic understanding of electrocatalysis of oxygen reduction on Pt and non-Pt surfaces: acid versus alkaline media, Advances in Physical Chemistry, 2012 (2012).

[94] N. Ramaswamy, S. Mukerjee, Influence of inner-and outer-sphere electron transfer mechanisms during electrocatalysis of oxygen reduction in alkaline media, The Journal of Physical Chemistry C, 115 (2011) 18015-18026.

[95] N. Ramaswamy, U. Tylus, Q. Jia, S. Mukerjee, Activity descriptor identification for oxygen reduction on nonprecious electrocatalysts: linking surface science to coordination chemistry, Journal of the American Chemical Society, 135 (2013) 15443-15449.

[96] A. Muthukrishnan, Y. Nabae, T. Hayakawa, T. Okajima, T. Ohsaka, Fe-containing polyimide-based high-performance ORR catalysts in acidic medium: a kinetic approach to study the durability of catalysts, Catalysis Science & Technology, 5 (2015) 475-483.

[97] J. Wu, D. Zhang, H. Niwa, Y. Harada, M. Oshima, H. Ofuchi, Y. Nabae, T. Okajima, T. Ohsaka, Enhancement in kinetics of the oxygen reduction reaction on a nitrogen-doped carbon catalyst by introduction of iron via electrochemical methods, Langmuir, 31 (2015) 5529-5536.

[98] J.A. Varnell, J.S. Sotiropoulos, T.M. Brown, K. Subedi, R.T. Haasch, C.E. Schulz, A.A. Gewirth, Revealing the role of the metal in non-precious-metal catalysts for oxygen reduction via selective removal of Fe, ACS Energy Letters, 3 (2018) 823-828.

[99] C.H. Choi, W.S. Choi, O. Kasian, A.K. Mechler, M.T. Sougrati, S. Brüller, K. Strickland, Q. Jia, S. Mukerjee, K.J. Mayrhofer, Unraveling the Nature of Sites Active toward Hydrogen Peroxide Reduction in Fe‐N‐C Catalysts, Angewandte Chemie International Edition, 56 (2017) 8809-8812.

[100] L. Lin, Q. Zhu, A.-W. Xu, Noble-metal-free Fe–N/C catalyst for highly efficient oxygen reduction reaction under both alkaline and acidic conditions, Journal of the American Chemical Society, 136 (2014) 11027-11033.

[101] H. Meng, F. Jaouen, E. Proietti, M. Lefèvre, J.-P. Dodelet, pH-effect on oxygen reduction activity of Fe-based electro-catalysts, Electrochemistry communications, 11 (2009) 1986-1989.

[102] W. Wang, Q. Jia, S. Mukerjee, S. Chen, Recent insights into the oxygen-reduction electrocatalysis of Fe/N/C materials, ACS Catalysis, 9 (2019) 10126-10141.

[103] H. Shen, T. Thomas, S.A. Rasaki, A. Saad, C. Hu, J. Wang, M. Yang, Oxygen reduction reactions of Fe-NC catalysts: current status and the way forward, Electrochemical Energy Reviews, (2019) 1-25.

[104] K. Wan, Z.-p. Yu, X.-h. Li, M.-y. Liu, G. Yang, J.-h. Piao, Z.-x. Liang, pH effect on electrochemistry of nitrogen-doped carbon catalyst for oxygen reduction reaction, ACS Catalysis, 5 (2015) 4325-4332.

[105] M. Rauf, Y.-D. Zhao, Y.-C. Wang, Y.-P. Zheng, C. Chen, X.-D. Yang, Z.-Y. Zhou, S.-G. Sun, Insight into the different ORR catalytic activity of Fe/N/C between acidic and alkaline media: protonation of pyridinic nitrogen, Electrochemistry Communications, 73 (2016) 71-74.

[106] J. Herranz, F. Jaouen, M. Lefèvre, U.I. Kramm, E. Proietti, J.-P. Dodelet, P. Bogdanoff, S. Fiechter, I. Abs-Wurmbach, P. Bertrand, Unveiling N-protonation and anion-binding effects on Fe/N/C catalysts for O_2 reduction in proton-exchange-membrane fuel cells, The Journal of Physical Chemistry C, 115 (2011) 16087-16097.

[107] Z.Y. Wu, X.X. Xu, B.C. Hu, H.W. Liang, Y. Lin, L.F. Chen, S.H. Yu, Iron carbide nanoparticles encapsulated in mesoporous Fe‐N‐doped carbon nanofibers for efficient electrocatalysis, Angewandte Chemie International Edition, 54 (2015) 8179-8183.

[108] Y. Hu, J.O. Jensen, W. Zhang, L.N. Cleemann, W. Xing, N.J. Bjerrum, Q. Li, Hollow spheres of iron carbide nanoparticles encased in graphitic layers as oxygen reduction catalysts, Angewandte Chemie International Edition, 53 (2014) 3675-3679.

[109] K. Strickland, E. Miner, Q. Jia, U. Tylus, N. Ramaswamy, W. Liang, M.-T. Sougrati, F. Jaouen, S. Mukerjee, Highly active oxygen reduction non-platinum group metal electrocatalyst without direct metal–nitrogen coordination, Nature communications, 6 (2015) 7343.

[110] J. Blomquist, H. Lång, R. Larsson, A. Widelöv, Pyrolysis behaviour of metalloporphyrins. Part 2.—A mössbauer study of pyrolysed Fe III tetraphenylporphyrin chloride, Journal of the Chemical Society, Faraday Transactions, 88 (1992) 2007-2011.

[111] Q. Jia, N. Ramaswamy, U. Tylus, K. Strickland, J. Li, A. Serov, K. Artyushkova, P. Atanassov, J. Anibal, C. Gumeci, Spectroscopic insights into the nature of active sites in iron–nitrogen–carbon electrocatalysts for oxygen reduction in acid, Nano Energy, 29 (2016) 65-82.

[112] P. Song, Y. Wang, J. Pan, W. Xu, L. Zhuang, Structure-activity relationship in high-performance iron-based electrocatalysts for oxygen reduction reaction, Journal of Power Sources, 300 (2015) 279-284.

[113] U.I. Kramm, I. Herrmann-Geppert, J. Behrends, K. Lips, S. Fiechter, P. Bogdanoff, On an easy way to prepare metal–nitrogen doped carbon with exclusive presence of MeN_4-type sites active for the ORR, Journal of the American Chemical Society, 138 (2016) 635-640.

[114] H. Zhang, H.T. Chung, D.A. Cullen, S. Wagner, U.I. Kramm, K.L. More, P. Zelenay, G. Wu, High-performance fuel cell cathodes exclusively containing atomically dispersed iron active sites, Energy & Environmental Science, 12 (2019) 2548-2558.

[115] S. Maldonado, K.J. Stevenson, Direct preparation of carbon nanofiber electrodes via pyrolysis of iron (II) phthalocyanine: electrocatalytic aspects for oxygen reduction, The Journal of Physical Chemistry B, 108 (2004) 11375-11383.

[116] G. Liu, X. Li, P. Ganesan, B.N. Popov, Studies of oxygen reduction reaction active sites and stability of nitrogen-modified carbon composite catalysts for PEM fuel cells, Electrochimica Acta, 55 (2010) 2853-2858.

[117] P. Wang, Z. Ma, Z. Zhao, L. Jia, Oxygen reduction on the electrocatalysts based on pyrolyzed non-noble metal/poly-o-phenylenediamine/carbon black composites: New insight into the active sites, Journal of Electroanalytical Chemistry, 611 (2007) 87-95.

[118] G. Zhang, R. Chenitz, M. Lefèvre, S. Sun, J.-P. Dodelet, Is iron involved in the lack of stability of Fe/N/C electrocatalysts used to reduce oxygen at the cathode of PEM fuel cells?, Nano Energy, 29 (2016) 111-125.

[119] J. Li, S. Ghoshal, W. Liang, M.-T. Sougrati, F. Jaouen, B. Halevi, S. McKinney, G. McCool, C. Ma, X. Yuan, Structural and mechanistic basis for the high activity of Fe–N–C catalysts toward oxygen reduction, Energy & Environmental Science, 9 (2016) 2418-2432.

[120] K. Gong, F. Du, Z. Xia, M. Durstock, L. Dai, Nitrogen-doped carbon nanotube arrays with high electrocatalytic activity for oxygen reduction, Science, 323 (2009) 760-764.

[121] D. Wang, D. Su, Energy Environ. Sci. 2014, 7, 576–591; c) G. Wu, KL More, CM Johnston, P. Zelenay, Science, 332 (2011) 443-447.

[122] G. Lalande, R. Cote, D. Guay, J. Dodelet, L. Weng, P. Bertrand, Is nitrogen important in the formulation of Fe-based catalysts for oxygen reduction in solid polymer fuel cells?, Electrochimica Acta, 42 (1997) 1379-1388.

[123] L. Zhang, Z. Xia, Mechanisms of oxygen reduction reaction on nitrogen-doped graphene for fuel cells, The Journal of Physical Chemistry C, 115 (2011) 11170-11176.

[124] N. Yang, L. Li, J. Li, W. Ding, Z. Wei, Modulating the oxygen reduction activity of heteroatom-doped carbon catalysts via the triple effect: charge, spin density and ligand effect, Chemical Science, 9 (2018) 5795-5804.

[125] X. Hu, Y. Wu, H. Li, Z. Zhang, Adsorption and activation of O_2 on nitrogen-doped carbon nanotubes, The Journal of Physical Chemistry C, 114 (2010) 9603-9607.

[126] Z. Zhao, M. Li, L. Zhang, L. Dai, Z. Xia, Design principles for heteroatom ‐ doped carbon nanomaterials as highly efficient catalysts for fuel cells and metal – air batteries, Advanced Materials, 27 (2015) 6834-6840.

[127] D. Guo, R. Shibuya, C. Akiba, S. Saji, T. Kondo, J. Nakamura, Active sites of nitrogen-doped carbon materials for oxygen reduction reaction clarified using model catalysts, Science, 351 (2016) 361-365.

[128] L. Qu, Y. Liu, J.-B. Baek, L. Dai, Nitrogen-doped graphene as efficient metal-free electrocatalyst for oxygen reduction in fuel cells, ACS nano, 4 (2010) 1321-1326.

[129] C.V. Rao, C.R. Cabrera, Y. Ishikawa, In search of the active site in nitrogen-doped carbon nanotube electrodes for the oxygen reduction reaction, The Journal of Physical Chemistry Letters, 1 (2010) 2622-2627.

[130] Z.-H. Sheng, L. Shao, J.-J. Chen, W.-J. Bao, F.-B. Wang, X.-H. Xia, Catalyst-free synthesis of nitrogen-doped graphene via thermal annealing graphite oxide with melamine and its excellent electrocatalysis, ACS nano, 5 (2011) 4350-4358.

[131] Y. Li, Y. Zhao, H. Cheng, Y. Hu, G. Shi, L. Dai, L. Qu, Nitrogen-doped graphene quantum dots with oxygen-rich functional groups, Journal of the American Chemical Society, 134 (2012) 15-18.

[132] N.P. Subramanian, X. Li, V. Nallathambi, S.P. Kumaraguru, H. Colon-Mercado, G. Wu, J.-W. Lee, B.N. Popov, Nitrogen-modified carbon-based catalysts for oxygen reduction reaction in polymer electrolyte membrane fuel cells, Journal of Power Sources, 188 (2009) 38-44.

[133] H. Niwa, K. Horiba, Y. Harada, M. Oshima, T. Ikeda, K. Terakura, J.-i. Ozaki, S. Miyata, X-ray absorption analysis of nitrogen contribution to oxygen reduction reaction in carbon alloy cathode catalysts for polymer electrolyte fuel cells, Journal of Power Sources, 187 (2009) 93-97.

[134] L. Lai, J. Potts, D. Zhan, L. Wang, C. Poh, C. Tang, H. Gong, Z. Shen, J. Lin, R. Ruoff, Exploration of the active center structure of nitrogen-doped graphene-based catalysts for oxygen reduction reaction, Energy & Environmental Science, (2012) 7936-7942.

[135] H. Kim, K. Lee, S.I. Woo, Y. Jung, On the mechanism of enhanced oxygen reduction reaction in nitrogen-doped graphene nanoribbons, Physical Chemistry Chemical Physics, 13 (2011) 17505-17510.

[136] T. Xing, Y. Zheng, L.H. Li, B.C. Cowie, D. Gunzelmann, S.Z. Qiao, S. Huang, Y. Chen, Observation of active sites for oxygen reduction reaction on nitrogen-doped multilayer graphene, ACS Nano, 8 (2014) 6856-6862.

[137] J. Masa, W. Xia, M. Muhler, W. Schuhmann, On the role of metals in nitrogen ‐ doped carbon electrocatalysts for oxygen reduction, Angewandte Chemie International Edition, 54 (2015) 10102-10120.

[138] Y. Ding, Y. Niu, J. Yang, L. Ma, J. Liu, Y. Xiong, H. Xu, A Metal‐Amino Acid Complex‐Derived Bifunctional Oxygen Electrocatalyst for Rechargeable Zinc–Air Batteries, Small, 12 (2016) 5414-5421.

[139] Y. Hou, T. Huang, Z. Wen, S. Mao, S. Cui, J. Chen, Metal– organic framework‐derived nitrogen‐doped core‐shell‐structured porous Fe/Fe3C@ C nanoboxes supported on graphene sheets for efficient oxygen reduction reactions, Advanced Energy Materials, 4 (2014) 1400337.

[140] D. Deng, L. Yu, X. Chen, G. Wang, L. Jin, X. Pan, J. Deng, G. Sun, X. Bao, Iron encapsulated within pod‐like carbon nanotubes for oxygen reduction reaction, Angewandte Chemie International Edition, 52 (2013) 371-375.

[141] X. Fan, Z. Peng, R. Ye, H. Zhou, X. Guo, M_3C (M: Fe, Co, Ni) nanocrystals encased in graphene nanoribbons: an active and stable bifunctional electrocatalyst for oxygen reduction and hydrogen evolution reactions, ACS nano, 9 (2015) 7407-7418.

[142] Z. Wen, S. Ci, F. Zhang, X. Feng, S. Cui, S. Mao, S. Luo, Z. He, J. Chen, Nitrogen‐enriched core‐shell structured Fe/Fe_3C‐C nanorods as advanced electrocatalysts for oxygen reduction reaction, Advanced Materials, 24 (2012) 1399-1404.

[143] C. Zhang, J. Liu, Y. Ye, Z. Aslam, R. Brydson, C. Liang, Fe–N-doped mesoporous carbon with dual active sites loaded on reduced graphene oxides for efficient oxygen reduction catalysts, ACS applied materials & interfaces, 10 (2018) 2423-2429.

[144] J. Liang, R.F. Zhou, X.M. Chen, Y.H. Tang, S.Z. Qiao, Fe–N decorated hybrids of CNTs grown on hierarchically porous carbon for high‐performance oxygen reduction, Advanced materials, 26 (2014) 6074-6079.

[145] Y. Qiao, P. Yuan, Y. Hu, J. Zhang, S. Mu, J. Zhou, H. Li, H. Xia, J. He, Q. Xu, Sulfuration of an Fe–N–C catalyst containing Fe_xC/Fe species to enhance the catalysis of oxygen reduction in acidic media and for use in flexible Zn–air batteries, Advanced Materials, 30 (2018) 1804504.

[146] X. Ao, W. Zhang, Z. Li, J.-G. Li, L. Soule, X. Huang, W.-H. Chiang, H.M. Chen, C. Wang, M. Liu, Markedly enhanced oxygen reduction activity of single-atom Fe catalysts via integration with Fe nanoclusters, ACS nano, 13 (2019) 11853-11862.

[147] W.-J. Jiang, L. Gu, L. Li, Y. Zhang, X. Zhang, L.-J. Zhang, J.-Q. Wang, J.-S. Hu, Z. Wei, L.-J. Wan, Understanding the high activity of Fe–N–C electrocatalysts in oxygen reduction: Fe/Fe_3C nanoparticles boost the activity of Fe–N_x, Journal of the American Chemical Society, 138 (2016) 3570-3578.

[148] U.I. Kramm, I. Herrmann-Geppert, S. Fiechter, G. Zehl, I. Zizak, I. Dorbandt, D. Schmeißer, P. Bogdanoff, Effect of iron-carbide formation on the number of active sites in Fe–N–C catalysts for

the oxygen reduction reaction in acidic media, Journal of Materials Chemistry A, 2 (2014) 2663-2670.

[149] K. Kumar, P. Gairola, M. Lions, N. Ranjbar-Sahraie, M. Mermoux, L. Dubau, A. Zitolo, F.d.r. Jaouen, F. Maillard, Physical and chemical considerations for improving catalytic activity and stability of non-precious-metal oxygen reduction reaction catalysts, ACS Catalysis, 8 (2018) 11264-11276.

[150] M. Tavakkoli, T. Kallio, O. Reynaud, A.G. Nasibulin, C. Johans, J. Sainio, H. Jiang, E.I. Kauppinen, K. Laasonen, Single‐shell carbon‐encapsulated iron nanoparticles: synthesis and high electrocatalytic activity for hydrogen evolution reaction, Angewandte Chemie International Edition, 54 (2015) 4535-4538.

[151] D.Y. Chung, S.W. Jun, G. Yoon, S.G. Kwon, D.Y. Shin, P. Seo, J.M. Yoo, H. Shin, Y.-H. Chung, H. Kim, Highly durable and active PtFe nanocatalyst for electrochemical oxygen reduction reaction, Journal of the American Chemical Society, 137 (2015) 15478-15485.

[152] W. Yang, M. Zhao, X. Ding, K. Ma, C. Wu, I.D. Gates, Z. Gao, The effect of coordination environment on the kinetic and thermodynamic stability of single-atom iron catalysts, Physical Chemistry Chemical Physics, 22 (2020) 3983-3989.

[153] A. Bouwkamp-Wijnoltz, W. Visscher, J. Van Veen, E. Boellaard, A. Van der Kraan, S. Tang, On active-site heterogeneity in pyrolyzed carbon-supported iron porphyrin catalysts for the electrochemical reduction of oxygen: an in situ mössbauer study, The Journal of Physical Chemistry B, 106 (2002) 12993-13001.

[154] H. Shen, E. Gracia-Espino, J. Ma, H. Tang, X. Mamat, T. Wagberg, G. Hu, S. Guo, Atomically FeN_2 moieties dispersed on mesoporous carbon: A new atomic catalyst for efficient oxygen reduction catalysis, Nano Energy, 35 (2017) 9-16.

[155] M. Lefèvre, J.-P. Dodelet, Fe-based catalysts for the reduction of oxygen in polymer electrolyte membrane fuel cell conditions: determination of the amount of peroxide released during electroreduction and its influence on the stability of the catalysts, Electrochimica Acta, 48 (2003) 2749-2760.

[156] C. Zhu, Q. Shi, B.Z. Xu, S. Fu, G. Wan, C. Yang, S. Yao, J. Song, H. Zhou, D. Du, Hierarchically Porous M‐N‐C (M= Co and Fe) Single‐Atom Electrocatalysts with Robust MN_x Active Moieties Enable Enhanced ORR Performance, Advanced Energy Materials, 8 (2018) 1801956.

[157] Q.-K. Li, X.-F. Li, G. Zhang, J. Jiang, Cooperative spin transition of monodispersed FeN_3 sites within graphene induced by CO adsorption, Journal of the American Chemical Society, 140 (2018) 15149-15152.

[158] Y. Zhu, B. Zhang, X. Liu, D.W. Wang, D.S. Su, Unravelling the structure of electrocatalytically active Fe–N complexes in carbon for the oxygen reduction reaction, Angewandte Chemie International Edition, 53 (2014) 10673-10677.

[159] Q. Lai, L. Zheng, Y. Liang, J. He, J. Zhao, J. Chen, Metal–organic-framework-derived Fe-N/C electrocatalyst with five-coordinated Fe-N x sites for advanced oxygen reduction in acid media, Acs Catalysis, 7 (2017) 1655-1663.

[160] S. Kabir, K. Artyushkova, B. Kiefer, P. Atanassov, Computational and experimental evidence for a new TM–N 3/C moiety family in non-PGM electrocatalysts, Physical Chemistry Chemical Physics, 17 (2015) 17785-17789.

[161] E.F. Holby, G. Wu, P. Zelenay, C.D. Taylor, Structure of Fe–N x–C Defects in Oxygen Reduction Reaction Catalysts from First-Principles Modeling, The Journal of Physical Chemistry C, 118 (2014) 14388-14393.

[162] Y. Li, X. Liu, L. Zheng, J. Shang, X. Wan, R. Hu, X. Guo, S. Hong, J. Shui, Preparation of Fe–N–C catalysts with FeN_x (x= 1, 3, 4) active sites and comparison of their activities for the oxygen reduction reaction and performances in proton exchange membrane fuel cells, Journal of Materials Chemistry A, 7 (2019) 26147-26153.

[163] M. Lefèvre, J. Dodelet, P. Bertrand, Molecular oxygen reduction in PEM fuel cells: evidence for the simultaneous presence of two active sites in Fe-based catalysts, The Journal of Physical Chemistry B, 106 (2002) 8705-8713.

[164] M. Lefevre, J. Dodelet, P. Bertrand, O2 reduction in PEM fuel cells: activity and active site structural information for catalysts obtained by the pyrolysis at high temperature of Fe precursors, The Journal of Physical Chemistry B, 104 (2000) 11238-11247.

[165] H.T. Chung, D.A. Cullen, D. Higgins, B.T. Sneed, E.F. Holby, K.L. More, P. Zelenay, Direct atomic-level insight into the active sites of a high-performance PGM-free ORR catalyst, Science, 357 (2017) 479-484.

[166] H. Fei, J. Dong, Y. Feng, C.S. Allen, C. Wan, B. Volosskiy, M. Li, Z. Zhao, Y. Wang, H. Sun, General synthesis and definitive structural identification of MN 4 C 4 single-atom catalysts with tunable electrocatalytic activities, Nature Catalysis, 1 (2018) 63-72.

[167] D. Deng, X. Chen, L. Yu, X. Wu, Q. Liu, Y. Liu, H. Yang, H. Tian, Y. Hu, P. Du, A single iron site confined in a graphene matrix for the catalytic oxidation of benzene at room temperature, Science advances, 1 (2015) e1500462.

[168] U.I. Kramm, M. Lefèvre, N. Larouche, D. Schmeisser, J.-P. Dodelet, Correlations between mass activity and physicochemical properties of Fe/N/C catalysts for the ORR in PEM fuel cell via ^{57}Fe

Mossbauer spectroscopy and other techniques, Journal of the American Chemical Society, 136 (2014) 978-985.

[169] Z. Yang, Y. Wang, M. Zhu, Z. Li, W. Chen, W. Wei, T. Yuan, Y. Qu, Q. Xu, C. Zhao, Boosting oxygen reduction catalysis with Fe–N_4 sites decorated porous carbons toward fuel cells, ACS Catalysis, 9 (2019) 2158-2163.

[170] K. Liu, S. Kattel, V. Mao, G. Wang, Electrochemical and computational study of oxygen reduction reaction on nonprecious transition metal/nitrogen doped carbon nanofibers in acid medium, The Journal of Physical Chemistry C, 120 (2016) 1586-1596.

[171] F. Calle-Vallejo, J.I. Martínez, J. Rossmeisl, Density functional studies of functionalized graphitic materials with late transition metals for oxygen reduction reactions, Physical Chemistry Chemical Physics, 13 (2011) 15639-15643.

[172] S. Kattel, P. Atanassov, B. Kiefer, Stability, electronic and magnetic properties of in-plane defects in graphene: a first-principles study, The Journal of Physical Chemistry C, 116 (2012) 8161-8166.

[173] S. Kattel, G. Wang, A density functional theory study of oxygen reduction reaction on Me–N 4 (Me= Fe, Co, or Ni) clusters between graphitic pores, Journal of Materials Chemistry A, 1 (2013) 10790-10797.

[174] M. Lefèvre, E. Proietti, F. Jaouen, J.-P. Dodelet, Iron-based catalysts with improved oxygen reduction activity in polymer electrolyte fuel cells, science, 324 (2009) 71-74.

[175] K. Liu, G. Wu, G. Wang, Role of local carbon structure surrounding FeN_4 sites in boosting the catalytic activity for oxygen reduction, The Journal of Physical Chemistry C, 121 (2017) 11319-11324.

[176] A. Zitolo, N. Ranjbar-Sahraie, T. Mineva, J. Li, Q. Jia, S. Stamatin, G.F. Harrington, S.M. Lyth, P. Krtil, S. Mukerjee, Identification of catalytic sites in cobalt-nitrogen-carbon materials for the oxygen reduction reaction, Nature communications, 8 (2017) 1-11.

[177] F. Jaouen, F. Charreteur, J. Dodelet, Fe-based catalysts for oxygen reduction in PEMFCs importance of the disordered phase of the carbon support, Journal of the Electrochemical Society, 153 (2006) A689-A698.

[178] N. Zhang, T. Zhou, M. Chen, H. Feng, R. Yuan, W. Yan, Y. Tian, X. Wu, W. Chu, C. Wu, High-purity pyrrole-type FeN 4 sites as a superior oxygen reduction electrocatalyst, Energy & Environmental Science, (2020).

[179] J. Li, F. Jaouen, Structure and activity of metal-centered coordination sites in pyrolyzed metal – nitrogen–carbon catalysts for the electrochemical reduction of O2, Current Opinion in Electrochemistry, 9 (2018) 198-206.

[180] U.I. Kramm, J. Herranz, N. Larouche, T.M. Arruda, M. Lefevre, F. Jaouen, P. Bogdanoff, S. Fiechter, I. Abs-Wurmbach, S. Mukerjee, Structure of the catalytic sites in Fe/N/C-catalysts for O 2-reduction in PEM fuel cells, Physical Chemistry Chemical Physics, 14 (2012) 11673-11688.

[181] S. Wagner, H. Auerbach, C.E. Tait, I. Martinaiou, S.C. Kumar, C. Kübel, I. Sergeev, H.C. Wille, J. Behrends, J.A. Wolny, Elucidating the Structural Composition of an Fe ‐ N ‐ C Catalyst by Nuclear ‐ and Electron ‐ Resonance Techniques, Angewandte Chemie International Edition, 58 (2019) 10486-10492.

[182] F. Xiao, G.-L. Xu, C.-J. Sun, M. Xu, W. Wen, Q. Wang, M. Gu, S. Zhu, Y. Li, Z. Wei, Nitrogen-coordinated single iron atom catalysts derived from metal organic frameworks for oxygen reduction reaction, Nano Energy, 61 (2019) 60-68.

[183] A. Zitolo, V. Goellner, V. Armel, M.-T. Sougrati, T. Mineva, L. Stievano, E. Fonda, F. Jaouen, Identification of catalytic sites for oxygen reduction in iron-and nitrogen-doped graphene materials, Nature materials, 14 (2015) 937-942.

[184] T. Mineva, I. Matanovic, P. Atanassov, M.-T. Sougrati, L. Stievano, M. Clémancey, A. Kochem, J.-M. Latour, F. Jaouen, Understanding Active Sites in Pyrolyzed Fe–N–C Catalysts for Fuel Cell Cathodes by Bridging Density Functional Theory Calculations and 57Fe Mössbauer Spectroscopy, ACS Catalysis, 9 (2019) 9359-9371.

[185] M. Xiao, J. Zhu, L. Ma, Z. Jin, J. Ge, X. Deng, Y. Hou, Q. He, J. Li, Q. Jia, Microporous framework induced synthesis of single-atom dispersed Fe-NC acidic ORR catalyst and its in situ reduced Fe-N4 active site identification revealed by X-ray absorption spectroscopy, ACS Catalysis, 8 (2018) 2824-2832.

[186] J. Li, M.T. Sougrati, A. Zitolo, J.M. Ablett, I.C. Oğuz, T. Mineva, I. Matanovic, P. Atanassov, A. Di Cicco, K. Kumar, Identification of durable and non-durable FeNx sites in Fe-NC materials for proton exchange membrane fuel cells, (2020).

[187] Q. Jia, N. Ramaswamy, H. Hafiz, U. Tylus, K. Strickland, G. Wu, B. Barbiellini, A. Bansil, E.F. Holby, P. Zelenay, Experimental observation of redox-induced Fe–N switching behavior as a determinant role for oxygen reduction activity, Acs Nano, 9 (2015) 12496-12505.

[188] J. Zagal, P. Bindra, E. Yeager, A mechanistic study of O 2 reduction on water soluble phthalocyanines adsorbed on graphite electrodes, Journal of The Electrochemical Society, 127 (1980) 1506-1517.

[189] H. Tributsch, U.I. Koslowski, I. Dorbandt, Experimental and theoretical modeling of Fe-, Co-, Cu-, Mn-based electrocatalysts for oxygen reduction, electrochimica acta, 53 (2008) 2198-2209.

[190] J. Li, A. Alsudairi, Z.-F. Ma, S. Mukerjee, Q. Jia, Asymmetric volcano trend in oxygen reduction activity of Pt and non-Pt catalysts: in situ identification of the site-blocking effect, Journal of the American Chemical Society, 139 (2017) 1384-1387.

[191] L. Osmieri, R.K. Ahluwalia, X. Wang, H.T. Chung, X. Yin, A.J. Kropf, J. Park, D.A. Cullen, K.L. More, P. Zelenay, Elucidation of Fe-NC electrocatalyst active site functionality via in-situ X-ray absorption and operando determination of oxygen reduction reaction kinetics in a PEFC, Applied Catalysis B: Environmental, 257 (2019) 117929.

[192] C.A. Reed, S.K. Cheung, On the bonding of FeO2 in hemoglobin and related dioxygen complexes, Proceedings of the National Academy of Sciences, 74 (1977) 1780-1784.

[193] H. Nakashima, J.Y. Hasegawa, H. Nakatsuji, On the reversible O2 binding of the Fe–porphyrin complex, Journal of computational chemistry, 27 (2006) 426-433.

[194] J.H. Zagal, M. Gulppi, M. Isaacs, G. Cárdenas-Jirón, M.J.´s Aguirre, Linear versus volcano correlations between electrocatalytic activity and redox and electronic properties of metallophthalocyanines, Electrochimica acta, 44 (1998) 1349-1357.

[195] U. Kramm, I. Abs-Wurmbach, I. Herrmann-Geppert, J. Radnik, S. Fiechter, P. Bogdanoff, Influence of the electron-density of FeN4-centers towards the catalytic activity of pyrolyzed FeTMPPCl-based ORR-electrocatalysts, Journal of the Electrochemical Society, 158 (2011) B69-B78.

[196] J.H. Zagal, I. Ponce, D. Baez, R. Venegas, J. Pavez, M. Paez, M. Gulppi, A possible interpretation for the high catalytic activity of heat-treated non-precious metal Nx/C catalysts for O2 reduction in terms of their formal potentials, Electrochemical and Solid-State Letters, 15 (2012) B90-B92.

[197] M.H. Seo, D. Higgins, G. Jiang, S.M. Choi, B. Han, Z. Chen, Theoretical insight into highly durable iron phthalocyanine derived non-precious catalysts for oxygen reduction reactions, Journal of Materials Chemistry A, 2 (2014) 19707-19716.

[198] G. Wu, C.M. Johnston, N.H. Mack, K. Artyushkova, M. Ferrandon, M. Nelson, J.S. Lezama-Pacheco, S.D. Conradson, K.L. More, D.J. Myers, Synthesis–structure–performance correlation for polyaniline–Me–C non-precious metal cathode catalysts for oxygen reduction in fuel cells, Journal of Materials Chemistry, 21 (2011) 11392-11405.

[199] T. Mineva, I. Matanovic, P. Atanassov, M.-T. Sougrati, L. Stievano, M. Clémancey, A. Kochem, J.-M. Latour, F. Jaouen, Understanding active sites in pyrolyzed Fe–N–C catalysts for fuel cell cathodes by bridging density functional theory calculations and 57Fe Mossbauer spectroscopy, ACS Catalysis, 9 (2019) 9359-9371.

[200] M. Primbs, Y. Sun, A. Roy, D. Malko, A. Mehmood, M.-T. Sougrati, P.-Y. Blanchard, G. Granozzi, T. Kosmala, G. Daniel, Establishing reactivity descriptors for platinum group metal (PGM)-free Fe–N–C catalysts for PEM fuel cells, Energy & Environmental Science, 13 (2020) 2480-2500.

[201] Y. Li, W. Zhou, H. Wang, L. Xie, Y. Liang, F. Wei, J.-C. Idrobo, S.J. Pennycook, H. Dai, An oxygen reduction electrocatalyst based on carbon nanotube–graphene complexes, Nature nanotechnology, 7 (2012) 394.

[202] E. Holby, C. Taylor, Control of graphene nanoribbon vacancies by Fe and N dopants: Implications for catalysis, Applied Physics Letters, 101 (2012) 064102.

[203] A. Serov, K. Artyushkova, P. Atanassov, Fe‐N‐C Oxygen Reduction Fuel Cell Catalyst Derived from Carbendazim: Synthesis, Structure, and Reactivity, Advanced Energy Materials, 4 (2014) 1301735.

[204] M.J. Workman, A. Serov, L.-k. Tsui, P. Atanassov, K. Artyushkova, Fe–N–C catalyst graphitic layer structure and fuel cell performance, ACS Energy Letters, 2 (2017) 1489-1493.

[205] X. Wang, Y. Jia, X. Mao, D. Liu, W. He, J. Li, J. Liu, X. Yan, J. Chen, L. Song, Edge‐Rich Fe–N4 Active Sites in Defective Carbon for Oxygen Reduction Catalysis, Advanced Materials, 32 (2020) 2000966.

[206] R. Jiang, L. Li, T. Sheng, G. Hu, Y. Chen, L. Wang, Edge-site engineering of atomically dispersed Fe–N4 by selective C–N bond cleavage for enhanced oxygen reduction reaction activities, Journal of the American Chemical Society, 140 (2018) 11594-11598.

[207] J.D. Benck, T.R. Hellstern, J. Kibsgaard, P. Chakthranont, T.F. Jaramillo, Catalyzing the hydrogen evolution reaction (HER) with molybdenum sulfide nanomaterials, Acs Catalysis, 4 (2014) 3957-3971.

[208] J. Li, H. Zhang, W. Samarakoon, W. Shan, D.A. Cullen, S. Karakalos, M. Chen, D. Gu, K.L. More, G. Wang, Thermally Driven Structure and Performance Evolution of Atomically Dispersed FeN4 Sites for Oxygen Reduction, Angewandte Chemie International Edition, (2019).

[209] J. Li, L. Jiao, E. Wegener, L.L. Richard, E. Liu, A. Zitolo, M.T. Sougrati, S. Mukerjee, Z. Zhao, Y. Huang, The evolution pathway from iron compounds to Fe1 (II)-N4 sites through gas-phase iron during pyrolysis, Journal of the American Chemical Society, (2019).

[210] L. Jiao, J. Li, L.L. Richard, Q. Sun, T. Stracensky, E. Liu, M.T. Sougrati, Z. Zhao, F. Yang, S. Zhong, Chemical vapour deposition of Fe–N–C oxygen reduction catalysts with full utilization of dense Fe–N4 sites, Nature Materials, (2021) 1-7.

[211] Y. Qu, Z. Li, W. Chen, Y. Lin, T. Yuan, Z. Yang, C. Zhao, J. Wang, C. Zhao, X. Wang, Direct transformation of bulk copper into copper single sites via emitting and trapping of atoms, Nature Catalysis, 1 (2018) 781-786.

[212] C. Zhao, Y. Wang, Z. Li, W. Chen, Q. Xu, D. He, D. Xi, Q. Zhang, T. Yuan, Y. Qu, Solid-diffusion synthesis of single-atom catalysts directly from bulk metal for efficient CO2 reduction, Joule, 3 (2019) 584-594.

[213] S. Wei, A. Li, J.-C. Liu, Z. Li, W. Chen, Y. Gong, Q. Zhang, W.-C. Cheong, Y. Wang, L. Zheng, Direct observation of noble metal nanoparticles transforming to thermally stable single atoms, Nature nanotechnology, 13 (2018) 856-861.

[214] Y. Qu, B. Chen, Z. Li, X. Duan, L. Wang, Y. Lin, T. Yuan, F. Zhou, Y. Hu, Z. Yang, Thermal emitting strategy to synthesize atomically dispersed Pt metal sites from bulk Pt metal, Journal of the American Chemical Society, 141 (2019) 4505-4509.

[215] J. Yang, Z. Qiu, C. Zhao, W. Wei, W. Chen, Z. Li, Y. Qu, J. Dong, J. Luo, Z. Li, In-situ thermal atomization to transfer supported metal nanoparticles to surface enriched Ni single atom catalyst, Angew. Chem. Int. Ed, 57 (2018) 14095-14100.

[216] W. Wei, X. Shi, P. Gao, S. Wang, W. Hu, X. Zhao, Y. Ni, X. Xu, Y. Xu, W. Yan, Well-elaborated, mechanochemically synthesized Fe-TPP⊂ ZIF precursors (Fe-TPP= tetraphenylporphine iron) to atomically dispersed iron–nitrogen species for oxygen reduction reaction and Zn-air batteries, Nano Energy, 52 (2018) 29-37.

[217] X. Chen, L. Yu, S. Wang, D. Deng, X. Bao, Highly active and stable single iron site confined in graphene nanosheets for oxygen reduction reaction, Nano Energy, 32 (2017) 353-358.

[218] J. Herranz, M. Lefevre, N. Larouche, B. Stansfield, J.-P. Dodelet, Step-by-step synthesis of non-noble metal electrocatalysts for O2 reduction under proton exchange membrane fuel cell conditions, The Journal of Physical Chemistry C, 111 (2007) 19033-19042.

[219] U.I. Koslowski, I. Abs-Wurmbach, S. Fiechter, P. Bogdanoff, Nature of the catalytic centers of porphyrin-based electrocatalysts for the ORR: a correlation of kinetic current density with the site density of Fe− N4 centers, The Journal of Physical Chemistry C, 112 (2008) 15356-15366.

[220] R. Ma, Y. Zhou, C. Hu, M. Yang, F. Wang, K. Yan, Q. Liu, J. Wang, Post iron-doping of activated nitrogen-doped carbon spheres as a high-activity oxygen reduction electrocatalyst, Energy Storage Materials, 13 (2018) 142-150.

[221] M. Lefèvre, J.-P. Dodelet, Fe-based electrocatalysts made with microporous pristine carbon black supports for the reduction of oxygen in PEM fuel cells, Electrochimica Acta, 53 (2008) 8269-8276.

[222] Q. Wei, G. Zhang, X. Yang, Y. Fu, G. Yang, N. Chen, W. Chen, S. Sun, Litchi-like porous Fe/N/C spheres with atomically dispersed FeN x promoted by sulfur as highly efficient oxygen electrocatalysts for Zn–air batteries, Journal of Materials Chemistry A, 6 (2018) 4605-4610.

[223] J. Xiao, Y. Xu, Y. Xia, J. Xi, S. Wang, Ultra-small Fe2N nanocrystals embedded into mesoporous nitrogen-doped graphitic carbon spheres as a highly active, stable, and methanol-tolerant electrocatalyst for the oxygen reduction reaction, Nano Energy, 24 (2016) 121-129.

[224] H. Tan, Y. Li, X. Jiang, J. Tang, Z. Wang, H. Qian, P. Mei, V. Malgras, Y. Bando, Y. Yamauchi, Perfectly ordered mesoporous iron-nitrogen doped carbon as highly efficient catalyst for oxygen reduction reaction in both alkaline and acidic electrolytes, Nano Energy, 36 (2017) 286-294.

[225] L. Bai, Z. Duan, X. Wen, J. Guan, Bifunctional atomic iron-based catalyst for oxygen electrode reactions, Journal of Catalysis, 378 (2019) 353-362.

[226] X. Cui, S. Yang, X. Yan, J. Leng, S. Shuang, P.M. Ajayan, Z. Zhang, Pyridinic‐nitrogen‐Dominated graphene aerogels with Fe‐N‐C coordination for highly efficient oxygen reduction reaction, Advanced Functional Materials, 26 (2016) 5708-5717.

[227] F. Jaouen, M. Lefèvre, J.-P. Dodelet, M. Cai, Heat-treated Fe/N/C catalysts for O2 electroreduction: are active sites hosted in micropores?, The Journal of Physical Chemistry B, 110 (2006) 5553-5558.

[228] F. Charreteur, F. Jaouen, S. Ruggeri, J.-P. Dodelet, Fe/N/C non-precious catalysts for PEM fuel cells: Influence of the structural parameters of pristine commercial carbon blacks on their activity for oxygen reduction, Electrochimica acta, 53 (2008) 2925-2938.

[229] Q. Zhang, I. Lee, J.B. Joo, F. Zaera, Y. Yin, Core–shell nanostructured catalysts, Accounts of chemical research, 46 (2013) 1816-1824.

[230] S.H. Joo, J.Y. Park, C.-K. Tsung, Y. Yamada, P. Yang, G.A. Somorjai, Thermally stable Pt/mesoporous silica core–shell nanocatalysts for high-temperature reactions, Nature materials, 8 (2009) 126-131.

[231] H. Zhang, S. Ding, S. Hwang, X. Zhao, D. Su, H. Xu, H. Yang, G. Wu, Atomically Dispersed Iron Cathode Catalysts Derived from Binary Ligand-Based Zeolitic Imidazolate Frameworks with Enhanced Stability for PEM Fuel Cells, Journal of The Electrochemical Society, 166 (2019) F3116-F3122.

[232] W. Ye, S. Chen, Y. Lin, L. Yang, S. Chen, X. Zheng, Z. Qi, C. Wang, R. Long, M. Chen, Precisely tuning the number of Fe atoms in clusters on N-doped carbon toward acidic oxygen reduction reaction, Chem, 5 (2019) 2865-2878.

[233] Q.-L. Zhu, W. Xia, L.-R. Zheng, R. Zou, Z. Liu, Q. Xu, Atomically dispersed Fe/N-doped hierarchical carbon architectures derived from a metal–organic framework composite for extremely efficient electrocatalysis, ACS Energy Letters, 2 (2017) 504-511.

[234] Y. Chen, S. Ji, Y. Wang, J. Dong, W. Chen, Z. Li, R. Shen, L. Zheng, Z. Zhuang, D. Wang, Isolated single iron atoms anchored on N‐doped porous carbon as an efficient electrocatalyst for the oxygen reduction reaction, Angewandte Chemie International Edition, 56 (2017) 6937-6941.

[235] Y. Ye, H. Li, F. Cai, C. Yan, R. Si, S. Miao, Y. Li, G. Wang, X. Bao, Two-Dimensional Mesoporous Carbon Doped with Fe–N Active Sites for Efficient Oxygen Reduction, ACS Catalysis, 7 (2017) 7638-7646.

[236] L. Tong, Y.-C. Wang, M.-X. Chen, Z.-Q. Chen, Q.-Q. Yan, C.-L. Yang, Z.-Y. Zhou, S.-Q. Chu, X. Feng, H.-W. Liang, Hierarchically porous carbons as supports for fuel cell electrocatalysts with atomically dispersed Fe–N x moieties, Chemical science, 10 (2019) 8236-8240.

[237] R. Cao, R. Thapa, H. Kim, X. Xu, M.G. Kim, Q. Li, N. Park, M. Liu, J. Cho, Promotion of oxygen reduction by a bio-inspired tethered iron phthalocyanine carbon nanotube-based catalyst, Nature communications, 4 (2013) 1-7.

[238] I. Kruusenberg, L. Matisen, K. Tammeveski, Oxygen electroreduction on multi-walled carbon nanotube supported metal phthalocyanines and porphyrins in alkaline media, Journal of nanoscience and nanotechnology, 13 (2013) 621-627.

[239] M. Li, X. Bo, Y. Zhang, C. Han, L. Guo, Comparative study on the oxygen reduction reaction electrocatalytic activities of iron phthalocyanines supported on reduced graphene oxide, mesoporous carbon vesicle, and ordered mesoporous carbon, Journal of Power Sources, 264 (2014) 114-122.

[240] I. Kruusenberg, J. Mondal, L. Matisen, V. Sammelselg, K. Tammeveski, Oxygen reduction on graphene-supported MN4 macrocycles in alkaline media, Electrochemistry communications, 33 (2013) 18-22.

[241] I. Hijazi, T. Bourgeteau, R. Cornut, A. Morozan, A. Filoramo, J. Leroy, V. Derycke, B. Jousselme, S.p. Campidelli, Carbon nanotube-templated synthesis of covalent porphyrin network for oxygen reduction reaction, Journal of the American Chemical Society, 136 (2014) 6348-6354.

[242] D. Liu, Y.-T. Long, Superior catalytic activity of electrochemically reduced graphene oxide supported iron phthalocyanines toward oxygen reduction reaction, ACS applied materials & interfaces, 7 (2015) 24063-24068.

[243] N. Zion, A. Friedman, N. Levy, L. Elbaz, Bioinspired electrocatalysis of oxygen reduction reaction in fuel cells using molecular catalysts, Advanced Materials, 30 (2018) 1800406.

[244] X. Wang, Z. Li, Y. Qu, T. Yuan, W. Wang, Y. Wu, Y. Li, Review of Metal Catalysts for Oxygen Reduction Reaction: From Nanoscale Engineering to Atomic Design, Chem 5(2019) 1486-1511.

[245] R. Ma, G. Lin, Y. Zhou, Q. Liu, T. Zhang, G. Shan, M. Yang, J. Wang, A review of oxygen reduction mechanisms for metal-free carbon-based electrocatalysts, Npj Comput. Mater., 5 (2019) 78 (15).

[246] L. Dai, Y. Xue, L. Qu, H.-J. Choi, J.-B. Baek, Metal-Free Catalysts for Oxygen Reduction Reaction, Chem. Rev., 115 (2015) 4823-4892.

[247] M. Shao, Q. Chang, J.-P. Dodelet, R. Chenitz, Recent Advances in Electrocatalysts for Oxygen Reduction Reaction, Chem. Rev., 116 (2016) 3594-3657.

[248] D.J. Berger, Fuel Cells and Precious-Metal Catalysts, Science, 286 (1999) 49.

[249] S.M. Hayes, E.A. McCullough, Critical minerals: A review of elemental trends in comprehensive criticality studies, Resour. Policy, 59 (2018) 192-199.

[250] B. Singh, V. Sharma, R.P. Gaikwad, P. Fornasiero, R. Zboril, M.B. Gawande, Single ‐ Atom Catalysts: A Sustainable Pathway for the Advanced Catalytic Applications, Small, 17 (2021) 2006473 (2006427).

[251] M.B. Gawande, P. Fornasiero, R. Zbořil, Carbon-Based Single-Atom Catalysts for Advanced Applications, ACS Catal., 10 (2020) 2231–2259.

[252] S.K. Kaiser, Z. Chen, D.F. Akl, S. Mitchell, J. Pérez-Ramírez, Single-Atom Catalysts across the Periodic Table, Chem. Rev., 120 (2020) 11703-11809.

[253] R.T. Hannagan, G. Giannakakis, M. Flytzani-Stephanopoulos, E.C.H. Sykes, Single-Atom Alloy Catalysis, Chem. Rev., 120 (2020) 12044-12088.

[254] J. Su, R. Ge, Y. Dong, F. Hao, L. Chen, Recent progress in single-atom electrocatalysts: concept, synthesis, and applications in clean energy conversion, J. Mater. Chem. A, 6 (2018) 14025-14042.

[255] Y. He, S. Liu, C. Priest, Q. Shi, G. Wu, Atomically dispersed metal–nitrogen–carbon catalysts for fuel cells: advances in catalyst design, electrode performance, and durability improvement, Chem. Soc. Rev., 49 (2020) 3484-3524.

[256] Z. Kou, W. Zang, Y. Ma, Z. Pan, S. Mu, X. Gao, B. Tang, M. Xiong, X. Zhao, A.K. Cheetham, L. Zheng, J. Wang, Cage-confinement pyrolysis route to size-controlled molybdenum-based oxygen electrode catalysts: From isolated atoms to clusters and nanoparticles, Nano Energy, 67 (2020) 104288 (104289).

[257] Y. Chen, S. ji, C. Chen, Q. Peng, D. Wang, Y. Li, Single-Atom Catalysts: Synthetic Strategies and Electrochemical Applications, Joule, 2 (2018) 1242-1264.

[258] C. Genovese, M.E. Schuster, E.K. Gibson, D. Gianolio, V. Posligua, R. Grau-Crespo, G. Cibin, P.P. Wells, D. Garai, V. Solokha, S.K. Calderon, J.J. Velasco-Velez, C. Ampelli, S. Perathoner, G. Held, G. Centi, R. Arrigo, Operando spectroscopy study of the carbon dioxide electro-reduction by iron species on nitrogen-doped carbon, Nat. Commun., 9 (2018) 935 (912).

[259] H. Ba, Y. Liu, L. Truong-Phuoc, C. Duong-Viet, X. Mu, W.H. Doh, T. Tran-Thanh, W. Baaziz, L. Nguyen-Dinh, J.-M. Nhut, I. Janowska, D. Begin, S. Zafeiratos, P. Granger, G. Tuci, G. Giambastiani, F. Banhart, M.J. Ledoux, C. Pham-Huu, A highly N-doped carbon phase ‘‘dressing’’ of macroscopic supports for catalytic applications, Chem. Commun., 51 (2015) 14393-14396.

[260] H. Ba, Y. Liu, L. Truong-Phuoc, C. Duong-Viet, J.-M. Nhut, L. Nguyen-Dinh, O. Ersen, G. Tuci, G. Giambastiani, C. Pham-Huu, N-Doped Food-Grade-Derived 3D Mesoporous Foams as Metal-Free Systems for Catalysis, ACS Catal., 6 (2016) 1408-1419.

[261] C. Pham-Huu, G. Giambastiani, Y. Liu, H. Ba, L. Nguyen-Dinh, J.-M. Nhut, Method for preparing highly nitrogen-doped mesoporous carbon composites., 2016.

[262] H. Ba, J. Luo, Y. Liu, C. Duong-Viet, G. Tuci, G. Giambastiani, J.-M. Nhut, L. Nguyen-Dinh, O. Ersen, D.S. Su, C. Pham-Huu, Macroscopically Shaped Monolith of Nanodiamonds @ Nitrogen-enriched Mesoporous Carbon Decorated SiC as a Superior Metal-free Catalyst for the Styrene Production, Appl. Catal. B: Environ., 200 (2017) 343-350.

[263] C. Duong-Viet, J.-M. Nhut, T. Truong-Huu, G. Tuci, L. Nguyen-Dinh, Y. Liu, C. Pham, G. Giambastiani, C. Pham-Huu, A Nitrogen-Doped Carbon Coated Silicon Carbide as a Robust and Highly Efficient Metal-Free Catalyst for Sour Gases Desulfurization in the Presence of Aromatics as Contaminants, Catal. Sci. Technol., 10 (2020) 5487-5500.

[264] C. Duong-Viet, J.-M. Nhut, T. Truong-Huu, G. Tuci, L. Nguyen-Dinh, C. Pham, G. Giambastiani, C. Pham-Huu, Tailoring Properties of Metal-Free Catalysts for the Highly Efficient Desulfurization of Sour Gases under Harsh Conditions, Catalysts, 11 (2021) 226 (215).

[265] P. Chen, T. Zhou, L. Xing, K. Xu, Y. Tong, H. Xie, L. Zhang, W. Yan, W. Chu, C. Wu, Y. Xie, Atomically Dispersed Iron–Nitrogen Species as Electrocatalysts for Bifunctional Oxygen Evolution and Reduction Reactions, Angew. Chem. Int. Ed., 56 (2016) 610-614.

[266] Y.-C. Wang, Y.-J. Lai, L. Song, Z.-Y. Zhou, J.-G. Liu, Q. Wang, X.-D. Yang, C. Chen, W. Shi, Y.-P. Zheng, M. Rauf, S.-G. Sun, S-Doping of an Fe/N/C ORR Catalyst for Polymer Electrolyte Membrane Fuel Cells with High Power Density, Angew. Chem. Int. Ed., 54 (2015) 9907-9910.

[267] U.I. Kramm, I. Herrmann, S. Fiechter, G. Zehl, I. Zizak, I. Abs-Wurmbach, J. Radnik, I. Dorbandt, P. Bogdanoff, E. Trans., 2009, 659 – 670., On the Influence of Sulphur on the Pyrolysis Process of FeTMPP-Cl-based Electro-Catalysts with Respect to Oxygen Reduction Reaction (ORR) in Acidic Media, ECS Trans., 25 (2009) 659-670.

[268] Y. Wang, L. Chen, Z. Mao, L. Peng, R. Xiang, X. Tang, J. Deng, Z. Wei, Q. Liao, Controlled synthesis of single cobalt atom catalysts via a facile one-pot pyrolysis for efficient oxygen reduction and hydrogen evolution reactions, Sci. Bull., 64 (2019) 1095-1102.

[269] R. Chenitz, U.I. Kramm, M. Lefèvre, V. Glibin, G. Zhang, S. Sun, J.-P. Dodelet, A specific demetalation of Fe–N 4 catalytic sites in the micropores of NC_Ar+ NH 3 is at the origin of the initial activity loss of the highly active Fe/N/C catalyst used for the reduction of oxygen in PEM fuel cells, Energy & Environmental Science, 11 (2018) 365-382.

[270] L. Zhang, H. Gu, H. Sun, F. Cao, Y. Chen, G.Z. Chen, Molecular level one-step activation of agar to activated carbon for high performance supercapacitors, Carbon, 132 (2018) 573-579.

[271] J. Li, N. Wang, J. Tian, W. Qian, W. Chu, Cross‐coupled macro‐mesoporous carbon network toward record high energy‐power density supercapacitor at 4 V, Advanced Functional Materials, 28 (2018) 1806153.

[272] G.-Q. Lu, S.-G. Sun, L.-R. Cai, S.-P. Chen, Z.-W. Tian, K.-K. Shiu, In situ FTIR spectroscopic studies of adsorption of CO, SCN-, and poly (o-phenylenediamine) on electrodes of nanometer thin films of Pt, Pd, and Rh: Abnormal infrared effects (AIREs), Langmuir, 16 (2000) 778-786.

[273] Q. Zhang, Y. Zhou, F. Xu, H. Lin, Y. Yan, K. Rui, C. Zhang, Q. Wang, Z. Ma, Y. Zhang, Topochemical Synthesis of 2D Carbon Hybrids through Self‐Boosting Catalytic Carbonization of a Metal‐Polymer Framework, Angewandte Chemie International Edition, 57 (2018) 16436-16441.

[274] J. Li, N. Wang, J. Deng, W. Qian, W. Chu, Flexible metal-templated fabrication of mesoporous onion-like carbon and Fe 2 O 3@ N-doped carbon foam for electrochemical energy storage, Journal of Materials Chemistry A, 6 (2018) 13012-13020.

[275] J. Li, Q. Jia, S. Mukerjee, M.-T. Sougrati, G. Drazic, A. Zitolo, F. Jaouen, The challenge of achieving a high density of Fe-based active sites in a highly graphitic carbon matrix, Catalysts, 9 (2019) 144.

[276] Y. Wang, L. Chen, Z. Mao, L. Peng, R. Xiang, X. Tang, J. Deng, Z. Wei, Q. Liao, Controlled synthesis of single cobalt atom catalysts via a facile one-pot pyrolysis for efficient oxygen reduction and hydrogen evolution reactions, Science Bulletin, 64 (2019) 1095-1102.

[277] N. Zhang, T. Zhou, M. Chen, H. Feng, R. Yuan, W. Yan, Y. Tian, X. Wu, W. Chu, C. Wu, High-purity pyrrole-type FeN 4 sites as a superior oxygen reduction electrocatalyst, Energy & Environmental Science, 13 (2020) 111-118.

[278] W. Liang, J. Chen, Y. Liu, S. Chen, Density-functional-theory calculation analysis of active sites for four-electron reduction of O2 on Fe/N-doped graphene, Acs Catalysis, 4 (2014) 4170-4177.

[279] X. Liu, H. Liu, C. Chen, L. Zou, Y. Li, Q. Zhang, B. Yang, Z. Zou, H. Yang, Fe2N nanoparticles boosting FeNx moieties for highly efficient oxygen reduction reaction in Fe-NC porous catalyst, (2019).

[280] H. Peng, Z. Mo, S. Liao, H. Liang, L. Yang, F. Luo, H. Song, Y. Zhong, B. Zhang, High performance Fe-and N-doped carbon catalyst with graphene structure for oxygen reduction, Scientific reports, 3 (2013) 1-7.

[281] U.I. Kramm, I. Herrmann-Geppert, P. Bogdanoff, S. Fiechter, Effect of an ammonia treatment on structure, composition, and oxygen reduction reaction activity of Fe–N–C catalysts, The Journal of Physical Chemistry C, 115 (2011) 23417-23427.

[282] P. Chen, T. Zhou, L. Xing, K. Xu, Y. Tong, H. Xie, L. Zhang, W. Yan, W. Chu, C. Wu, Atomically dispersed iron–nitrogen species as electrocatalysts for bifunctional oxygen evolution and reduction reactions, Angewandte Chemie, 129 (2017) 625-629.

[283] Y.C. Wang, Y.J. Lai, L. Song, Z.Y. Zhou, J.G. Liu, Q. Wang, X.D. Yang, C. Chen, W. Shi, Y.P. Zheng, S‐doping of an Fe/N/C ORR catalyst for polymer electrolyte membrane fuel cells with high power density, Angewandte Chemie, 127 (2015) 10045-10048.

[284] J. Liang, Y. Jiao, M. Jaroniec, S.Z. Qiao, Sulfur and nitrogen dual‐doped mesoporous graphene electrocatalyst for oxygen reduction with synergistically enhanced performance, Angewandte Chemie International Edition, 51 (2012) 11496-11500.

[285] F. Jaouen, J.-P. Dodelet, Non-noble electrocatalysts for O2 reduction: how does heat treatment affect their activity and structure? Part I. Model for carbon black gasification by NH3: parametric calibration and electrochemical validation, The Journal of Physical Chemistry C, 111 (2007) 5963-5970.

[286] F. Jaouen, A.M. Serventi, M. Lefèvre, J.-P. Dodelet, P. Bertrand, Non-noble electrocatalysts for O2 reduction: how does heat treatment affect their activity and structure? Part II. Structural changes observed by electron microscopy, Raman, and mass spectroscopy, The Journal of Physical Chemistry C, 111 (2007) 5971-5976.

[287] F.M. Michel, L. Ehm, S.M. Antao, P.L. Lee, P.J. Chupas, G. Liu, D.R. Strongin, M.A.A. Schoonen, B.L. Phillips, J.B. Parise, The Structure of Ferrihydrite, a Nanocrystalline Material, Science, 316 (2007) 1726-1729.

[288] P.-E. Petit, F. Farges, M. Wilke, V.A. Solé, Determination of the iron oxidation state in Earth materials using XANES pre-edge information, J. Synchrotron Radiat., 8 (2001) 952-954.

[289] H. Yang, R. Lu, R.T. Downs, G. Costin, Goethite, α-FeO (OH), from single-crystal data, Acta Crystallogr. E, 62 (2006) 250-252.

[290] G. Chen, P. Liu, Z. Liao, F. Sun, Y. He, H. Zhong, T. Zhang, E. Zschech, M. Chen, G. Wu, Zinc‐mediated template synthesis of Fe‐N‐C electrocatalysts with densely accessible Fe‐N_x active sites for efficient oxygen reduction, Advanced Materials, 32 (2020) 1907399.

[291] Y. Liu, B. Huang, X. Zhang, X. Huang, Z. Xie, In-situ fabrication of nitrogen-doped carbon nanosheets containing highly dispersed single iron atoms for oxygen reduction reaction, Journal of Power Sources, 412 (2019) 125-133.

[292] H. Zhong, K.H. Ly, M. Wang, Y. Krupskaya, X. Han, J. Zhang, J. Zhang, V. Kataev, B. Büchner, I.M. Weidinger, A Phthalocyanine‐Based Layered Two‐Dimensional Conjugated Metal–Organic Framework as a Highly Efficient Electrocatalyst for the Oxygen Reduction Reaction, Angewandte Chemie International Edition, 58 (2019) 10677-10682.

[293] L. Shang, H. Yu, X. Huang, T. Bian, R. Shi, Y. Zhao, G.I. Waterhouse, L.Z. Wu, C.H. Tung, T. Zhang, Well‐dispersed ZIF‐derived Co, N‐co‐doped carbon nanoframes through mesoporous‐silica‐protected calcination as efficient oxygen reduction electrocatalysts, Advanced Materials, 28 (2016) 1668-1674.

[294] Q. Li, R. Cao, J. Cho, G. Wu, Nanocarbon electrocatalysts for oxygen reduction in alkaline media for advanced energy conversion and storage, Advanced energy materials, 4 (2014) 1301415.

[295] F. Jaouen, E. Proietti, M. Lefèvre, R. Chenitz, J.-P. Dodelet, G. Wu, H.T. Chung, C.M. Johnston, P. Zelenay, Recent advances in non-precious metal catalysis for oxygen-reduction reaction in polymer electrolyte fuel cells, Energy & Environmental Science, 4 (2011) 114-130.

[296] G. Wu, K.L. More, C.M. Johnston, P. Zelenay, High-performance electrocatalysts for oxygen reduction derived from polyaniline, iron, and cobalt, Science, 332 (2011) 443-447.

[297] H. Jahnke, M. Schönborn, G. Zimmermann, Organic dyestuffs as catalysts for fuel cells, Physical and chemical applications of dyestuffs, (1976) 133-181.

[298] V. Bagotzky, M. Tarasevich, K. Radyushkina, O. Levina, S. Andrusyova, Electrocatalysis of the oxygen reduction process on metal chelates in acid electrolyte, Journal of Power Sources, 2 (1978) 233-240.

[299] D. Scherson, S. Gupta, C. Fierro, E. Yeager, M. Kordesch, J. Eldridge, R. Hoffman, J. Blue, Cobalt tetramethoxyphenyl porphyrin—emission Mossbauer spectroscopy and O2 reduction electrochemical studies, Electrochimica Acta, 28 (1983) 1205-1209.

[300] M. Tarasevich, K. Radyuskina, Pyropolymers of N4-complexes: Structure and elegtrocatalytic properties, Materials chemistry and physics, 22 (1989) 477-502.

[301] C. Wang, H. Zhang, J. Wang, Z. Zhao, J. Wang, Y. Zhang, M. Cheng, H. Zhao, J. Wang, Atomic Fe embedded in carbon nanoshells–graphene nanomeshes with enhanced oxygen reduction reaction performance, Chemistry of Materials, 29 (2017) 9915-9922.

[302] Z. Huang, H. Pan, W. Yang, H. Zhou, N. Gao, C. Fu, S. Li, H. Li, Y. Kuang, In situ self-template synthesis of Fe–N-doped double-shelled hollow carbon microspheres for oxygen reduction reaction, ACS nano, 12 (2018) 208-216.

[303] X. Chen, D.-D. Ma, B. Chen, K. Zhang, R. Zou, X.-T. Wu, Q.-L. Zhu, Metal–organic framework-derived mesoporous carbon nanoframes embedded with atomically dispersed Fe–Nx active sites for efficient bifunctional oxygen and carbon dioxide electroreduction, Applied Catalysis B: Environmental, 267 (2020) 118720.

[304] L.T. Song, Z.Y. Wu, F. Zhou, H.W. Liang, Z.Y. Yu, S.H. Yu, Sustainable Hydrothermal Carbonization Synthesis of Iron/Nitrogen‐Doped Carbon Nanofiber Aerogels as Electrocatalysts for Oxygen Reduction, Small, 12 (2016) 6398-6406.

[305] S. Zhang, H. Zhang, Q. Liu, S. Chen, Fe–N doped carbon nanotube/graphene composite: facile synthesis and superior electrocatalytic activity, Journal of materials chemistry a, 1 (2013) 3302-3308.

[306] F.L. Meng, Z.L. Wang, H.X. Zhong, J. Wang, J.M. Yan, X.B. Zhang, Reactive multifunctional template‐induced preparation of Fe‐N‐doped mesoporous carbon microspheres towards highly efficient electrocatalysts for oxygen reduction, Advanced Materials, 28 (2016) 7948-7955.

[307] Z. Miao, X. Wang, M.C. Tsai, Q. Jin, J. Liang, F. Ma, T. Wang, S. Zheng, B.J. Hwang, Y. Huang, Atomically Dispersed Fe‐Nx/C Electrocatalyst Boosts Oxygen Catalysis via a New Metal‐Organic Polymer Supramolecule Strategy, Advanced Energy Materials, 8 (2018) 1801226.

[308] G. Lalande, D. Guay, J. Dodelet, G. Denes, Influence of Nitrogen‐Containing Precursors on the Electrocatalytic Activity of Heat‐Treated Fe (OH) 2 on Carbon Black for O 2 Reduction, Journal of the Electrochemical Society, 145 (1998) 2411.

[309] H. Wang, R. Cote, G. Faubert, D. Guay, J. Dodelet, Effect of the pre-treatment of carbon black supports on the activity of Fe-based electrocatalysts for the reduction of oxygen, The Journal of Physical Chemistry B, 103 (1999) 2042-2049.

[310] D. Deng, L. Yu, X. Chen, G. Wang, L. Jin, X. Pan, J. Deng, G. Sun, X. Bao, Iron encapsulated within pod‐like carbon nanotubes for oxygen reduction reaction, Angewandte Chemie, 125 (2013) 389-393.

[311] K. Parvez, S. Yang, Y. Hernandez, A. Winter, A. Turchanin, X. Feng, K. Müllen, Nitrogen-doped graphene and its iron-based composite as efficient electrocatalysts for oxygen reduction reaction, ACS nano, 6 (2012) 9541-9550.

[312] S. Ren, S. Ma, Y. Yang, Q. Mao, C. Hao, Hydrothermal synthesis of Fe2O3/polypyrrole/graphene oxide composites as highly efficient electrocatalysts for oxygen reduction reaction in alkaline electrolyte, Electrochimica Acta, 178 (2015) 179-189.

[313] Z.-S. Wu, S. Yang, Y. Sun, K. Parvez, X. Feng, K. Müllen, 3D nitrogen-doped graphene aerogel-supported Fe3O4 nanoparticles as efficient electrocatalysts for the oxygen reduction reaction, Journal of the American Chemical Society, 134 (2012) 9082-9085.

[314] J. Guo, Y. Cheng, Z. Xiang, Confined-space-assisted preparation of Fe3O4-nanoparticle-modified Fe–N–C catalysts derived from a covalent organic polymer for oxygen reduction, ACS Sustainable Chemistry & Engineering, 5 (2017) 7871-7877.

[315] G. Ren, X. Lu, Y. Li, Y. Zhu, L. Dai, L. Jiang, Porous core–shell Fe_3C embedded N-doped carbon nanofibers as an effective electrocatalysts for oxygen reduction reaction, ACS applied materials & interfaces, 8 (2016) 4118-4125.

[316] X. Ao, W. Zhang, Z. Li, L. Lv, Y. Ruan, H.-H. Wu, W.-H. Chiang, C. Wang, M. Liu, X.C. Zeng, Unraveling the high-activity nature of Fe–N–C electrocatalysts for the oxygen reduction reaction:

the extraordinary synergy between Fe–N 4 and Fe 4 N, Journal of Materials Chemistry A, 7 (2019) 11792-11801.

[317] X. Liu, H. Liu, C. Chen, L. Zou, Y. Li, Q. Zhang, B. Yang, Z. Zou, H. Yang, Fe 2 N nanoparticles boosting FeN x moieties for highly efficient oxygen reduction reaction in Fe-NC porous catalyst, Nano Research, 12 (2019) 1651-1657.

[318] W. Ni, Y. Gao, Y. Zhang, H.A. Younus, X. Guo, C. Ma, Y. Zhang, J. Duan, J. Zhang, S. Zhang, O-Doping Boosts the Electrochemical Oxygen Reduction Activity of a Single Fe Site in Hydrophilic Carbon with Deep Mesopores, ACS applied materials & interfaces, 11 (2019) 45825-45831.

[319] K. Yuan, S. Sfaelou, M. Qiu, D. Lützenkirchen-Hecht, X. Zhuang, Y. Chen, C. Yuan, X. Feng, U. Scherf, Synergetic contribution of boron and Fe–N x species in porous carbons toward efficient electrocatalysts for oxygen reduction reaction, ACS Energy Letters, 3 (2017) 252-260.

[320] Y. Mun, S. Lee, K. Kim, S. Kim, S. Lee, J.W. Han, J. Lee, Versatile strategy for tuning ORR activity of a single Fe-N4 site by controlling electron-withdrawing/donating properties of a carbon plane, Journal of the American Chemical Society, 141 (2019) 6254-6262.

[321] L. Zhao, Y. Zhang, L.-B. Huang, X.-Z. Liu, Q.-H. Zhang, C. He, Z.-Y. Wu, L.-J. Zhang, J. Wu, W. Yang, Cascade anchoring strategy for general mass production of high-loading single-atomic metal-nitrogen catalysts, Nature communications, 10 (2019) 1-11.

[322] D. Malko, A. Kucernak, T. Lopes, In situ electrochemical quantification of active sites in Fe–N/C non-precious metal catalysts, Nature communications, 7 (2016) 1-7.

[323] S.H. Lee, J. Kim, D.Y. Chung, J.M. Yoo, H.S. Lee, M.J. Kim, B.S. Mun, S.G. Kwon, Y.-E. Sung, T. Hyeon, Design principle of Fe–N–C electrocatalysts: how to optimize multimodal porous structures?, Journal of the American Chemical Society, 141 (2019) 2035-2045.

[324] X. Zhang, L. Truong-Phuoc, X. Liao, G. Tuci, E. Fonda, V. Papaefthymiou, S. Zafeiratos, G. Giambastiani, S. Pronkin, C. Pham-Huu, An Open Gate for High-Density Metal Ions in N-Doped Carbon Networks: Powering Fe–N–C Catalyst Efficiency in the Oxygen Reduction Reaction, ACS Catalysis, 11 (2021) 8915-8928.

[325] Y. Ye, F. Cai, H. Li, H. Wu, G. Wang, Y. Li, S. Miao, S. Xie, R. Si, J. Wang, Surface functionalization of ZIF-8 with ammonium ferric citrate toward high exposure of Fe-N active sites for efficient oxygen and carbon dioxide electroreduction, Nano Energy, 38 (2017) 281-289.

[326] D. Wyrzykowski, E. Hebanowska, G. Nowak-Wiczk, M. Makowski, L. Chmurzyński, Thermal behaviour of citric acid and isomeric aconitic acids, Journal of Thermal Analysis and Calorimetry, 104 (2011) 731-735.

[327] J. Wang, G. Wang, S. Miao, X. Jiang, J. Li, X. Bao, Synthesis of Fe/Fe3C nanoparticles encapsulated in nitrogen-doped carbon with single-source molecular precursor for the oxygen reduction reaction, Carbon, 75 (2014) 381-389.

[328] K.S. Sing, D. Everett, R. Haul, L. Moscou, R. Pierotti, J. Rouquerol, T. Siemieniewska, Reporting physisorption data for gas/solid systems with special reference to the determination of surface area and porosity (Recommendations 1984), Pure appl. chem, 57 (1985) 603-619.

[329] J.-C. Li, Z.-Q. Yang, D.-M. Tang, L. Zhang, P.-X. Hou, S.-Y. Zhao, C. Liu, M. Cheng, G.-X. Li, F. Zhang, N-doped carbon nanotubes containing a high concentration of single iron atoms for efficient oxygen reduction, NPG Asia Materials, 10 (2018) e461-e461.

[330] X. Fu, N. Li, B. Ren, G. Jiang, Y. Liu, F.M. Hassan, D. Su, J. Zhu, L. Yang, Z. Bai, Fuel Cells: Tailoring FeN4 Sites with Edge Enrichment for Boosted Oxygen Reduction Performance in Proton Exchange Membrane Fuel Cell (Adv. Energy Mater. 11/2019), Advanced Energy Materials, 9 (2019) 1970031.

[331] C. Genovese, M.E. Schuster, E.K. Gibson, D. Gianolio, V. Posligua, R. Grau-Crespo, G. Cibin, P.P. Wells, D. Garai, V. Solokha, Operando spectroscopy study of the carbon dioxide electro-reduction by iron species on nitrogen-doped carbon, Nature communications, 9 (2018) 1-12.

[332] Y. Chen, Z. Li, Y. Zhu, D. Sun, X. Liu, L. Xu, Y. Tang, Atomic Fe Dispersed on N‐Doped Carbon Hollow Nanospheres for High‐Efficiency Electrocatalytic Oxygen Reduction, Advanced Materials, 31 (2019) 1806312.

[333] J. Gu, C.-S. Hsu, L. Bai, H.M. Chen, X. Hu, Atomically dispersed Fe3+ sites catalyze efficient CO2 electroreduction to CO, Science, 364 (2019) 1091-1094.

[334] T.N. Huan, N. Ranjbar, G. Rousse, M. Sougrati, A. Zitolo, V. Mougel, F. Jaouen, M. Fontecave, Electrochemical reduction of CO2 catalyzed by Fe-NC materials: A structure–selectivity study, ACS catalysis, 7 (2017) 1520-1525.

[335] D.J. Wasylenko, C. Rodríguez, M.L. Pegis, J.M. Mayer, Direct comparison of electrochemical and spectrochemical kinetics for catalytic oxygen reduction, Journal of the American Chemical Society, 136 (2014) 12544-12547.

[336] Y. Feng, N. Alonso‐Vante, Nonprecious metal catalysts for the molecular oxygen‐reduction reaction, physica status solidi (b), 245 (2008) 1792-1806.

[337] F. Tuinstra, J.L. Koenig, Raman spectrum of graphite, The Journal of chemical physics, 53 (1970) 1126-1130.

[338] I. Herrmann, U. Kramm, J. Radnik, S. Fiechter, P. Bogdanoff, Influence of sulfur on the pyrolysis of CoTMPP as electrocatalyst for the oxygen reduction reaction, Journal of The Electrochemical Society, 156 (2009) B1283.

[339] L. Cançado, K. Takai, T. Enoki, M. Endo, Y. Kim, H. Mizusaki, A. Jorio, L. Coelho, R. Magalhaes-Paniago, M. Pimenta, General equation for the determination of the crystallite size L a of nanographite by Raman spectroscopy, Appl Phys Lett, 88 (2006) 163106.

[340] Q. Li, H. Liu, L.-C. Zhang, H. Chen, H. Zhu, Y. Wu, M. Xu, S.-J. Bao, Highly efficient Fe-NC oxygen reduction electrocatalyst engineered by sintering atmosphere, Journal of Power Sources, 449 (2020) 227497.

[341] H. Zhang, P. An, W. Zhou, B.Y. Guan, P. Zhang, J. Dong, X.W.D. Lou, Dynamic traction of lattice-confined platinum atoms into mesoporous carbon matrix for hydrogen evolution reaction, Science advances, 4 (2018) eaao6657.

[342] S. Hu, W. Ni, D. Yang, C. Ma, J. Zhang, J. Duan, Y. Gao, S. Zhang, Fe3O4 nanoparticles encapsulated in single-atom Fe–N–C towards efficient oxygen reduction reaction: Effect of the micro and macro pores, Carbon, 162 (2020) 245-255.

[343] S.T. Thompson, B.D. James, J.M. Huya-Kouadio, C. Houchins, D.A. DeSantis, R. Ahluwalia, A.R. Wilson, G. Kleen, D. Papageorgopoulos, Direct hydrogen fuel cell electric vehicle cost analysis: System and high-volume manufacturing description, validation, and outlook, Journal of Power Sources, 399 (2018) 304-313.

[344] M. Oezaslan, F. Hasche, P. Strasser, Pt-based core–shell catalyst architectures for oxygen fuel cell electrodes, The Journal of Physical Chemistry Letters, 4 (2013) 3273-3291.

[345] C. Chen, Y. Kang, Z. Huo, Z. Zhu, W. Huang, H.L. Xin, J.D. Snyder, D. Li, J.A. Herron, M. Mavrikakis, Highly crystalline multimetallic nanoframes with three-dimensional electrocatalytic surfaces, Science, 343 (2014) 1339-1343.

[346] C. Cui, L. Gan, H.-H. Li, S.-H. Yu, M. Heggen, P. Strasser, Octahedral PtNi nanoparticle catalysts: exceptional oxygen reduction activity by tuning the alloy particle surface composition, Nano letters, 12 (2012) 5885-5889.

[347] P. Song, M. Luo, X. Liu, W. Xing, W. Xu, Z. Jiang, L. Gu, Zn single atom catalyst for highly efficient oxygen reduction reaction, Advanced Functional Materials, 27 (2017) 1700802.

[348] J. Li, M. Chen, D.A. Cullen, S. Hwang, M. Wang, B. Li, K. Liu, S. Karakalos, M. Lucero, H. Zhang, Atomically dispersed manganese catalysts for oxygen reduction in proton-exchange membrane fuel cells, Nature Catalysis, 1 (2018) 935-945.

[349] X. Zhu, X. Tan, K.-H. Wu, C.-L. Chiang, Y.-C. Lin, Y.-G. Lin, D.-W. Wang, S. Smith, X. Lu, R. Amal, N, P co-coordinated Fe species embedded in carbon hollow spheres for oxygen electrocatalysis, Journal of Materials Chemistry A, 7 (2019) 14732-14742.

[350] P.G. Santori, F.D. Speck, J. Li, A. Zitolo, Q. Jia, S. Mukerjee, S. Cherevko, F. Jaouen, Effect of pyrolysis atmosphere and electrolyte pH on the oxygen reduction activity, stability and spectroscopic

signature of FeNx moieties in Fe-NC catalysts, Journal of The Electrochemical Society, 166 (2019) F3311.

[351] W. Liu, L. Zhang, X. Liu, X. Liu, X. Yang, S. Miao, W. Wang, A. Wang, T. Zhang, Discriminating catalytically active FeN x species of atomically dispersed Fe–N–C catalyst for selective oxidation of the C–H bond, Journal of the American Chemical Society, 139 (2017) 10790-10798.

[352] J. Li, H. Zhang, W. Samarakoon, W. Shan, D.A. Cullen, S. Karakalos, M. Chen, D. Gu, K.L. More, G. Wang, Thermally driven structure and performance evolution of atomically dispersed FeN4 sites for oxygen reduction, Angewandte Chemie, 131 (2019) 19147-19156.

[353] S. Sui, X. Wang, X. Zhou, Y. Su, S. Riffat, C.-j. Liu, A Comprehensive Review of Pt Electrocatalysts for the Oxygen Reduction Reaction: Nanostructure, Activity, Mechanism and Carbon Support in PEM Fuel Cells, J. Mater. Chem. A, 5 (2017) 1808-1825.

[354] R. Zhou, S.Z. Qiao, An Fe/N co-doped graphitic carbon bulb for high-performance oxygen reduction reaction, Chemical communications, 51 (2015) 7516-7519.

[355] Y. Jia, L. Zhang, A. Du, G. Gao, J. Chen, X. Yan, C.L. Brown, X. Yao, Defect graphene as a trifunctional catalyst for electrochemical reactions, Advanced materials, 28 (2016) 9532-9538.

[356] T.-N. Tran, M.Y. Song, K.P. Singh, D.-S. Yang, J.-S. Yu, Iron–polypyrrole electrocatalyst with remarkable activity and stability for ORR in both alkaline and acidic conditions: a comprehensive assessment of catalyst preparation sequence, Journal of Materials Chemistry A, 4 (2016) 8645-8657.

[357] J.L. Figueiredo, M. Pereira, M. Freitas, J. Orfao, Modification of the surface chemistry of activated carbons, carbon, 37 (1999) 1379-1389.

[358] T. Ivanova, K. Maslakov, S. Savilov, A. Ivanov, A. Egorov, R. Linko, V. Lunin, Carboxylated and decarboxylated nanotubes studied by X-ray photoelectron spectroscopy, Russian Chemical Bulletin, 62 (2013) 640-645.

[359] K.S. Sing, Reporting physisorption data for gas/solid systems with special reference to the determination of surface area and porosity (Recommendations 1984), Pure and applied chemistry, 57 (1985) 603-619.

[360] K. Blurton, An electrochemical investigation of graphite surfaces, Electrochimica Acta, 18 (1973) 869-875.

[361] M. Ferrandon, A.J. Kropf, D.J. Myers, K. Artyushkova, U. Kramm, P. Bogdanoff, G. Wu, C.M. Johnston, P. Zelenay, Multitechnique characterization of a polyaniline–iron–carbon oxygen reduction catalyst, The Journal of Physical Chemistry C, 116 (2012) 16001-16013.

[362] Q. Zhang, X. Tan, N.M. Bedford, Z. Han, L. Thomsen, S. Smith, R. Amal, X. Lu, Direct insights into the role of epoxy groups on cobalt sites for acidic H 2 O 2 production, Nature communications, 11 (2020) 1-11.

[363] E. Jung, H. Shin, B.-H. Lee, V. Efremov, S. Lee, H.S. Lee, J. Kim, W.H. Antink, S. Park, K.-S. Lee, Atomic-level tuning of Co–N–C catalyst for high-performance electrochemical H 2 O 2 production, Nature materials, 19 (2020) 436-442.

[364] X. Cheng, Z. Shi, N. Glass, L. Zhang, J. Zhang, D. Song, Z.-S. Liu, H. Wang, J. Shen, A review of PEM hydrogen fuel cell contamination: Impacts, mechanisms, and mitigation, Journal of Power Sources, 165 (2007) 739-756.

[365] D.-W. Wang, D. Su, Heterogeneous nanocarbon materials for oxygen reduction reaction, Energy & Environmental Science, 7 (2014) 576-591.

[366] J. Zhang, L. Dai, Heteroatom-doped graphitic carbon catalysts for efficient electrocatalysis of oxygen reduction reaction, ACS Catalysis, 5 (2015) 7244-7253.

[367] R. Ohnishi, Y. Takahashi, A. Takagaki, J. Kubota, K. Domen, Niobium oxides as cathode electrocatalysts for platinum-free polymer electrolyte fuel cells, Chemistry letters, 37 (2008) 838-839.

[368] G. Zhang, B.Y. Xia, X. Wang, X.W. Lou, Strongly coupled NiCo2O4 ‐ rGO hybrid nanosheets as a methanol ‐ tolerant electrocatalyst for the oxygen reduction reaction, Advanced materials, 26 (2014) 2408-2412.

[369] J. Guo, J. Huo, Y. Liu, W. Wu, Y. Wang, M. Wu, H. Liu, G. Wang, Nitrogen ‐ doped porous carbon supported nonprecious metal single ‐ atom electrocatalysts: from synthesis to application, Small Methods, 3 (2019) 1900159.

[370] X. Luo, X. Wei, H. Wang, W. Gu, T. Kaneko, Y. Yoshida, X. Zhao, C. Zhu, Secondary-atom-doping enables robust Fe–N–C single-atom catalysts with enhanced oxygen reduction reaction, Nano-Micro Letters, 12 (2020) 1-11.

[371] D. Ohms, S. Herzog, R. Franke, V. Neumann, K. Wiesener, S. Gamburcev, A. Kaisheva, I. Iliev, Influence of metal ions on the electrocatalytic oxygen reduction of carbon materials prepared from pyrolyzed polyacrylonitrile, Journal of power sources, 38 (1992) 327-334.

[372] A. Widelöv, R. Larsson, ESCA and electrochemical studies on pyrolysed iron and cobalt tetraphenylporphyrins, Electrochimica acta, 37 (1992) 187-197.

[373] G. Lalande, G. Faubert, R. Cote, D. Guay, J. Dodelet, L. Weng, P. Bertrand, Catalytic activity and stability of heat-treated iron phthalocyanines for the electroreduction of oxygen in polymer electrolyte fuel cells, Journal of power sources, 61 (1996) 227-237.

[374] D. Liu, C. Wu, S. Chen, S. Ding, Y. Xie, C. Wang, T. Wang, Y.A. Haleem, Z. ur Rehman, Y. Sang, In situ trapped high-density single metal atoms within graphene: Iron-containing hybrids as representatives for efficient oxygen reduction, Nano Research, 11 (2018) 2217-2228.

[375] Q. Lai, Q. Su, Q. Gao, Y. Liang, Y. Wang, Z. Yang, X. Zhang, J. He, H. Tong, In situ self-sacrificed template synthesis of Fe-N/G catalysts for enhanced oxygen reduction, ACS applied materials & interfaces, 7 (2015) 18170-18178.

[376] J. Shui, M. Wang, F. Du, L. Dai, N-doped carbon nanomaterials are durable catalysts for oxygen reduction reaction in acidic fuel cells, Science advances, 1 (2015) e1400129.

[377] H. Ba, J. Luo, Y. Liu, C. Duong-Viet, G. Tuci, G. Giambastiani, J.-M. Nhut, L. Nguyen-Dinh, O. Ersen, D.S. Su, C. Pham-Huu, Macroscopically shaped monolith of nanodiamonds @ nitrogen-enriched mesoporous carbon decorated SiC as a superior metal-free catalyst for the styrene production, Applied Catalysis B: Environmental, 200 (2017) 343-350.

[378] H. Ba, Y. Liu, L. Truong-Phuoc, C. Duong-Viet, X. Mu, W.H. Doh, T. Tran-Thanh, W. Baaziz, L. Nguyen-Dinh, J.M. Nhut, I. Janowska, D. Begin, S. Zafeiratos, P. Granger, G. Tuci, G. Giambastiani, F. Banhart, M.J. Ledoux, C. Pham-Huu, A highly N-doped carbon phase "dressing" of macroscopic supports for catalytic applications, Chem Commun (Camb), 51 (2015) 14393-14396.

[379] H. Ba, Y. Liu, W. Wang, C. Duong-Viet, V. Papaefthimiou, L. Nguyen-Dinh, G. Tuci, G. Giambastiani, C. Pham-Huu, Carbon Felt Monoliths Coated with a Highly Hydrophobic Mesoporous Carbon Phase for the Continuous Oil Sorption/Filtration from Water, Advanced Sustainable Systems, 2 (2018) 1800040.

[380] H. Ba, L. Truong-Phuoc, Y. Liu, C. Duong-Viet, J.-M. Nhut, L. Nguyen-Dinh, P. Granger, C. Pham-Huu, Hierarchical carbon nanofibers/graphene composite containing nanodiamonds for direct dehydrogenation of ethylbenzene, Carbon, 96 (2016) 1060-1069.

[381] Y. Liu, H. Ba, J. Luo, K.-H. Wu, J.-M. Nhut, D.S. Su, C. Pham-Huu, Structure-performance relationship of nanodiamonds @ nitrogen-doped mesoporous carbon in the direct dehydrogenation of ethylbenzene, Catalysis Today, 301 (2018) 38-47.

[382] H. Ba, S. Podila, Y. Liu, X. Mu, J.-M. Nhut, V. Papaefthimiou, S. Zafeiratos, P. Granger, C. Pham-Huu, Nanodiamond decorated few-layer graphene composite as an efficient metal-free dehydrogenation catalyst for styrene production, Catalysis Today, 249 (2015) 167-175.

[383] W. Yang, X. Liu, X. Yue, J. Jia, S. Guo, Bamboo-like carbon nanotube/Fe3C nanoparticle hybrids and their highly efficient catalysis for oxygen reduction, Journal of the American Chemical Society, 137 (2015) 1436-1439.

[384] Y. Li, H. Huang, S. Chen, X. Yu, C. Wang, T. Ma, 2D nanoplate assembled nitrogen doped hollow carbon sphere decorated with Fe 3 O 4 as an efficient electrocatalyst for oxygen reduction reaction and Zn-air batteries, Nano Research, 12 (2019) 2774-2780.

[385] Y. Su, H. Jiang, Y. Zhu, X. Yang, J. Shen, W. Zou, J. Chen, C. Li, Enriched graphitic N-doped carbon-supported Fe 3 O 4 nanoparticles as efficient electrocatalysts for oxygen reduction reaction, Journal of Materials Chemistry A, 2 (2014) 7281-7287.

[386] H. Wang, W. Wang, M. Gui, M. Asif, Z. Wang, Y. Yu, J. Xiao, H. Liu, Uniform Fe3O4/nitrogen-doped mesoporous carbon spheres derived from ferric citrate-bonded melamine resin as an efficient synergistic catalyst for oxygen reduction, ACS applied materials & interfaces, 9 (2017) 335-344.

[387] Z. Li, L. Wei, W.-J. Jiang, Z. Hu, H. Luo, W. Zhao, T. Xu, W. Wu, M. Wu, J.-S. Hu, Chemical state of surrounding iron species affects the activity of Fe-Nx for electrocatalytic oxygen reduction, Applied Catalysis B: Environmental, 251 (2019) 240-246.

[388] Y. Zhang, J. Liu, G. Wu, W. Chen, Porous graphitic carbon nitride synthesized via direct polymerization of urea for efficient sunlight-driven photocatalytic hydrogen production, Nanoscale, 4 (2012) 5300-5303.

[389] F. Pan, W. Deng, C. Justiniano, Y. Li, Identification of champion transition metals centers in metal and nitrogen-codoped carbon catalysts for CO2 reduction, Applied Catalysis B: Environmental, 226 (2018) 463-472.

[390] A.A. Eissa, S.G. Peera, N.H. Kim, J.H. Lee, gC 3 N 4 templated synthesis of the Fe 3 C@ NSC electrocatalyst enriched with Fe–N x active sites for efficient oxygen reduction reaction, Journal of Materials Chemistry A, 7 (2019) 16920-16936.

[391] G. Ouedraogo, D. Benlian, L. Porte, X‐ray photoelectron spectroscopy of phthalocyanine compounds, The Journal of Chemical Physics, 73 (1980) 642-647.

[392] R.-X. Wang, X.-D. Yang, L.-Y. Wan, B.-A. Lu, L.-F. Shen, Y.-Y. Li, S.-G. Sun, Z.-Y. Zhou, Graphene-covered FePc as a model of the encapsulated type of catalyst for the oxygen reduction reaction, Electrochemistry Communications, 112 (2020) 106670.

[393] Q. Wang, M. Chen, P. Lin, Z. Cui, C. Chu, B. Shen, Investigation of FePC amorphous alloys with self-renewing behaviour for highly efficient decolorization of methylene blue, Journal of Materials Chemistry A, 6 (2018) 10686-10699.

[394] M.S. Thorum, J.M. Hankett, A.A. Gewirth, Poisoning the oxygen reduction reaction on carbon-supported Fe and Cu electrocatalysts: evidence for metal-centered activity, The Journal of Physical Chemistry Letters, 2 (2011) 295-298.

[395] X. Zhang, Y.B. Mollamahale, D. Lyu, L. Liang, F. Yu, M. Qing, Y. Du, X. Zhang, Z.Q. Tian, P.K. Shen, Molecular-level design of Fe-NC catalysts derived from Fe-dual pyridine coordination complexes for highly efficient oxygen reduction, Journal of Catalysis, 372 (2019) 245-257.

[396] G. Gulino, R. Vieira, J. Amadou, P. Nguyen, M.J. Ledoux, S. Galvagno, G. Centi, C. Pham-Huu, C2H6 as an active carbon source for a large scale synthesis of carbon nanotubes by chemical vapour deposition, Applied Catalysis A: General, 279 (2005) 89-97.

[397] L. Li, Y. Li, Y. Xiao, R. Zeng, X. Tang, W. Yang, J. Huang, K. Yuan, Y. Chen, Fe 3 O 4-Encapsulating N-doped porous carbon materials as efficient oxygen reduction reaction electrocatalysts for Zn–air batteries, Chemical Communications, 55 (2019) 7538-7541.

[398] J. LH, L. JL, Ionic Liquids as Precursors for Efficient Mesoporous Iron-Nitrogen-Doped Oxygen Reduction Electrocatalyst, (2014).